

# Thermal Sprayed Coatings for Tribological Applications and Corrosion Protection in Hydroelectric Power Stations

Alexandre Romão Costa Nascimento

A Thesis  
In the Department  
Of  
Mechanical, Industrial and Aerospace Engineering

Presented in Partial Fulfillment of the Requirements  
For the Degree of  
Doctor of Philosophy (Mechanical Engineering) at  
Concordia University  
Montreal, Québec, Canada

March 2019

©Alexandre Romão Costa Nascimento 2019

**Concordia University  
School of Graduate Studies**

This it to certify that the thesis prepared

By: Alexandre Romão Costa Nascimento

Entitled: Thermal Sprayed Coatings for Tribological Applications and Corrosion Protection in Hydroelectric Power Stations

and submitted in partial fulfillment of the requirements for the degree of

**Doctor of Philosophy**

complies with the regulations of the University and meets the accepted standards with respect to originality and quality.

Signed by the final examining committee:

_____	Chair
Dr. Leila Kosseim	
_____	External Examiner
Dr. Fardad Azarmi, North Dakota State University	
_____	External to Program
Dr. Saifur Rahaman, Building Civil and Environmental Engineering	
_____	Examiner
Dr. Martin Pugh, Mechanical, Industrial and Aerospace Engineering	
_____	Examiner
Dr. Ali Dolatabadi, Mechanical, Industrial and Aerospace Engineering	
_____	Thesis Supervisor
Dr. Christian Moreau, Mechanical, Industrial and Aerospace Engineering	
_____	Thesis Supervisor
Dr. Robert Schulz, Institut de Recherche d'Hydro-Québec	

Approved by \_\_\_\_\_  
Dr. Ivan Contreras, Graduate Program Director

24/04/2019  
Date of Defence \_\_\_\_\_  
Dr. Amir Asif ,Dean, Gina Cody School of Engineering and Computer Science

## **ABSTRACT**

# **Thermal Sprayed Coatings for Tribological Applications and Corrosion Protection in Hydroelectric Power Stations**

**Alexandre Romão Costa Nascimento, PhD**  
**Concordia University, 2019**

In the context of global warming, the life-cycle and reliability of machine parts supporting hydroelectric turbine structures cannot be overlooked. The advent of surface engineering provides useful venues for engineers to ensure a safe and long-lasting supply of green energy. In this work, thermal spraying was proposed as a method to develop coatings with high tribological performance and corrosion protection for key components in hydroelectric power stations.

The work is structured in three main sections. The first concerns the development of Sn-alloy coatings, used in large thrust bearings. It was shown that high-density sprayed coatings can be produced if proper control of particle size and velocities are used.

In the second section, chemical leaching is proposed as a method to create porous coatings to bond a high-performance polymer to an underlying bearing pad. A metallic pore former is mixed and sprayed along with stainless steel particles. An optimal combination of matrix and pore former particles allowed the successful infiltration of a self-lubricating polymer in pore openings as narrow as 10  $\mu\text{m}$ .

The final section of the work concerns the behavior of sprayed stainless steel coatings in Cl-ion rich aqueous solution. It was demonstrated that the substantial drop in the corrosion resistance of the coatings compared to wrought materials is mostly due to the high density of coating defects, including pores and oxides. The changes in the electrochemical behavior during the first week of immersion was attributed to surface chemistry changes including enrichment in Cr-oxides and the dissolution of active phases.

## **Acknowledgements**

My deepest gratitude to Dr. Robert Schulz for providing me with the unique opportunity to pursue my research career in a new country. I am forever indebted to his gestures of trust and openness.

I would like to express my thanks to Dr. Christian Moreau, for his leadership and guidance, his patience, friendliness, and for offering me with opportunities that goes beyond the academic environment. I could not have asked for a better supervisor.

My sincerest thanks to my colleagues sharing the daily routines of the laboratory. If not for Dr. Fadhel Ben Ettouil, Silvio Savoie, and Dr. Robert Lacasse, this work would have never been finished. Their knowledge and devotion to their roles has served me as inspiration.

My recognition to l'Institut de Recherche d'Hydro-Québec (IREQ) and to Concordia University for providing me with excellent research facilities.

Warm thanks to my parents who always encouraged me in my studies and to my wife Rie Maeda, for her love and for understanding the challenges involved in the obtention of a doctoral degree.

# Table of Contents

List of Figures .....	vii
List of Tables .....	x
Introduction .....	1
Chapter 1 – Thermal Spraying .....	4
1.1 Plasma Spraying.....	5
1.2 Arc Spraying .....	5
1.3 Flame Spraying.....	5
1.4 High-velocity Oxygen Fuel (HVOF) or Air Fuel (HVAF) Spraying .....	5
1.5 Cold Spray .....	6
1.6 HVOF Process Description and Spray Parameters .....	6
1.7 In-Flight Particle Characterization .....	9
Chapter 2 – Surface Engineering of Thrust Bearings .....	12
2.1 Thrust Bearings in Hydropower.....	12
2.2 Production of Babbitt Coatings by High-Velocity Oxygen Fuel Spraying .....	15
2.2.1 Introduction.....	15
2.2.2 Methodology .....	17
2.2.3 Results and Discussion.....	20
2.2.4 Summary and Conclusions .....	28
2.3 Tailored Porosity for Polymer Infiltration in Stainless Steel Coatings.....	29
2.3.1 Introduction.....	29
2.3.2 Experimental Methods .....	30
2.3.3 Results.....	36
2.3.4 Discussion .....	47
2.3.5 Conclusions .....	50
Chapter 3 – Corrosion Resistance of Thermally Sprayed Coatings.....	51
3.1 Basic Electrochemistry Concepts.....	51
3.2 Corrosion Resistance of Thermally Sprayed Coatings .....	58
3.3 Changes in the Electrochemical Behavior, Microstructure and Surface Chemistry of Stainless-Steel Coatings .....	61
3.3.1 Introduction.....	61
3.3.2 Materials and Methods.....	62
3.3.3 Results.....	66
3.3.4 Discussion .....	83

3.3.5	Conclusions .....	86
4.	Concluding Remarks and Suggestions for Future Work .....	87
	References .....	90
	Appendix A – Processing of Polyimide Composites .....	99
	Appendix B – Supplementary Material: Corrosion of Thermally Sprayed Stainless Steel Coatings.....	106

## List of Figures

Figure 1 – Schematic illustration of a hydroelectric power station. Part of the unit’s axial loads are supported by a thrust bearing, which consists of several bearing pads. ....	1
<i>Figure 2 – Typical range of in-flight particle temperatures and velocities for several thermal spray processes. Adapted from [18]. ....</i>	<i>4</i>
Figure 3 – Cross section schematics of the spray torches used for the development of this work. ....	6
Figure 4 – Gas flow and particle interactions for gas-fueled HVOF determined by CFD [22].....	8
Figure 5 – The methods used to determine in-flight particle velocity differ in each diagnostics tool. In DPV-evolution a two-slit mask is used to control the signal from individual particles. In Accuraspray, a large group of particles generate signals at two well-defined positions. ....	10
Figure 6 – In thermal spraying, the two-color pyrometry technique is used to determine particle in-flight temperature. The ratio of the thermal radiation intensity measured at two similar wavelengths has a monotonic increase with temperature. In this figure, the units are arbitrary. ....	11
Figure 7 – Oil pressure distribution in a hydrodynamic bearing .....	12
Figure 8 – Cross section images of PTFE-lined (left) and PEEK-lined (right) thrust bearings. Extracted from [5].....	14
Figure 9 – Schematic illustration of the failure mode observed in porous babbitt coatings deposited by arc spraying.....	16
Figure 10 – Babbitt feedstock morphology and size distribution. The fine particles have $D_{50} = 80 \pm 18 \mu\text{m}$ while the coarse particles have $D_{50} = 127 \pm 35 \mu\text{m}$ .....	18
<i>Figure 11 – Assessment of particle thermal radiation emission by means of Accuraspray CCD camera.....</i>	<i>21</i>
<i>Figure 12 – Surface of Babbitt coatings produced at different spray parameters: (left) high heat; (right) low heat. ....</i>	<i>22</i>
Figure 13 – Effect of flame heat on babbitt particle in-flight velocity .....	22
<i>Figure 14 – Correlation between deposition efficiency and particle velocity for six different spray tests. ....</i>	<i>23</i>
<i>Figure 15 - Polished cross section image of Babbitt coatings produced by casting, flame spraying, arc spraying and HVOF (as produced with low heat and coarse particles). ....</i>	<i>25</i>
<i>Figure 16 – Intermetallic phase distribution in Babbitt coatings produced by casting, flame spraying, arc spraying and HVOF (as produced with low heat and coarse particles). ....</i>	<i>26</i>
<i>Figure 17 - Indentation imprint on the Arc Sprayed Babbitt Coating. The fine intermetallics offer little resistance to the indentation imprint.....</i>	<i>27</i>
Figure 18- Morphology of SS444 and Fe <sub>3</sub> Al particles. (a) Atomized & sieved SS444. (b) Atomized & sieved (fine) Fe <sub>3</sub> Al. (c) Milled 6h and sieved SS444. (d) Atomized and sieved (coarse)Fe <sub>3</sub> Al. (e) Milled (8h) and sieved 444. (f) Milled (9h) and sieved Fe <sub>3</sub> Al. ....	32

Figure 19- Composite HVOF coating during the leaching procedure. A black sealing paint was brushed around the disk edges to prevent from chemical attack at the coating/substrate interface, which limited the exposed coating surface area to the solution. ....35

*Figure 20 - As-sprayed structure of LH coatings. The coarse stainless steel particles experience little in-flight melting as opposed to the Fe<sub>3</sub>Al pore former, which appears to melt completely. As a result, the coating composite structure is comprised of deformed semi-molten SS444 splats (highlighted in red) surrounded by a Fe<sub>3</sub>Al network. ....37*

Figure 21 - As-sprayed structure of HL coatings. The coarse Fe<sub>3</sub>Al pore former particles (highlighted in red) did not melt prior to deposition contrary to the SS444 splats, which seem to have experienced melting and high-temperature oxidation.....39

Figure 22 - As-sprayed structure of the HH coatings. Both matrix and pore forming phases experience a high melting degree creating the typical “splat pile-up” structure. ....40

Figure 23 – Comparison between as-sprayed and etched cross sections of coating LH(70/30). The Fe<sub>3</sub>Al pore former dissolves more quickly than the SS444 matrix. The areas highlighted in red used in the image analysis procedure correspond to the pores found in the as-sprayed and etched coatings. ....42

Figure 24 – The leaching process in the LH coatings leads to the formation of poorly bonded SS444 splats that may be easily detached from the underlying coating. (a) The low volume fraction of Fe<sub>3</sub>Al in LH(90/10) leads to localized leaching zones (dashed lines). (b) Even after three hours most of the Fe<sub>3</sub>Al remains in the LH(70/30 coating). ....43

Figure 25 – The leaching process in the HL group of coatings leads to the formation of thin sheathes of SS444 surrounding large pores. After three hours the sheathes are no longer observed, possibly due to their chemical degradation and impaired mechanical integrity.....44

*Figure 26 – The leaching process in the HH group of coatings is more homogenous. Both the SS444 and Fe<sub>3</sub>Al splats are leached in the solution and while a porous layer forms after two hours of immersion, its mechanical properties are insufficient to withstand the loads applied during the sectioning and polishing. ....44*

Figure 27 - Leaching at 45 °C increases the leaching rate and different pore sizes and morphologies may be achieved depending on the feedstock. ....46

Figure 28 - Polyimide-infiltrated LH(70/30) coating. The PI-25wt.%Graphite mixture penetrates most of the leached coating pore network. It is possible to observe some Al-rich residues that were not completely removed after leaching. The regions in the dashed circles indicate regions of splat coalescence caused by the sintering heat-treatment. ....47

Figure 29 – This diagram qualitatively depicts the role of feedstock condition on the outcome of spraying a mixture of particles containing a matrix and a leachable pore former. The diameter ratio controls the pore geometry and may interfere on coating deposition efficiency. The pore former volume fraction affects the mean coordination numbers, hence interfering with the leaching behavior and the as-leached final mechanical properties. ....49

*Figure 30 – Polarization behavior for an idealized corrosion processes. ....53*

*Figure 31 – Complex, phase angle and magnitude impedance plots for two hypothetical faradaic reactions modelled by a Randles circuit. ....56*

<i>Figure 32 – Illustration of the graphical method used to calculate the WE’s CPE exponent <math>\alpha</math> and effective capacitance (CPE parameter Q) for case B.</i> .....	57
Figure 33 – Effect of electrode potential on the loop diameters measured in a complex plot of porous nickel electrodes in 1M NaOH solution. Extracted from [114]. .....	60
Figure 34 – The flowchart illustrates the preparation and characterization steps to which each coating was subject.....	65
Figure 35 - Effect of spray parameters on the in-flight particle temperature and velocity. The results are grouped according to levels of combustion pressure and O/F Ratio. Each error bars correspond to two standard deviations calculated for 1000 particles. ....	66
Figure 36 - (a)Small Si-rich precipitates (highlighted in dashed-line circles) can be found in the powder feedstock as well as in the sprayed coatings. EDX analysis reveals that the precipitates are rich in Si, Mn and O when compare with the neighbouring areas. (b) The coatings main microstructural features are highlighted and include semi-molten splats (circled in yellow) surrounded by a re-solidified zone containing oxides and pores. ....	68
Figure 37 – As-sprayed SS444 coating microstructures contain similar microstructural features including semi-molten splats, a re-solidified zone containing splats and oxides and finally, pores which are particularly present at coating HVOF #5.....	70
Figure 38 - The arc melted SS444 showed a dense structure. However, a few pores were observed due to the presence of air entrapped in the melt pool. Moreover, some Cr-rich precipitates formed. The arrows indicate the position where the EDX analysis was carried out.	73
Figure 39 – Polarisation curves measured for a bulk SS444, a HVOF-sprayed coating and a sample produced by arc melting the spray feedstock.....	74
Figure 40 – Evolution of the stainless steel coating’s parameters (a) corrosion potential, (b) corrosion current, (c) cathodic slope, (d) anodic slope. The dashed line corresponds to the averaged values of all coatings. ....	75
Figure 41 – (a) 3-week evolution of impedance spectra for coating HVOF #1. (b) Effect of spray parameters on EIS spectra after 1 hour and after 3 weeks of immersion.....	76
Figure 42 – Fitting of the Randles circuit to the impedance spectra of coatings in two instances. ....	77
Figure 43 - 3-week evolution of the EIS analog circuit element values used to model the sprayed stainless steel coatings. The electrolyte resistance values (not plotted) ranged between 9.8 – 11 $\Omega \cdot \text{cm}^2$ . ....	78
Figure 44 – Effect of electrode potential on the EIS spectra of HVOF and HVAF coatings.....	79
Figure 45 – Change of coating HVOF #3 surface features with prolonged exposure to the test solution. Metal dissolution and the formation of corrosion products occur preferably at the re-solidified zones while the semi-molten splats remain unchanged.....	80
Figure 46 – Formation of micropits on the splats of coating HVAF #1. ....	81
Figure 47 - High resolution of Cr oxidation state on the surface of stainless steel surfaces. The grey lines indicate which peaks are used for spectra deconvolution. The red line is the resulting of the three peaks. ....	83

Figure 48 - Synthesis of BMI by chemical dehydration of bismaleamic acid. The symbol (CO-M) represents an aromatic co-monomer [136].	99
Figure 49 - 3D model of the mold used to produce PI composites in manual preparation and hot pressing I methods.	100
Figure 50 - 3D model of the mold used to produce PI composites in hot pressing II method.	101
Figure 51 - Porosity present in the cross section of PI discs prepared by the manual method.	101
Figure 52 - Formation of gases during PI polymerization at 132 C in vacuum. (a) Pre-compacted pure PI powder. (b) As-molten PI. (c) Formation and coalescing of gas bubbles. The time span between (b) and (c) is approximately 30 minutes.	102
Figure 53 - The BMI resin can penetrate the narrow pores of the stainless steel coating by capillarity.	103
Figure 54 - Two examples of PI+Gr-infiltrated coatings produced with method hot pressing I. The different results are attributed to poor control of pressure and heat transfer from the platens to the PI composite.	104
Figure 55 - The heat transfer rates have a drastic effect on the polymerization of the BMI. Both discs were produced with the same quantity of PI powder. The PI disc on the left was produced in contact with a stainless steel lid, which increased the heat transfer from the furnace to the powder bed.	104
Figure 56 - Bulk PI sections produced with method hot pressing II.	105
Figure 57 - Arc melt furnace chamber containing a water-cooled Cu substrate, a titanium oxygen getter and a tungsten electrode.	106
Figure 58 - Application of a simple kinetic model to describe the effect of an applied potential to the impedance spectra of a hypothetical interface with $i_{corr} = 1 \times 10^{-4} \text{ A.cm}^{-2}$ , $\beta_a = 0.05 \text{ V.dec}^{-1}$ , $\beta_c = 0.5 \text{ V.dec}^{-1}$ , electrolyte resistance $R_e = 10 \text{ } \Omega.\text{cm}^{-2}$ and double-layer capacitance $C_{dl} = 20 \text{ } \mu\text{F.cm}^{-2}$ . Notice that each loop in the complex plot corresponds to a potential value highlighted in the polarization curve.	107
Figure 59 - (a) Sectioned coating HVOF #1 after the 3-week test period. The dashed red line separates the center exposed to the electrochemical tests, and the outer area, covered by the sample holder's O-ring. The dashed black circle highlights a blister which is magnified in (b) by means of a confocal microscope.	108

## List of Tables

Table 1 - Gas flow rates used during HVOF spray of BatTec® 29240 powder.	19
Table 2 - Microhardness results measured by instrumented vickers indentation. Error corresponds to the standard deviation.	27
Table 3 - Summary of powder fabrication method and particle size distribution.	31
Table 4 - Chemical composition of SS444 and Fe <sub>3</sub> Al milled powders as measured by EDX analysis.	33

<i>Table 5 - Coating identification with corresponding powder blends and volume fractions of SS444 and Fe<sub>3</sub>Al. ....</i>	<i>34</i>
<i>Table 6 – Spray parameters used to produce composite SS444/Fe<sub>3</sub>Al coatings. ....</i>	<i>34</i>
<i>Table 7 - Summary of composite coatings thicknesses and deposition efficiencies. *Only five passes were done for coating LH (50/50). **Only eight spray passes were done for coating HH(50/50). ....</i>	<i>41</i>
<i>Table 8 - Nominal composition of a bulk SS444. The * indicates the maximum element in wt.% the steel should bare. ....</i>	<i>63</i>
<i>Table 9 – Summary of the spray parameters used for HVOF and HVOF spraying. ....</i>	<i>63</i>
<i>Table 10 – In-flight particle temperatures and velocities used for coating deposition. The term s corresponds to the sample standard deviation. The substrate temperature was taken on the coating surface immediately after the end of the spray deposition. ....</i>	<i>67</i>
<i>Table 11 - Area fraction of coating microconstituents as determined by image analysis. ....</i>	<i>71</i>
<i>Table 12 - EDX analysis performed over the coatings microconstituents as well as over a 260 x 180 μm<sup>2</sup> area. Reported values with * were detected once or twice out of the three measurements ....</i>	<i>72</i>
<i>Table 13 – Survey XPS analysis of the investigated materials. ....</i>	<i>82</i>
<i>Table 15 - Summary of the ball-on-disk test results performed on PI discs produced manually. ....</i>	<i>102</i>

## Introduction

Global warming effects are pushing society into a quick transition from fossil to renewable energy sources. In this context, hydroelectric power stations are expected to produce more energy, for longer periods, and with minimum maintenance. If such goals are to be achieved, reliability and life of components such as turbines, guide vanes, and bearings must be ensured by careful design steps, which may include the use of novel material processing technologies to avoid component failure.

Common causes for hydroelectric turbine failures include cavitation (formation and collapse of high pressure bubbles) and erosion caused by the presence of silt in water [1]. Improved turbine design or the use of de-silting chambers are typical preventive measures that attenuate the wear process. Prolonged effects of erosion and cavitation are often remediated by weld overlay deposition which, due to the process high heat input, affect the base metal's corrosion resistance, eventually leading to catastrophic failure [2], [3]. Modern surface engineering technologies like thermal spray enables the deposition of erosion-corrosion resistant coatings [4] with a much decreased heat load on the substrate.

Apart from turbines, other machine elements compose the structure of hydroelectric stations. For example, thrust bearings are used to hold the axial loads generated by the weight of the entire power unit, including the turbine and the generator (Figure 1). Their operation principle is based on hydrodynamic lubrication (further discussed in Chapter 2), in which an oil film with a thickness of a few tens of microns withstands axial loads that may be as high as 6000 tons [5]. The load is distributed over several tilting pads positioned around the shaft.

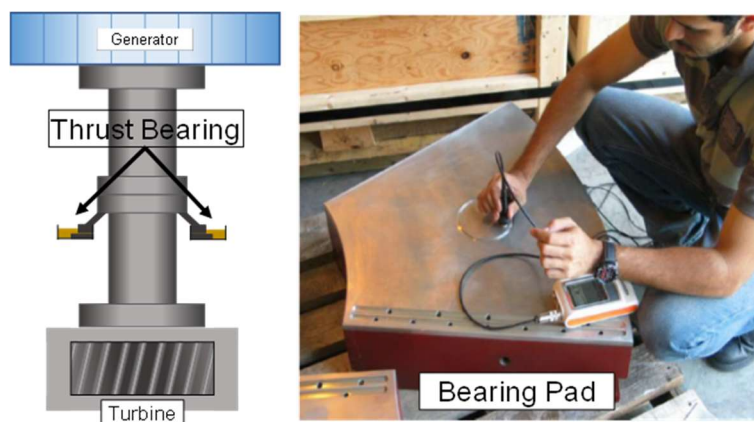


Figure 1 – Schematic illustration of a hydroelectric power station. Part of the unit's axial loads are supported by a thrust bearing, which consists of several bearing pads.

Failure of large thrust bearings are often related to high oil temperature [6]–[8], which may exceed the operation limit of the bearing lining, usually made of Sn-based alloys known as white metal or babbitt. Though the introduction of polymer-lined bearings starting in the 70's [9] has led to substantial improvements in load bearing capacity and operation temperature limits, babbitt-lined bearings are still easily found in operation in several instances. For example, Hydro Québec recent investigations on the failure of thrust bearings [10] revealed that some of the thermally sprayed babbitt linings were excessively porous, probably due to poor process control. In fact, it was found that scientific literature on the methodology to produce babbitt coatings by thermal spray was very scarce.

The integration of intermittent power sources (solar and wind) to the electrical grid had created new challenges for hydropower stations. In some turbine units, the flow of water through guide vanes must be constantly adjusted to compensate for the inconsistent supply from renewable sources. The frequent sliding of guide vanes has substantially increased concerns about the wear rates of their self-lubricated (or greaseless) bearings [11]–[13]. Self-lubricated bearings are often composed of several materials that combine a matrix providing load-bearing capacity and solid lubricants such as graphite and poly-tetrafluoroethylene (PTFE) which must be carefully chosen based on the operation conditions. Their manufacturing often involves filament weaving or powder-metallurgy techniques, but several reports show that thermal spray can also be used for that same purpose [14]–[16].

It may be stated that the versatility of thermal spray can be beneficial for several engineering components of hydropower stations. In the present thesis, three applications for sprayed coatings were identified as potentially valuable for hydroelectric production units:

- the production of dense babbitt coatings by improved process parameter control;
- creation of coatings with tailored porosity for self-lubricant, polymer-lined bearings and;
- development of corrosion-resistant surfaces for extension of component lifecycle.

These three material issues were explored in three different manuscripts.

In Chapter 1, a brief introduction to thermal spraying is presented. Different techniques are compared in terms of temperatures and velocities that may be transferred from gases to the in-flight particles. The relevance of important spray parameters to the final coating properties are discussed. Finally, an introduction to the working principles of diagnostic tools used to characterize in-flight particle temperatures and velocities is presented.

In Chapter 2, an introduction on the operation principles and manufacturing methods used to produce hydrodynamic thrust bearings is presented. The first manuscript of the present thesis discusses the use of high-velocity spray techniques to create dense Sn-alloy coatings. The use of different spray parameters and feedstock size distributions were correlated to process efficiency, in-flight particle properties as well as to the final coating structure and porosity. The second manuscript of the thesis deals with the production of porous stainless steel coatings that serve as a bond coat between bearing pads and a polymeric lining. A metallic pore former is mixed with a stainless steel powder in different volume fractions and particle size distributions, in a total of 9 different blends. The composite coatings are then immersed in an acidic solution to leach the pore former. The effects of leaching temperature and time are investigated. Optimal feedstock mixing conditions are discussed.

In Chapter 3, basic electrochemistry principles used for polarization and impedance spectroscopy tests are introduced. Then, a literature review on the corrosion resistance of thermally sprayed coatings is presented, identifying the points requiring further scientific investigation. In the third manuscript of this thesis, spray parameters were carefully investigated so that stainless steel coatings could be produced with a wide range of in-flight temperatures and velocities. The electrochemical behavior of the coatings was monitored for 3 weeks and compared to a wrought steel plate of same nominal composition. By arc melting the feedstock into a solid disc, another material of reference was created. Changes in the electrode microstructural features and surface chemistry were monitored by microscopy and x-ray photoelectron spectroscopy.

A general thesis conclusion is presented in Chapter 4. Finally, in Chapter 5 the thesis main contributions and suggestions for future work are presented.

In Appendix A, the challenges involving the production of dense polymeric linings for thrust bearings are analyzed. Preliminary tribological tests are also available. In Appendix B supporting information for the third manuscript is provided.

## Chapter 1 – Thermal Spraying

Generally, thermal spraying consists in injecting a powder (metal, ceramic or polymer) in a stream of high-temperature, high-speed gases. The particles heat, eventually melt, and accelerate before impacting in a substrate, where they quickly solidify and anchor. The resulting coating structure can be highly heterogeneous, containing:

- **Splats:** lamellar solid formed upon impact and solidification of a molten droplet;
- **Unmolten or partially molten particles;**
- **Oxides:** that may have been intentionally added to the spraying powder or formed in-flight during exposure to the high-temperature gases;
- **Pores.**

Thermal spray coatings are applied in a myriad of different environments, from orthopedic implants to high-temperature gas turbines. There are several different spraying techniques, each one adapted and optimized to different coating requirements. For example, ceramic coatings are usually produced by plasma spraying, due to its ability to generate extremely hot gases (7000 – 8000 K) [17], capable of melting highly stable ceramics such as alumina or titania. When coatings are required to be as dense as possible, techniques such as high velocity oxygen fuel (HVOF) are capable of accelerating particles up to 800 m/s. It is useful to classify thermal spray processes by the range of in-flight particle temperature and velocities they may generate as illustrated in Figure 2. In the following section some popular spray techniques are briefly described.

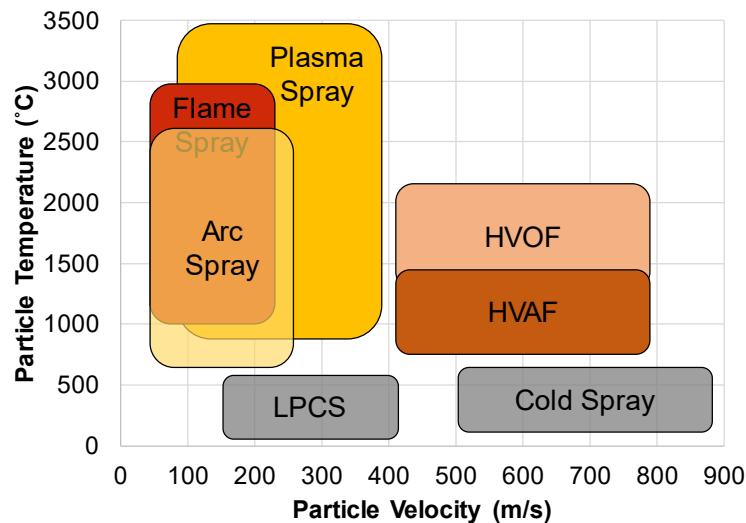


Figure 2 – Typical range of in-flight particle temperatures and velocities for several thermal spray processes. Adapted from [18].

## 1.1 Plasma Spraying

In plasma spraying, an arc is formed between a tungsten cathode and a copper anode which also behaves as a gas expansion nozzle. Gases such as Ar, H<sub>2</sub>, He or N<sub>2</sub> passing through the arc become ionized, forming a hot plasma plume. The powder is radially injected in the plume outside the spray torch. Therefore, the injection angle and the feedstock carrier gas flow rate must be carefully controlled for optimal heating and acceleration of particles. On the other hand, modern plasma spray torches (Mettech Axial III System) are now capable of delivering the feedstock along the axis of the plasma plume, which considerably reduces the process complexity.

## 1.2 Arc Spraying

In this process, two metallic wires of opposite charges are fed in such a manner that they contact at the spray torch exit, which causes an arc to form and the wires to melt. At this moment, a flow of compressed air (or inert gas) is forced upon the molten wire tips, causing the metal to atomize and accelerate towards a substrate. Arc-spraying is characterized by high deposition rates up to 55 kg/h. However, the process is limited to electrically conductive metals.

## 1.3 Flame Spraying

In combustion spraying processes, gas or liquid fuels are ignited, generating heat and gas expansion. In flame-spraying, some torches can be adapted to melt and atomize a wire, like arc-spraying. However, the flame causes significant substrate heating. Other flame-spray torches are adapted to powder feedstock, which adds in versatility, since materials other than metals may now be sprayed.

## 1.4 High-velocity Oxygen Fuel (HVOF) or Air Fuel (HVOF) Spraying

The use of converging-diverging nozzles (Figure 3) in thermal spray torches allowed the acceleration of sprayed particles to velocities above two times that of the sound (342 m/s at room temperature), which proved to be particularly useful for the development of highly-dense metallic or metal/carbide composite coatings. In gas-fueled HVOF torches, like Oerlikon's diamond jet, powder is injected inside the combustion chamber, which requires the use of highly pressurized powder-feeders so that the particles can be sprayed axially. In liquid-fueled HVOF torches, like Praxair's JP-8000, the powder is injected in the low pressure zones inside the nozzle, which allows the use of simpler powder feeders. In HVOF, instead of oxygen, the combustion gases are mixed with very high volumes of compressed air, resulting in substantial in-flight particle temperature reduction. The high volume of air is also used to cool the torch down whereas in HVOF systems, large water chillers must be used for torch cooling.

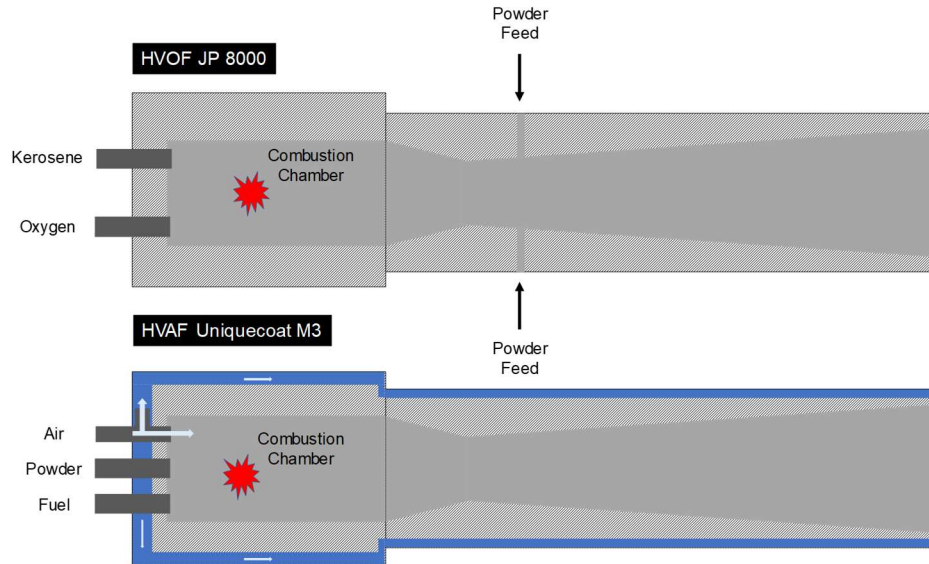


Figure 3 – Cross section schematics of the spray torches used for the development of this work.

## 1.5 Cold Spray

Converging-diverging nozzles are also used in cold spraying. However, as compared to all other spray techniques, the particle's temperatures are significantly lower than their melting point, thus avoiding problems associated with substrate heating or particle oxidation. A carrier gas is pre-heated to temperatures up to 700 °C and accelerated by high-pressure pumps. The metallic or metal/cermet composite particles anchor on the substrate by mechanical anchorage or by a mechanism known as adiabatic shearing in which the high strain rates lead to localized melting [19]. Upon cooling, these molten sites promote a “metallurgical bond” with its surroundings. Depending on particle size, each material displays a different range of impact velocities leading to efficient deposition. That is why a low-pressure cold spray (LPCS) was developed for the deposition of low melting point materials such as aluminum, tin or zinc [20].

## 1.6 HVOF Process Description and Spray Parameters

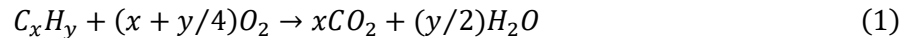
For the development of this thesis, most of the coatings were produced with HVOF. Therefore, it is important to describe in more detail how the process gas dynamics, the combustion reaction, as well as how the choice of different spray parameters may affect coating properties. These aspects are described in the following paragraphs.

HVOF is a well-established industrial process. The spray rates can vary from 1 kg to 5 kg per hour with 45 – 80% **deposition efficiency** (DE), i.e., the ratio of powder adhering to a substrate to that introduced in the spray torch. Applications of HVOF generally involve protection against corrosion and wear. One of the most commonly sprayed materials is a WC-Co composite which

combines a tough cobalt matrix with another tough and hard ceramic, the tungsten carbide. As example it is applied in landing gears of aircrafts as a substitute for hard chrome coatings. Another common example of HVOF application includes printing rollers that are coated with wear resistant alumina.

Fuel gases used in HVOF spraying include acetylene, hydrogen, propylene and propane. Kerosene is used in liquid-fueled torches. The fuel is fed to a chamber where an ignition spark generates a combustion reaction with oxygen. Depending on total gas flow rates, combustion pressures may vary in the 0.3 – 0.9 MPa range [21]. By passing through the nozzle, gas velocities can be as high as 1900 m/s. Moreover, the nozzle design makes the gas to flow in an under expanded fashion, i.e., at the nozzle exit the gas pressure is inferior to atmospheric pressure [22]. As a result, a series of gas shock waves appear. They can be visualized in the form of “diamonds” which are brighter due to local higher pressure and temperature. This phenomenon is commonly observed in jet engine exhausts.

In HVOF, the gases are often mixed in a non-stoichiometric combination affecting the flame temperature and hence, particle heating. To characterize a combustion reaction, it is useful to compare the used gas mixture’s oxygen-to-fuel ratio  $(O/F)_m$  to the stoichiometric  $(O/F)_s$  ratio. The stoichiometry of a generic combustion reaction can be easily assessed by observation of the coefficients in equation (1).



To determine whether a given process combustion is oxygen- or fuel-rich, one can simply calculate the O/F ratio as described by equation (2).

$$O/F = \frac{(O/F)_m}{(O/F)_s} \quad (2)$$

In principle, stoichiometric mixtures ( $O/F = 1$ ) generate maximum flame temperature. However, oxygen-rich ( $O/F > 1$ ) flames can trigger exothermic oxidation reactions on a particle surface, which might increase their temperature to higher values when compared to stoichiometric or fuel-rich flames. Therefore, the O/F ratio is an important spray parameter that can be used for in-flight particle temperature and melting degree.

Ultimately, the goal of controlling the spray parameters is to condition particles so coatings are produced with optimal properties as well as with reasonable deposition efficiency. Therefore, computational fluid dynamic (CFD) models have been developed to better understand the

interactions between gas dynamics and particle in-flight characteristics [22]–[25]. Despite the complexity of the mathematical formulations, CFD modelling results for HVOF systems are quite intuitive and may be summarized (Figure 4) as follows:

- Higher total gas flow rates lead to higher particle acceleration;
- Smaller particles (diameter  $\leq 1 \mu\text{m}$ ) accelerate and decelerate faster and are prone to follow the gas stream trajectories. Accordingly, they are easier to heat and melt but also cool down so quickly that they may solidify before depositing on the substrate.
- Larger particles take more time to accelerate and heat. In some instances, they reach the substrate before complete melting.

In practice, the particle diameter cut for HVOF spraying usually lies between  $5 \mu\text{m}$  to  $45 \mu\text{m}$ .

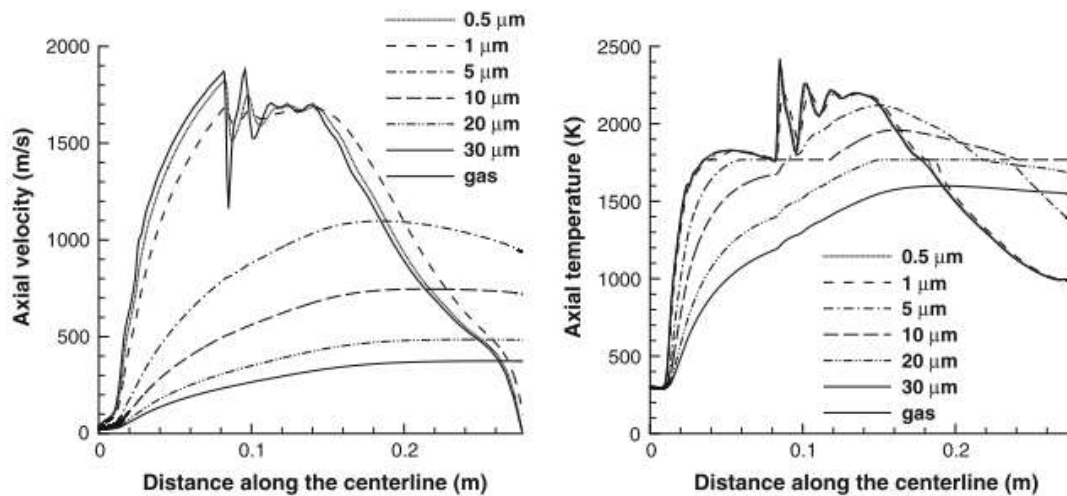


Figure 4 – Gas flow and particle interactions for gas-fueled HVOF determined by CFD [22]

Apart from fuel flow rates, other spray parameters may also play an important role in the final coating properties.

- **Spray Distance:** Defined as the distance between the spray nozzle exit and the substrate. The choice is a compromise between optimal in-flight particle characteristics (temperature and velocity) and substrate heating. Typical HVOF spray distances range between 300 – 350 mm.
- **Powder Feeding:** When feeding powder to the spray torch, one must ensure that throughout the entire deposition process, all particles experience similar acceleration and thermal histories. In radial injection processes such as plasma spraying, if the mass flow rate is suddenly increased, the plasma temperature may decrease too much [26].

Additionally, radial powder injection requires careful control of inert carrier gas flow rates, so that particles effectively penetrate the plasma plume. Otherwise, particles may either go across the plume, or may not penetrate it at all. Finally, powder feeding may be affected by particle morphology. While gas atomized particles are more spherical and flow easily, angular and/or lamellar ball-milled feedstock may require vibration systems so that a continuous flow of material is ensured during the spray deposition period.

## 1.7 In-Flight Particle Characterization

Regular assessment of in-flight particle temperatures and velocities is crucial to ensure spray process reliability. In this section the principles behind the diagnostic tools (DPV-evolution and Accuraspray) used for quantitative in-flight particle properties are briefly introduced.

Particle velocities are determined differently in each diagnostics system. In DPV-evolution, a two-slit mask is used in front of an optical fiber with a measurement volume inferior to  $1 \text{ mm}^3$ . As a radiating particle passes in front of the mask, two signal peaks are detected. The time between the two maxima and the known distance between the slits are then used for velocity calculation. Usually, the radiation derives from the particle's high-temperature. If the temperature is too low, a laser may be used to illuminate the particle which now emits the scattered light. In the Accuraspray system, the particle velocities are measured by cross correlation of two radiation signals measured at two closely-spaced positions. If superposition of the signals is satisfactory, one may consider that both are derived from the same set of particles. It is important to mention that in Accuraspray, the processed signals derive from a group of particles in a measurement volume of  $177 \text{ mm}^3$ . In DPV-evolution, each particle is characterized individually, which allows the statistical treatment of the data. Figure 5 illustrates the concepts used for particle velocity determination in both diagnostic systems.

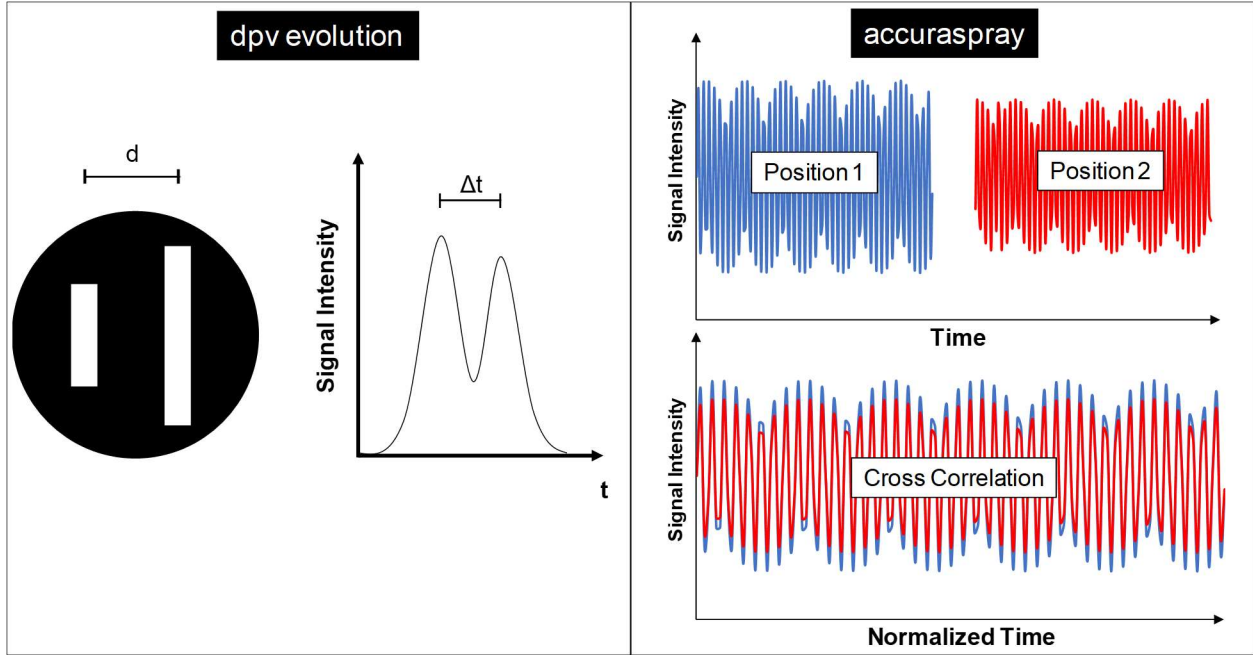


Figure 5 – The methods used to determine in-flight particle velocity differ in each diagnostics tool. In DPV-evolution a two-slit mask is used to control the signal from individual particles. In Accuraspray, a large group of particles generate signals at two well-defined positions.

In both DPV-evolution and Accuraspray, particle temperatures are determined by two-color pyrometry. The technique consists in measuring the particle's thermal radiation intensity ( $I$ ) which, according to Planck's law, is given by equation (3):

$$I = \varepsilon \frac{C_1}{\lambda^5} d^2 \frac{1}{\left[ \exp \frac{C_2}{\lambda T} - 1 \right]} d\lambda \quad (3)$$

where  $\varepsilon$  is the emissivity,  $d$  is the diameter,  $\lambda$  is the wavelength,  $T$  is the temperature and,  $C_1$  and  $C_2$  are constants. If emissivity ratio is assumed independent of temperature, the ratio of emitted intensities  $I_1/I_2$  measured at two closely-spaced wavelengths ( $\lambda_1, \lambda_2$ ) follows a monotonic increase with temperature as illustrated in Figure 5. In thermal spraying, particle emissions are determined at carefully chosen wavelengths to avoid measurement interference from particle-scattered plasma radiation [27], [28].

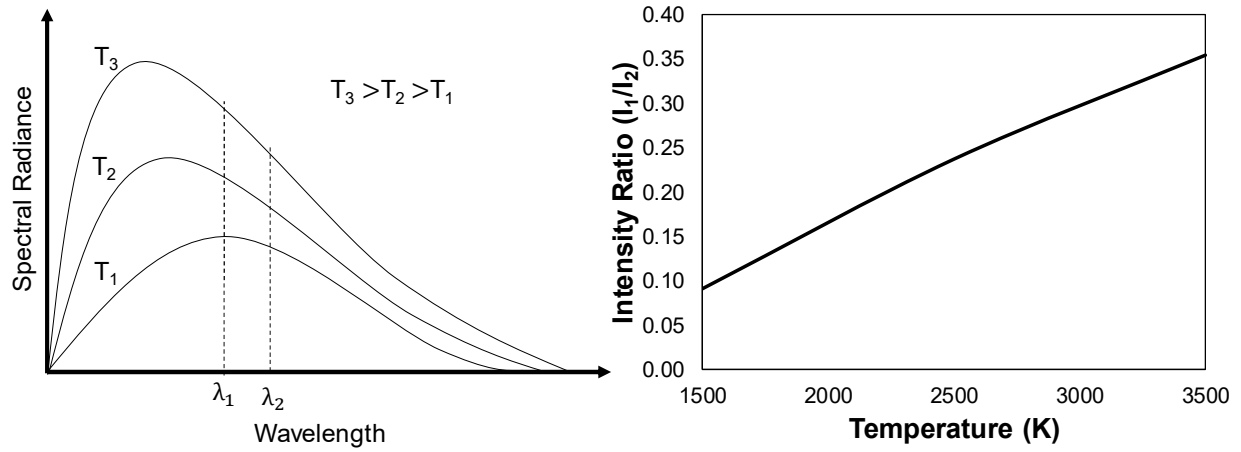


Figure 6 – In thermal spraying, the two-color pyrometry technique is used to determine particle in-flight temperature. The ratio of the thermal radiation intensity measured at two similar wavelengths has a monotonic increase with temperature. In this figure, the units are arbitrary.

## Chapter 2 – Surface Engineering of Thrust Bearings

### 2.1 Thrust Bearings in Hydropower

In hydroelectric power plants, turbine shafts cause large axial loads due to the usual component's large weight as well as due to the hydraulic thrust generated at the turbine blades. These axial loads must be balanced using hydrodynamic thrust bearings. The increasing need for renewable energy sources has motivated the construction of ever larger hydro-powerplants. As a consequence, axial loads in thrust bearings passed from a few tons in the 1950's to 6000 tons in 2015 [5], stressing the need for bearing technology development.

One of the main characteristics of hydraulic bearings concerns its sensitivity to the operating parameters. Their outstanding low wear and friction performance relies on the development of hydrodynamic pressure in a lubricating oil that separates two sliding surfaces by a few micrometers (Figure 7). The hydrodynamic pressure and hence, the thrust **load bearing capacity** depends on the bearing geometry, on the sliding velocity as well as on the oil viscosity [29]. If for any reason the oil pressure is reduced, one risks contacting two surfaces at very high loads and velocities.

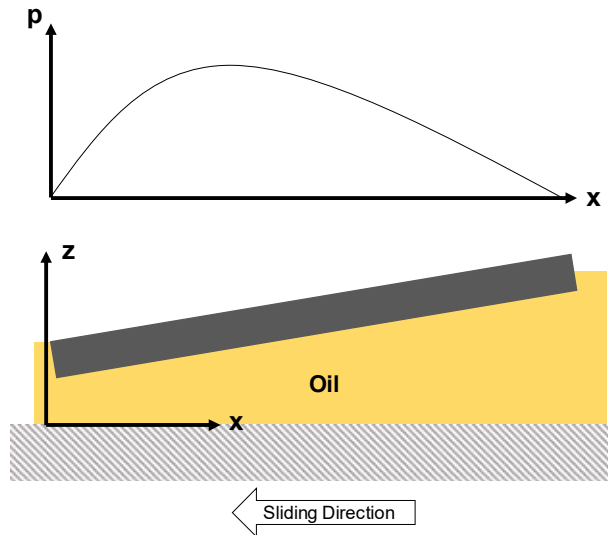


Figure 7 – Oil pressure distribution in a hydrodynamic bearing

Failure in hydrodynamic bearings are relatively common [30] and their impact for the hydropower generation business can be severe. In some plants, the time to repair damaged bearings can be as long as a few months [5].

Traditionally, bearing pads are coated with “white metal” or “babbitt”, which are Sn-based alloys as standardized in ASTM B23 – 00(2014). Their low melting point (close to that of pure tin 232 °C) makes it relatively easy to cast and repair. In the event of inadequate hydrodynamic lubrication, the contact between a steel shaft collar and the bearing surface will likely wear the babbitt surface, due to its low hardness. These properties have allowed white metals to be found in industrial production and several bearing applications up to present days.

However, the same properties that facilitate babbitt coating production, limits the bearing operation temperature. Shearing of the lubricant oil leads to frictional heating, which may cause a drastic decrease in oil viscosity as well as deflections of the bearing geometry, compromising the load bearing capacity [29]. This motivated the use of different coating materials such as PTFE [9], perfluoro alkoxy alkanes (PFA) [31] as well as polyether ether ketone (PEEK) [32]. The polymeric layer’s compliant surface, thermal insulation and low friction coefficient has improved thrust bearing load capacity up to three times while reducing the need for oil pressuring (jacking) during turbine start-up or shut down activities.

Since thrust bearings are expected to operate for a few decades with minimum maintenance, it is important to know which polymer-lining provides the best properties for the longest period. However, based on recent investigations it is difficult to determine which polymer properties are the most relevant with respect to bearing performance. For example, while developing significantly different oil pressure curves and oil film dimensions, PFA and PTFE linings gave bearings similar steady-state load capacities and bearing geometry deflections [31].

In transient or near-static conditions, relevant differences between the polymers do appear. For example, at low rotation speeds the hydrodynamic film was not well developed in a PTFE-lined bearing, requiring high driving powers for shaft rotation [31]. This was attributed to PTFE’s low elastic modulus. Additionally, compression tests performed on PTFE- and PEEK-lined steel specimens reveals that the bond layer (between steel and polymer) has an influence on the bearing’s apparent young’s moduli [33] and may affect the oil’s thermal and hydrodynamic responses. Upon scheduled turbine stops and re-starts, near-dry sliding between steel counter parts and the bearing may occur. Therefore, valuable information may be drawn from break-away coefficient of friction measurements to evaluate different material options. As reported in [34], pure PTFE linings outperform PTFE-infiltrated porous bronze as well as babbitt coatings.

Since they do not display glass transition or melting, thermosetting resins soften linearly with increasing temperature, whereas thermoplastic polymers may display an abrupt effect as the

service temperature increase. Polyimide (PI) thermosetting resins are used in self-lubricated (no oil) bearing applications [35]. Their excellent mechanical and chemical stabilities makes them strong candidates for space applications [36], [37]. While the resin in its pure state has a relatively high friction coefficient against steels [38], addition of graphite or PTFE fillers may greatly reduce friction effects. Therefore, PIs could also represent an interesting choice for the lining of thrust bearing pads.

As illustrated in Figure 8, thermoplastic sheets are hot pressed on bearing pads previously covered with a wire mesh or a porous scaffold. With the melting of the sheets, the polymer can penetrate the voids, and anchor to the bond layers. Since PIs do not have a melting point, their bonding to the substrate represents an obstacle. On the other hand, if the components that form polyimides could penetrate the pores prior to complete polymerization, the obstacle may be overcome.

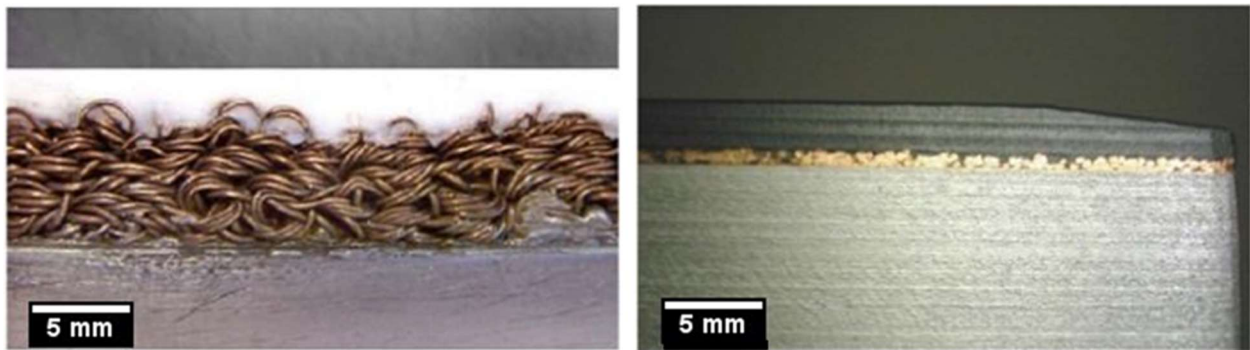


*Figure 8 – Cross section images of PTFE-lined (left) and PEEK-lined (right) thrust bearings. Extracted from [5].*

In this brief discussion, two venues for the use of thermal spray in thrust bearings have been identified: the production of dense babbitt coatings and porous bond coats for the infiltration of polymer linings.

## 2.2 Production of Babbitt Coatings by High-Velocity Oxygen Fuel Spraying

*Published in the Journal of Thermal Spray Technology [10]*

### 2.2.1 Introduction

The term Babbitt or white metal refers to a group of tin or lead alloys used in journal or thrust bearings. Babbitting, therefore, is the process by which those alloys are bonded to a stronger supporting base metal, usually steel, cast-iron or a bronze. The alloy development dates to the 19<sup>th</sup> century [39]. Yet, due to its interesting properties, they are still used in present days. In the context of hydrodynamic bearing applications, the use of white metals is justified by their:

- **Low Hardness:** In the event of oil starvation, the contact between two metals may cause significant wear to sensitive machine components. In such a case, babbitt coatings will behave as a sacrificial surface. Additionally, when the lubricating oil is contaminated with hard debris, white metal surfaces can trap the contaminants on their surface by plastic deformation.
- **Galling Resistance:** Babbitt is also known for its low tendency to adhere to steel surfaces, which is another advantage should the two metals contact each other during motion.
- **Low Stiffness:** Usually, multiple bearings are used in an assembly and small misalignments may significantly affect the machine's performance and durability. The low stiffness of white metals allows them to conform to the eventuality of such misalignments.

Traditionally, babbitting is accomplished by static or centrifugal casting. To ensure good bonding to the substrate, pre-treatments such as dovetailing and Sn-soldering are used. The substrate is pre-heated to ensure good bonding and adequate cooling is required to avoid metallurgical problems such as segregation of alloying elements and hot tearing [40].

In comparison to casting, thermal spraying does not require extensive heat control of substrate and may be used to produce Babbitt coatings at industrial production rates. However, depending on the spray parameters, coating porosity may become a source of bearing failure. As schematically illustrated in Figure 9, pressurized oil used during a hydro-power turbine start-up was able to percolate through pores in arc-sprayed babbitt coatings, leading to cracking and spallation. Therefore, if proper control of spraying parameters is not ensured, the use of thermal spraying to produce high-performance bearing surfaces is jeopardized.



Figure 9 – Schematic illustration of the failure mode observed in porous babbitt coatings deposited by arc spraying.

Since porosity led to the failure of some babbitt coatings, it is of interest to understand which spray parameters are relevant to produce dense white metal deposits at high deposition efficiencies. Early studies on the deposition of pure Sn by plasma spraying [41] reveal that 500  $\mu\text{m}$  thick coatings can be produced on LiF substrates. However, significant closed porosity (4.1 – 5.1%) remain in the coatings demanding further densification procedures. The works of Pistofidis and Vourlias et al. [42], [43], [44] on the other hand, show that plasma-sprayed tin coatings can have as-sprayed porosities inferior to 1%. The use of tin powder (melting point of 232  $^{\circ}\text{C}$ ) in a hot plasma may raise concerns of material volatilization that may interfere with deposition efficiency (DE). While in [41] the reported DE was of 30  $\mu\text{m}/\text{pass}$ , in [42]–[44] little can be said about the process efficiency. Metallic coatings are more often produced by wire- and powder flame-spraying due to their high throughputs. A recent work specifically focused on the production of Babbitt coatings [45] reports deposition efficiencies as high 164  $\mu\text{m}/\text{pass}$  while maintaining the porosity inferior to 5% and a tribological performance equivalent to that of a centrifugally cast white metal.

When high-temperature exposure needs to be avoided, cold spraying (CS) emerges as an alternative spraying technique, which is characterized by a process window i.e., the impacting particle velocities must fall within a desirable range to effectively deposit on the substrate [19]. If impact velocity is too low, the particles bounce on the substrate; if too high, they erode previously deposited layers. In the case of cold-sprayed Sn coatings, Legoux et al. [46] showed that the DE is very low ( $\sim 5\%$ ), due to excessive impact velocity. Li et al. [47] cold sprayed a mechanically milled pure Sn and 5wt.%Cu. They produced single-pass 25 – 40  $\mu\text{m}$  layers of Sn-5%Cu on aluminum. Subsequent passes led to coating de-boding from the substrates. One possible way of increasing the DE of thermally sprayed tin and its alloys would be by reducing the particle's impact velocity, avoiding the onset of erosion. As compared with the conventional cold spray, the

low pressure cold spray technique (LPCS) uses much lower gas flow rates, resulting in particle velocities ranging from 300 – 400 m/s [21]. In fact, Winnicki et al. [20] used LPCS to produce dense tin coatings, however, no information regarding the deposition efficiency was provided.

Based on the modelling of Schmidt et al. [19], another approach to increase the deposition efficiency of Sn particles during thermal spray is to use larger particles which, while being harder to accelerate, have lower critical velocities. This approach is investigated in the present work by using a modified HVOF set-up in which the particles are injected radially in the flame. The main objective is to find the right process parameters that yield particles of right impact velocity, while keeping low porosity and acceptable deposition efficiencies.

By using the diagnostic systems DPV-evolution and Accuraspray, a valuable assessment of the in-flight state of particles is used to correlate the different spray parameters with deposition efficiency as well as with coating microstructures. Finally, the microstructure and hardness of Babbitt coatings produced by casting, arc spray, flame spray and HVOF were compared.

### 2.2.2 Methodology

In this work, gas atomized Babtec® 29240 powder from Eutectic Castolin was used. According to the manufacturer, the powder composition lies within ASTM B23 Grade 2 specification which in weight percentage is 89Sn7.5Sb3.5Cu. The alloy's solidus temperature is 241 °C and its density is 7.39 g/cm<sup>3</sup>. The powder was mechanically sieved through a 200 mesh and subsequently divided into two different groups of particle sizes which from here on will be termed "fine" and "coarse". Particle size distribution was determined by laser diffraction with an HORIBA LEA-950 analyzer. It must be mentioned that both groups have sizes largely exceeding the typical values of diameters used in HVOF. Figure 10 illustrates particle size distribution measurements, and powder morphology.

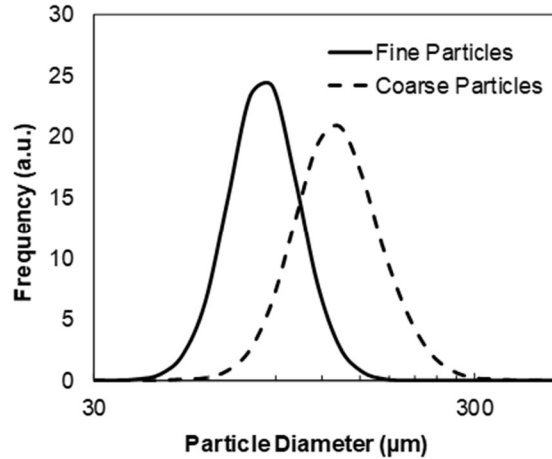
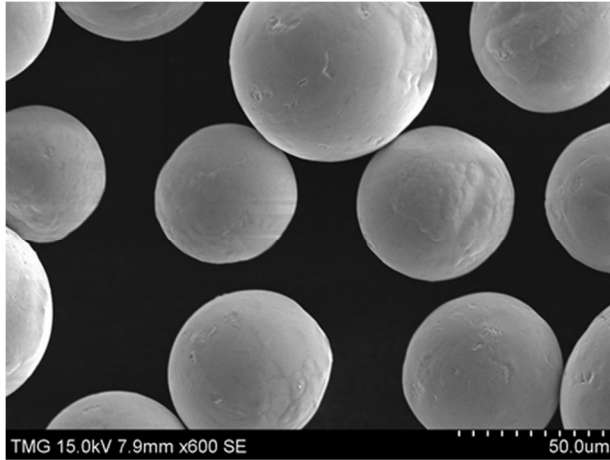


Figure 10 – Babbitt feedstock morphology (secondary electron image) and size distribution. The fine particles have  $D_{50} = 80 \pm 18 \mu\text{m}$  while the coarse particles have  $D_{50} = 127 \pm 35 \mu\text{m}$ .

To avoid excessive particle heating, oxidation, evaporation and potential nozzle clogging, a radial injection system was developed and adjusted to the Diamond Jet (Oerlikon Metco) HVOF gun, allowing the Babbitt powder to be injected perpendicularly to the nozzle’s axis. The radial injector nozzle exit was positioned at axial and radial distances of 2 cm away from the gun exit.

In HVOF, the heat transfer to particles is affected by the choice of spray parameters. In the present work, three different total gas flow rates were chosen, resulting in three different flame temperatures or combustion powers. For comparison purposes, the chosen spray parameters were designated as high heat (HH), medium heat (MH) and low heat (LH) as described in Table 1. The combustion powers were calculated based on the combustion of propylene  $\text{C}_3\text{H}_6(\text{g}) + \frac{9}{2}\text{O}_2(\text{g}) \rightarrow 3\text{CO}_2(\text{g}) + 3\text{H}_2\text{O}(\text{g})$   $\Delta H_c = -2077 \text{ kJ/mol}$ , where  $\Delta H_c$  is propylene’s enthalpy of combustion from [48]. Since all spray conditions are oxygen-rich, it was assumed that all propylene reacts in the chamber. The air flow rate was not considered in the combustion power calculations because it is used for cooling of the Diamond Jet torch nozzle, as shown in [22].

Table 1 - Gas flow rates used during HVOF spray of BatTec® 29240 powder.

Spray Parameters	Flow Rates (SCFH)			Combustion Power (kJ/s)
	Air	Oxygen	Propylene	
<b>HH (High Heat)</b>	710	360	50	35
<b>MH (Medium Heat)</b>	550	290	40	28
<b>LH (Low Heat)</b>	395	215	30	21

Even though no powder was injected through the combustion chamber, nitrogen was used at 25 LPM to keep the axial powder injector properly cooled. Argon was chosen as carrier gas for the Babbitt powder. After several attempts, its flow rate was fixed at 8 LPM. The powder feed rate was fixed at 20 grams per minute.

To assess the effects of different spray conditions as well as particle diameter on particle's in-flight temperature and velocity, the Accuraspray (Tecnar Automation Ltd., St-Bruno, Canada) was used at an axial distance of 100 mm. The optical intensity of the particles was measured along a sampling line positioned along the spray-axis by using Accuraspray's charge-coupled device (CCD) camera. Use of DPV-evolution (Tecnar Automation Ltd., St-Bruno, Canada) in laser illumination mode was necessary to properly measure particle velocity at a 200 mm axial distance.

Deposition efficiency tests were performed at 200 mm stand-off distance and the gun's traverse speed (coupled to a robot-arm) was set to 1 m/s. DE tests for all the six spray parameters (three flame heats and two types of particle sizes) were performed by translating the gun in front of carbon steel substrates (3 in x 3 in) in a single horizontal line (step = 0 mm) for a total of 100 times. The calculation of the DE was done by determining the ratio of the mass of material that was effectively deposited on the substrate to the mass of powder that is sprayed while the spray gun was in front of the substrate.

Ni-Al bond coated steel coupons were used as substrates. 100 passes were applied with step values of 5 mm.

### **Microstructure and Hardness Characterization**

Instrumented indentation with a Vickers pyramid was used to determine hardness of Babbitt coatings produced by casting, arc spray, flame spray and HVOF (low heat and coarse particles).

Loading and unloading rates were set to 10 N/min with maximum load of 500 mN, which was held for a total of 30s, totaling one minute of characterization. Each coating was characterized for a total of 9 times, each indent separated by 150  $\mu\text{m}$ . All indentations were performed on the cross section of coatings.

The analysis of the coating structures was performed by means of optical and confocal microscopy. Samples were molded in epoxy resin and then cut prior to grinding with SiC paper and polishing with colloidal silica suspension. Porosity measurements were performed by image analysis using Image J software.

## 2.2.3 Results and Discussion

### 2.2.3.1 *Particle In-Flight Temperature*

The choice to avoid particle overheating led to the choice of process parameters that minimize flame as well as particle temperatures. When positioning the Accuraspray at a 100 mm axial distance from the exit nozzle, it was possible to characterize the thermal radiation emission of particles by means of the system's couple charged device (CCD) camera.

When exposed to radiation, each section of the CCD builds up a charge proportional to the intensity of the incoming radiation. At a higher temperature, particles will generate more thermal radiation and appear brighter, i.e. with a higher optical intensity in the digitalized image. This effect is illustrated in Figure 11. One will readily observe that at higher heat spray conditions, the optical intensity is also higher. Moreover, at a fixed flame heat, the finer particles emit more radiation. This is also expected since smaller particles, having a smaller mass, require less heat energy to have their temperature increased. This is also supported by previous work on numerical modelling [22].

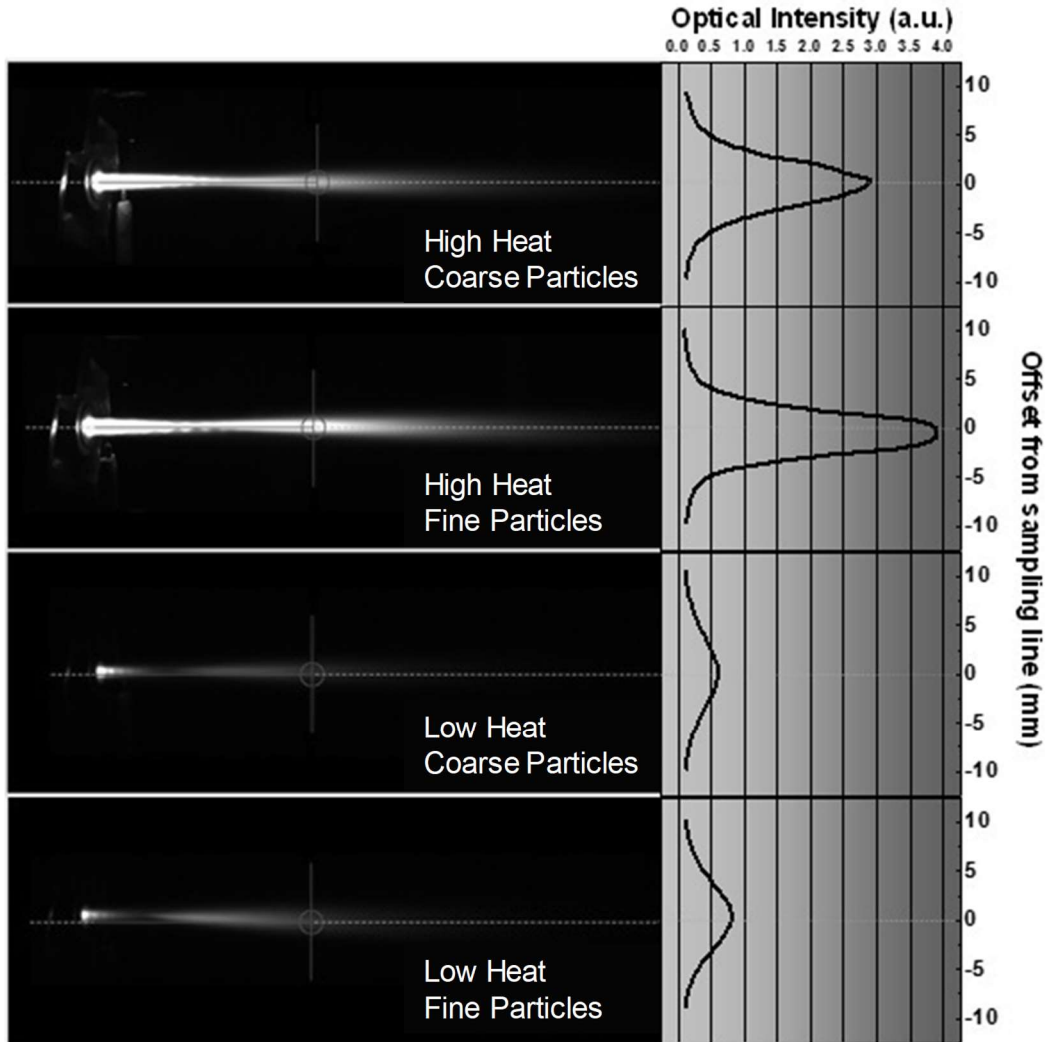


Figure 11 – Assessment of particle thermal radiation emission by means of Accuraspray CCD camera.

Quantitative analysis of particle temperature by two-color pyrometry was attempted with both DPV-evolution and Accuraspray. However, due to the choice of spray parameters, the overall particle temperatures fell to values below the system's detection limit ( $\sim 1000$  °C). Despite the effort to minimize heat transfer to particles as much as possible, many particles were clearly liquid prior to deposition as shown in Figure 12 which shows the surface features of the Babbitt coatings. While at high heat, molten and widely spread splats are observed, at low heat the surface features are markedly different, indicating a much lower degree of melting.

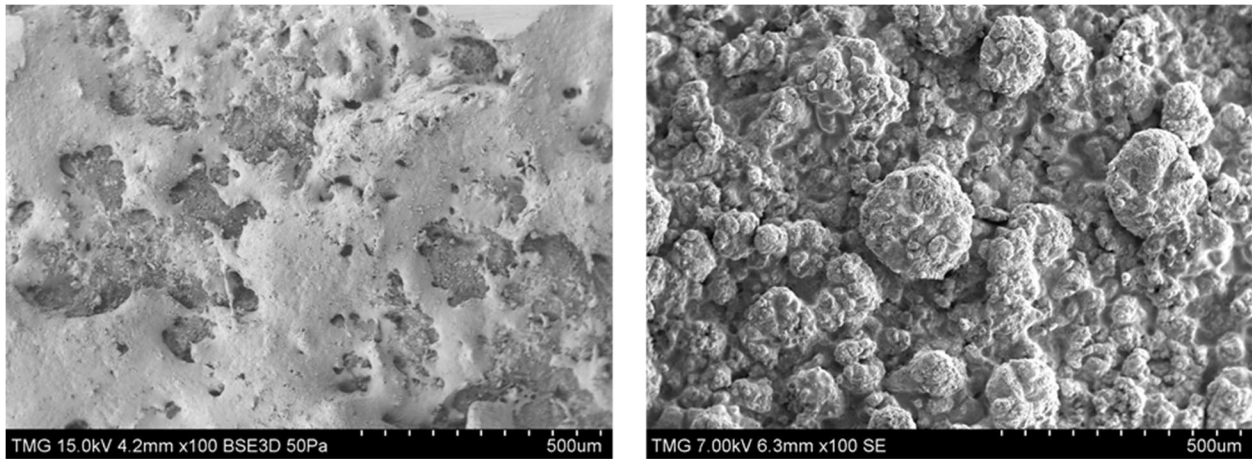


Figure 12 – Backscattered electron image shows the surface of Babbitt coatings produced at different spray parameters: (left) high heat; (right) low heat.

### 2.2.3.2 Particle Velocity and Deposition Efficiency

Using DPV-evolution in laser illumination mode allowed reliable determination of particle velocities for all choice of spray parameters. As shown in Figure 13, both coarse and fine particles groups show increasing velocities with increasing flame heat or total gas flow rate. The linear relationship between particle in-flight velocity and total gas flow rate has been reported in several publications such as [15 – 17].

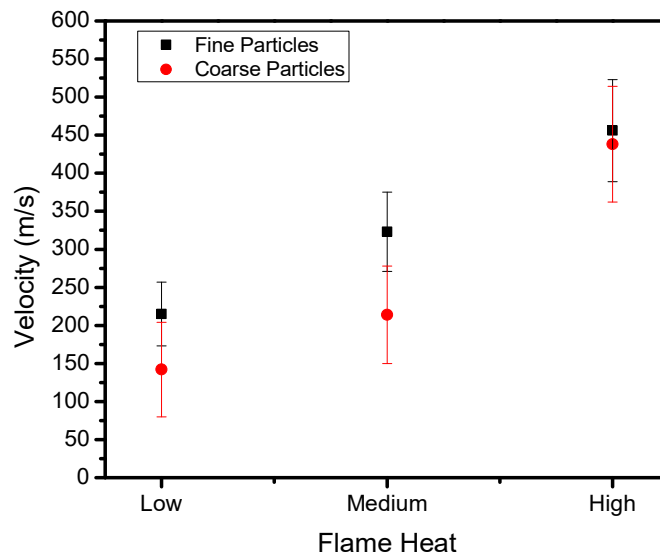


Figure 13 – Effect of flame heat on babbitt particle in-flight velocity

Figure 14 shows the general trend pointing out higher deposition efficiencies for lower particle velocities (or flame heat). Two factors may contribute to this outcome: particle evaporation as well as coating erosion. The contribution of each factor is now discussed.

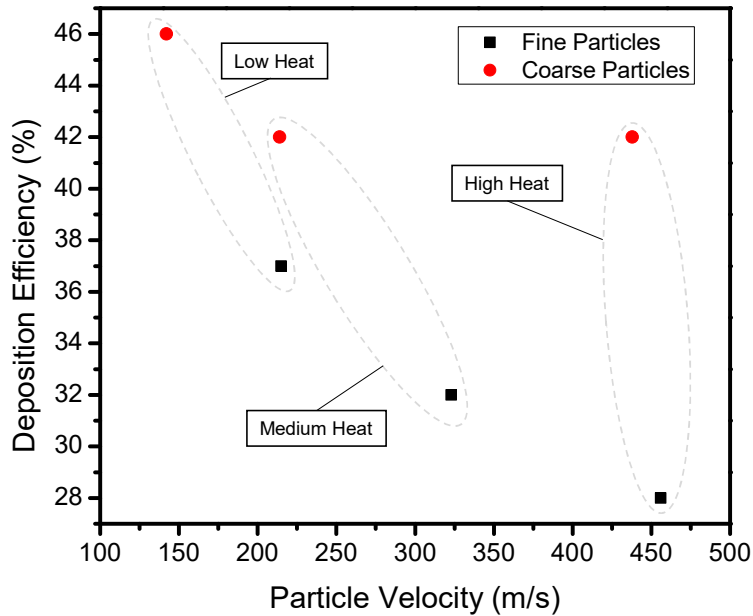


Figure 14 – Correlation between deposition efficiency and particle velocity for six different spray tests.

To estimate the contribution of evaporation to material loss during spray, one may use Langmuir's equation  $dN/dt = \alpha A p^* / \sqrt{2\pi MRT}$ , where  $dN/dt$  is the rate of evaporating molecules,  $A$  is the surface area,  $p^*$  is the material's vapor pressure,  $M$  is the molecular weight,  $R$  is the perfect gas constant,  $T$  is the absolute temperature, and  $\alpha$  is a constant varying between 0 – 1. Using the surface area ( $A = 2.01 \times 10^{-8} \text{ m}^2$ ) of the average size of fine particles, the material's vapor pressure of Sn ( $p^* = 1.67 \times 10^{-2} \text{ Pa}$ ) and a temperature of 1000 °C, one finds for a constant  $\alpha$  of 1, an evaporation rate of  $2.69 \times 10^{-8} \text{ g/min}$  which is negligible compared to the powder feed rate of 20 g/min. Therefore, evaporation cannot explain the changes in the DE values observed in each spray parameter.

On the other hand, if one assumes that a significant part of particles are flying at a temperature close to the alloy's liquidus temperature, it is possible to use the equations derived for cold spray deposition [19] to calculate the critical and the erosion velocities. The so-called window of sprayability is defined as the impact velocity range between these two velocities. Using the properties of pure Sn given in [52], one observes that by increasing the impact temperature from

50 °C to 150 °C, the window of sprayability narrows from 110 m/s – 220 m/s to 46 m/s – 92 m/s. This means that if other variables are kept constant, one should expect an increase in the DE if the impact temperature is reduced. This is what one observes in Figure 14. As the flame heat is decreased, the deposition efficiency increases. The effect is further enhanced if particle size is considered: from high to low heat flame the DE of the fine group changes from 28% to 37%. For the coarser group of particles, the DE changes from 42% to 46%. For the fine group, it appears that when one reduces the flame heat, a significant fraction of particles enters the desirable sprayability window. For the case of the coarse group, the fraction of particles already in the desirable window is much higher, which would explain its lower sensitivity to the spray parameters.

Even though it is unlikely that the Babbitt particles were completely solid prior to impact, the experimental data suggests that, proper bonding and deposition are achieved within a specific process window, like in cold spraying.

Using cold spray, Legoux et al. [46] have shown that at the impact velocity of 500 m/s, pure tin with average diameter of 13.6  $\mu\text{m}$  hardly deposits on stainless steel substrates. DE values reach a maximum of 5%. In this work, at a similar impact velocity of 450 m/s, Babbitt particles have much higher DE (28% - 42%), most likely due to the much larger particle sizes and different material composition. The present DE values are more comparable with those reported by J. F. Li et al. [47]. Their DE increases from about 42% to 46% by reducing the spray pressure and therefore, by decreasing particle velocities as in the present case.

### 2.2.3.3 *Coating Structure and Hardness*

While six spray parameters were investigated, actual Babbitt coatings were produced only at the spray parameter that generated the highest DE, i.e. with low flame heat and coarse particles. This section compares the Babbitt coatings produced by HVOF with those produced with more traditional techniques.

Figure 15 illustrates the cross section of Babbitt coatings produced by casting, flame spray, arc spray and HVOF. One may observe that the cast sample presents no pores and a relatively coarse distribution of intermetallic phases with varying shapes and sizes. According to [52], ASTM Grade 2 Babbitt microstructures are characterized by needle-shaped Cu-rich and fine rounded SbSn intermetallic precipitates dispersed in a solid solution matrix. Flame and arc sprayed Babbitt coatings show very similar structures with a high porosity (10% and 16%, respectively) and pore diameters as large as 100  $\mu\text{m}$ . One may also notice some pores in the structure of the coating

produced by HVOF. The dense structure of the HVOF coating resembles those of Sn-coatings produced by low pressure cold spraying [20] and encourages the use of processes leading to low particle temperature and higher velocities as compared with more traditional spray techniques.

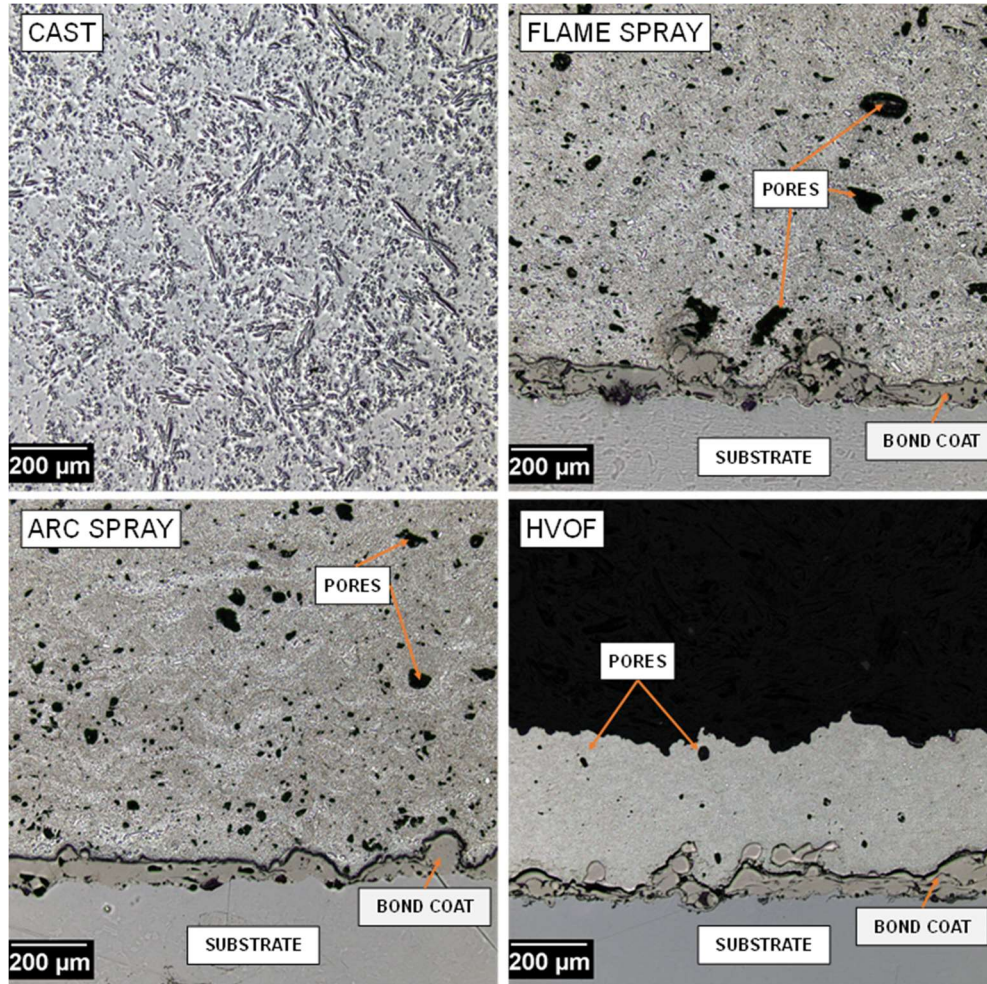


Figure 15 - Polished cross section image of Babbitt coatings produced by casting, flame spraying, arc spraying and HVOF (as produced with low heat and coarse particles).

A closer look at the Babbitt coating structures reveals that all techniques lead to the formation of intermetallic phases. Figure 16 compares the size distribution of intermetallics for each technique. On the one hand, cast coatings have intermetallic particles with sizes ranging from a few microns to two hundred microns (as seen in Figure 15). On the other hand, the intermetallics in the HVOF coating have a more uniform size distribution, with most having a size smaller than 3 μm. The intermetallic size distribution in arc and flame sprayed coatings is closer to that of the HVOF however, some particles with sizes as large as 70 μm can be found.

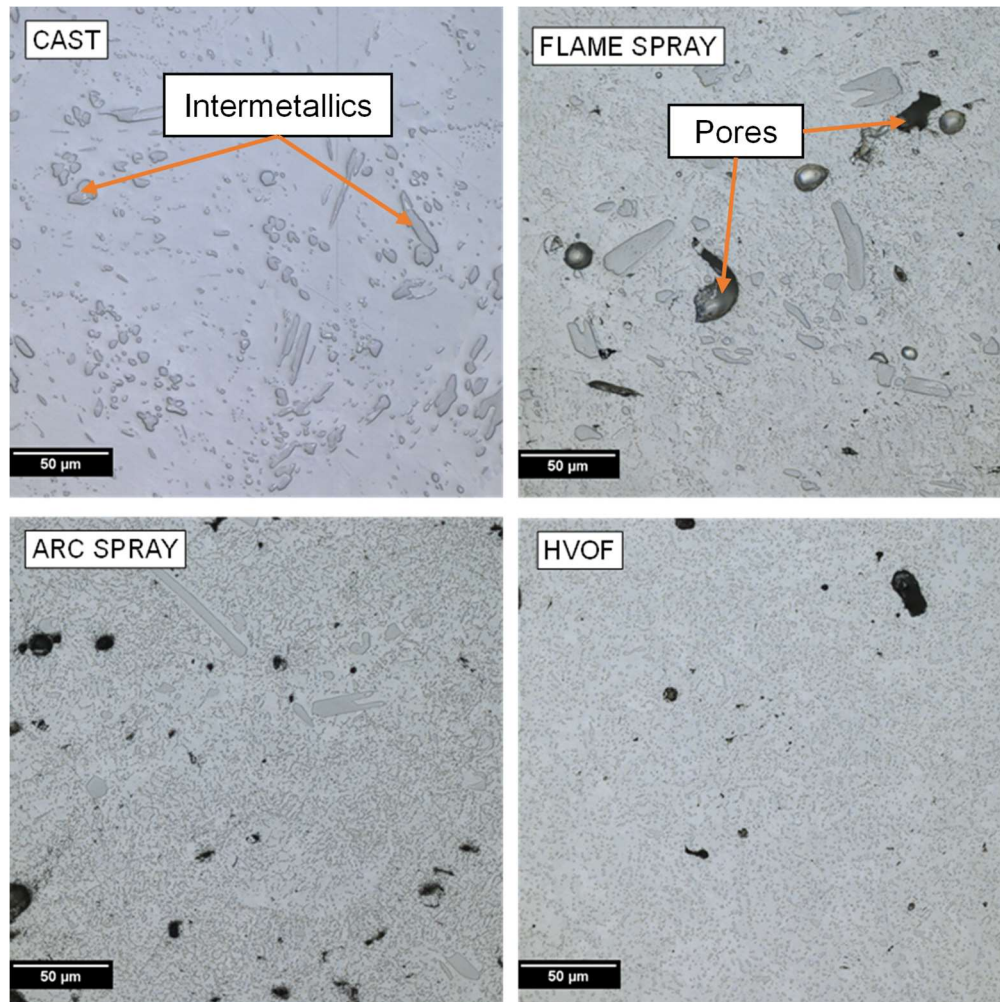


Figure 16 – Intermetallic phase distribution in Babbitt coatings produced by casting, flame spraying, arc spraying and HVOF (as produced with low heat and coarse particles).

The finer distribution of intermetallic phases in Babbitt coatings produced by thermal spray is expected because the cooling rates experienced by each molten splat is much higher than those observed in conventional casting. As a reference, one may cite the work of McDonald et al. [53], who showed that plasma sprayed splat cooling rates can be as high  $10^8$  K/s. Therefore, when compared to a molten Babbitt pool, in a recently deposited Babbitt splat there is little time for atoms to diffuse and for the intermetallics to grow. Since arc and flame spray techniques lead to higher in-flight particle temperatures as compared with HVOF [54], one may use the same reasoning to explain the presence of larger intermetallic phases in the former group of coatings.

Table 2, summarizes the results of Vickers microhardness as measured by instrumented indentation. When comparing arc, flame and HVOF sprayed coatings, the hardness values have

significant overlap. Moreover, while the difference in absolute values is small, the cast coating seems to have a superior hardness as compared to those produced by thermal spray.

Table 2 - Microhardness results measured by instrumented vickers indentation. Error corresponds to the standard deviation.

	<b>HV<sub>0.5N</sub></b>
<b>Cast</b>	28.9 ± 1.8
<b>Flame Spray</b>	21.2 ± 2.7
<b>Arc Spray</b>	23.6 ± 3.2
<b>HVOF</b>	23.5 ± 2.1

As illustrated in Figure 17, when observing the indentation imprint on the coating's cross sections, one finds that the intermetallics offer little resistance to the penetrating Vickers tip, which helps to explain the similar hardness values of thermal spray coatings. The higher values of hardness for the cast coating may be explained by its lower porosity.

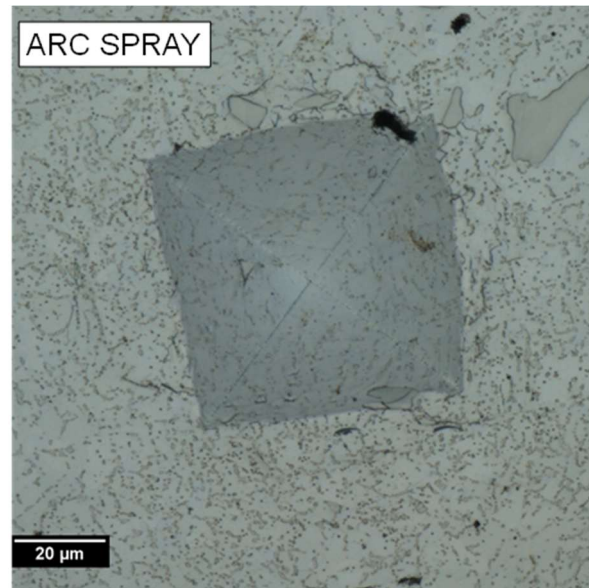


Figure 17 - Indentation imprint on the Arc Sprayed Babbitt Coating. The fine intermetallics offer little resistance to the indentation imprint.

Finally, considering the performance requirements of a bearing alloy, the fact that the hardness of the Babbitt coatings produced by thermal spray is not very different from those produced by

casting is satisfactory since this indicates, for instance, that they will have similar ability to embed contaminant abrasive grits, or that they will act as a sacrificial surface in the event of a contact with a more sensitive metallic component.

#### 2.2.4 Summary and Conclusions

In the present work, it was shown that it is possible to produce Babbitt coatings by HVOF with radial powder injection. It was shown that in-flight powder evaporation is probably negligible. By using a proper set of spray parameters combining low flame heat and coarse particles, it was possible to produce a 370  $\mu\text{m}$  thick Babbitt coating with high density and a fine distribution of intermetallics.

The main findings of the present investigation were:

- Deposition efficiency depends on particle impact velocity and diameter. Higher impact velocity decreases deposition efficiency especially for finer particles.
- Reduction of flame heat and increase of particle diameter led to a deposition efficiency of 46%.
- When compared with other spray techniques Babbitt coatings produced with HVOF have lower porosity and similar intermetallic size distribution.
- The mechanical properties of Babbitt coatings produced by thermal spray are similar to those produced by casting.

## 2.3 Tailored Porosity for Polymer Infiltration in Stainless Steel Coatings

*Submitted to the Journal of Thermal Spray Technology*

### 2.3.1 Introduction

Lubrication is essential to minimize the effects of the direct contact between bearings and other rotating or sliding surfaces. Dry-lubrication or self-lubrication refers to the ability of some components to provide to the contact interface a solid material that substantially reduces friction and wear. These components are desirable in machine parts that are hard to access and maintain. Additionally, dry-lubrication reduces the potentially negative environmental impacts that oil or grease may have if they leak to the surrounding environment.

Self-lubricating materials such as poly tetrafluoroethylene (PTFE), graphite and molybdenum disulfide (MoS<sub>2</sub>) owe their low friction properties to the relatively low stresses required for them to shear when sliding against a harder counter surface [55], [56]. To avoid excessively high wear rates, these lubricants are usually combined with stronger load-bearing materials. For example, polyimides (PI) have excellent load-bearing capacity [38] and, with the addition of graphite, PI composites display low friction coefficients [57]–[59] and are considered strong candidates for space exploration missions [36], [37]. On the other hand, bonding between polyimides and flat metals tends to be difficult [60], requiring the use of adhesives that may be very sensitive to service temperature or environmentally hazardous [61].

Standard methods of producing self-lubricated bearings usually involves powder metallurgy (P/M). In polymer-lined plain bearings, a porous metallic bond layer provides mechanical anchorage between a thermoplastic material and a metal [62]. The bond layer is usually formed in a production line where bronze powder is layered and pressed against a metallic sheet prior to sintering. This method is limited to simple surfaces as the union of bronze powder to more complex shapes is difficult. In this scenario thermal spray emerges as an interesting process as it may produce coating with tailored properties for relatively large and complex parts such as thrust bearings [5] and wicket gates [13] used in hydroelectric stations.

Several authors explored thermal spraying as a method of producing self-lubricated coatings. One remarkable example is the work of H. E. Sliney [14] who developed coatings capable of sustaining low friction at temperatures ranging from -150 °C up to 870 °C. In most cases however, the exposure to high-temperature gases causes lubricants to deteriorate during spray, compromising the bearing performance [16], [63], [64]. A possible way to avoid this problem would be to deposit porous bond coatings which would subsequently be infiltrated by a lubricating composite.

As shown in [65], narrow pores in plasma-sprayed alumina coatings may be difficult to infiltrate by industrial sealants. Therefore, if highly viscous resins are to be infiltrated into sprayed bond coats, a well-defined interconnected porosity must be established throughout the coating's cross-section. Porosity control in thermal spraying can be achieved by using pore formers. For example, polyester (PS) can be co-sprayed with other materials to produce solid oxide fuel cells [66], [67], abradable seal coatings [68], [69] and thermal barrier coatings [70]. As the physical properties of PS are very different from other coating materials, one of the difficulties with this approach concerns finding proper carrier gas flow rates to adjust the trajectory and melting of particles while flying towards the substrate. As the main method to spray porous coatings is plasma spraying, one must also bear in mind the potentially deleterious effects that high-temperature oxidation may have on metallic particles.

It has been recently shown [71] that iron aluminide Fe<sub>3</sub>Al ( $\rho_{Fe_3Al} = 6.61 \text{ g/cm}^3$ ) can be used as a pore former in stainless steel (UNS S44400) coatings ( $\rho_{444} = 7.8 \text{ g/cm}^3$ ). As both materials have similar melting points (1520 °C) and densities, they can be co-sprayed through the nozzle of a high-velocity oxygen fuel (HVOF) torch. The pore former is removed by chemical leaching in a 0.5M HCl solution. In this work, the objective is to extend the results in [71], tailoring the porous network in the stainless steel coatings so they can be later infiltrated by a polyimide-graphite composite.

### 2.3.2 Experimental Methods

#### **Powder Production, Morphology and Size Distribution**

Both SS444 (Eutectic Castolin, Granby, Quebec, Canada) and Fe<sub>3</sub>Al (Ametek, Eighty Four, Pennsylvania, USA) powders were received from water atomizers in a broad range of sizes. Sieving and ball milling in a horizontal stainless steel mill CM08 (ZoZ Simoloyer Inc) with stainless steel balls (3 mm diameter) were used. Table 1 summarizes the method to produce each powder, the milling times involved, the sieve openings, as well as the mean particle diameters and standard deviations after sieving as measured by laser diffraction with a HORIBA LA-900.

Table 3 - Summary of powder fabrication method and particle size distribution.

	<b>Powder Condition</b>	<b>Sieve Opening (<math>\mu\text{m}</math>)</b>	<b>Milling Time (h)</b>	<b>Mean Diameter (<math>\mu\text{m}</math>)</b>	<b>Standard Deviation (<math>\mu\text{m}</math>)</b>
SS444	Atomized	20-53	0	63	19
	Milled	20-53	6	40	23
	Milled	20-53	8	37	15
Fe <sub>3</sub> Al	Atomized	20-53	0	30	13
	Atomized	75-150	0	151	58
	Milled	20-53	9	25	11

As illustrated in Figure 18 (a) and (b) the atomized powders have a typical morphology generated by water atomization i.e. a combination of spherical and elongated particles. After sieving, most SS444 particles are spherical with diameters between 30 to 50  $\mu\text{m}$ . However, due to their high aspect ratio, some of the large elongated particles were able to pass through the sieve openings, which explains why the average diameter was higher than the nominal sieve opening size. The same effect was not observed for the atomized Fe<sub>3</sub>Al particles. Their size and elongated morphology are more uniform. These differences in the sieving behavior can only be explained by the different sieving treatment each manufacturer gave to the powders before delivery. The milled powders (Figure 18(c), (e) and (f)) are composed of large platelets and a group of smaller angular particles which become more numerous with increasing milling time. It can be noticed that the angular particles can have a diameter inferior to 10  $\mu\text{m}$ , while the platelets can have dimensions as large as 50  $\mu\text{m}$ . This explains the relatively high standard deviations (with respect to the mean particle diameter) of the powders produced by milling.

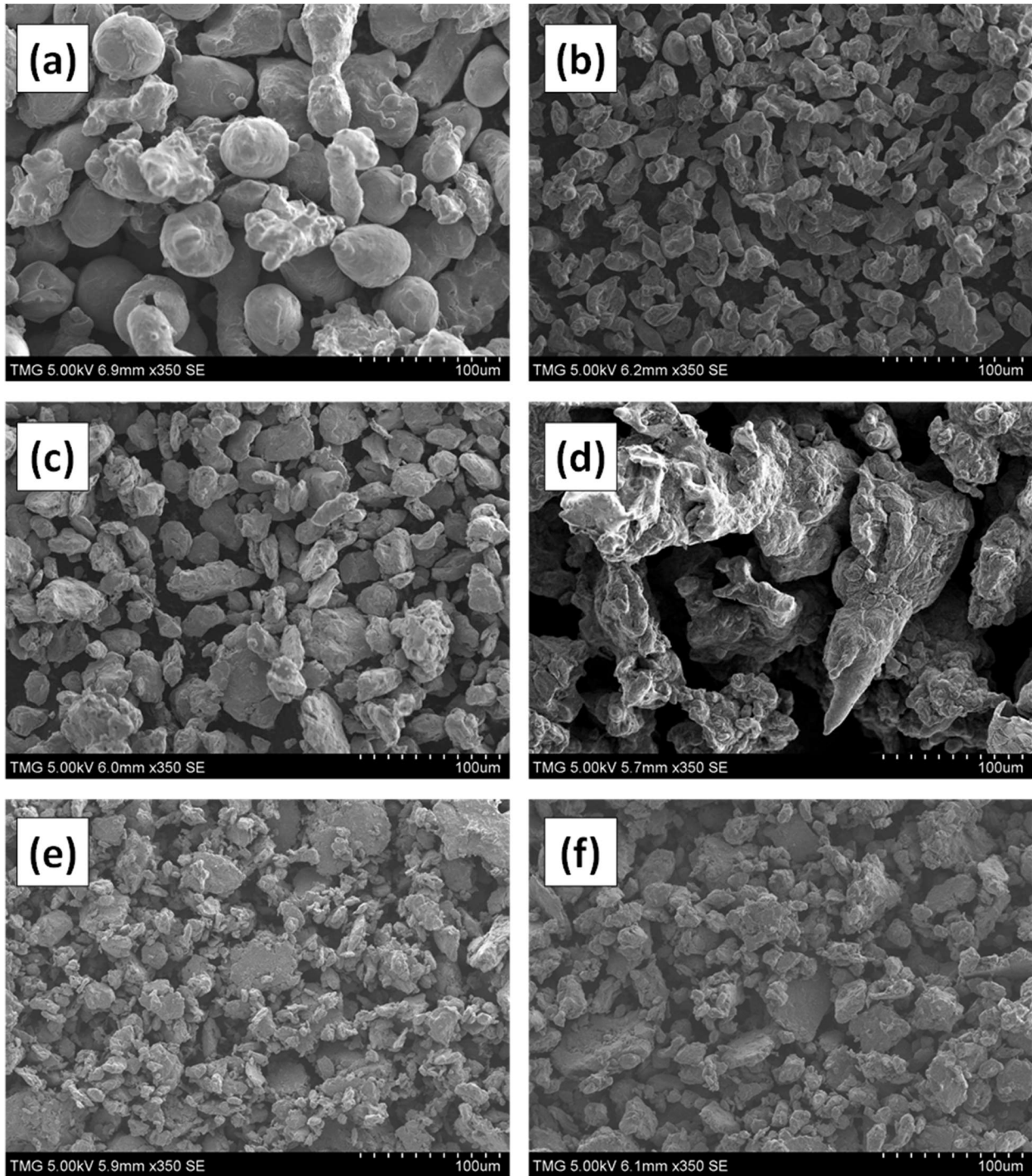


Figure 18- Secondary electron image illustrates the morphology of SS444 and Fe<sub>3</sub>Al particles. (a) Atomized & sieved SS444. (b) Atomized & sieved (fine) Fe<sub>3</sub>Al. (c) Milled 6h and sieved SS444. (d) Atomized and sieved (coarse) Fe<sub>3</sub>Al. (e) Milled (8h) and sieved 444. (f) Milled (9h) and sieved Fe<sub>3</sub>Al.

The chemical composition of the materials used in this work were measured by EDX analysis. The results are summarized in Table 4. The 2.5wt.% Cr addition in the Fe<sub>3</sub>Al increases the material's ductility [72].

The chemical composition of the materials used in this work were measured by EDX analysis. The results are summarized in Table 4.

*Table 4 – Chemical composition of SS444 and Fe<sub>3</sub>Al milled powders as measured by EDX analysis*

	<b>O</b>	<b>Al</b>	<b>Si</b>	<b>Cr</b>	<b>Fe</b>	<b>Mo</b>
SS444	3	-	0.4	19	76	2
Fe <sub>3</sub> Al	3	17	-	2.5	79	-

### **HVOF Spraying**

Two variables were considered for the combination of the steel and pore former. The first parameter was the volume fraction of Fe<sub>3</sub>Al (10%, 30% and 50%) as it controls the coating's total porosity after leaching. The second variable was the melting degree. By using a feedstock with a small mean diameter, or by selecting fuel gases leading to a high heat generation, one can expect that a larger fraction of particles will be completely molten prior to deposition. In other words, the melting degree will be higher. Molten particles form lamellar “splats” upon deposition, whereas semi-molten particles partly retain their original morphology. Therefore, the melting degree experienced by Fe<sub>3</sub>Al particles during spray affects the coating's pore geometry. In this work two melting degree levels, qualitatively defined as “high” and “low”, were obtained by controlling particle mean diameter and spray parameters.

All mixing was simply done by inserting the powders in a bottle and thoroughly shaking it for 1 – 3 minutes. A total of nine powder blends were created. Their characteristics are summarized in Table 5.

Table 5 - Coating identification with corresponding powder blends and volume fractions of SS444 and Fe<sub>3</sub>Al.

Coating ID	Powder Blends		Volume Fraction		Spray Parameter
	SS444	Fe <sub>3</sub> Al	SS444	Fe <sub>3</sub> Al	Set
LH(90/10)			90	10	A
LH(70/30)	Atomized	Atomized	70	30	A
LH(50/50)			50	50	A
HL(90/10)			90	10	B
HL(70/30)	Milled (6h)	Atomized	70	30	B
HL(50/50)			50	50	B
HH(90/10)			90	10	B
HH(70/30)	Milled (8h)	Milled (9h)	70	30	B
HH(50/50)			50	50	B

Each powder blend was sprayed with a liquid kerosene-fueled HVOF torch model JP-8000 from Praxair. The substrates were 190 x 120 mm<sup>2</sup> 444 stainless steel plates which were sandblasted to a roughness of R<sub>a</sub>=21 μm prior to deposition. Two spray parameter sets were used. Parameter set A was used first to spray coatings LH(90/10), LH(70/30) and LH(50/50). To obtain a higher melting degree, the remaining coatings were sprayed with the parameter set B, which has a O/F ratio close to the stoichiometric ratio between oxygen and kerosene, leading to higher in-flight particle temperature. Modelling and experimental results support this claim [22]. Except for oxygen and kerosene flow rates, all spray parameters displayed in Table 6 were identical in both parameter sets.

Table 6 – Spray parameters used to produce composite SS444/Fe<sub>3</sub>Al coatings.

Spray Set	O <sub>2</sub> Flow Rate (L/Min)	Fuel Flow Rate (L/Hour)	O/F Ratio	Comb. Pressure (kPa)	Shared Spray Parameters	
A	732	28	0.79	655	Powder Feeder	6 RPM
					Stand-off Distance	33 cm
					Argon Flow Rate	4.5 LPM
					Number of Passes	15
B	802	25	0.99	662	Transversal Speed	500 mm/s
					Step Size	10 mm
					Nozzle Length	10 cm

### Etched Cross Sections Analysis

To evaluate the feasibility of the porosity control method, it is important to ascertain that the leaching rate of the Fe<sub>3</sub>Al is fast and at the same time, little degradation is observed in the SS444

matrix. Therefore, it is important to evaluate whether the coating steel-to-iron aluminide ratio corresponds to that of the feedstock. The issue was addressed by immersing coatings LH(70/30), HL(70/30) and HH(70/30) **cross sections** before and after immersion into 0.5M HCl at room temperature solution for 3 minutes. The pore area fraction was then determined by image analysis. The coating's Fe<sub>3</sub>Al fraction was determined by subtracting the as-sprayed coating porosity from the etched coating porosity.

### Chemical Leaching

The coated steel plates were water-jet cut in small disks of 1.6 cm in diameter. Prior to leaching, the disk edges were coated with a sealant to avoid chemical attack at the substrate/coating interface. The coatings were then submerged in a stagnant 0.5M HCl solution held at room temperature or at 45 °C achieved with the help of a heating plate. As presented in the results section, the solution temperature was found to be an important parameter as it substantially affects the leaching rates. Figure 19 illustrates the procedure.

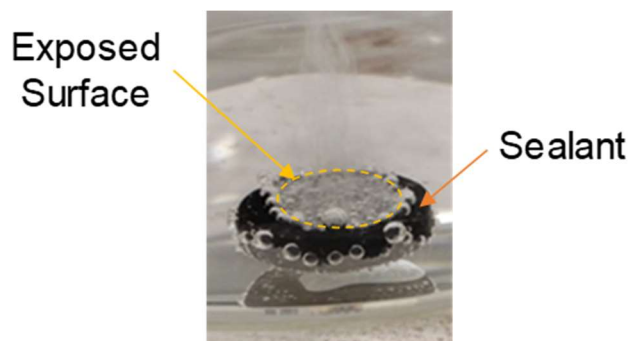


*Figure 19- Composite HVOF coating during the leaching procedure. A black sealing paint was brushed around the disk edges to prevent from chemical attack at the coating/substrate interface, which limited the exposed coating surface area to the solution.*

The leaching behavior at room temperature (RT) was investigated by optical microscopy as a function of the immersion times of 1h, 2h and 3 h. The leached coatings were sectioned, hot-mounted in resin, ground on SiC papers and polished with diamond suspensions. The final polishing step was done with a 0.05 μm alumina suspension. As will be discussed in the results section, leaching at RT was insufficient for complete pore former removal. Therefore, analysis of coatings leached at room temperature was limited to microstructure observations.

For the coatings leached at 45 °C, a vacuum-sintering post-heat treatment was applied for 1h at 1300 °C. The leached and sintered coatings were vacuum-impregnated with Struers' EpoFix to avoid further damage during sectioning. For electronic microscopy analysis, the coatings were

cold mounted and then subjected to the same polishing procedure described for the hot-mounted coatings.

### **Polyimide Infiltration**

Polyimide was purchased as powder PI1031 (VTEC Richard Blaine International, Reading, PA, USA) and mixed with 25 wt.% graphite (Grade 4827 - Asbury Graphite Mills Inc – Asbury NJ USA) in a planetary ball mill for one hour at 100 RPM. The mixture was carefully laid down over the leached specimens prior to a three-step hot pressing (Carver Inc Model 3889 Indiana USA). The first step was done for one hour with no pressure at 132 °C which yields optimal flowability for the PI resin. The second is done for 1.5 hours at 180 °C for high imidization rates [38], and a final 1h-step at 200 °C to complete the resin's polymerization reaction. Both second and third steps are done under a pressure of 2.7 MPa. Finally, the system was air-cooled until room temperature was achieved.

### 2.3.3 Results

#### 2.3.3.1 *As-Sprayed Coatings*

As illustrated in Figure 20, the LH coatings are composed of large SS444 splats that underwent little to no melting prior to deposition. They are surrounded by a continuous network created by small Fe<sub>3</sub>Al particles that experienced complete melting prior to deposition. Despite their similar melting points, the different melting degrees experienced by matrix and pore forming phases can be mostly attributed to their large differences in particle sizes and morphologies (for reference see Table 3 and Figure 18).

One may easily notice that, as the volume fraction of Fe<sub>3</sub>Al increases, so does the separation between the SS444 splats. The deposition efficiencies of LH(90/10), LH(70/30) and LH (50/50) were respectively 19, 20 and 27 μm per pass suggesting a better deposition efficiency (DE) of the smaller pore former phase in detriment of the coarse matrix particles.

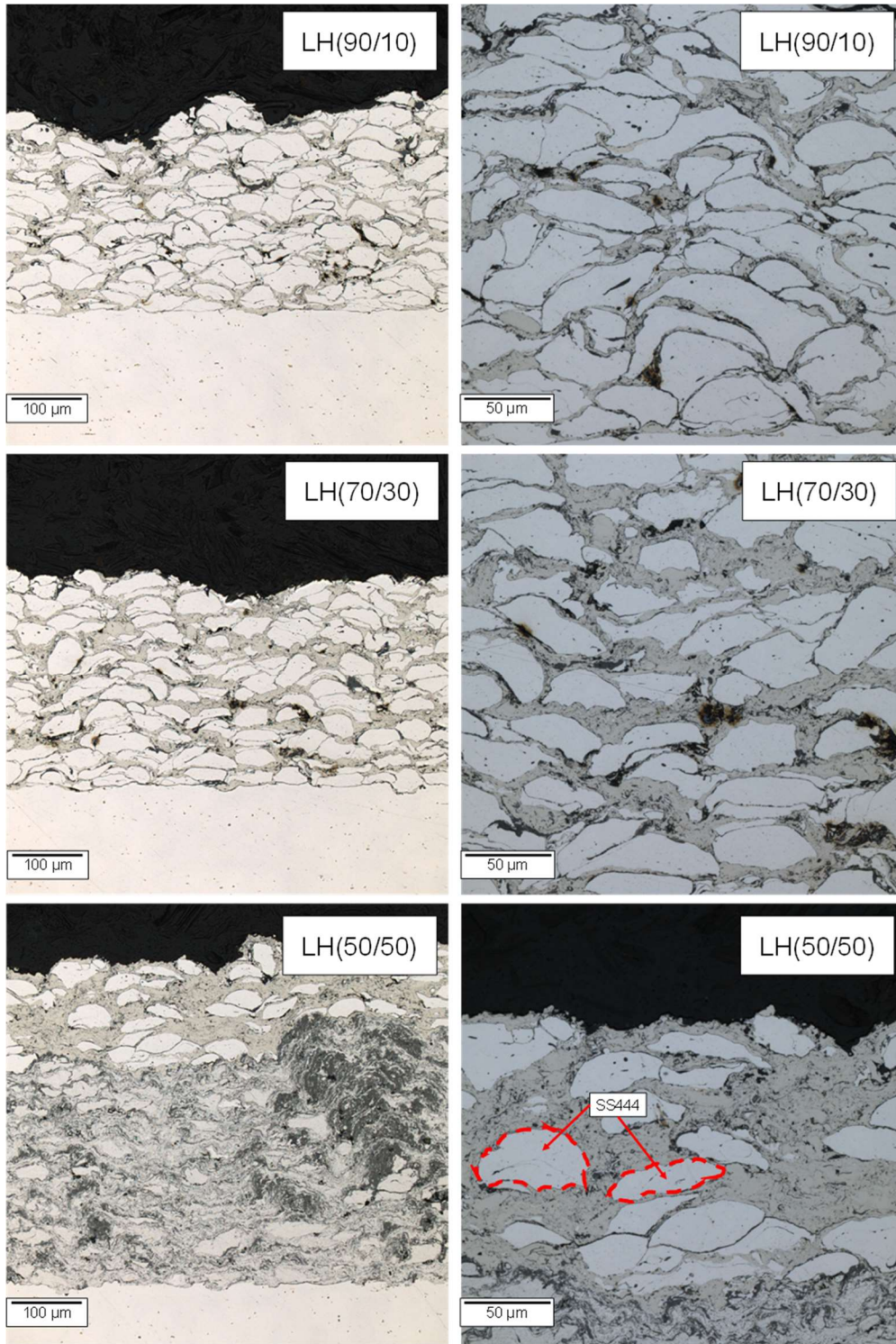


Figure 20 - As-sprayed structure of LH coatings. The coarse stainless steel particles experience little in-flight melting as opposed to the  $Fe_3Al$  pore former, which appears to melt completely. As a result, the coating composite structure is comprised of deformed semi-molten SS444 splats (highlighted in red) surrounded by a  $Fe_3Al$  network.

As opposed to the LH coatings, the HL coatings illustrated in Figure 21 have large pore forming particles separated by a SS444 network. The matrix structure displays oxides which were not observed (by optical microscopy) in the previous group of coatings. This may be due not only to the smaller 444 particles used but also to their angular and or lamellar morphology which, according to modelling results, increase their in-flight heating rates [25]. The DE for HL(90/10), HL(70/30) and HL(50/50) were 17, 13 and 10  $\mu\text{m}$  per pass and, like the LH coatings, decreases as the fraction of coarse particles increase in the feedstock.

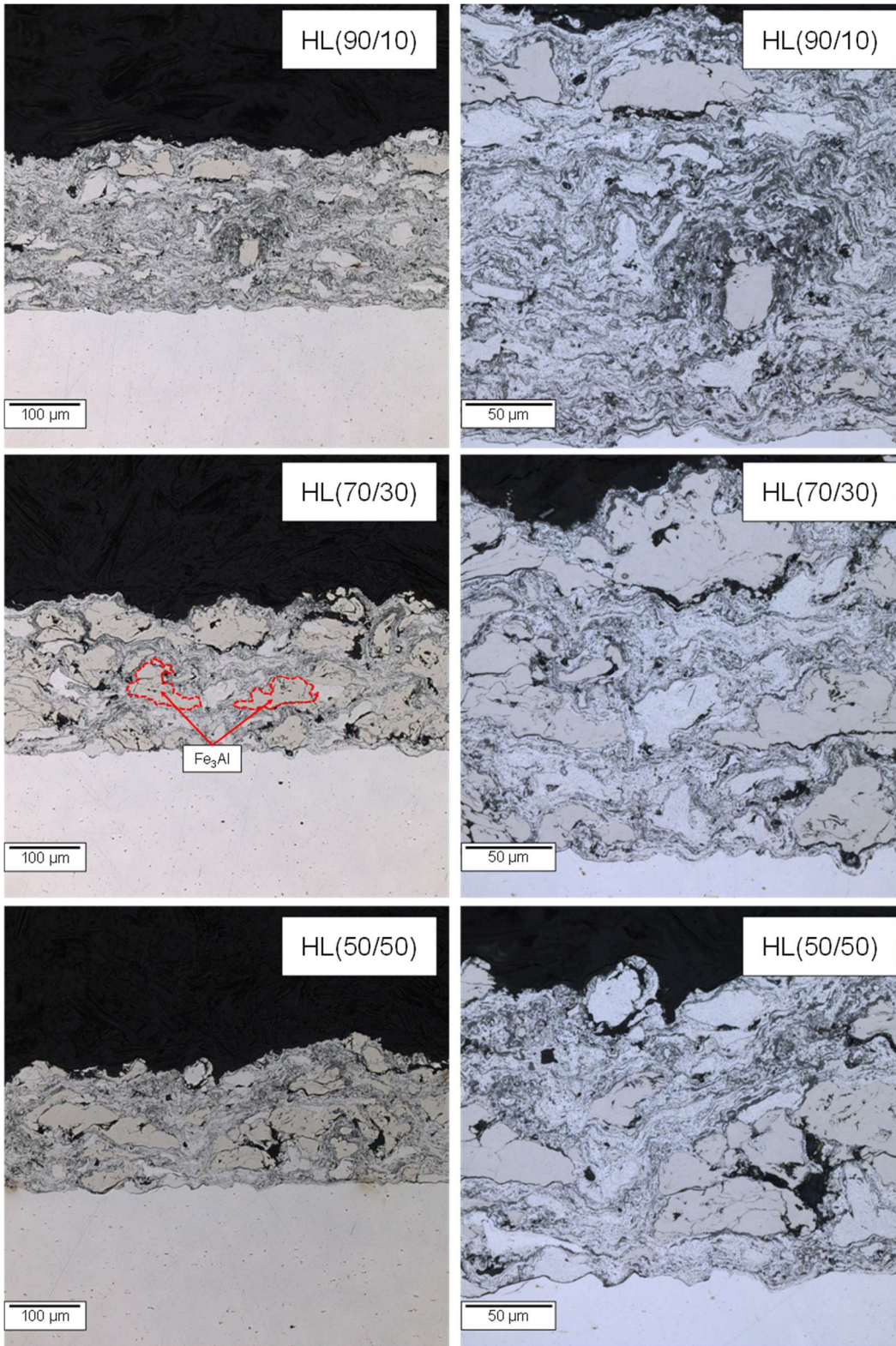


Figure 21 - As-sprayed structure of HL coatings. The coarse Fe<sub>3</sub>Al pore former particles (highlighted in red) did not melt prior to deposition contrary to the SS444 splats, which seem to have experienced melting and high-temperature oxidation.

In the last group of coatings shown in Figure 22, matrix and pore former phases experience a high degree of melting, which is a consequence of using finer 444 and Fe<sub>3</sub>Al particles, as well as to the use of an oxygen-rich flame (spray parameter B). Based on the presence of dark “grey” zones one could also argue that the level of oxidation in the HH coatings is higher than in the previous groups. The deposition efficiency for HH(90/10) was 14 μm per pass while for HH(70/30) and HH(50/50) it was about 10 μm per pass.

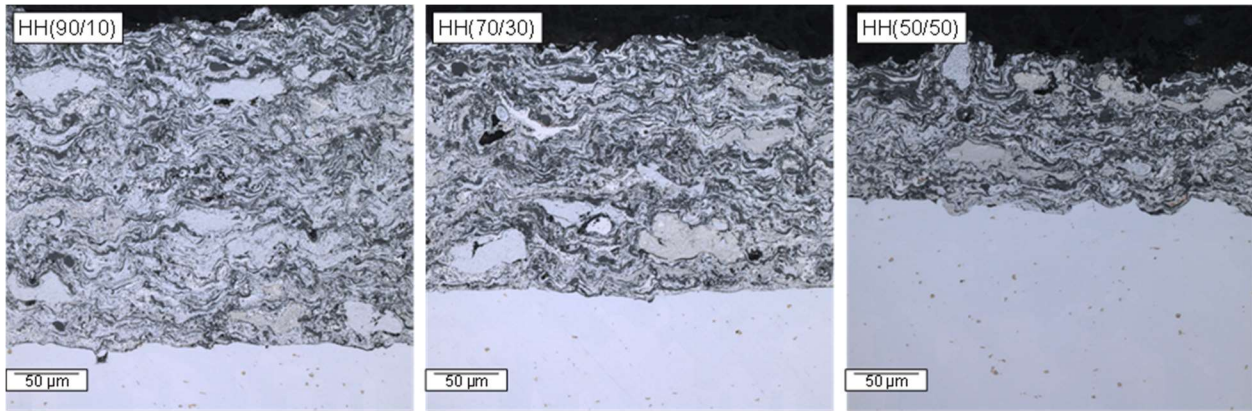


Figure 22 - As-sprayed structure of the HH coatings. Both matrix and pore forming phases experience a high melting degree creating the typical “splat pile-up” structure.

It must be clarified that after eight passes, a clogging problem led to a complete interruption of powder feeding during the deposition of coating HH(50/50). As shown in Figures 19(e) and 19(f) a significant portion of the particles used for the deposition of the HH coatings had a diameter inferior to 20 μm. Additionally, the angular shape of milled powders impairs its flowability. Therefore, one can argue that the changes observed in the deposition rates are not strongly related to volume fractions of SS444 and Fe<sub>3</sub>Al. As the sequence of deposition happened first for HH(90/10) and finished with HH(50/50), it is more likely that the decreasing thicknesses are probably caused by an increasing obstruction of the powder feed lines culminating with the clogging problem.

The coating’s thicknesses and DEs are summarized in Table 7.

Table 7 - Summary of composite coatings thicknesses and deposition efficiencies. \*Only five passes were done for coating LH (50/50). \*\*Only eight spray passes were done for coating HH(50/50).

Volume Fraction	LH Coatings		HL Coatings		HH Coatings	
	Thickness ( $\mu\text{m}$ )	DE ( $\mu\text{m/pass}$ )	Thickness ( $\mu\text{m}$ )	DE ( $\mu\text{m/pass}$ )	Thickness ( $\mu\text{m}$ )	DE ( $\mu\text{m/pass}$ )
90/10	290	19	257	17	205	14
70/30	303	20	201	13	157	10
50/50	135*	27	157	10	86**	11

### 2.3.3.2 Etched Cross-Section Analysis

As illustrated in Figure 23, the 3-minute period of immersion in the HCl solution was enough to etch the  $\text{Fe}_3\text{Al}$ . While some etching residues appeared, the SS444 particles remain mostly intact, proving that the leaching rate of the pore former is much higher than that of the matrix. Image analysis performed on etched cross sections revealed that the  $\text{Fe}_3\text{Al}$  fractions of coatings LH(70/30), HL(70/30) and HH(70/30) were 22%, 36% and 23% respectively. The deviations between coating and feedstock pore former fractions ranged from 4-8%, which suggest that the deposition efficiencies of SS444 and  $\text{Fe}_3\text{Al}$  are not very different and may be considered a positive trait of the chosen pair of materials.

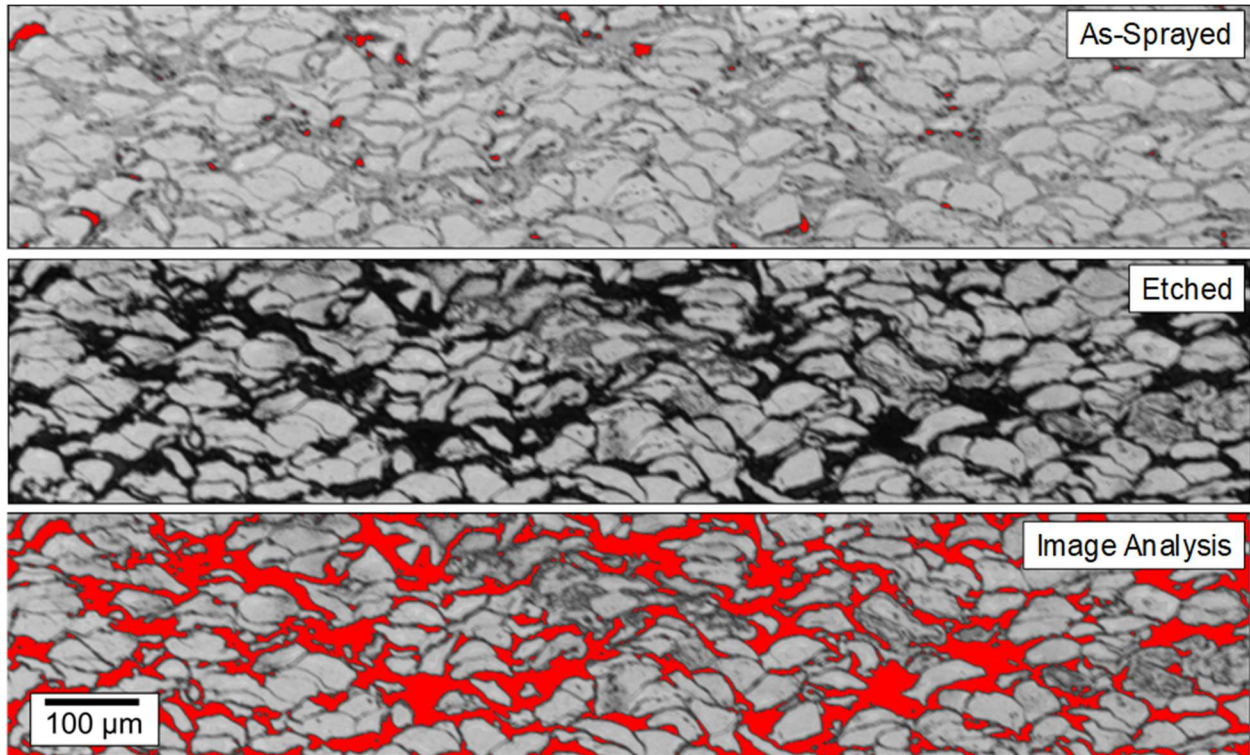


Figure 23 – Comparison between as-sprayed and etched cross sections of coating LH(70/30). The  $Fe_3Al$  pore former dissolves more quickly than the SS444 matrix. The areas highlighted in red used in the image analysis procedure correspond to the pores found in the as-sprayed and etched coatings.

### 2.3.3.3 Chemical Leaching

While the results shown in the previous section show that the pore former is dissolved more quickly than the SS444 matrix, the proposed leaching method relies on the chemical's ability to penetrate the pore former network from the coating's surface. Figure 24 illustrates that as the  $Fe_3Al$  is dissolved, it reveals poorly connected stainless steel splats which can be easily pulled out of the coating with a scotch tape or even during the sectioning/polishing procedures. Additionally, Figure 24(a) illustrates that for low pore former fractions, the leaching paths are heterogeneous, being very narrow at some points and wider at others. As a result, the chemical leaching rate is also heterogenous, revealing zones of localized leaching, where the path for acid

penetration is more spacious. After three hours (Figure 24(b)), while the leaching effects are more noticeable, the leaching process is far from completion and most of the  $\text{Fe}_3\text{Al}$  remain undissolved.

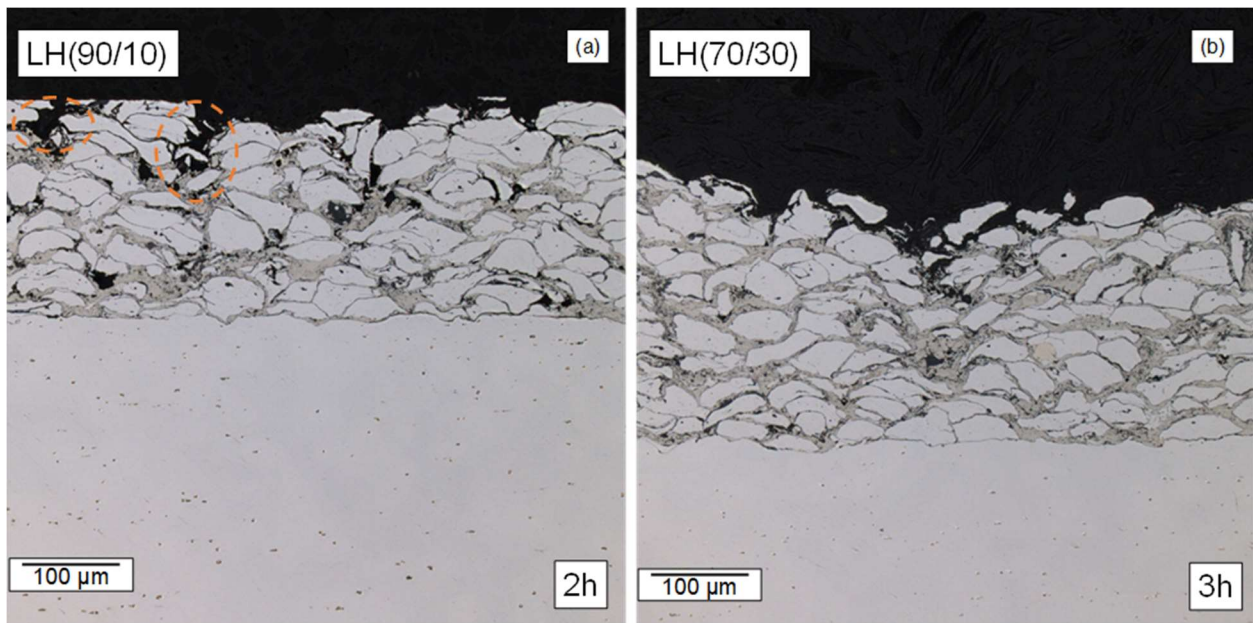


Figure 24 – The leaching process in the LH coatings leads to the formation of poorly bonded SS444 splats that may be easily detached from the underlying coating. (a) The low volume fraction of  $\text{Fe}_3\text{Al}$  in LH(90/10) leads to localized leaching zones (dashed lines). (b) Even after three hours most of the  $\text{Fe}_3\text{Al}$  remains in the LH(70/30 coating).

For the HL group of coatings, as the leaching process progresses, the large  $\text{Fe}_3\text{Al}$  particles close to the surface are quickly dissolved, leaving a thin sheath of SS444 matrix around the pore. This is illustrated in Figure 25. While these features are observed after 1h and 2h of immersion in HCl, they were not found after three hours, suggesting that the sheaves cannot withstand the stresses applied during section/polishing. The effect probably worsens as the volume fraction of pore former increases because the thickness of the remaining sheaths decreases, further impairing the remaining matrix's mechanical properties.

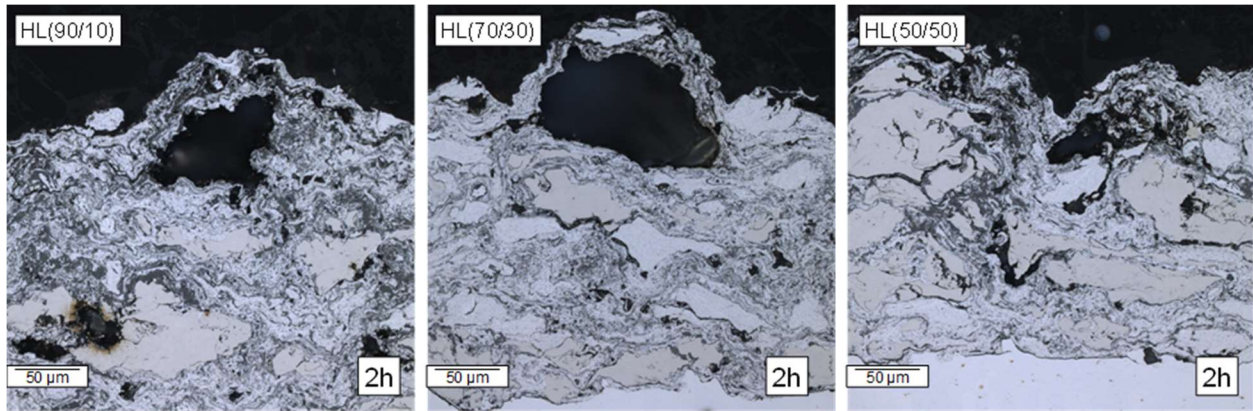


Figure 25 – The leaching process in the HL group of coatings leads to the formation of thin sheathes of SS444 surrounding large pores. After three hours the sheathes are no longer observed, possibly due to their chemical degradation and impaired mechanical integrity.

As illustrated in Figure 26, the leaching process in the HH coatings was more homogeneous than the preceding group of coatings, creating a leached layer with a depth of nearly 60 μm for the HH(70/30) after two hours of immersion. The leached zone displays not only small pores originated by the pore former dissolution, but also reveals a “darkened” steel matrix, suggesting that a highly oxidized SS444 matrix is less capable of withstanding the exposure to the HCl solution. The leached zone was not found after three hours of immersion which indicates that it was pulled out during the sectioning/polishing procedures.

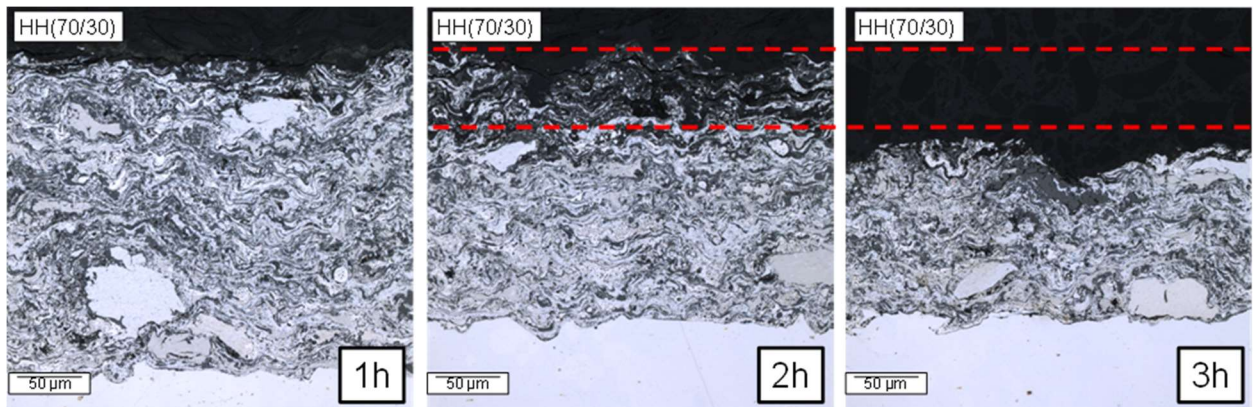


Figure 26 – The leaching process in the HH group of coatings is more homogenous. Both the SS444 and Fe<sub>3</sub>Al splats are leached in the solution and while a porous layer forms after two hours of immersion, its mechanical properties are insufficient to withstand the loads applied during the sectioning and polishing.

In summary, the leaching done at room temperature was inadequate to completely remove the Fe<sub>3</sub>Al phase from all three groups of coatings. Moreover, the remaining “as-leached” layers did not have appreciable mechanical strength that would be necessary for bearing applications.

Therefore, it was necessary to increase the pore former leaching rate, as well as to strengthen the SS444 matrix's strength after leaching.

Based on the fact that iron is the main element being leached from the coatings, one may refer to the work of Taneja who showed that the dissolution rate constant of iron in hydrochloric acid solutions can be roughly doubled by increasing the solution temperature from 26 °C to 45 °C [73].

As shown in Figure 27, up to two thirds (depth of 175 – 200 μm) of the Fe<sub>3</sub>Al network was dissolved when the leaching was done at 45 °C for three hours. Moreover, due to the sintering treatment done at 1300 °C and the resin impregnation in vacuum, the matrix's structure remains nearly intact after sectioning and polishing. The LH coating's pores are clearly interconnected, and their sizes correspond to the previously deposited aluminide network.

As for the HL coatings, the leaching at 45 °C was enough to almost completely remove the pore former from the coating after three hours. However, the exposure to the acidic solution seems to degrade the matrix's chemistry. As illustrated in Figure 27, two hours of leaching is enough to create a deep leached layer where the matrix is “darker” than the unleached matrix underneath.

As for the HH coatings, the leached layer depth after two hours was of approximately 100 μm. The SS444 matrix appears to suffer an even stronger chemical degradation as compared with the HL coatings. Spraying a feedstock with small average diameter with angular and/or lamellar morphology may have aggravated the high-temperature oxidation experienced during flight towards the substrate. Higher oxygen contents in stainless steel coatings has been shown to impair their corrosion resistance [49], [50]. Apart from the degradation, the resulting pore structure is finer than those observed in previous groups of coatings which can be attributed to the use of finer Fe<sub>3</sub>Al and SS444 particle sizes.

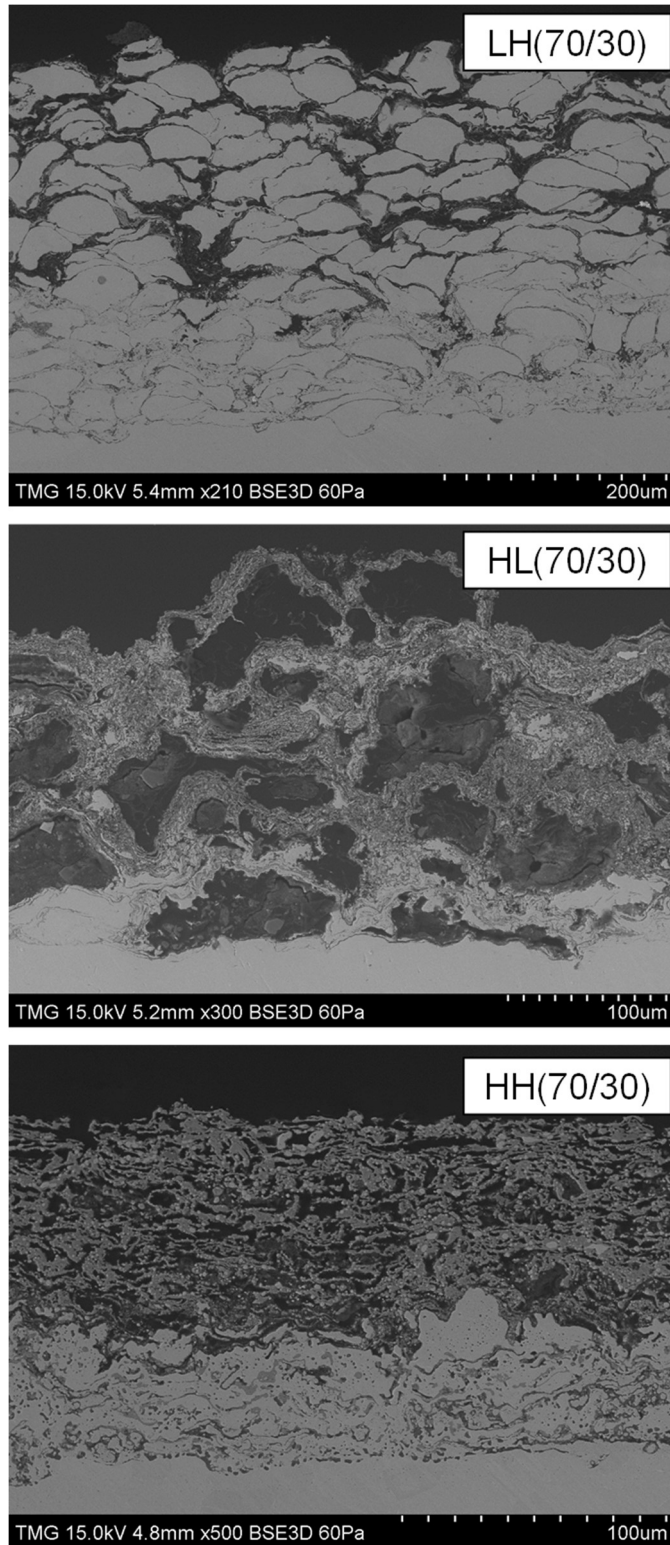


Figure 27 – Backscattered electron image of leached coatings. Increasing the immersion temperature to 45 °C increases the leaching rate and different pore sizes and morphologies may be achieved depending on the feedstock.

### 2.3.3.4 Polyimide Infiltration

The final step in the production of polymer-lined bearings consists in hot pressing the PI-25wt.%graphite mixture on the leached and sintered coatings. As illustrated in Figure 28, a 1 mm thick PI coating was formed over a LH(70/30) coating and the PI resin effectively penetrates the pore network. The presence of a few pores in the polyimide was expected due to the imidization process that generates water vapor [38], [74]. The presence of some Al-rich precipitates indicates that some residual  $\text{Fe}_3\text{Al}$  remained in the coating after the 3h of leaching. Finally, some splats seem to have coalesced with each other, forming a “neck”, which is an expected result from the sintering heat-treatment. However, the effect does not seem to compromise the PI ability to penetrate the coating’s pores.

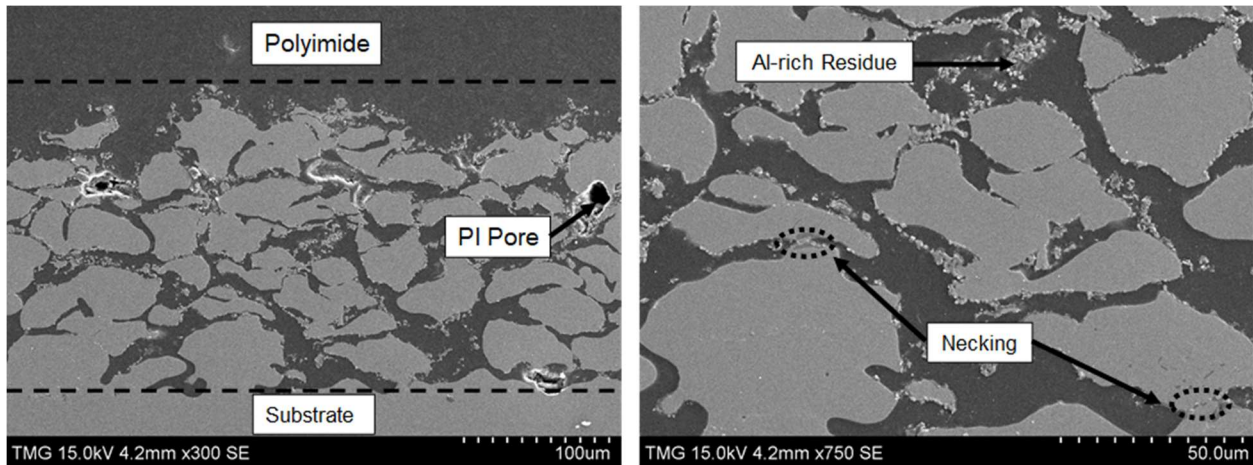


Figure 28 – Secondary electron image of Polyimide-infiltrated LH(70/30) coating. The PI-25wt.%Graphite mixture penetrates most of the leached coating pore network. It is possible to observe some Al-rich residues that were not completely removed after leaching. The regions in the dashed circles indicate regions of splat coalescence caused by the sintering heat-treatment.

As for the other groups of coatings, it was not possible to observe PI infiltration due either to excessive chemical leaching or coating spallation during sintering. In HH and HL coatings, the SS444 splats undergo chemical and mechanical degradations that, in the context of this work, prohibit their use in the envisaged bearing application.

### 2.3.4 Discussion

The observed 444/ $\text{Fe}_3\text{Al}$  coating structures can be partially analyzed by the theory developed for the packing of a binary mixture of particles formally studied in [75], [76]. The mean coordination number, i.e. the average number of a given contact type each particle forms in a binary 444/ $\text{Fe}_3\text{Al}$  mixture, depends on the particle diameter ratio (DR) and their respective volume fractions.

The use of thermal spraying includes variables not accounted for in the context of packing of spheres. For example, if the deposition efficiencies of matrix and pore former are different, their volume fractions in the deposited coating will differ from that of the original powder blend. As the results in Table 5 suggest, the deposition rate decreases when the fraction of larger particles in the mixture increases. This effect has been observed for HVOF [77] and flame sprayed stainless steel coatings [78]. Therefore, one may argue that the current approach to produce porous stainless steel coatings has a limit on the maximum pore size that can be obtained.

The melting degree experienced by the particles prior to deposition can affect the coating packing density and hence the mean coordination number of all types of contacts. This may be particularly useful to improve the coating “as-leached” coating mechanical properties. In the present work, this effect was probably overshadowed by the combined deleterious effects of in-flight oxidation and the chemical degradation that affected the HH coatings. Three alternatives are suggested to contour this issue: using lower temperature processes such as HVOF or cold spraying; employ more heat and oxidation resistant matrix metals such as Ni-alloys (which also have equivalent corrosion resistance [79]) and; select a different pore former and/or leaching environment such as aluminum which may be dissolved in basic solutions [80].

To overcome the problem of low coating mechanical integrity, the sintering heat-treatment was found to be crucial. Sintering is also used to produce polymer-lined steel-backed bearings [81]. The sintering conditions may interfere on their tribological behavior [82] and may be a subject of interest to those interested in using the current approach to produce self-lubricated surfaces.

The observations extracted from the leaching of 444/Fe<sub>3</sub>Al composite coatings, may be used to specify general feedstock preparation guidelines for a matrix/pore former pair used to create porous thermal-sprayed coatings by chemical leaching. The pore former volume fraction has significant effects on the final coating performance. Using volume fractions significantly lower than to 30% may lead to localized leaching and heterogenous coating structures. For higher volume fractions, the “as-leached” integrity may be jeopardized, imposing further high-temperature sintering treatments if appreciable coating strength is required. The pore former to matrix particle diameter ratio influences the geometry of pores. For diameter ratios significantly lower than to 1, the pores will tend to be flat as the particles experience a high in-flight melting degree. As the DR values become higher than 1, the pores will tend to maintain the original feedstock morphology. However, if the pore former diameter is too large, one should expect a decrease in the process deposition efficiency.

It is important to mention that these guidelines (summarized in Figure 12), were developed under the assumption that matrix and pore former have, for the same particle diameter, similar deposition efficiencies. If such is not the case, the ideal pore former volume fraction range in the feedstock may differ from the suggested 30%. However, in a qualitative sense, the effects of diameter ratio and pore former volume fraction on coating leaching behavior should remain as discussed.

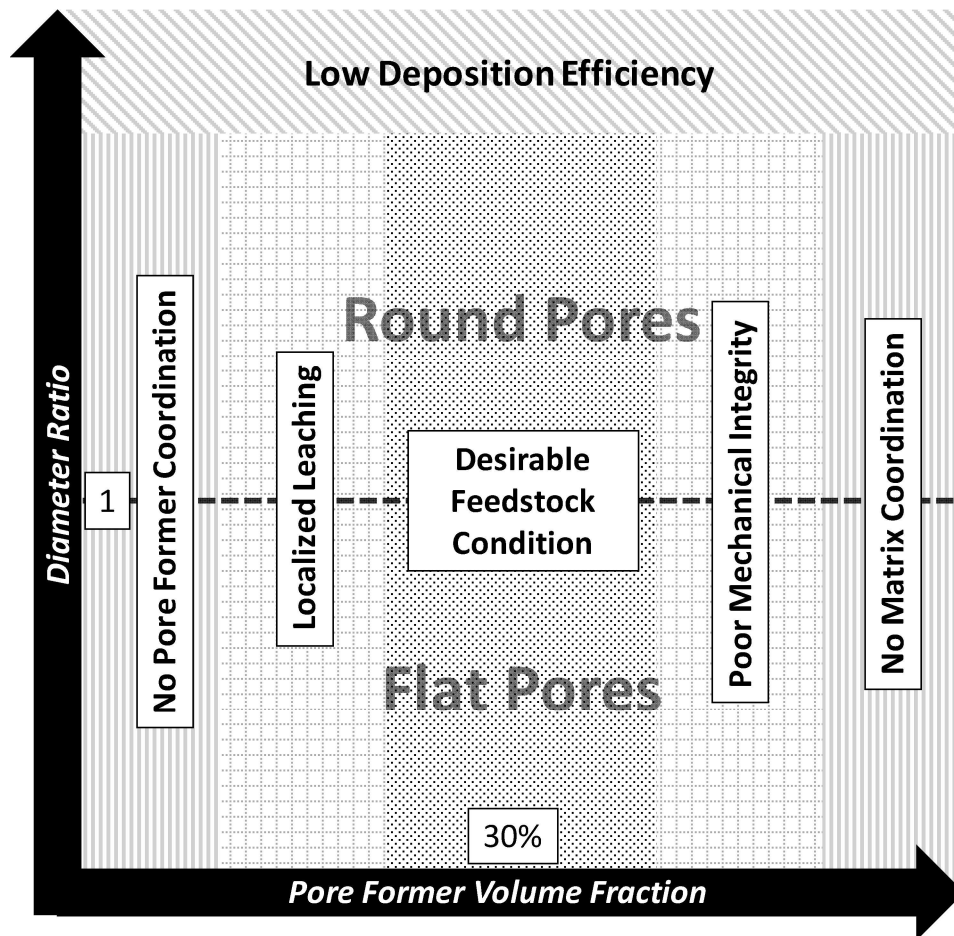


Figure 29 – This diagram qualitatively depicts the role of feedstock condition on the outcome of spraying a mixture of particles containing a matrix and a leachable pore former. The diameter ratio controls the pore geometry and may interfere on coating deposition efficiency. The pore former volume fraction affects the mean coordination numbers, hence interfering with the leaching behavior and the as-leached final mechanical properties.

The ability of the polyimide binder to penetrate the porous network was a major concern in this study as the viscosity of thermoset resins tend to be particularly high [65]. As shown in Figure 28, the PI-25wt.%graphite mixture was able to penetrate pores with openings as narrow as 10  $\mu\text{m}$ .

The results are very encouraging and suggest that other lubricant formulations with higher graphite content, or with PTFE could be used. In summary, it is believed that if proper caution is exercised during feedstock preparation and during leaching, the methodology proposed in this work allows one to create interesting composite metal-polymer structures.

### 2.3.5 Conclusions

In the present work, a method to produce porous stainless steel coatings is presented as an alternative method to bond a polyimide composite to large surfaces without the use of adhesives. The method also avoids exposure of the self-lubricating graphite to the high-temperatures of the spray gases.

Acid leaching in 0.5M HCl solution was used to control the porosity in HVOF-sprayed SS444/Fe<sub>3</sub>Al coatings. Nine different feedstock blends were prepared with varying volume fractions and size distributions of SS444 and Fe<sub>3</sub>Al particles. The main observations in the study were:

- While the Fe<sub>3</sub>Al particles are dissolved more quickly than the steel splats, immersion in the HCl solution significantly degrades the remaining SS444 structure, compromising its “as-leached” mechanical properties. The effect worsens if the solution temperature is increased from room temperature to 45 °C or if the stainless steel particles excessively oxidize during spray.
- A sintering heat treatment is crucial for the porous coatings to develop enough strength to withstand the stresses experienced during the hot pressing and infiltration of the polymer.
- It has been shown that stainless steel bond coatings with an interconnected pore network can be produced by combining, in appropriate fractions, stainless steel particles that do not endure excessive high-temperature oxidation during spray and; Fe<sub>3</sub>Al pore forming particles that melt before deposition into a substrate. A polyimide composite containing 25 wt.% graphite was successfully infiltrated in a bond coating with pore opening diameters as narrow as 10 μm.

## Chapter 3 – Corrosion Resistance of Thermally Sprayed Coatings

The idea of spraying corrosion-resistant coatings on different surfaces with well-established industrial processes is interesting for numerous reasons including:

- Cathodic protection of reinforced concrete bridges [83];
- Easy on-site repair of worn and/or corroded valves or pumps used in aggressive environments [84];
- Protection of bores in lightweight automotive parts [85].
- Replace environmentally- and health-hazardous plated coatings [86], [87].

The successful application of corrosion resistant coatings in a wide range of applications must be endorsed by solid performance assessment techniques. In the following section, basic electrochemistry concepts used for general corrosion performance assessment will be presented. Then, a critical overview of early and recent publications on the corrosion resistance of metallic sprayed coatings will be presented.

### 3.1 Basic Electrochemistry Concepts

When a metal corrodes, some atoms move away from the solid surface into the solution, attaining a charged state. For example, iron may corrode according to the oxidation (or anodic) reaction  $Fe \rightarrow Fe^{2+} + 2e^-$ . The two electrons “released” from the metal’s surface participate in a reduction (or cathodic) reaction which in this example could be  $2Fe^{3+} + 2e^- \rightarrow 2Fe^{2+}$ . In this case, for every dissolving Fe atom, the electrons perform a closed loop, ensuring electrical neutrality, which is typical of spontaneous corrosion processes. If instead, these electrons were directed into an organized flow, the resulting *faradaic current* could be measured and used (under some assumptions) to estimate the rate at which iron corrodes. Faraday’s law can be described by equation (4) as:

$$\frac{\Delta\varepsilon}{\Delta t} = \frac{i}{2F} \cdot \frac{M}{2\rho} \quad (4)$$

where  $\Delta\varepsilon/\Delta t$  is the thickness loss rate,  $i$  is the current density,  $F = 96486 \text{ C} \cdot \text{mol}^{-1}$  is Faraday’s constant,  $M$  is the molar weight and  $\rho$  is the metal’s density.

The investigation of corrosion processes is often done in 3-electrode cells which contain a:

- **Working electrode (WE):** consists of the specimen of interest with a controlled geometry and exposed surface area.

- **Counter Electrode (CE):** a large electrode (as compared to the WE) made of inert materials such as carbon, platinum, TiO<sub>2</sub>-stabilized RuO<sub>2</sub> or IrO<sub>2</sub>, etc.
- **Reference Electrode (RE):** used to probe the thermodynamic state at the interface between the WE and the solution (or electrolyte).

By connecting the 3-electrode cell to a potentiostat, it is possible to measure as well as to deliberately change the potential (or voltage) between RE and WE, which affects the kinetics of the ongoing reactions. Additionally, the electrons delivered by the anodic reaction now flow from the WE through the potentiostat to finally reach the CE, where the cathodic reaction takes place (and vice-versa). This allows one to determine the faradaic currents ( $i$ ) associated with the corrosion process.

The response of an electrochemical cell to an externally applied voltage is significantly different from that of a simple resistor. While the latter obeys Ohm's law, hence a linear relationship with voltage, the former follows Butler-Volmer's equation, where the faradaic currents vary exponentially with the changes in the electrode potential ( $E$ ) as detailed in equation (5):

$$i = i_{corr}[\exp(b_a \cdot \eta) - \exp(b_c \cdot \eta)] \quad (5)$$

where  $i_{corr}$  is the corrosion current measured at the rest potential,  $b_a > 0$  and  $b_c < 0$  are the anodic and cathodic Tafel slopes respectively, and  $\eta = E - E_{corr}$  is the overpotential, which corresponds to the shift of the electrode potential from the *rest* or *corrosion potential*  $E_{corr}$ .

Important kinetic parameters may be derived by plotting the measured faradaic currents as a function of the electrode potential (polarization curve). As illustrated in Figure 30, the  $E_{corr}$  can be readily identified at the "valley" formed between the anodic and cathodic branches. Each branch is characterized by their slopes  $\beta_a = 2.303/b_a$  and  $\beta_c = 2.303/b_c$  (notice that  $\ln 10 = 2.302$ ) which depend on the nature of the cathodic and anodic reactions as well as on the electrolyte temperature. In this example,  $\beta_c = 10 \times \beta_a$ , hence it is ten times more difficult to drive the cathodic reaction, than it is to drive the anodic. The determination of  $i_{corr}$  relies on extrapolating the current density response at high  $|\eta|$  to  $\eta = 0$ .

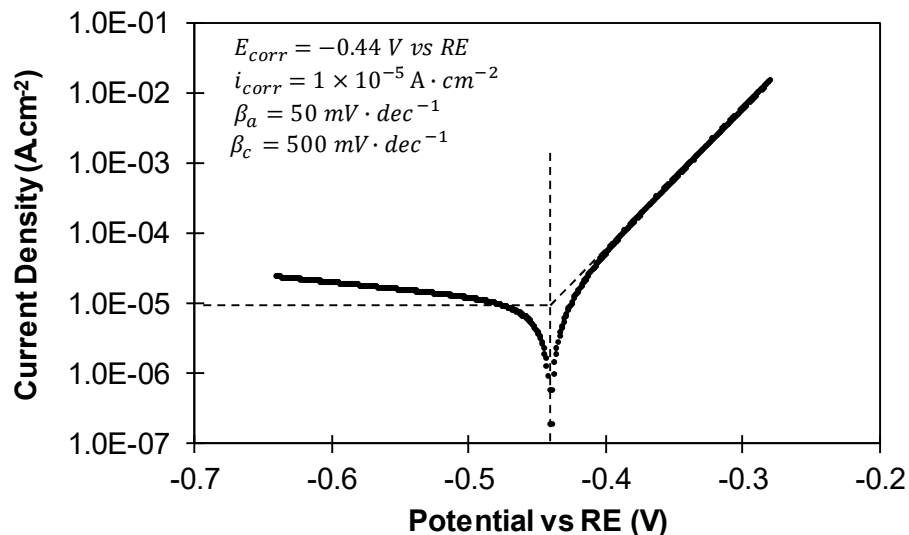


Figure 30 – Polarization behavior for an idealized corrosion processes.

There are several factors that complicate the use of polarization curves to determine the corrosion rates. Diffusion of reacting species from the bulk electrolyte or through corrosion products deposited on the electrode surface may control the reaction kinetics. For example, stainless steels are known for their ability to spontaneously form a thin protective (also known as passive) film that limits the anodic reaction to significantly lower rates when compared to carbon steels. When a stainless steel is polarized, the anodic branch does not display a single slope. In this scenario, one must choose a potential range ( $\Delta E$ ) in which the anodic slope is considered linear before the  $\eta \rightarrow 0$  extrapolation can be done. Different  $\Delta E$  choices, will lead to different  $i_{corr}$  values, entailing significant uncertainties when determining corrosion rates, which is why some researchers are now developing models to obtain more reliable estimations [88].

The principles used to derive Butler-Volmer's equation assume that the electrochemical reactions are occurring on a homogenous flat surface with a well-known exposed surface area. In thermal spray coatings, the presence of oxides and especially pores contradict such assumptions, further complicating the interpretation of polarization curves which are, nevertheless, one of the most popular methods used to assess the corrosion of thermal sprayed coatings.

One must also bear in mind that polarization may have irreversible effects on the working electrode's behavior. For example, when stainless steels are polarized anodically  $\eta > 0$ , the passive film is enriched in Cr [89], leading to a further increase in its resistance to corrosion. However, at a sufficiently high  $\eta \gg 0$ , the protectiveness of the passive film may be disrupted at

small sites or pits, where the anodic reaction occurs preferentially at much higher rates than those measured before passivity breakdown.

### Impedance Spectroscopy

Another technique becoming increasingly popular to assess the corrosion properties of coatings is the electrochemical impedance spectroscopy (EIS). It consists in applying small potential perturbations ( $\tilde{V}$ ) of 5 mV – 15 mV amplitude at the WE with varying frequencies. Therefore, Impedance ( $Z$ ) can be defined as the ratio between the perturbation  $\tilde{V}$  and the resulting current  $\tilde{i}$ .

Due to the low amplitude of  $\tilde{V}$ , EIS has the advantage of having a negligible effect on the electrode response. Additionally, due to the out-of-phase response of the WE to the applied  $\tilde{V}$ , EIS spectra allows one to identify non-faradaic contributions to the measured currents, such as the charging and discharging of the electrical double layer (EDL) and mass transfer resistances (diffusion). The influence of each factor to EIS spectra will be discussed in the following sections.

#### Electrical Double Layer

The spontaneous formation of an EDL is a direct consequence of the high energy state at the surface of a material. The phenomenon may be illustrated by an excess of negative charges (electrons) at the surface of a metal. At the interface with a surrounding solution, water molecules align their dipoles so that the more electronegative oxygen atoms are positioned far from the metallic surface. The result is the formation of two parallel layers of charges separated by a few angstroms. The structure and electrical behavior of the EDL is analogous to that of a capacitor. For bare metals in aqueous solutions, the EDL capacitance usually ranges between 10 – 50  $\mu\text{F}\cdot\text{cm}^{-2}$  [90], [91].

During a faradaic reaction, the exchange of charges is always coupled with the charging and discharging of the EDL. This may be represented by a circuit analog where a resistor is connected in parallel with a capacitor. The former represents the resistance to the charge transfer ( $R_{ct}$ ) while the latter models (to some extent) the EDL. In practice, the EDL response is not ideally capacitive and a constant-phase element (CPE) is often used as an analog. The impedance of a CPE is described by equation (6):

$$Z_{CPE} = \frac{1}{Q(j\omega)^\alpha} \quad (6)$$

where  $0 < \alpha < 1$  is the dimensionless CPE exponent, and  $Q$  is the CPE parameter measured in  $F \cdot s^{-(1-\alpha)}$ . Notice when  $\alpha = 1$ ,  $Z_{CPE}$  is exactly that of a perfect capacitor. Additionally, if a CPE behavior is observed,  $Q$  cannot be directly related to the value of the EDL capacitance.

The physical origin of the CPE behavior in electrochemistry is subject of ongoing research and has been associated with inhomogeneous current and potential distributions at the WE [92]–[94].

### Mass Transfer Impedance

The study of mass and charge transport in solutions with concentration gradients provides the theoretical background to address the effects of diffusion in EIS spectra. Depending on the boundary conditions, mass transfer impedance  $Z_W$  may [95], [96]:

- **Semi-infinite linear diffusion:** monotonically increase with decreasing perturbation pulse frequency, with  $Z_W \propto \frac{1}{\sqrt{\omega}}$ ;
- **Reflective boundary:** monotonically increase with decreasing  $\omega$ , until charge starts to accumulate at the boundary when quickly  $Z_W \rightarrow \infty$ ;
- **Transmissive boundary:** monotonically increase with decreasing  $\omega$ , but tends to a purely resistive behavior  $Z_W \rightarrow Real$  when  $\omega \rightarrow 0$ .

There are no single classical electric circuit elements (resistor, capacitor or inductor) capable of modelling mass transfer. For this purpose, resistive-capacitive transmission lines or Warburg elements may be useful. In this work, most of the impedance spectra were modelled with the aid of a generalized Warburg element (GWE) with a transmissive boundary for which:

$$Z_{GWE} = \sigma \frac{\tanh[(j\omega T)^p]}{(j\omega T)^p} \quad 7$$

where  $\sigma$  is the mass transfer coefficient measured in  $\Omega \cdot cm^{-2}$ , which depends on the character of the redox couple and the reactants concentrations,  $j = \sqrt{-1}$ ,  $T$  is the effective diffusion time in seconds, and  $p$  is a dimensionless experimental parameter used to account for the non-linearity of the diffusion process. Its value range between 0 – 1.

### Impedance Spectra Analysis

Generally, analysis of the EIS data has two main steps: observation of raw data on the complex, phase angle and magnitude plots and; choice of the best analog circuit that fits the measured spectra. Some details of EIS data analysis and interpretation will be briefly discussed in this section.

As discussed in previous sections, corrosion processes involve at least one pair of faradaic reactions as well as the diffusion of reacting species. One of the most popular analog circuits used to interpret faradaic reactions is the Randles circuit [96], [97]. It contains the electrolyte resistance  $R_e$ , which represents the resistance to the flow of charge in the solution, in series with a parallel array containing in one branch a CPE, and on the other branch the charge transfer resistance  $R_{ct}$  in series with a GWE with transmissive boundary.

Figure 31 illustrates two artificial impedance plots generated with a Randles circuit. In case A (blue points), it is assumed that the reactions occur in an ideal bare metallic surface, hence  $\alpha = 1$  and  $Q = 20 \mu\text{F}\cdot\text{cm}^{-2}$ . The mass transport is modelled by linear diffusion, therefore  $p = 0.5$ . In the complex plot, two loops are formed. The high-frequency loop forms due to the coupling between the charge transfer and the EDL, while the second loop is caused by the mass transfer resistance. Accordingly, the phase angle plot displays two maxima at the characteristic frequencies of each phenomena. At high frequencies, the magnitude impedance equals  $15 \Omega\cdot\text{cm}^{-2}$ , which is the value of  $R_e$ . As the frequency decreases,  $|Z|$  displays two inflections at the same characteristic frequencies. The maximum  $|Z| = R_e + R_{ct} + \sigma$  can also be observed in the complex plot at  $\omega = 0.001 \text{ Hz}$ .

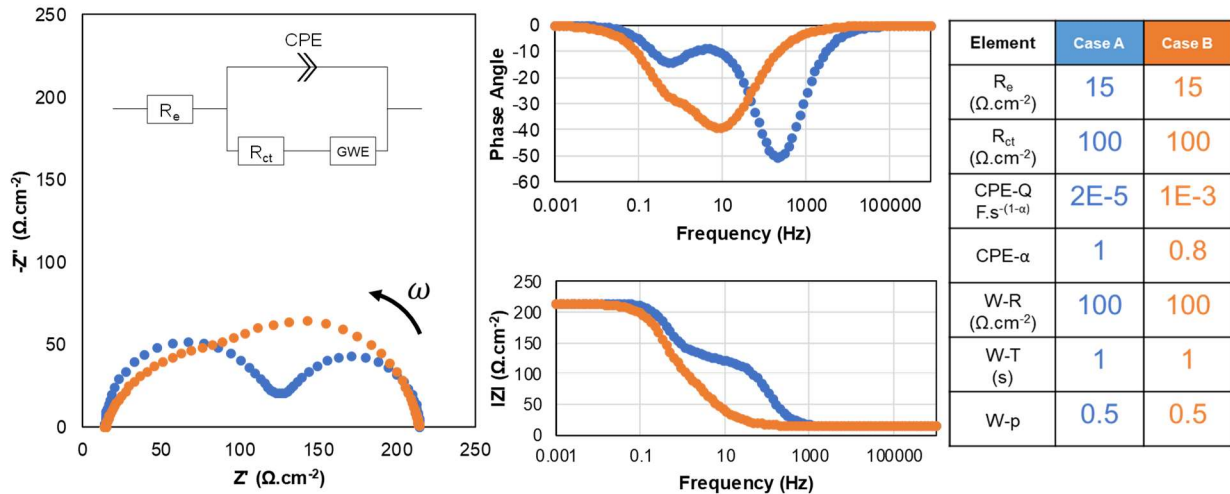


Figure 31 – Complex, phase angle and magnitude impedance plots for two hypothetical faradaic reactions modelled by a Randles circuit.

In case B, the electrode has a non-ideal CPE behavior with  $\alpha = 0.8$  and  $Q = 0.001$ . These numbers are consistent with that of a carbon steel in neutral chloride solutions, where a semi-conductive corrosion product quickly forms [98]. Noticeably, the charge transfer and diffusion

processes are not as easy to distinguish as in case A. This example highlights the impact that some corrosion products may have on the impedance spectra.

After collecting EIS data, the following step is usually to choose an analog circuit providing a best fit to the measured spectra. This step is critical not only because it requires good knowledge of the processes happening at the WE interface, but also because several different analog circuits may provide equally good fits. Luckily, there are preliminary graphical analyses that allow one to assess the electrode behavior before any deeper interpretation is required. As described in [99], log-plotting of the imaginary part of the impedance as a function of frequency not only allows for easy identification of the process characteristic frequencies, but may also provide indication of time-constant dispersion. The effective CPE exponent ( $\alpha_{eff}$ ) of the WE may be assessed by quantifying the slope  $d|Z''|/d\omega$  at high frequencies, where the effects of EDL or diffusion do not interfere with  $Z''(\omega)$ . As illustrated in Figure 32, the power law  $Z'' = 208.83 \cdot \omega^{0.8}$  satisfactorily fits the data for nearly three frequency decades.

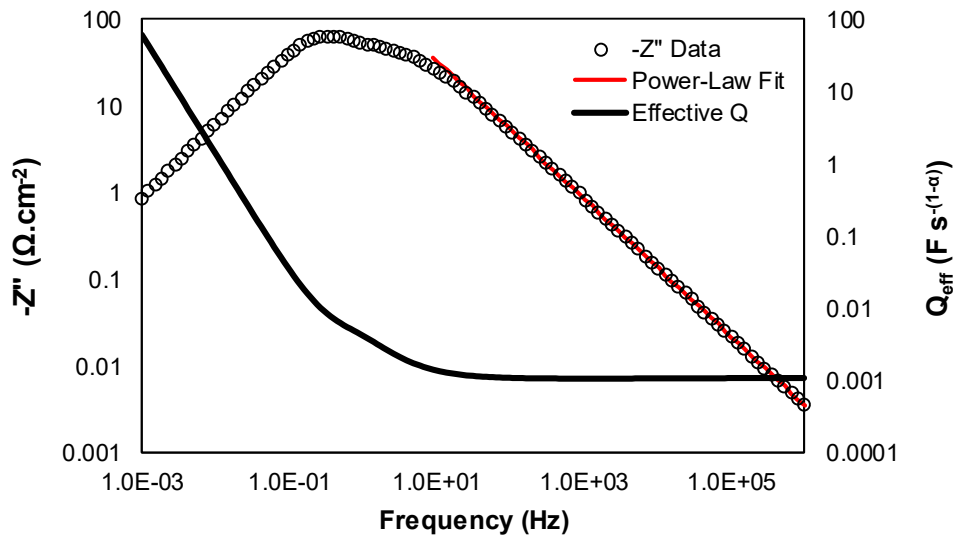


Figure 32 – Illustration of the graphical method used to calculate the WE's CPE exponent  $\alpha$  and effective capacitance (CPE parameter Q) for case B.

The fit result may be used to determine the effective CPE-Q as described by equation (8):

$$Q_{eff} = \sin\left(\frac{\pi\alpha_{eff}}{2}\right) \frac{-1}{Z'' \cdot (2\pi\omega)^{\alpha_{eff}}} \quad 8$$

One may easily notice that at high  $\omega$ ,  $Q_{eff} = 0.001 \text{ F}\cdot\text{s}^{-(1-\alpha)}$ , which exactly corresponds to the CPE parameter for the electrode in case B.

In summary, the preliminary graphical analysis allows one to develop a good sense of the electrode response, in both a physical and numerical sense. Such knowledge is particularly helpful during the fitting of the chosen analog circuit to the measured spectra. The fitting method is known as complex nonlinear least squares (CNLS) method which requires good initial numerical guesses for each element of the analog circuit. In the present work, all CNLS fitting was done with the aid of ZView® software, from Schreiber associates Inc NC USA 28387.

### 3.2 Corrosion Resistance of Thermally Sprayed Coatings

While the use of thermal spray to produce corrosion-resistant coatings is well established, there are important and unclear aspects on the interpretation of their electrochemical behavior. For example, it is well-known that the corrosion resistance of sprayed stainless steel as well as Cr-containing amorphous metallic coatings is inferior as compared to that of wrought/cast metals of similar composition [49], [100]–[102]. The effect is usually attributed to two main factors:

- **Porosity:** the role of pores in thermal sprayed coatings is often associated with the penetration of electrolyte and the onset of localized reactions. In extreme cases, the electrolyte quickly reaches the coating/substrate interface where strong galvanic corrosion takes place [103], [104].
- **High-Temperature Oxidation:** It is often argued that that particle exposure to high-temperature gases leads to the formation of chromium-depleted zones in the coating [105], [106] where corrosion reactions occur preferentially.

These observations led researchers to use spray processes that reduce particle in-flight temperatures while keeping supersonic gas velocities. Examples include the use of warm-spraying [107], gas-shrouded HVOF torches [108], HVOF [109] and cold-spraying [100].

Despite the improvements, the performance gap between coating and solid metallic surfaces persists. In polarization curves, authors often report that the former group has higher corrosion current densities and lower corrosion potentials. One could interpret that the spraying process permanently affects the material's chemistry (hence the shift in  $E_{corr}$ ), permanently degrading the originally protective nature of the stainless steel (hence the increase in  $i_{corr}$ ). However, the presence of pores suggest that the high corrosion current values are derived from an increased electrode surface area, and/or from Cr-depleted zones where reactions occur at higher rates, both

of which compromise the use of  $i_{corr}$  as a parameter to calculate homogenous thickness loss rates.

Microscopic observations of preferential corrosion sites in coatings has strongly influenced the interpretation of EIS spectra. For example, in [110], the chosen analog circuit contains two constant phase elements and suggest that reactions at the electrode surface occur in parallel with reactions inside coating pores. On the other hand, in [102], [111] the chosen circuit analogs imply that the electrode response is mainly dominated by reactions inside pores. Despite the microstructural evidence of localized reactions inside coating pores, these works do not show any electrochemical evidence that the electrode response is being dominated by reactions inside pores.

Porous electrodes are useful in many applications and their electrochemical behavior has been extensively analysed by Andrzej Lasia both theoretically and experimentally [112]. The impedance response of porous electrodes depends on pore geometry and on the concentration of reacting species inside the porous electrode. When a perturbation signal  $\tilde{V}$  reaches the electrode surface, its amplitude decreases with pore depth due to the electrolyte's ohmic drop. This geometric potential drop was so important in porous Ni electrodes [113], [114] that, when immersed in 1M NaOH, two capacitive loops were observed in the impedance spectra. By applying several constant overpotentials to the electrode, the low frequency loop diameter was significantly affected, and hence associated with faradaic hydrogen reduction reaction. On the other hand, the high-frequency loop was not affected by the potential and was hence associated with the geometric potential drop inside the pores. The effect is illustrated in Figure 33.

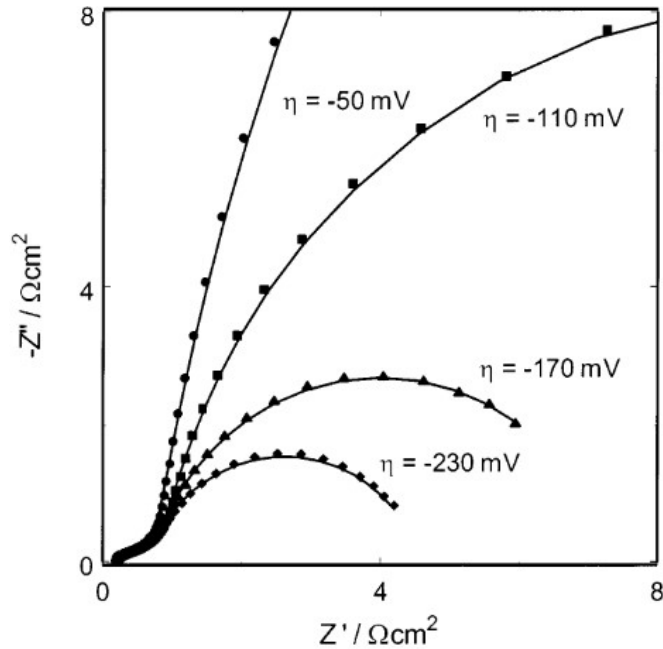


Figure 33 – Effect of electrode potential on the loop diameters measured in a complex plot of porous nickel electrodes in 1M NaOH solution. Extracted from [114].

Obtaining experimental evidence of the contribution of pores to the electrochemical response of an electrode is not always possible. The pores may be too shallow (flat electrode response) or the impedance contributions from faradaic reactions may be overwhelmingly more important than the coupling between the solution resistance and the EDL inside pores.

In summary, research on the electrochemical behavior of sprayed metallic coatings suggest that their impaired corrosion resistance (when compared to that of bulk parts) originates from structural and chemical flaws. Furthermore, interpretation of important parameters derived from polarization curves and EIS spectra remain dubious and subjective. If thermally sprayed corrosion resistant coatings are to be used in a consistent and predictable manner in engineering applications, further investigations are necessary.

### 3.3 Changes in the Electrochemical Behavior, Microstructure and Surface Chemistry of Stainless-Steel Coatings

*Submitted to the Corrosion Science Journal*

#### 3.3.1 Introduction

In thermal spraying, the successive impingements of hot gas-accelerated molten and semi-molten particles in a substrate lead to the formation of a coating. The development of such technique enables the protection of surfaces with corrosion-resistant coatings at industrial-scale production rates [115]. When compared with other standard coating deposition methods such as welding, thermal spray has a reduced effect on the substrate's chemistry and geometry.

However, it is well-known that when compared to wrought or "bulk" parts of similar composition, sprayed coatings display an inferior corrosion performance. The reasons are vaguely attributed to in-flight high-temperature oxidation, which is presumed to affect the particle's chemistry, as well as to coating porosity, which could lead to localized corrosion. Kawakita et al. studied the corrosion behavior in 3.4 wt.% NaCl aqueous solution of HVOF-sprayed 316L stainless steel [49] and Hastelloy C coatings[50], [116]. Based on current density measurements and the observation of corrosion products inside pores, the authors noticed that the coatings with minimum oxygen absorption and lowest porosity outperformed the others. This motivated the development of new spray processes that kept the supersonic gas velocities of high velocity oxygen fuel (HVOF) spraying, while pursuing lower flame temperatures. Examples of such processes include the warm-spray or "shrouded HVOF" [107], [108] as well as the HVAF (high velocity air fuel), which has received considerable attention in the scientific community. For example, Zeng et al. [109] compared 316L coatings produced by HVAF and HVOF in a salt-spray chamber, concluding that the lower amount of rust formation on HVAF coatings was due to their lower level of in-flight oxidation. Despite the recent improvements, the performance gap between sprayed and dense materials remains.

The degradation of sprayed coatings does not seem to be of homogeneous nature. An early study from Suegama et al. [104], [117] assessed the electrochemical behavior of HVOF-sprayed 316L coatings in 3.4% NaCl aqueous solution. It was observed that depending on the spray parameters, the electrolyte could penetrate through pores and reach the substrate in 24 hours, leading to localized attack at the coating/substrate interface. The use of modern spray equipment allowed the community to deposit denser coatings, which appears to have solved the issue of fast electrolyte penetration. Nevertheless, the observed changes of the electrode features suggest that corrosion occurs preferentially at coating defects such as pores and voids between the splats

[118]. In some instances, the formation of pits are reported [105], [119] while no passivation breakdown was shown in the polarization curves. The onset of localized corrosion complicates the interpretation of parameters such as the corrosion current, so important for engineering applications.

In addition to the polarization curves, electrochemical impedance spectroscopy (EIS) is a useful method to assess the corrosion performance of sprayed coatings. However, the complexity of their structures and that of the corrosion process itself leads to varying interpretations of the impedance spectra. For example, Milanti et al. [120] used an analog circuit containing two constant phase elements (CPE) and, while acknowledging the presence of porosity in HVAF-sprayed coatings, diffusion of reactants at the electrode surface was not considered. On the other hand, Guo et al. [102] used a Randles circuit and assumed that the corrosion process occurs mainly at voids to where the reactants must diffuse. These apparent inconsistencies indicate the need for further clarification on the usefulness of EIS characterization of thermally sprayed coatings. In fact, EIS may provide useful insights on the kinetics of the reactions happening at the electrode interface, allowing one to correlate observations on the polarization curves to the features of impedance spectra [121]. Moreover, simple tests may be carried out to assess if porosity is affecting the electrode response [112]. As far as the present thesis author is aware, these aspects were not explored in other works concerning the corrosion resistance of sprayed coatings and may enlighten particularities of their electrochemical behavior.

The main objective of this work is to establish solid processing-structure-property relationships for ferritic stainless steel (grade AISI444) coatings with a focus on the corrosion performance in 3.5 wt.% NaCl aqueous solution. Modern HVOF and HVAF spraying equipment were used and the effect of spraying methods were assessed by using in-flight particle diagnostic tools. Changes in the electrode responses were critically discussed based on periodic coating structure evaluation and compared with the typical behavior of a bulk stainless steel of same nominal composition. Changes in the surface chemistry of the coatings was evaluated by x-ray photoelectron spectroscopy (XPS).

### 3.3.2 Materials and Methods

#### **Feedstock and Spray Parameters**

Water-atomized (Eutectic Castolin, Granby, Quebec, Canada) stainless steel grade 444 (SS444 nominal composition in Table 8) powder was ball milled for 6h to achieve appropriate particle size

distribution  $D_{50} = 44 \mu m$ . The ball-milled powder was used to spray all coatings except for the coating HVOF #1, in which the powder was used in the atomised state  $D_{50} = 60 \mu m$ .

The water atomized feedstock was arc-melted in the form of a disc. The process consisted in compacting 8 g of the feedstock with a pressure of 5 MPa. The compact is then put inside a vacuum ( $10^{-6}$  mbar) furnace at 1000 °C for 1h to develop some strength. Subsequently, the sintered part is placed inside an arc furnace chamber containing a tungsten electrode, a titanium getter and a water cooled plate (Appendix B, Figure 57). The arc melting process was carried under vacuum of  $10^{-3}$  mbar.

Table 8 - Nominal composition of a bulk SS444. The \* indicates the maximum element in wt.% the steel should bare.

Composition	C	Mn	P	S	Si	N	Cr	Ni	Mo	Ti + Nb
Wt %	0.025*	1.00*	0.04*	0.03*	1.00*	0.035*	17.5 – 19.5	1.00*	1.75 – 2.5	0.2*

Nine preliminary HVOF spray parameters were used to assess their effect on the in-flight particle temperature and velocities. The HVOF spray torch used was Praxair’s JP-8000. The HVOF coatings were produced with the Uniquecoat M3 system with two different spray parameters summarized in Table 9.

Table 9 – Summary of the spray parameters used for HVOF and HVOF spraying.

HVOF #	Feedstock	O <sub>2</sub> Flow Rate (LPM)	Kerosene Flow Rate (LPM)	O/F Ratio -	Combustion Pressure (kPa)	Other Parameters	
1		470	18	0.80	372	Feed Rate	44 g/min
2		705	22	0.99	565	Stand-off Distance	33 cm
3		870	23	1.17	689	Argon Flow Rate	9.4 LPM
4		799	25	0.99	662	Number of Passes	15
5	Ball Milled	588	15	1.18	414	Transversal Speed	500 mm/s
6		635	24	0.80	545		
7		776	20	1.20	586		
8		729	28	0.79	655		
9		517	16	0.99	379		

HVOF #	Feedstock	Air Pressure (kPa)	Propylene Pressure (kPa)	Powder Feed Rate (g/min)	Other Parameters	
1	Atomized			70	Stand-off distance	30 cm
4	Ball Milled	780	690	50	Number of Passes	20
					Transversal Speed	1 m/s

The tools used for in-flight particle diagnostics were, the DPV-evolution for HVOF and Accuraspray for HVOF both from Tecnar Inc (Saint-Bruno, Québec – CA).

## Microstructure and Chemical Analysis

The feedstock and coating structures were analysed by optical and scanning electron microscopy (SEM). Image analysis was performed by using Image J 1.52A (National Institute of Health, USA). The methodology used to determine the coating's chemistry by EDX consisted in doing point-analysis at the coating's microconstituents, i.e. semi-molten particles, re-solidified splats and oxides, as well as by measuring a general composition over an area of  $260 \times 180 \mu\text{m}^2$ . Each point analysis was carried out three times while the general analysis only once.

## Electrochemical Characterization

All coatings were initially ground on SiC (grit #320) paper then polished to mirror finish with diamond ( $3 \mu\text{m}$ ) and alumina ( $0.05 \mu\text{m}$ ) suspensions. Tests were carried out in stagnant 3.5wt% NaCl solution with a three electrode cell having a Ag/AgCl reference electrode and a RuO<sub>2</sub>-coated titanium (dimensionally stable anode) as a counter electrode. The disc samples (diameter of 16 mm) were rinsed in distilled water and immersed for one hour in the test solution, while the open circuit potential (OCP) was monitored. The impedance test was performed at OCP with pulse amplitude of 10 mV for the frequency range starting at 40 kHz and finishing at 0.01 Hz. Potentiodynamic polarization tests were then performed starting at -0.75 V vs Ag/AgCl until -0.21 V vs Ag/AgCl at a scan rate of 0.167 mV/s. After the polarization test, the samples are immersed in stagnant solution of same composition for a week. The non-adherent corrosion products are then removed by repeating the final 0.05  $\mu\text{m}$  alumina polishing and the test routine is repeated for three times, as illustrated in Figure 34. Determination of electrochemical parameters such as the corrosion potential ( $E_{corr}$ ), corrosion current ( $i_{corr}$ ) and Tafel slopes was done by using CView software (Schreibner associates Inc NC USA 28387). Fitting by complex non-linear square regression (CNLS) was done by means of ZView software (Schreibner associates Inc NC USA 28387).

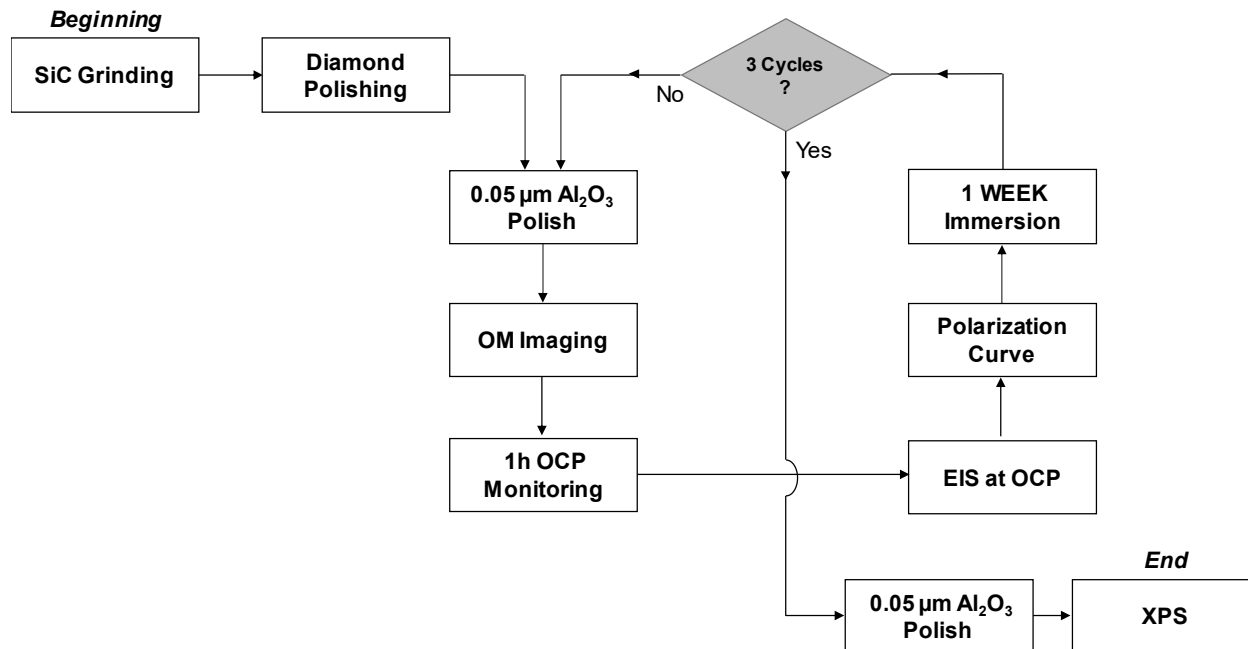


Figure 34 – The flowchart illustrates the preparation and characterization steps to which each coating was subject.

### Effect of Electrode Potential on EIS Spectra

In the present work, the effect of the applied potential to the EIS spectra was done firstly at the open circuit potential (OCP), followed by OCP-50 mV and finally at OCP+50mV. The choice of the values was such that it created a visible effect in the complex plane (Nyquist) plot, while keeping the electrode potential as close to OCP as possible, thus minimizing structural or chemical changes at the electrode interface. Surface preparation, pulse amplitude (10 mV) and used frequency ranges (40 kHz – 0.01 Hz) were the same as the other EIS tests. The theoretical background for this analysis is given on Appendix B.

### XPS Analysis

Prior to the XPS analysis, bulk SS444 and arc-melt feedstock underwent SiC grinding and diamond and alumina suspension polishing. All samples were then dried in warm air and placed in a vacuum chamber. A standard aluminium X-ray source ( $Al\ k\alpha = 1486.6\ eV$ ) was used to record survey spectra (1 – 1486 eV). Argon-plasma etching was done over an area of 2 mm x 4 mm prior to each analysis. The probed area was a circle with 400 μm diameter, located at the center of the plasma etched zone. High resolution spectra have been done on C1s, O1s, Fe2p and Cr2p. For each sample, three different analyses were performed to verify the homogeneity of the layer composition.

### 3.3.3 Results

#### 3.3.3.1 In-Flight Particle Diagnostics & Spray Parameter Selection

For better interpretation the average velocities and temperatures were grouped according to the levels of combustion pressures (386, 565 and 669 kPa) and O/F Ratios (0.8, 1.0 and 1.2). As illustrated in Figure 35, the particle velocity has a close correlation with the combustion pressure while the particle temperature correlates more strongly with the normalized O/F ratio. These outcomes were expected based on previous modelling [22], [23] and experimental [49], [50] studies.

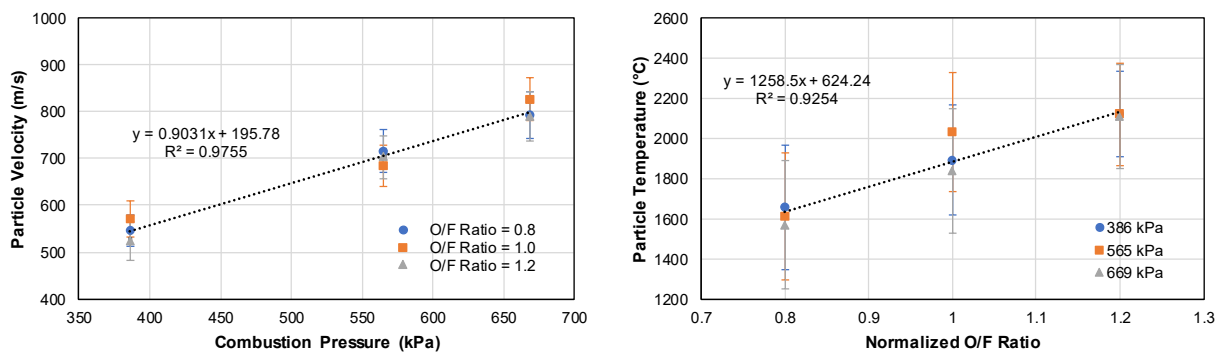


Figure 35 - Effect of spray parameters on the in-flight particle temperature and velocity. The results are grouped according to levels of combustion pressure and O/F Ratio. Each error bars correspond to two standard deviations calculated for 1000 particles.

The coating deposition was made with the spray parameters that led to minimum overlap of in-flight particle properties. As summarized in Table 10, average velocities may range from 519 to 798 m/s. While the particles sprayed by HVOF display temperatures below the theoretical liquidus temperature of a bulk SS444 (1520 °C), particles sprayed by HVAF may have in-flight temperatures as high as 2200 °C. It should be mentioned that the diagnostic tool used to characterize the HVAF-sprayed particles was the Accuraspray system which determines temperatures and velocities as an ensemble (which is why the statistical errors are not reported) in a space volume of approximately 176 mm<sup>3</sup>. As for the HVOF-sprayed particles, the system used was the DPV-evolution, which can determine individual in-flight particle characteristics in a

measurement volume inferior to 1 mm<sup>3</sup>. Readers can refer to [122] if further information on these diagnostic tools are required.

The results in Table 10 show that the final substrate temperature is linked to the combustion O/F ratio used for spraying. For example, coatings HVOF #1 and HVOF #8 were produced with fuel-rich flames, burning kerosene at higher rates when compared to HVOF #3 and HVOF #5.

*Table 10 – In-flight particle temperatures and velocities used for coating deposition. The term s corresponds to the sample standard deviation. The substrate temperature was taken on the coating surface immediately after the end of the spray deposition.*

Coating ID	Velocity (m/s)		Temperature (°C)		Substrate Temperature (°C)
	average	s	average	s	
HVOF #1	546	69	1658	309	421
HVOF #3	790	104	2107	259	338
HVOF #5	524	82	2122	214	282
HVOF #8	792	101	1569	320	533
HVAF #1	782		1372		232
HVAF #4	668		1435		244

### 3.3.3.2 *Microstructure and EDX Analysis*

The powder feedstock displayed small dark precipitates which may also be found in the coatings' microstructures, as highlighted in Figure 36. Local EDX analysis was complicated due to the precipitate's small size. However, it was possible to identify an increase in silicon, manganese and oxygen contents. It is believed that such precipitates originate at the particle surface during the atomization and/or spraying processes and are then dragged inside the particles by liquid convection [26].

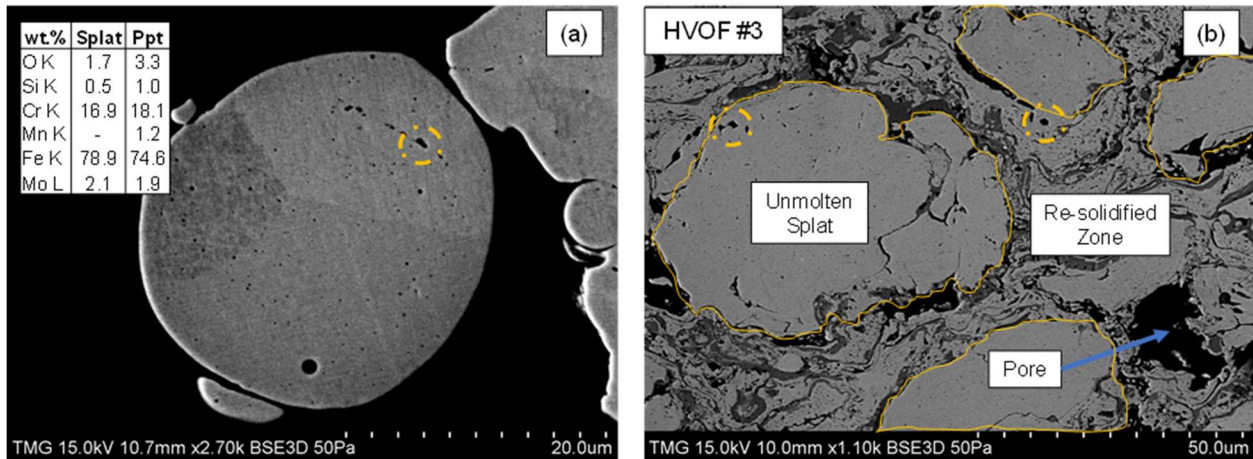


Figure 36 – Backscattered electron image of (a) Small Si-rich precipitates (highlighted in dashed-line circles) can be found in the powder feedstock as well as in the sprayed coatings. EDX analysis reveals that the precipitates are rich in Si, Mn and O when compare with the neighbouring areas. (b) The coatings main microstructural features are highlighted and include semi-molten splats (circled in yellow) surrounded by a re-solidified zone containing oxides and pores.

A closer look at Figure 36 reveals that the HVOF-sprayed SS444 coatings have three main microconstituents: semi-molten splats that partially retain the feedstock morphology; a re-solidified zone comprising lamellar metallic and oxide splats and; pores. These constituents are present in all the sprayed coatings as illustrated in Figure 37. Table 11 summarizes the fraction of each constituent as measured by image analysis. The coatings produced at higher O/F ratio (HVOF #3 and #5) also have a higher fraction of semi-molten particles. Conversely, the coatings produced with lower O/F Ratio (HVOF #1 and #8) are mostly composed of re-solidified splats. As will be discussed later, this effect is attributed to different particle trajectories.

The porosity in coating HVOF #5 was significantly higher than the others, which probably derives from an undesirable combination of high in-flight particle temperatures and low velocities. Another important remark concerns the coating HVOF #8 which, despite being formed by particles that experienced lowest in-flight temperature, also exhibited oxide clusters characterized by a darker grey color. On the other hand, the substrate temperature was highest after deposition of HVOF #8.

It is evident from Figure 37 that the coating HVOF #1 was formed mainly by semi-molten splats. This may be explained by the larger particle sizes used and the relatively low in-flight particle temperatures. On the other hand, the HVOF #4 coating shows a microstructure like those observed in the HVOF coatings. This may be explained by the facts that the feedstock used to produce coating HVOF #4 was the same used to produce HVOF coatings and that the particle

velocities prior to impact were relatively slow as compared with those that generated coating HVAF #1.

Based on thickness measurements (Table 11), higher deposition efficiencies (DE) are achieved when HVOF-spraying with lower O/F ratios. According to [77], increasing the in-flight particle temperature also increases its ductility, which increases the process deposition efficiency until the material's melting point is reached, coinciding with the process highest attainable DE. Coatings HVOF #1 and #8 contain a higher fraction of particles that experienced complete melting prior to deposition, hence their higher DE. The same rationale may explain why the DE of HVOF coatings was higher than that of HVAF. However, due to the use of a different, self-regulated powder feeding system, the flow rate for depositing coating HVAF #4 was significantly lower than the rest, which explain why this coating had the lowest thickness.

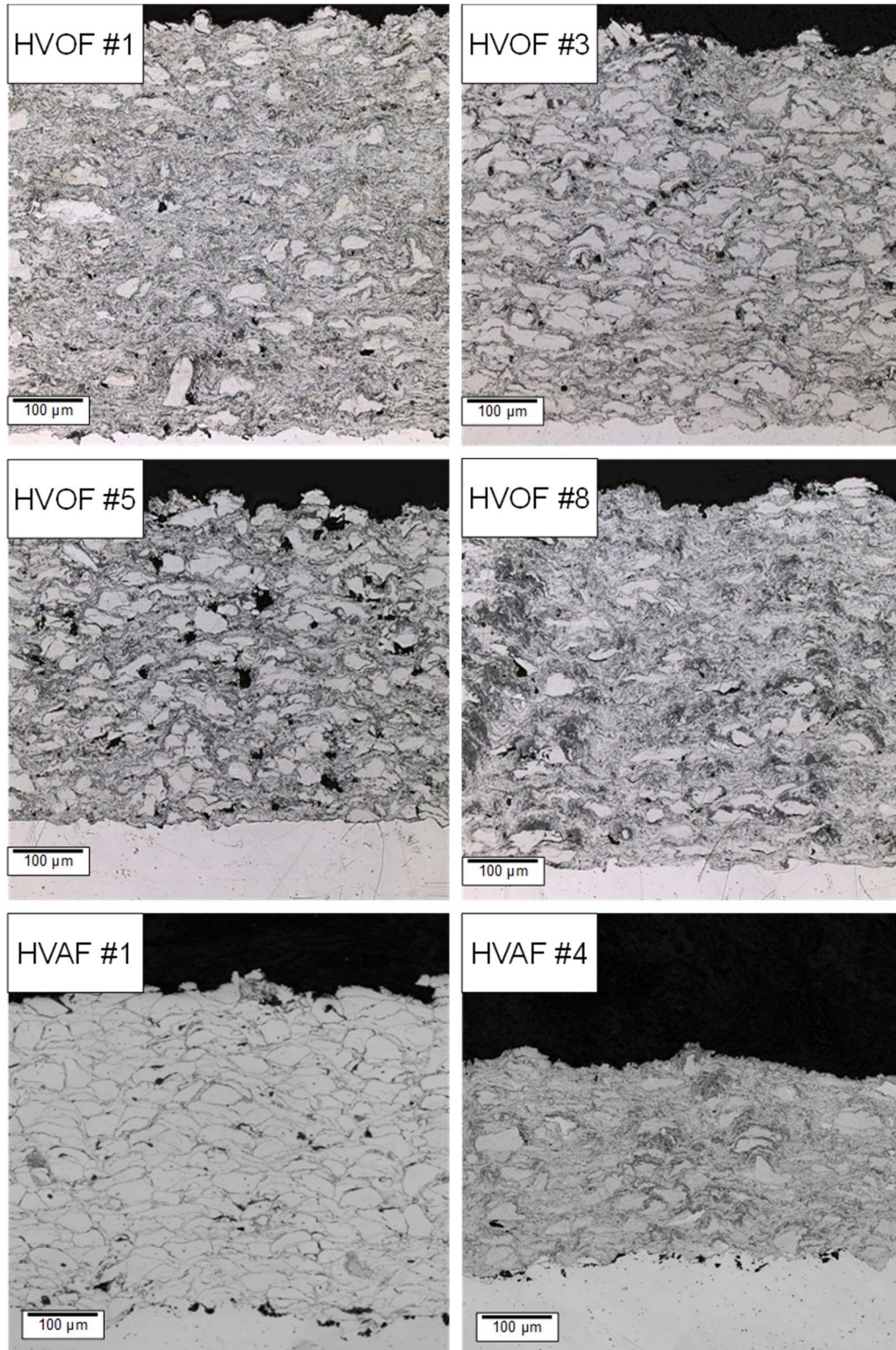


Figure 37 – As-sprayed SS444 coating microstructures contain similar microstructural features including semi-molten splats, a re-solidified zone containing splats and oxides and finally, pores which are particularly present at coating HVOF #5.

Table 11 - Area fraction of coating microconstituents as determined by image analysis.

Coating ID	% Semi-molten	% Re-solidified	% Pores	Thickness ( $\mu\text{m}$ )
HVOF #1	15.9	83.8	0.3	612
HVOF #3	28.5	70.2	1.3	564
HVOF #5	26.4	71.5	2.1	462
HVOF #8	14.5	85.0	0.5	574
HVAF #1	99.3	-	0.7	472
HVAF #4	31	68.7	0.3	280

The EDX analysis main results (Table 12) reveal that the semi-molten particles have less oxygen than the re-solidified zone, which is not surprising since the oxides are more frequently observed on the latter. The general composition results point to a higher oxygen uptake in coating HVOF #8, which can be linked to the presence of the large oxide clusters (Figure 37). Additionally, the HVAF coatings have an overall lower oxygen content, especially in the case of HVAF #1.

It is useful to compare the coating's chemistry with that of the wrought SS444 which, under the same analysis conditions, exhibits an oxygen content below 0.5 wt.%. In terms of chromium content, the main element responsible for the electrochemical response of stainless steels, most coatings display weight percentage values slightly inferior to that of the expected nominal range of 17.5% – 19.5%. This apparent reduction of %Cr may be a result of the interaction volume of the beam, exciting electrons from Cr-less phases such as  $\text{Fe}_2\text{O}_3$ . In fact, the chromium content of the semi-molten splats falls within the required nominal range. Additionally, the chromium content in martensitic stainless steels is 13% [123], significantly less than the quantity measured for the coatings. Therefore, as far as the weight percentage of chromium is concerned, the electrochemical response of the coatings should be like that of wrought stainless steels.

Table 12 - EDX analysis performed over the coatings microconstituents as well as over a 260 x 180 μm<sup>2</sup> area. Reported values with \* were detected once or twice out of the three measurements.

Element	HVOF #1				HVOF #3				HVOF #5			
	Unmolten	Re-solidified	Oxide	General	Unmolten	Re-solidified	Oxide	General	Unmolten	Re-solidified	Oxide	General
<b>O K</b>	2.1 ± 0.5	4.9 ± 2.4	22 ± 13	8.7	3 ± 1	3 ± 2	27 ± 5	8.5	2.0 ± 0.3	6 ± 4	30 ± 1	8.1
<b>Si K</b>	0.5 ± 0.1	0.5 ± 0.3	0.3 ± 0.1	0.4	0.6 ± 0.2	0.4 ± 0.1	0.4 ± 0.3	0.4	0.4 ± 0.1	0.5 ± 0.2		0.4
<b>Cr K</b>	18.1 ± 0.3	18 ± 2	16 ± 3	16.7	18.4 ± 0.3	16.4 ± 1.6	14 ± 2	16.4	17.8 ± 0.6	20 ± 3	13.5 ± 0.3	16.6
<b>Mn K</b>	0.6 ± 0.3	0.8 ± 0.7	0.4 ± 0.1	0.4	0.5 ± 0.1	0.6 ± 0.1	0.4 ± 0.1	0.6	0.4 ± 0.1	6 ± 5	0.4*	0.5
<b>Fe K</b>	76 ± 1	74 ± 4	59 ± 12	71.7	75 ± 3	77 ± 1	57 ± 3	71.7	77.1 ± 0.2	72 ± 6	55.0 ± 0.3	71.8
<b>Ni K</b>	-	-	-	0.0	0.6*	-	-	-	0.7*			
<b>Mo K</b>	2.2 ± 0.2	2.2 ± 0.1	1.5 ± 0.6	2.1	2.0 ± 0.1	2.3 ± 0.1	1.4 ± 0.1	2.1	2.1 ± 0.1	1.9 ± 0.4	1.3 ± 0.4	2.2
<b>Cr/Fe</b>	0.24	0.24	0.27	0.23	0.24	0.21	0.25	0.23	0.23	0.27	0.24	0.23
Element	HVOF #8				HVOF #1		HVOF #4					
	Unmolten	Re-solidified	Oxide	General	Unmolten	General	Unmolten	Re-solidified	Oxide	General		
<b>O K</b>	2.5 ± 0.7	3 ± 2	29.8 ± 0.3	10.7	0.6 ± 0.1	2.5	2.2 ± 0.8	2.8 ± 0.8	25 ± 5	5.2		
<b>Si K</b>	0.5 ± 0.1	0.2 ± 0.1	0.4 ± 0.2	0.3	0.2 ± 0.1	0.4	0.5 ± 0.2	0.4 ± 0.1	0.4 ± 0.1	0.4		
<b>Cr K</b>	18.1 ± 0.1	16.7 ± 0.3	14 ± 3	16.4	17.8 ± 0.2	18.0	18.4 ± 0.3	18.0 ± 0.5	16 ± 2	17.4		
<b>Mn K</b>	0.4 ± 0.1	0.4*	0.4 ± 0.1	0.5	-	0.5	0.4*	0.5 ± 0.1	0.6*			
<b>Fe K</b>	76 ± 1	78 ± 3	54 ± 3	69.8	79.6 ± 0.5	76.0	76.7 ± 0.9	76.3 ± 0.9	57 ± 3	74.5		
<b>Ni K</b>	0.6*	-	-	-			-	-	-			
<b>Mo K</b>	2.2 ± 0.2	2.3 ± 0.2	1.3 ± 0.1	2.0	2.2 ± 0.1	2.1	2.2 ± 0.2	2.2 ± 0.3	1.3 ± 0.1	2.1		
<b>Cr/Fe</b>	0.24	0.22	0.26	0.23	0.22	0.24	0.24	0.24		0.23		

The arc melting process led to significant densification of the sintered pack of particles, creating a structure like that of a wrought or cast stainless steel. However, pores and precipitates were still present (Figure 38). Due to their spherical geometry, it is believed that the pores are originated from gases entrapped in the melting pool. The EDX analysis performed on the precipitates revealed a Cr weight fraction of 54%. During arc melting, a slag formed on top of the melt pool. Upon solidification, the slag separated from the bulk by spallation. This may explain why the oxygen content of the arc melted steel was of 0.5wt.%, considerably lower than what was measured for the coatings.

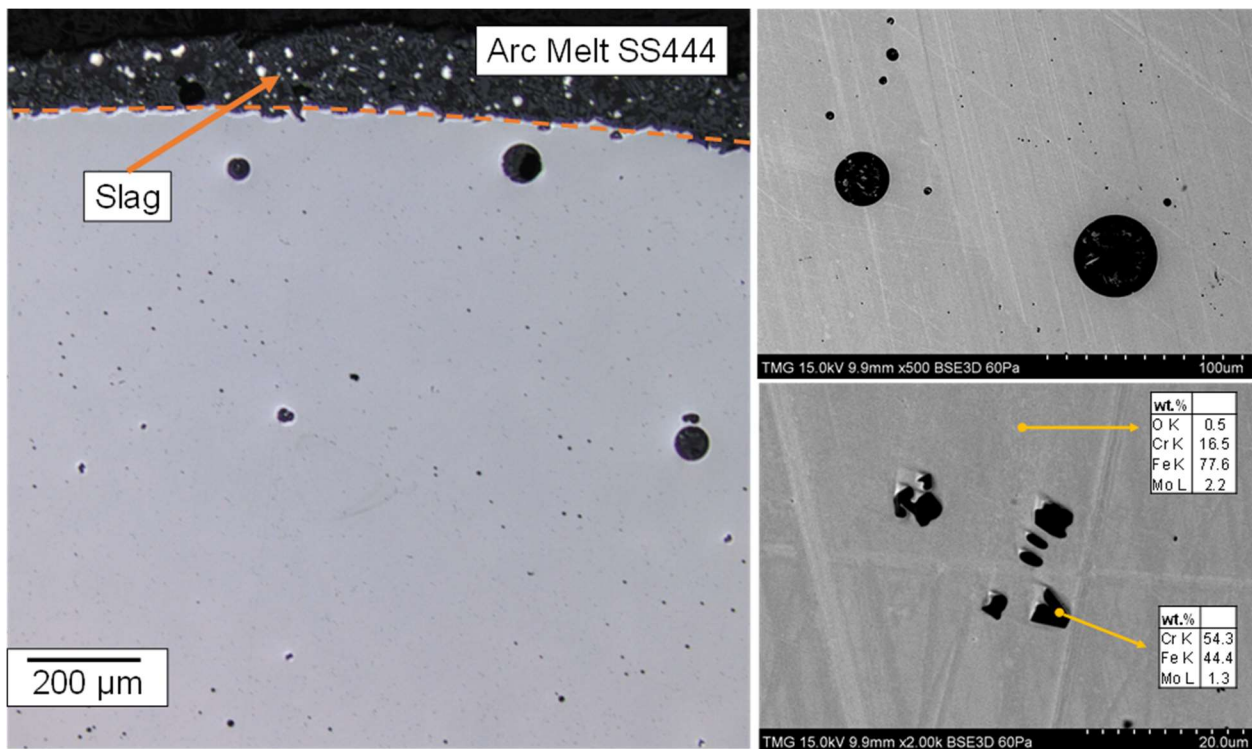


Figure 38 – Arc melting densifies the atomized stainless steel powder. However, a few pores were observed due to the presence of air entrapped in the melt pool. In backscattered electron imaging, some Cr-rich precipitates were observed. The arrows indicate the position where the EDX analysis was carried out.

### 3.3.3.3 Potentiodynamic Polarization

When comparing the polarization curves of the as-sprayed (HVOF #1 – 1 Hour) coating to that of the wrought SS444 (Figure 39), one will notice a significantly lower corrosion potential as well as a two-order of magnitude higher corrosion current. The measured  $E_{corr}$  and  $i_{corr}$  values for the as-sprayed coatings are in good agreement with other stainless steel coatings produced by HVOF [104], [117] as well as with a vacuum-sintered 434L powder metallurgy (PM) stainless steel [124].

Important differences are also observed in the Tafel slopes. After 1 hour immersion, the HVOF coatings have a comparatively higher  $\beta_c$  and a much lower  $\beta_a$ , which indicates that the sprayed materials do not tend to form a protective passive film.

Considering the  $E_{corr}$  and  $i_{corr}$  values only, the corrosion properties of the arc melted feedstock are not so different from the bulk SS444. However, in the anodic branch of the polarization curve, one may observe an early breakdown at  $E = 0.17 V$  indicating that the protective properties of the film formed on the re-melted feedstock was inferior to that of the bulk SS444.

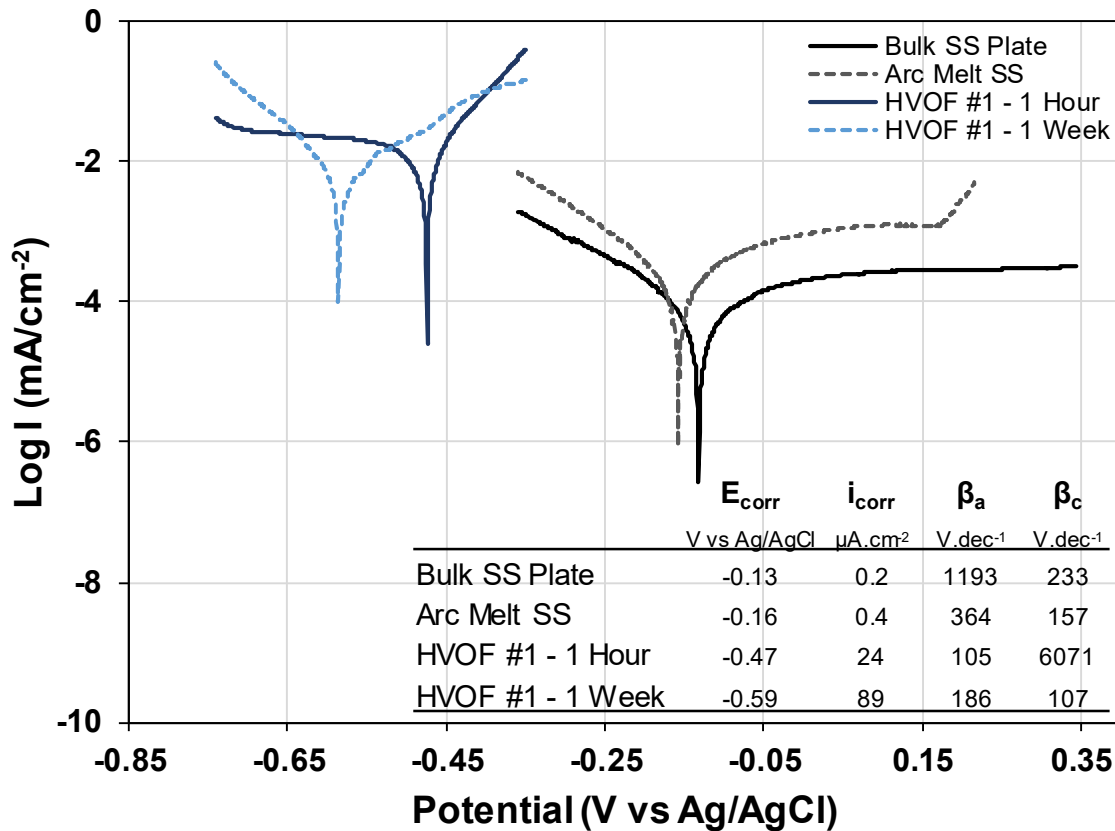


Figure 39 – Polarisation curves measured for a bulk SS444, a HVOF-sprayed coating and a sample produced by arc melting the spray feedstock.

The polarization behavior of the SS444 coatings was similar in almost all instances and is summarized in Figure 40. The corrosion potentials of most coatings drop about 0.1V during the first week of immersion, after which the  $E_{corr}$  values display a slight tendency to increase with immersion time. A similar behavior is displayed for the cathodic slopes  $\beta_c$ : an initial sharp drop of nearly two orders of magnitude followed by a slight growth trend. In all the coatings, the anodic slope seems to follow a steady growth trend with immersion time. For coating HVOF #1, the  $\beta_a$

was particularly high at the second week of immersion, which coincided with the formation of a permanent surface film visible by naked eye (Appendix B, Figure 59). Despite all changes, the corrosion current  $i_{corr}$  of all coatings did not display any strong trend and the values ranged between 10 – 60  $\mu\text{A}\cdot\text{cm}^{-2}$ .

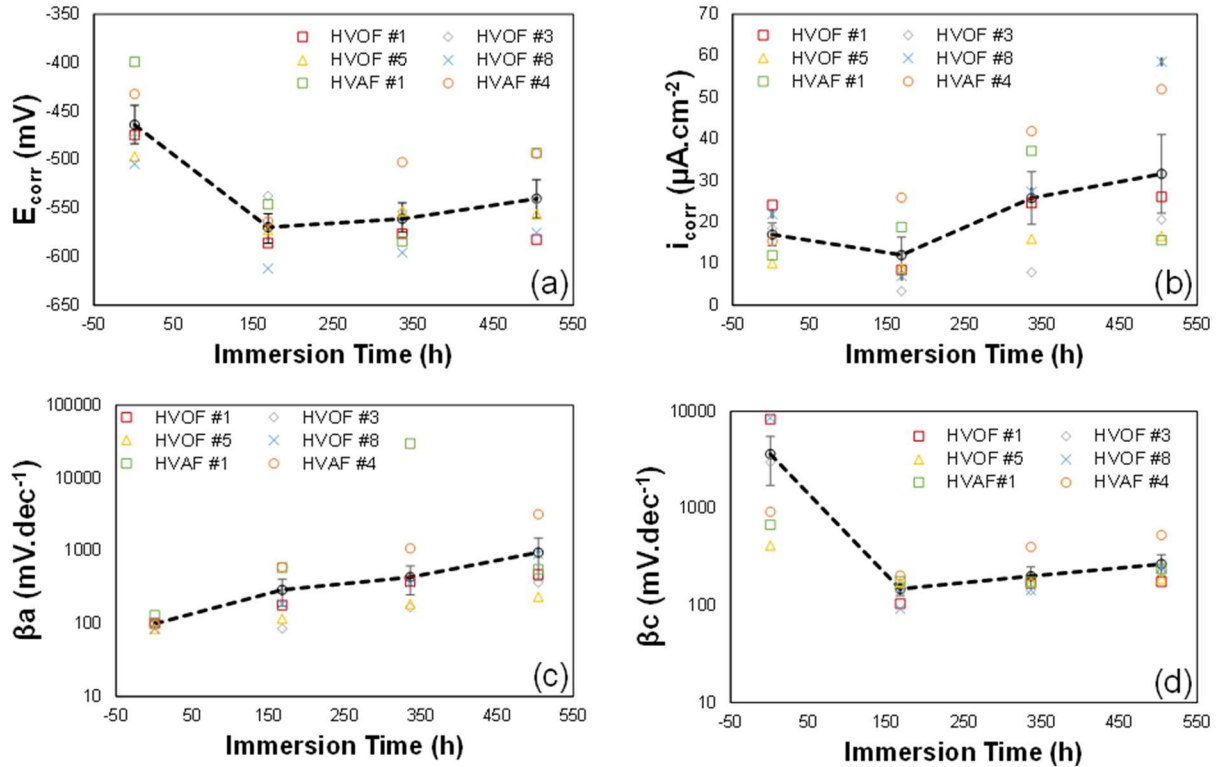


Figure 40 – Evolution of the stainless steel coating's parameters (a) corrosion potential, (b) corrosion current, (c) cathodic slope, (d) anodic slope. The dashed line corresponds to the averaged values of all coatings.

### 3.3.3.4 Impedance Spectroscopy

As illustrated in Figure 41(a), after 1 hour of immersion, a single depressed loop is formed in the complex plane plot of the sprayed coatings. Accordingly, a single maximum at approximately 1 Hz is observed in the phase angle plot. The main changes on the impedance spectra occur during the first week of immersion. On the complex plot, real and imaginary impedances have close values forming an angle of nearly  $45^\circ$ , which is often attributed to reactions limited by mass diffusion. In the phase angle plot, the maximum is shifted to a frequency of nearly 0.1 Hz and the total impedance  $|Z|$  drop from values above  $1000 \Omega\cdot\text{cm}^{-2}$  to close to  $400 \Omega\cdot\text{cm}^{-2}$ .

The use of different spray parameters does not seem to affect the impedance spectra of coatings very strongly. The main remarks can be observed after 1 hour of immersion when coating HVOF

#5 displays lower impedance values, resulting in a lower loop (Figure 41(b)). However, after the first hour of immersion, the differences between the HVOF coatings virtually disappear in the complex plot. The HVAF coatings also display decreasing impedance with increasing immersion time. However, when compared to HVOF coatings, they retain higher  $|Z|$ .

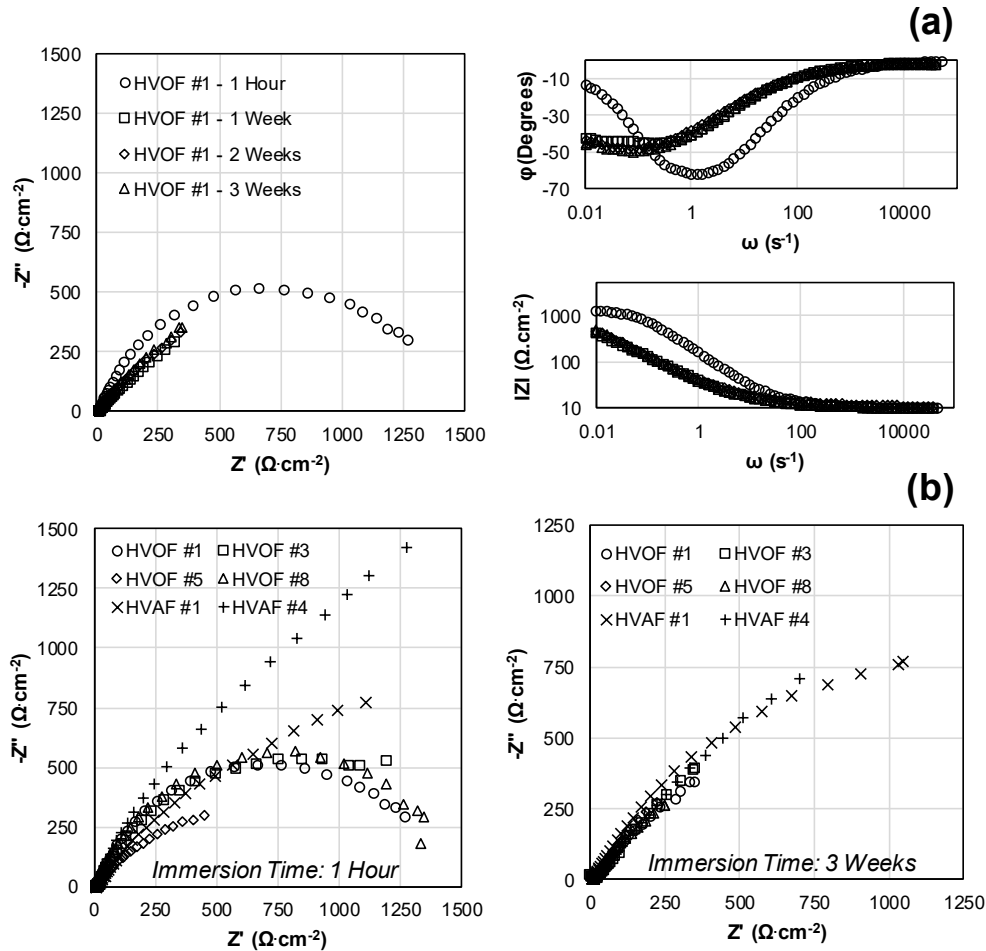


Figure 41 – (a) 3-week evolution of impedance spectra for coating HVOF #1. (b) Effect of spray parameters on EIS spectra after 1 hour and after 3 weeks of immersion.

In the present work, the Randles circuit was chosen to model the electrochemical response of the SS444 electrodes. It contains the electrolyte resistance  $R_e$ , the charge transfer resistance  $R_{ct}$ , a Warburg element and a constant phase element (CPE). The Warburg element was used to model the diffusion of reacting species through the visible corrosion products that formed over the coating surfaces. Another supporting evidence for the use of a Warburg element comes from the observation of the complex plots forming nearly  $45^\circ$  angles. It contains three sub-parameters:  $W-R$  ( $\Omega \cdot \text{cm}^{-2}$ ) which corresponds to the mass transfer resistance at  $\omega \rightarrow 0$ ;  $W-t$  (s) corresponding to

the diffusion time of the reacting species and;  $W-p$  (dimensionless;  $0 < p \leq 1$ ) which is an experimental parameter associating the mass transfer impedance with the frequency [96]. The CPE contains the parameter CPE-Q ( $F.s^{-(1-\alpha)}$ ), which is associated with the double-layer capacitance, and the exponent CPE- $\alpha$ . When the CPE exponent for a given interface is  $\alpha = 1$ , one may say the system behaves as an ideal capacitor, with a single time-constant. More frequently one finds  $0.7 < \alpha < 0.95$ , [94] indicating that the interface displays not a single, but a distribution of time-constants. In the present work, the main evidence supporting the use of CPEs is the formation of “depressed” loops in the complex plots. Based on visual inspection, the fitting of the Randles circuit to the impedance spectra was satisfactory in all instances. Figure 42 illustrates two fitting examples.

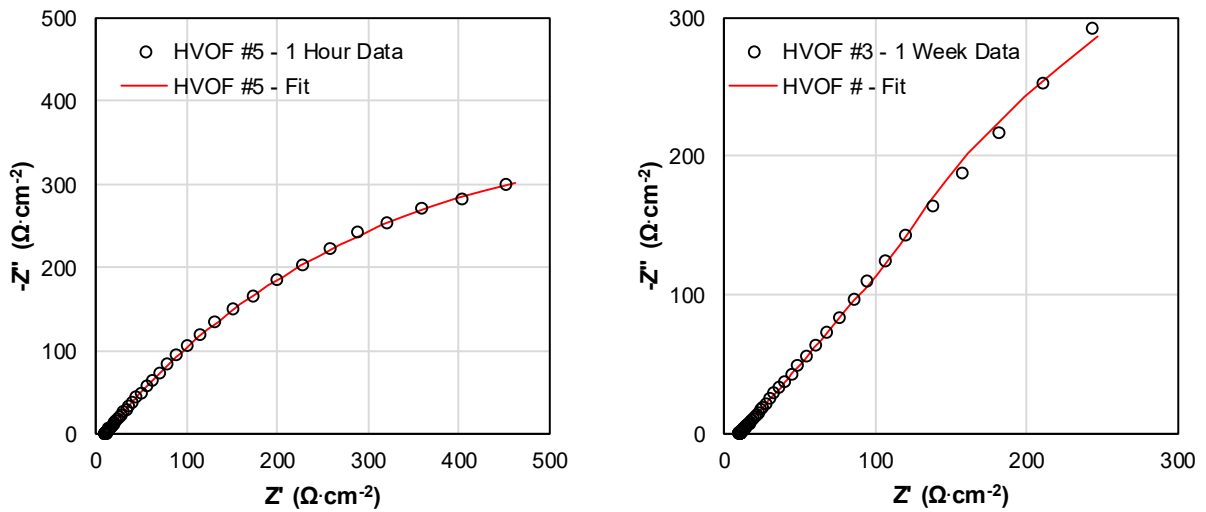


Figure 42 – Fitting of the Randles circuit to the impedance spectra of coatings in two instances.

Figure 43 summarizes the evolution of the analog circuit element values obtained by complex non-linear square regression (CNLS). In most instances, the diffusion time-constant changes from a value close to 1s at the first hour of immersion, to a few tens of seconds after the first week. The other circuit parameters that comprise the Warburg element as well as the charge transfer resistance do not have strong variations during the experiment. Interestingly, the  $W-p$  values obtained in this work are in good agreement with those reported for Fe-based amorphous coatings tested in similar conditions [102]. The CPE-Q of most coatings start close to  $1E-3 F.s^{-(1-\alpha)}$  and stabilizes at  $1E-2 F.s^{-(1-\alpha)}$ . Such values are much higher than what is expected from a bare metallic surface ( $20-50 \mu F.cm^{-2}$ ) and can be attributed to the surface area and dielectric properties of the corrosion product formed over the coating surfaces. Same order of magnitude CPE-Q values are reported for a carbon steel in neutral chloride solution [98] and for sintered ferritic stainless steels

[125]. Except for coatings HVOF #1 and HVOF #5, the CPE exponent of the SS444 coatings start close to  $\alpha = 0.7$ . After the first week, all coating's exponents stabilize at approximately  $\alpha = 0.5$ , which is precisely the value expected when an electrode response is controlled by semi-infinite linear diffusion.

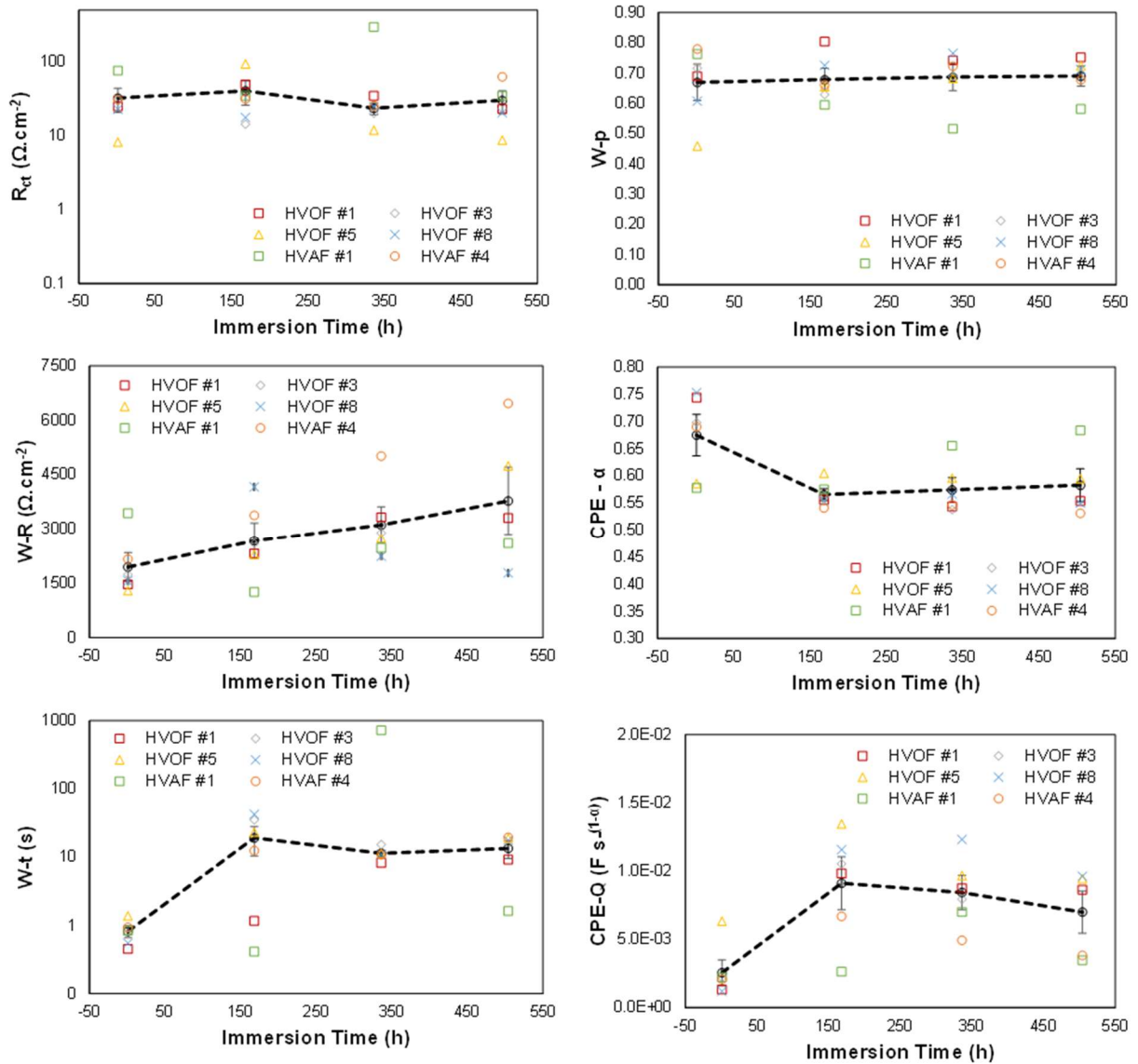


Figure 43 - 3-week evolution of the EIS analog circuit element values used to model the sprayed stainless steel coatings. The electrolyte resistance values (not plotted) ranged between 9.8 – 11  $\Omega \cdot \text{cm}^2$ .

### Effect of Electrode Potential

As illustrated in Figure 44, the EIS spectra of the as-sprayed coatings form larger loops when a cathodic (OCP-50mV) potential is applied to the electrode. The effect can be explained based on the kinetic model (Appendix B, Figure 58) since, at the first hour of immersion,  $\beta_a \ll |\beta_c|$ . After

the 3-week test period,  $\beta_a \approx |\beta_c|$ , and the range of applied potentials had a much less important effect on the EIS spectra. When comparing the structure of coatings HVAF #1 and HVAF #4 in the as-sprayed state (Figure 37), the latter clearly appears to have been more affected by high-temperature oxidation. It is possible that the different sensitivities of these two coatings to the applied potential during impedance measurements is associated with the formation of active phases during the spray deposition.

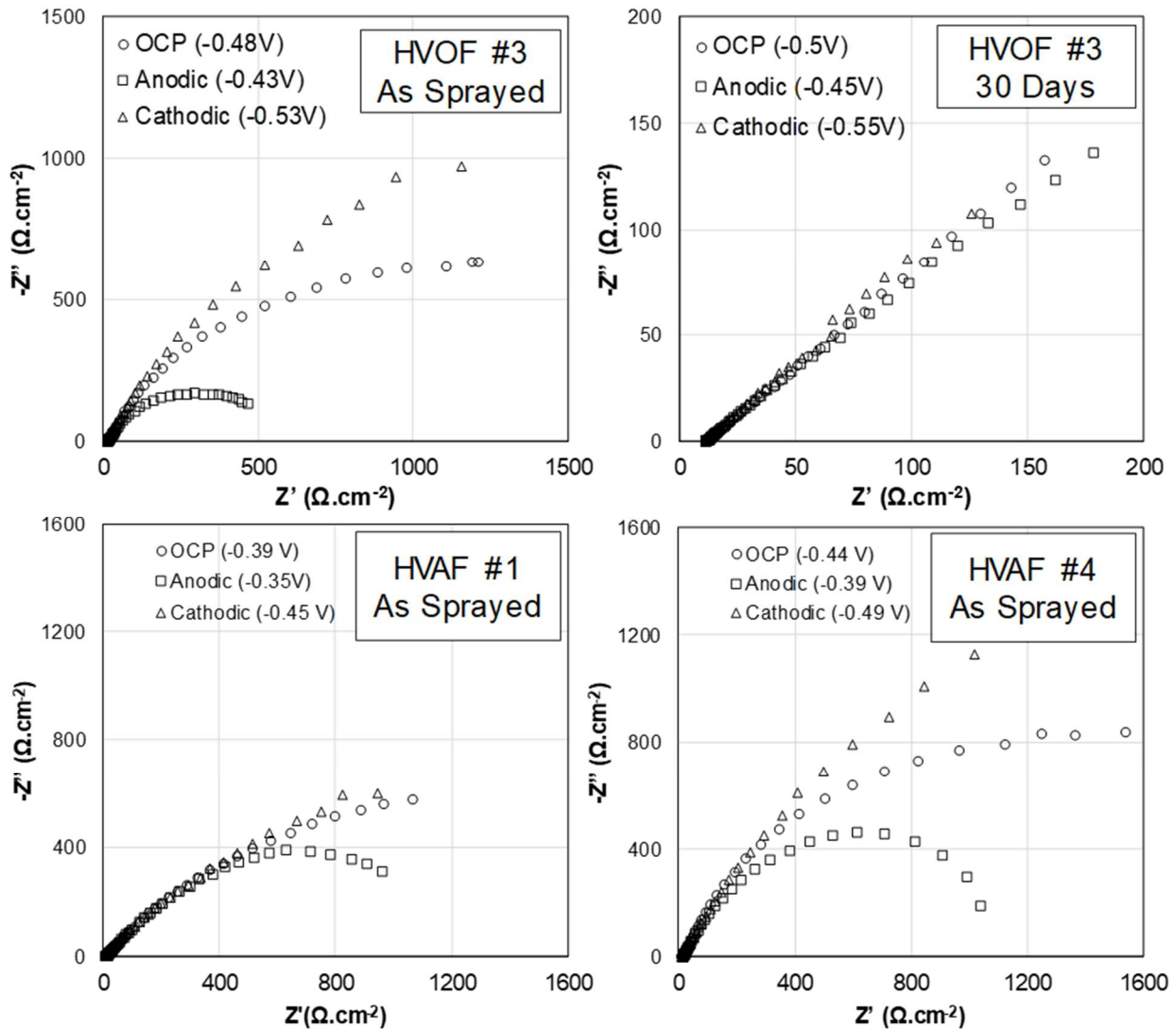
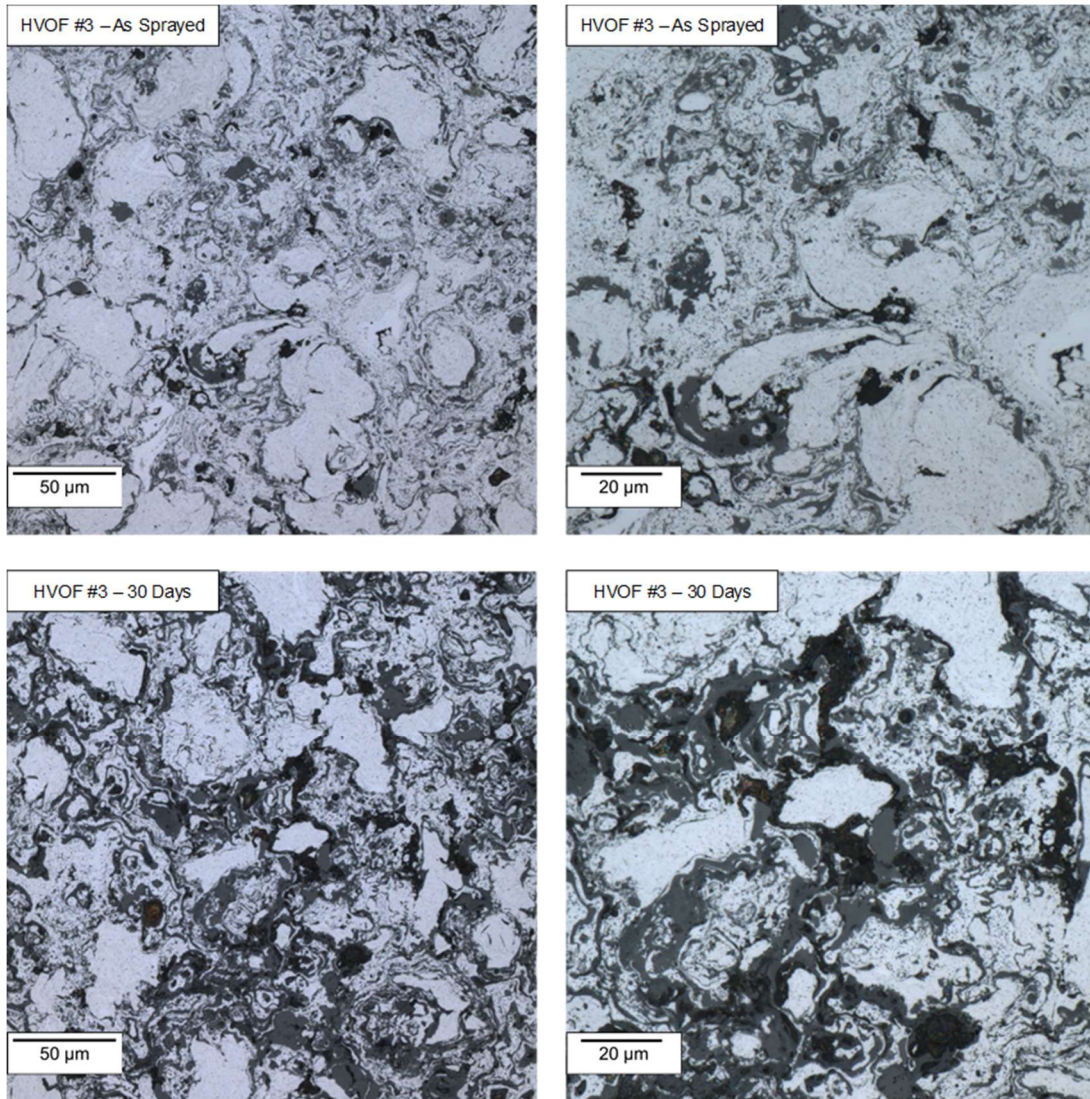


Figure 44 – Effect of electrode potential on the EIS spectra of HVOF and HVAF coatings.

### 3.3.3.5 Changes in Electrode Surface Features

The effects of corrosion on the SS444 coating surface features are illustrated in Figure 45 for the case of the coating HVOF #3. As compared with the as-sprayed coating, one may notice an

increase in porosity and in the quantity of corrosion products and/or oxides. In fact, image analysis performed on the microstructures illustrated in Figure 45 reveals that porosity increases from 1% to 3% while the oxide/corrosion product area fraction increases from 6% to 20%. Pores and corrosion products seem to form preferentially on the re-solidified zone, while the semi-molten particles remain apparently unaffected. These results suggest that the corrosion process is not homogeneous, and that metal dissolution preferentially occurs on regions that experienced high temperature oxidation during or prior (in-flight) to deposition.



*Figure 45 – Change of coating HVOF #3 surface features with prolonged exposure to the test solution. Metal dissolution and the formation of corrosion products occur preferentially at the re-solidified zones while the semi-molten splats remain unchanged.*

In contrast to the HVOF coatings, the corrosion process affected the HVAF surface features in a distinct manner. After the first week of tests, some of the corrosion products that formed were more strongly adhered to the coating surface and could not be removed from it by the final 0.05  $\mu\text{m}$  alumina polishing step. Additionally, after the second week of immersion, it was observed that the formation of a continuous transparent and adherent film formed on the entire HVAF #1 surface (Appendix B, Figure 59). Closer inspection revealed the formation of several small pits on the semi-molten particles as well as the indication of preferential attack on the boundaries between splats. These features are illustrated in Figure 46.

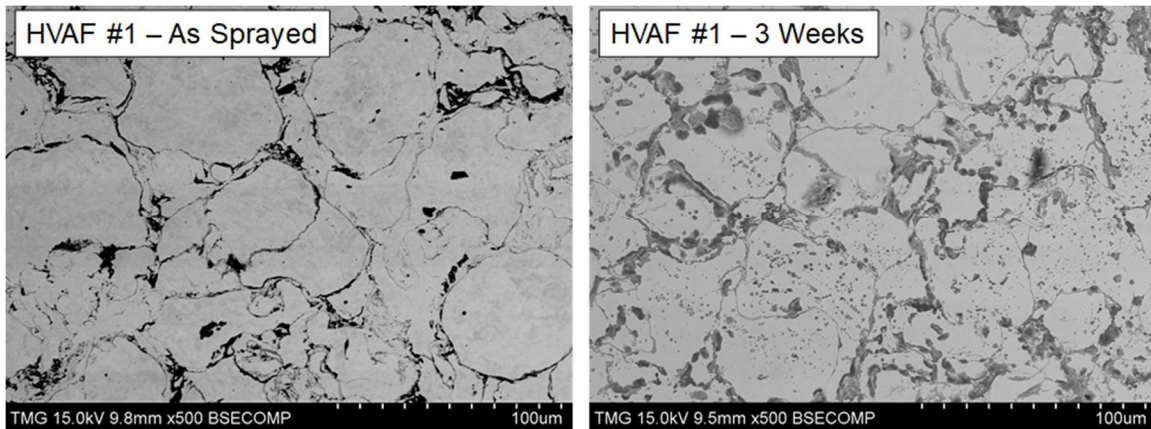


Figure 46 – Backscattered electron image shows the formation of micropits on the splats of coating HVAF #1.

### XPS Analysis

The survey XPS analysis summarized in Table 13 reveals that the Bulk SS444, arc-melt feedstock and the HVAF #1 coating have similar oxygen concentrations, substantially lower than what was measured for the remaining coatings. When comparing as-sprayed coatings to those exposed to the test solution for 3-weeks, one notices an increase in the Cr/Fe ratio. The at.% Mo also seems to be decreased as a consequence of the increased exposure time to the test conditions.

Table 13 – Survey XPS analysis of the investigated materials.

Material	Fe2p	O1s	% atomic			Bal.	Cr/Fe
			Cr2p	Mo3d			
Bulk SS444	46.0	22.9	16.5	2.4	12.1	0.36	
Arc Melt	53.8	20.1	16.9	1.5	7.7	0.31	
HVAF #1 - As Sprayed	42.7	23.1	12.8	1.3	20.2	0.30	
HVAF #1 - Corroded	32.1	31.2	11.7	1.2	23.9	0.36	
HVAF #4 - Corroded	32.2	41.0	17.5	0.8	8.5	0.54	
HVOF #1 - Corroded	29.7	39.6	14.3	1.1	15.2	0.48	
HVOF #3 - As Sprayed	33.1	40.7	15.0	0.5	10.7	0.46	
HVOF #3 - Corroded	28.4	46.8	16.0	0.4	8.4	0.57	
HVOF #5 - Corroded	36.0	37.3	13.8	1.3	11.6	0.38	
HVOF # 8 - Corroded	30.7	43.1	16.9	0.8	8.5	0.55	

The deconvolution of a sample's high-resolution XPS spectra allows one to estimate the contribution of each element oxidation state to the overall signal. Following the rationale used in [123], observation of Figure 47 implies that chromium surface atoms manifest in three main oxidation states, corresponding to metallic Cr(0), Cr(III) - ( $\text{Cr}_2\text{O}_3$ ) and Cr(II) -  $\text{Cr}(\text{OH})_3$ . One may easily notice that the contributions of the Cr oxidation states are very similar in the Bulk SS444, arc-melt feedstock and in the HVAF #1 coating. However, during the 3-week tests, the surface of

coating HVOF #1 is enriched in Cr-oxides and depleted in hydroxides, resembling the other sprayed coatings, which have a marked presence of Cr<sub>2</sub>O<sub>3</sub> in the as-sprayed condition.

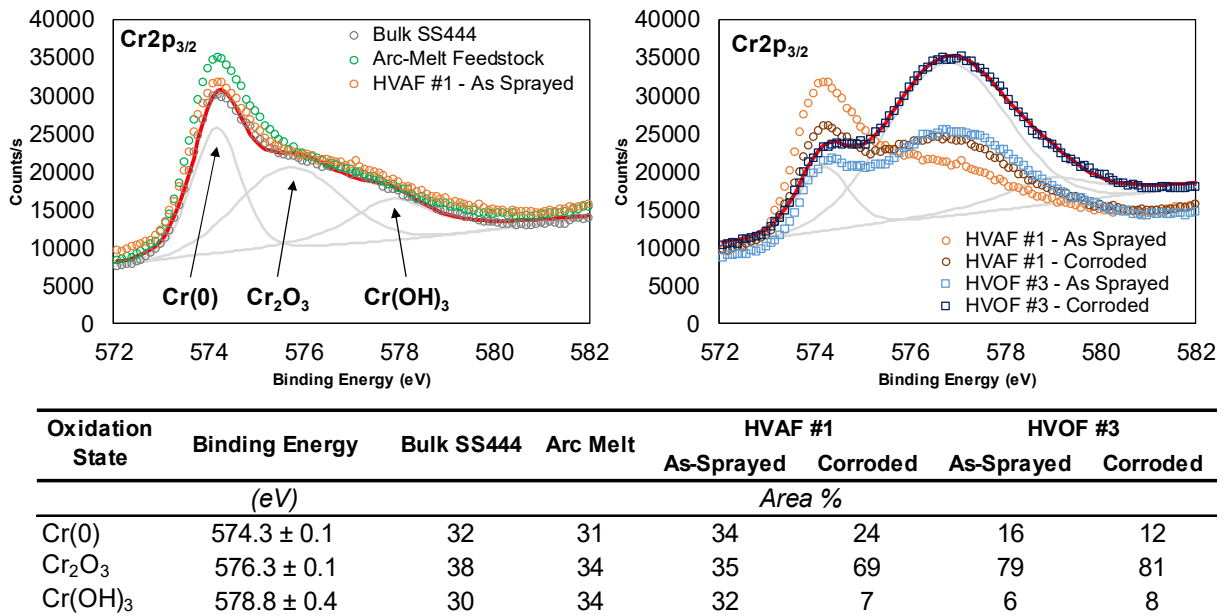


Figure 47 - High resolution of Cr oxidation state on the surface of stainless steel surfaces. The grey lines indicate which peaks are used for spectra deconvolution. The red line is the resulting of the three peaks.

### 3.3.4 Discussion

One of the factors that may explain the substantial drop observed in the corrosion resistance of sprayed coatings is not related to thermal spraying itself, but on the quality of the feedstock production. One of the main characteristics of the bulk SS444 is the presence of evenly distributed Ti- and Nb-rich precipitates that form upon solidification. These elements added in small quantities are strong carbide formers and prevent the onset of chromium carbide precipitation and hence, intergranular corrosion [126]–[129]. It was observed that neither the powder feedstock (atomized or ball-milled) nor the arc-melted pellets had any of such Ti- or Nb-rich precipitates. One could argue that due to their small weight fractions (<0.2%) and to the relatively high cooling rates experienced in the atomization process ( $10^3 - 10^6$  °C/s [130]), these elements could have remained in solid solution, which would make their detection by EDX nearly impossible. However, according to the isothermal precipitation diagrams of ferritic stainless steels [126], a comparatively much lower cooling rate of 15 °C/s should avoid CrC precipitation. Still, Cr-rich precipitates were observed in the arc melted disk microstructure. Therefore, it is safe to assume that the cooling rates experienced by the arc melted feedstock were a few orders of magnitude lower than those experienced by atomized or sprayed [53] particles. Under these conditions, if Ti and Nb were still present in the feedstock composition, their presence in the microstructure should have manifested

in the form of Ti- or Nb-rich precipitates. One may assume these elements were lost during the melting and atomization processes which, according to the manufacturers, is done without control of the surrounding atmosphere.

Despite the clear metallurgical flaws, the polarization response of the arc melted feedstock was much closer to that of the bulk SS444 than that of the sprayed coatings. Considering these observations, the changes in the feedstock chemical composition alone cannot explain the significant drop in the corrosion behavior of the sprayed coatings. More likely, is that the coating's high density of defects (including pores, splat boundaries and oxides) prevent the development of an effectively protective film. While different spray parameters or techniques clearly affect the relative fraction of each coating constituent, the overall defect density does not. Stainless steels produced by powder metallurgy [124], [125], [131] share similar structural defects and also an inferior corrosion resistance when compared to that of wrought parts. By melting the feedstock, the density of defects is drastically reduced, allowing the entire surface to respond more homogeneously when exposed to the electrolyte. In fact, the use of laser re-melting in Ni-alloy HVOF coatings has been shown to substantially improve its response in polarization tests [132].

The correlation between particle in-flight properties measured with DPV-evolution and the coating structures presented some unexpected results. For example, coating HVOF #8 showed the highest level of oxidation (as measured by EDX) even though the particles experienced a relatively short period of exposure to the flame. As previously mentioned, it was during the production of HVOF #8 that the highest consumption of kerosene as well as the highest post-spraying substrate temperature was measured. It is believed that the oxidation of HVOF #8 particles did not occur during their flight, but while exposed to the HVOF torch flame following their deposition on the substrate. The use of a substrate cooling method might have prevented such effect, improving the coating's performance. Another apparent incoherence arises from the higher fraction of unmolten splats in coatings HVOF #5 and HVOF #3 which, according to the DPV-evolution diagnostics experienced the highest in-flight temperatures. The JP-8000 HVOF torch is characterized by a radial powder feeding system [23]. One may argue that the change in the O/F ratio interferes with the regions of high and low pressures in the torch's nozzle, which ultimately affected the particles trajectory along the gas stream. Since the measurement volume of the DPV-evolution system is less than 1 mm<sup>3</sup>, it is possible that the temperature measurements did not account for the contributions from relatively cold and large particles. Different feedstock carrier gas flow rates might be necessary to improve particle trajectory and melting along the flame stream.

The substantial drop in the coating's  $E_{corr}$  after one week of immersion imply changes in the chemical nature at the electrode/electrolyte interface. Two factors observed in this work could cause this effect: the preferential dissolution of an active phase and; the changes in Cr oxidation state at the coating surfaces as determined by XPS analysis.

The existence of a more active site in thermally sprayed coatings has been attributed to the effects of particle exposure to high-temperatures, leading to the formation of Cr-depleted zones which are galvanically coupled to neighbouring Cr-rich areas [105], [106], [132]. While a Cr-depleted zone was not identified in this work, the regions of preferential dissolution seemed to be at the HVOF coating re-solidified zones (Figure 9) which, based on EDX analysis had relatively higher %O and lower %Cr. It is possible that the electrode's corrosion potential is controlled by these active areas until their complete dissolution. However, the  $E_{corr}$  drop was also experienced by coating HVOF #1, even though its structure was mainly composed of unmolten splats.

If one considers the standard electrode potentials of Cr(III) and Fe(II), respectively -0.74 V and -0.41 V versus a standard hydrogen electrode, one could say that the shift observed in the  $E_{corr}$  of the coatings during the first week of immersion is caused by the surface Cr-enrichment, as determined by XPS analysis. In fact, XPS analysis often reveal a Cr-enrichment on the surface of stainless steels [133]. Auger electron spectroscopy studies on bulk ferritic 430 steels show that the more the surface is enriched in Cr, the higher are the  $E_{corr}$  values [134]. This may be the reason behind the increasing trend for  $E_{corr}$ ,  $\beta_a$  and  $\beta_c$  values after the first week of testing. Despite the increased presence of Cr-oxides revealed by XPS analysis, the corrosion products formed on the surface of the sprayed coatings did not provide a protection like the passive films formed on wrought stainless steels. One may speculate that the structure of the coating films is highly defective, mirroring the underlying structurally and chemically heterogenous sprayed metal.

The non-ideal capacitive response of the electrical double-layer is a well-known phenomenon and arises due to inhomogeneous current and potential distributions in an electrode [94]. For instance, the 2D-geometry of disk electrodes alone has been shown to be a cause for such inhomogeneities [135]. The energy state of the electrode also plays a role in the current distribution and, by consequence, on the CPE response of the electrode [93]. As thoroughly shown in this work, the SS444 coating surfaces are highly heterogenous, and the non-ideal response of the electrical double layer was not surprising. The CPE- $\alpha$  exponent starts at values between 0.70 – 0.75 which are in good agreement with the results of Guo et al. for Fe-based amorphous coatings produced by HVOF and HVOF [102]. However, after 1 week of immersion, the CPE exponent decreases to approximately 0.5. This transition coincides with the reduction of  $E_{corr}$  measured in the

polarization tests and suggests that the observed changes in CPE- $\alpha$  are associated with a change in the chemistry (or energy state) of the electrode interface.

### 3.3.5 Conclusions

In the present work, the impedance and polarization responses of ferritic stainless steel (AISI 444) coatings produced by HVOF and HVAF were continuously monitored for 3 weeks and correlated with changes in the electrode surface chemistry and microstructural features. The main conclusions that may be drawn from the study are summarized as follows.

The corrosion resistance of sprayed stainless-steel coatings is significantly inferior to that of wrought parts. The effect of spraying parameters on the coating's electrochemical behavior is very limited. The polarization behavior of the arc-melt feedstock, despite the absence of important Cr-stabilizing elements (Ti- and Nb-rich precipitates), was much closer to that of a bulk stainless steel plate. Therefore, it can be said that the significant reduction of the corrosion resistance of coatings when compared to the wrought stainless steels arise primarily due to the defects (pores, boundaries between splats, oxides, etc.) inherent to the spray deposition method.

The strong transitions in the coating's electrochemical parameters during the first week of immersion are due to the preferential dissolution of coating regions experiencing substantial melting and high-temperature oxidation prior to deposition, as well as to the changes in the oxidation state of chromium at the coating surface.

The observed changes in the coating's surface chemistry, microstructure, electrochemical properties and the EIS spectra response to different applied potentials strongly support the thesis of a flat electrode behavior. Localized reactions in pores may have happened but their contribution to the electrode response could not be experimentally probed with the used techniques.

## 4. Concluding Remarks and Suggestions for Future Work

The necessary transition from fossil to renewable energy sources poses a challenge to the reliability and longevity of machine parts that compose hydroelectric stations. In the present work, thermal spraying has been proposed as a method to reduce or mitigate some of the factors that are known to compromise the operation and longevity of the complex structures that generate hydroelectric power. The versatility of the method proves that it can be used in a wide range of applications including thrust bearings, draft tubes, wicket gates, guide vanes, etc. In each case, coating structure and properties must be tailored and assessed to ensure they can extend the service time of the parts being coated. In this thesis, three potential applications for thermal-sprayed coatings in hydroelectric stations were identified. The main findings are presented in the following paragraphs.

Thrust bearings are important elements that allow the rotation of large turbines in a stable and controlled fashion. They are usually coated with a soft Sn-based alloy known as Babbitt, which are often produced by spray techniques such as arc and flame spraying. In these processes, the coating deposition is often done manually, and the sprayed droplets are accelerated to relatively low velocities (<200 m/s). These factors may easily cause Babbitt coatings to have large interconnected pores that can be infiltrated by pressurized oil, eventually leading to bearing failure. As presented in section 2.2, an HVOF torch was adapted to allow low melting-point Babbitt particles to be injected radially into the flame. The use of in-flight diagnostic tools allowed the confirmation that particles can be accelerated to velocities higher than particles used in arc- and flame-spraying. However, it was shown that maximum deposition efficiencies were obtained for lower impact velocities and by using coarser feedstock particle diameters. This observation suggests the existence of a process window i.e. an ideal range of particle impact temperatures and velocities that, like cold spraying processes, allows them to effectively deposit in the substrate without eroding previously deposited splats. In this context, the use of low-pressure cold-spraying systems may be interesting as they may produce Babbitt coatings with dense structures while further increasing the deposition efficiencies. In a broader sense, the results of section 2.2 are very relevant for the thermal spray community as it highlights the importance of controlling the spray parameters to obtain dense coatings and avoid problems such as the severe porosity noticed in thermal-sprayed Babbitt bearings.

Recent trends in industrial practice suggest that polymeric materials will replace Babbitt coatings due to the former group abilities to develop higher hydrodynamic pressures and to withstand higher service temperatures. As discussed in section 2.3, the present thesis proposed the use of

thermal spraying as a method to develop porous bond coatings allowing the polymers to adhere to metallic substrate. One positive aspect of the proposed method includes the ability to spray the matrix (stainless steel) and pore forming ( $\text{Fe}_3\text{Al}$ ) particles coaxially through the HVOF torch combustion chamber. Usually, the properties of the pore forming particles are so different from that of the matrix that radial injection is mandatory, which increases the overall process complexity. Moreover, as far as the author of this thesis is aware, the work has originality as this was the first attempt to use supersonic spraying to create the matrix of a porous coating. On the other hand, coating exposure to the acid leaching process led to substantial degradation of its mechanical properties, requiring further high-temperature treatment before polymer infiltration could be done. Some suggestions to improve the as-leached state of the coatings include the use of more chemically stable metals such as Ni-alloys and/or the use of pore formers that dissolve in less aggressive environments such as aluminium in NaOH. The significant number of steps involved in producing the stainless steel bond-coatings may pose an important obstacle to its implementation in actual industrial practice. Moreover, the adhesion strength between the polymer/porous coating/substrate remains yet to be assessed quantitatively. While several technical difficulties were reported, appropriate selection of feedstock and spray parameters allowed the successful production of the polyimide-infiltrated stainless steel coating setting an important milestone in the development of surface-engineered composite structures they may be useful in other tribological and related applications.

In section 3.3, a thorough study of the corrosion of thermal-sprayed stainless steel coatings was presented. The goal was not solely to assess the coatings protective ability but also to address certain aspects of their behavior that, based on the present literature are difficult to understand. Six coatings were produced with spray parameters leading to a minimum overlap in terms of in-flight particle temperatures and velocities. While the coating structures had varying fractions of molten and semi-molten splats as well as pores and oxides, their electrochemical behavior was nearly independent of the spray parameters. When compared to a bulk stainless steel plate, the coatings displayed significantly higher corrosion currents and much lower corrosion potentials. By re-melting the feedstock used for spraying, a solid disc was produced. It had a few remaining pores and Cr-rich precipitates, implying pre-existing compositional and structural flaws. Despite the issues, the arc re-melted feedstock had an electrochemical behavior much closer to that of the bulk plate when compared to the coatings. This suggests that the typical performance gap that exists between bulk plates and coatings of similar composition arises mostly from the high density of defects inherent to the thermal spray process. These results suggest that further

pursuing lower in-flight temperatures and higher in-flight velocities would not improve the sprayed coating's corrosion resistance to the level of a bulk material.

It was shown that the electrochemical response of the coatings changed during the first week of tests. During the same time, the regions in the coatings experiencing high degree of melting prior to deposition in the substrate (re-solidified zone) were preferentially corroded, while semi-molten splats remained mostly intact. Additionally, XPS analysis revealed a surface enrichment in Cr-oxides at the surface of the coatings. These changes indicate the presence of a spontaneously formed electrochemically active film that appears on the surface of the coatings as a result of the corrosion process. This film controls the reaction rates and the overall electrode response to changes in the electrode potential.

The formation of blisters in one of the HVOF coatings implies the onset of corrosion reactions underneath the electrode surface. Based on impedance spectra analysis and the use of a simple kinetic model, the contribution of reactions occurring underneath the electrode surfaces was considered secondary to the overall electrode response. Further analysis with microelectrodes could shed light on the reaction rates that happen in these small stagnant corrosion sites and should be subject of future studies.

## References

- [1] U. Dorji and R. Ghomashchi, "Hydro turbine failure mechanisms: An overview," *Eng. Fail. Anal.*, vol. 44, pp. 136–147, 2014.
- [2] M. Horynová, L. Klakurková, J. Švejcar, M. Juliš, P. Gejdoš, and L. Čelko, "Failure analysis of casing of draft tube of turbine used in hydropower plant," *Eng. Fail. Anal.*, vol. 82, no. August, pp. 848–854, 2017.
- [3] J. C. Chávez, J. A. Valencia, G. A. Jaramillo, J. J. Coronado, and S. A. Rodríguez, "Failure analysis of a Pelton impeller," *Eng. Fail. Anal.*, vol. 48, pp. 297–307, 2015.
- [4] N. Espallargas, J. Berget, J. M. Guilemany, A. V. Benedetti, and P. H. Suegama, "Cr<sub>3</sub>C<sub>2</sub>–NiCr and WC–Ni thermal spray coatings as alternatives to hard chromium for erosion–corrosion resistance," *Surf. Coatings Technol.*, vol. 202, no. 8, pp. 1405–1417, Jan. 2008.
- [5] Z. Liming, L. Yongyao, W. Zhengwei, L. Xin, and X. Yexiang, "A review on the large tilting pad thrust bearings in the hydropower units," *Renew. Sustain. Energy Rev.*, vol. 69, no. September 2016, pp. 1182–1198, 2017.
- [6] S.B.Glavatskih, "Tilting Pad Thrust Bearings," pp. 379–390, 2003.
- [7] H. Iliev, "Failure analysis of hydro-generator thrust bearing," *Wear*, vol. 225–229, no. PART II, pp. 913–917, 1999.
- [8] M. P. Porto, L. C. Porto, R. N. N. Koury, E. W. Soares, F. G. Coelho, and L. Machado, "A case study on thrust bearing failures at the SÃO SIMÃO hydroelectric power plant," *Case Stud. Therm. Eng.*, vol. 1, no. 1, pp. 1–6, 2013.
- [9] J. E. L. Simmons, R. T. Knox, and W. O. Moss, "The development of PTFE (polytetrafluoroethylene)-faced hydrodynamic thrust bearings for hydrogenerator application in the United Kingdom," *Proc. Inst. Mech. Eng. Part J J. Eng. Tribol.*, vol. 212, no. 5, pp. 345–352, 1998.
- [10] A. R. C. Nascimento, F. B. Ettouil, C. Moreau, S. Savoie, and R. Schulz, "Production of Babbitt Coatings by High Velocity Oxygen Fuel (HVOF) Spraying," *J. Therm. Spray Technol.*, vol. 26, no. 7, pp. 1732–1740, 2017.
- [11] W. Yang, P. Norrlund, L. Saarinen, J. Yang, W. Zeng, and U. Lundin, "Wear Reduction for Hydropower Turbines Considering Frequency Quality of Power Systems: A Study on Controller Filters," *IEEE Trans. Power Syst.*, vol. 32, no. 2, pp. 1191–1201, 2017.
- [12] M. Rodiouchkina *et al.*, "Material Characterization and Influence of Sliding Speed and Pressure on Friction and Wear Behavior of Self-Lubricating Bearing Materials for Hydropower Applications," *Lubricants*, vol. 6, no. 2, p. 39, 2018.
- [13] R. Gawarkiewicz and M. Wasilczuk, "Wear measurements of self-lubricating bearing materials in small oscillatory movement," *Wear*, vol. 263, no. 1-6 SPEC. ISS., pp. 458–462, 2007.
- [14] H. E. Sliney, "Wide temperature spectrum self-lubricating coatings prepared by plasma spraying," *Thin Solid Films*, vol. 64, no. 2, pp. 211–217, Dec. 1979.
- [15] R. Gadow and D. Scherer, "Composite coatings with dry lubrication ability on light metal substrates," *Surf. Coatings Technol.*, vol. 151–152, pp. 471–477, 2002.
- [16] J. Yuan, Y. Zhu, X. Zheng, H. Ji, and T. Yang, "Fabrication and evaluation of atmospheric

- plasma spraying WC–Co–Cu–MoS<sub>2</sub> composite coatings,” *J. Alloys Compd.*, vol. 509, no. 5, pp. 2576–2581, Feb. 2011.
- [17] P. L. Fauchais, “Fundamentals of Combustion and Thermal Plasma,” in *Thermal Spray Fundamentals. From Powder to Part.*, 2014, pp. 73–111.
- [18] T. S. Society, “Thermal Spray Technology White Paper,” no. Figure 1. pp. 1–9.
- [19] T. Schmidt, F. Gärtner, H. Assadi, and H. Kreye, “Development of a generalized parameter window for cold spray deposition,” *Acta Mater.*, vol. 54, no. 3, pp. 729–742, Feb. 2006.
- [20] M. Winnicki, A. Baszczuk, M. Rutkowska-Gorczyca, A. Małachowska, and A. Ambroziak, “Corrosion resistance of tin coatings deposited by cold spraying,” *Surf. Eng.*, vol. 32, no. 9, pp. 691–700, 2016.
- [21] P. L. Fauchais, J. V. R. Heberlein, and M. I. Boulos, *Thermal Spray Fundamentals*. Springer, 2014.
- [22] M. Li and P. D. Christofides, “Modeling and control of high-velocity oxygen-fuel (HVOF) thermal spray: A tutorial review,” *J. Therm. Spray Technol.*, vol. 18, no. 5–6, pp. 753–768, 2009.
- [23] S. Kamnis and S. Gu, “3-D modelling of kerosene-fuelled HVOF thermal spray gun,” *Chem. Eng. Sci.*, vol. 61, no. 16, pp. 5427–5439, 2006.
- [24] M. Li and P. D. Christofides, “Multi-scale modeling and analysis of an industrial HVOF thermal spray process,” *Chem. Eng. Sci.*, vol. 60, no. 13, pp. 3649–3669, Jul. 2005.
- [25] D. Cheng, Q. Xu, G. Trapaga, E. J. Lavernia, and I. Introduction, “The Effect of Particle Size and Morphology on the In-Flight,” *Metall. Mater. Trans. B*, vol. 32, no. June, pp. 525–535, 2001.
- [26] P. L. Fauchais, J. V. R. Heberlein, and M. I. Boulos, “Gas Flow–Particle Interaction,” in *Thermal Spray Fundamentals: From Powder to Part*, 2014, pp. 113–215.
- [27] P. Gougeon and C. Moreau, “In-Flight Particle Surface Temperature Measurement: Influence of the Plasma Light Scattered by the Particles,” vol. 2, no. 3, pp. 229–234, 1993.
- [28] B. Aziz and C. Moreau, “Influence of the Plasma Radiation Scattered by Inflight Particles on Temperature Measurement in Suspension Plasma Spraying,” in *ITSC 2015 - Proceedings of the International Thermal Spray Conference*, 2015, pp. 520–525.
- [29] G. W. Stachowiak, “Hydrodynamic Lubrication,” in *Engineering Tribology*, 2006, pp. 105–210.
- [30] Branagam L. A., “Survey of Damage Investigation of Babbitted Industrial Bearings,” *Lubrication*, vol. 3, pp. 91–112, 2015.
- [31] C. a. Mahieux, “Experimental Characterization of the Influence of Coating Materials on the Hydrodynamic Behavior of Thrust Bearings: A Comparison of Babbitt, PTFE, and PFA,” *J. Tribol.*, vol. 127, no. 3, p. 568, 2005.
- [32] J. Zhou, B. Blair, J. Argires, and D. Pitsch, “Experimental Performance Study of a High Speed Oil Lubricated Polymer Thrust Bearing,” *Lubricants*, vol. 3, no. 1, pp. 3–13, 2015.
- [33] M. Wodtke and M. Wasilczuk, “Evaluation of apparent Young’s modulus of the composite polymer layers used as sliding surfaces in hydrodynamic thrust bearings,” *Tribol. Int.*, vol. 97, pp. 244–252, 2016.

- [34] A. Golchin, G. F. Simmons, and S. B. Glavatskih, "Break-away friction of PTFE materials in lubricated conditions," *Tribol. Int.*, vol. 48, pp. 54–62, 2012.
- [35] J. H. Jia, H. D. Zhou, S. Q. Gao, and J. M. Chen, "A comparative investigation of the friction and wear behavior of polyimide composites under dry sliding and water-lubricated condition," *Mater. Sci. Eng. A*, vol. 356, no. 1–2, pp. 48–53, 2003.
- [36] M. Lv, F. Zheng, Q. Wang, T. Wang, and Y. Liang, "Effect of proton irradiation on the friction and wear properties of polyimide," *Wear*, vol. 316, no. 1–2, pp. 30–36, 2014.
- [37] M. Lv, F. Zheng, Q. Wang, T. Wang, and Y. Liang, "Friction and wear behaviors of carbon and aramid fibers reinforced polyimide composites in simulated space environment," *Tribol. Int.*, vol. 92, pp. 246–254, 2015.
- [38] P. Samyn and G. Schoukens, "The effect of processing method on dry sliding performance of polyimides at high load/high velocity conditions," *Eur. Polym. J.*, vol. 44, no. 3, pp. 716–732, 2008.
- [39] E. S. Hedges, "Tin in bearing alloys," in *Tin and its alloys*, 1960, pp. 238–295.
- [40] W. P. Bardet and D. J. Wengler, "Babbitting," in *Surface Engineering, Vol5, ASM Handbook*, 1994, pp. 372–377.
- [41] J. P. Beaulieu, F. Borit, V. Guipont, M. Jeandin, and C. Mabire, "Plasma Spraying of Tin on to a Monocrystalline Lithium Fluoride Window," in *Proceedings of the International Thermal Spray Conference*, 2001, pp. 79–85.
- [42] N. Pistofidis, G. Vourlias, E. Pavlidou, P. Patsalas, G. Stergioudis, and E. K. Polychroniadis, "Study of the structure and morphology of plasma-sprayed tin coating," *Surf. Coatings Technol.*, vol. 200, no. 22, pp. 6245–6250, 2006.
- [43] G. Vourlias, N. Pistofidis, and G. Stergioudis, "Ability of metallic coatings to protect low carbon steels from aqueous corrosion," *Corros. Sci. Technol.*, vol. 43, no. 2, pp. 163–172, 2008.
- [44] G. Vourlias, N. Pistofidis, G. Stergioudis, and E. K. Polychroniadis, "Structural study near the film/substrate interface of a plasma sprayed tin coating on low carbon steel," *J. Alloys Compd.*, vol. 416, no. 1, pp. 183–187, 2006.
- [45] P. R. C. Alcover Junior and A. G. M. Pukasiewicz, "Evaluation of microstructure, mechanical and tribological properties of a Babbitt alloy deposited by arc and flame spray processes," *Tribol. Int.*, vol. 131, no. July 2018, pp. 148–157, 2019.
- [46] J. Legoux, E. Irissou, and C. Moreau, "Effect of Substrate Temperature on the Formation Mechanism of Cold-Sprayed Aluminum, Zinc and Tin Coatings," *J. Therm. Spray Technol.*, vol. 16, no. 5, pp. 619–626, 2007.
- [47] J. F. Li, P. A. Agyakwa, C. M. Johnson, D. Zhang, T. Hussain, and D. G. McCartney, "Characterization and solderability of cold sprayed Sn–Cu coatings on Al and Cu substrates," *Surf. Coatings Technol.*, vol. 204, no. 9–10, pp. 1395–1404, Jan. 2010.
- [48] M. S. Kharasch, "Heats of combustion of organic compounds," *Bur. Stand. J. Res.*, vol. 2, no. 2, p. 359, 1929.
- [49] J. Kawakita, T. Fukushima, S. Kuroda, and T. Kodama, "Corrosion behaviour of HVOF sprayed SUS316L stainless steel in seawater," *Corros. Sci.*, vol. 44, no. 11, pp. 2561–2581, Nov. 2002.
- [50] J. Kawakita, S. Kuroda, T. Fukushima, and T. Kodama, "Corrosion resistance of HVOF

- sprayed HastelloyC nickel base alloy in seawater," *Corros. Sci.*, vol. 45, no. 12, pp. 2819–2835, Dec. 2003.
- [51] D. Zois, T. Wentz, R. Dey, S. Sampath, and C. M. Weyant, "Simplified model for description of HVOF NiCr coating properties through experimental design and diagnostic measurements," *J. Therm. Spray Technol.*, vol. 22, no. 2–3, pp. 299–315, 2013.
- [52] W. B. Hampshire, "Tin and Tin Alloys," in *Properties and Selection: Nonferrous Alloys and Special-Purpose Materials, Vol 2, ASM Handbook*, 1990, pp. 517–526.
- [53] A. McDonald, M. Lamontagne, C. Moreau, and S. Chandra, "Impact of plasma-sprayed metal particles on hot and cold glass surfaces," *Thin Solid Films*, vol. 514, no. 1–2, pp. 212–222, Aug. 2006.
- [54] P. L. Fauchais, J. V. R. Heberlein, and M. I. Boulos, *Thermal Spray Fundamentals*. Boston, MA: Springer US, 2014.
- [55] G. W. Stachowiak and A. W. Batchelor, "Solid lubrication and surface treatments," in *Engineering Tribology*, 2005, pp. 419–459.
- [56] G. W. Stachowiak, "Wear of non-metallic materials," in *Engineering Tribology*, 2005, pp. 651–704.
- [57] U. S. Tewari and J. Bijwe, "Comparative studies on sliding wear of polyimide composites," *Composites*, vol. 22, no. 3, pp. 204–210, 1991.
- [58] P. Samyn, P. De Baets, G. Schoukens, and B. Hendrickx, "Tribological Behavior of Pure and Graphite-Filled Polyimides Under Atmospheric Conditions," *Polym. Eng. Sci.*, vol. 43, no. 8, pp. 1477–1487, 2003.
- [59] G. Theiler and T. Gradt, "Tribological characteristics of polyimide composites in hydrogen environment," *Tribol. Int.*, vol. 92, pp. 162–171, 2015.
- [60] Y. Nakamura, Y. Suzuki, and Y. Watanabe, "Effect of oxygen plasma etching on adhesion between polyimide films and metal," *Thin Solid Films*, vol. 291, pp. 367–369, 1996.
- [61] S. T. Amancio-Filho and J. F. dos Santos, "Joining of Polymers and Polymer–Metal Hybrid Structures: Recent Developments and Trends," *Polym. Eng. Sci.*, vol. 49, no. 8, pp. 1461–1476, 2009.
- [62] G. C. Pratt and W. H. Wilson, "The performance of steel-backed acetal copolymer bearings," *Wear*, vol. 12, no. 2, pp. 73–90, 1968.
- [63] C. Tekmen, K. Iwata, Y. Tsunekawa, and M. Okumiya, "Controlling graphite content in plasma sprayed cast iron coatings via in-flight particle diagnostic," *J. Mater. Process. Technol.*, vol. 209, no. 14, pp. 5417–5422, Jul. 2009.
- [64] C. Tekmen, K. Iwata, Y. Tsunekawa, and M. Okumiya, "Influence of methane and carbon dioxide on in-flight particle behavior of cast iron powder by atmospheric plasma spraying," *Mater. Lett.*, vol. 63, no. 28, pp. 2439–2441, Nov. 2009.
- [65] J. Knuuttila, P. Sorsa, T. Mäntylä, J. Knuuttila, and P. Sorsa, "Sealing of thermal spray coatings by impregnation," *J. Therm. Spray Technol.*, vol. 8, no. June, pp. 249–257, 1999.
- [66] S.-L. Zhang, C.-X. Li, C.-J. Li, and G.-J. Yang, "Microstructure and Properties of Porous Ni50Cr50-Al2O3 Cermet Support for Solid Oxide Fuel Cells," *J. Therm. Spray Technol.*, vol. 22, no. 2–3, pp. 158–165, 2013.

- [67] M. Gupta, a. Weber, N. Markocsan, and N. Heiden, "Development of plasma sprayed Ni/YSZ anodes for metal supported solid oxide fuel cells," *Surf. Coatings Technol.*, vol. 318, pp. 178–189, 2017.
- [68] D. Aussavy *et al.*, "YSZ-Polyester Abradable Coatings Manufactured by APS," *J. Therm. Spray Technol.*, vol. 25, no. 1–2, pp. 252–263, 2016.
- [69] M. Arai and T. Suidzu, "Porous ceramic coating for transpiration cooling of gas turbine blade," *J. Therm. Spray Technol.*, vol. 22, no. 5, pp. 690–698, 2013.
- [70] J. Medřický *et al.*, "Optimization of High Porosity Thermal Barrier Coatings Generated with a Porosity Former," *J. Therm. Spray Technol.*, vol. 24, no. 4, pp. 622–628, 2015.
- [71] A. R. C. Nascimento, S. Devaraj, C. Moreau, S. Savoie, and R. Schulz, "Porous Stainless-Steel Coatings Produced by HVOF and Chemical Leaching," in *Proceedings of the International Thermal Spray Conference*, 2018, pp. 321–329.
- [72] J. H. Schneibel, H. Rühle, M. Heilmaier, H. Saage, M. Goncharenko, and P. Loboda, "Low cycle fatigue of Fe<sub>3</sub>Al-based iron aluminide with and without Cr," *Intermetallics*, vol. 18, no. 7, pp. 1369–1374, 2010.
- [73] J. N. Taneja, "Dissolution of Iron in Hydrochloric Acid," University of Windsor, 1967.
- [74] B. H. Kim, H. Park, H. Park, and D. C. Moon, "Degree of imidization for polyimide films investigated by evolved gas analysis-mass spectrometry," *Thermochim. Acta*, vol. 551, pp. 184–190, 2013.
- [75] D. Pinson, R. P. Zou, a B. Yu, P. Zulli, and M. J. McCarthy, "Coordination number of binary mixture of spheres," *J. Phys. D. Appl. Phys.*, vol. 31, pp. 457–462, 1998.
- [76] I. Biazzo, F. Caltagirone, G. Parisi, and F. Zamponi, "Theory of amorphous packings of binary mixtures of hard spheres," *Phys. Rev. Lett.*, vol. 102, no. 19, pp. 1–4, 2009.
- [77] T. C. Hanson and G. S. Settles, "Particle Temperature and Velocity Effects on the Porosity and Oxidation of an HVOF Corrosion-Control Coating," *J. Therm. Spray Technol.*, vol. 12, no. 3, pp. 403–415, 2003.
- [78] J. T. Yao, J. Q. Ren, H. Bin Huo, G. J. Yang, C. X. Li, and C. J. Li, "Deposition behavior of semi-molten spray particles during flame spraying of porous metal alloy," *J. Therm. Spray Technol.*, vol. 23, no. 6, pp. 991–999, 2014.
- [79] P. Crook, "Corrosion of Nickel and Nickel-Base Alloys," in *Corrosion: Materials, Vol 13B, ASM Handbook, ASM International*, 2005, pp. 228–251.
- [80] C. Feng, S. Yugeswaran, and S. Chandra, "Capillary rise of liquids in thermally sprayed porous copper wicks," *Exp. Therm. Fluid Sci.*, vol. 98, no. October 2017, pp. 206–216, 2018.
- [81] P. Tallafuss and J. Johnston, "Defects , causes and prevention controls in the continuous bronze / steel bimetal strip sintering process," *Eng. Fail. Anal.*, vol. 92, no. December 2017, pp. 32–43, 2018.
- [82] F. Martin, C. García, and Y. Blanco, "Influence of residual porosity on the dry and lubricated sliding wear of a powder metallurgy austenitic stainless steel," *Wear*, vol. 328–329, pp. 1–7, 2015.
- [83] M. D. Pritzl, H. Tabatabai, and A. Ghorbanpoor, "Laboratory Evaluation of Select Methods of Corrosion Prevention in Reinforced Concrete Bridges," *Int. J. Concr. Struct. Mater.*, vol. 8, no. 3, pp. 201–212, 2014.

- [84] A. Kumar, J. Boy, R. Zatorski, and L. D. Stephenson, "Thermal spray and weld repair alloys for the repair of cavitation damage in turbines and pumps: A technical note," *J. Therm. Spray Technol.*, vol. 14, no. 2, pp. 177–182, 2005.
- [85] A. Candel and R. Gadow, "Optimized multiaxis robot kinematic for HVOF spray coatings on complex shaped substrates," *Surf. Coatings Technol.*, vol. 201, no. 5, pp. 2065–2071, 2006.
- [86] J. M. Guilemany, N. Espallargas, P. H. Suegama, and A. V. Benedetti, "Comparative study of Cr<sub>3</sub>C<sub>2</sub>-NiCr coatings obtained by HVOF and hard chromium coatings," *Corros. Sci.*, vol. 48, no. 10, pp. 2998–3013, 2006.
- [87] Y. Ishikawa *et al.*, "Evaluation of corrosion and wear resistance of hard cermet coatings sprayed by using an improved HVOF process," *J. Therm. Spray Technol.*, vol. 14, no. 3, pp. 384–390, 2005.
- [88] L. I. Stephens, S. C. Perry, S. M. Gateman, R. Lacasse, R. Schulz, and J. Mauzeroll, "Development of a Model for Experimental Data Treatment of Diffusion and Activation Limited Polarization Curves for Magnesium and Steel Alloys," *J. Electrochem. Soc.*, vol. 164, no. 11, pp. E3576–E3582, 2017.
- [89] N. Le Bozec, C. Compère, M. L'Her, a. Laouenan, D. Costa, and P. Marcus, "Influence of stainless steel surface treatment on the oxygen reduction reaction in seawater," *Corros. Sci.*, vol. 43, no. 4, pp. 765–786, 2001.
- [90] M. E. Orazem and B. Tribollet, "Electrochemistry," in *Electrochemical Impedance Spectroscopy*, 2008, pp. 73–96.
- [91] B. Conway, "Impedance Behavior of Electrochemical Supercapacitors and Porous Electrodes," in *Impedance Spectroscopy. Theory, Experiment and Applications*, 2005, pp. 469–470.
- [92] V. M.-W. Huang, V. Vivier, M. E. Orazem, N. Pébère, and B. Tribollet, "The Apparent Constant-Phase-Element Behavior of a Disk Electrode with Faradaic Reactions," *J. Electrochem. Soc.*, vol. 154, no. 2, p. C99, 2007.
- [93] T. J. Mesquita and R. P. Nogueira, "Relationship between the Origin of Constant-Phase Element Behavior in Electrochemical Impedance Spectroscopy and Electrode Surface Structure," 2015.
- [94] P. Córdoba-Torres, T. J. Mesquita, O. Devos, B. Tribollet, V. Roche, and R. P. Nogueira, "On the intrinsic coupling between constant-phase element parameters  $\alpha$  and  $Q$  in electrochemical impedance spectroscopy," *Electrochim. Acta*, vol. 72, pp. 172–178, 2012.
- [95] I. D. Raistrick, D. R. Franceschetti, and J. R. Macdonald, "Mass and charge transport in the presence of concentration gradients," in *Impedance Spectroscopy. Theory, Experiment and Applications*, 2005, pp. 54–58.
- [96] A. Lasia, "Impedance of the Faradaic Reactions in the Presence of Mass Transfer," in *Electrochemical Impedance Spectroscopy and its Applications*, 2014, pp. 85–138.
- [97] B. Conway, "Charge transfer at the electrode-electrolyte interface," in *Impedance Spectroscopy. Theory, Experiment and Applications*, 2005, pp. 68–72.
- [98] A. Bonnel, F. Dabosi, C. Deslouis, M. Duprat, M. Keddam, and B. Tribollet, "Corrosion Study of a Carbon Steel in Neutral Chloride Solutions by Impedance Techniques," *J. Electrochem. Soc.*, vol. 130, no. 4, pp. 753–761, 1983.
- [99] M. E. Orazem and B. Tribollet, "Preliminary graphical methods," in *Electrochemical*

- Impedance Spectroscopy*, 2008, pp. 332–342.
- [100] K. Spencer and M. X. Zhang, “Optimisation of stainless steel cold spray coatings using mixed particle size distributions,” *Surf. Coatings Technol.*, vol. 205, no. 21–22, pp. 5135–5140, 2011.
- [101] G. Y. Koga *et al.*, “Corrosion properties of Fe-Cr-Nb-B amorphous alloys and coatings,” *Surf. Coatings Technol.*, vol. 254, pp. 238–243, 2014.
- [102] R. Q. Guo, C. Zhang, Q. Chen, Y. Yang, N. Li, and L. Liu, “Study of structure and corrosion resistance of Fe-based amorphous coatings prepared by HVOF and HVOF,” *Corros. Sci.*, vol. 53, no. 7, pp. 2351–2356, Jul. 2011.
- [103] S. García-Rodríguez, a. J. López, B. Torres, and J. Rams, “316L stainless steel coatings on ZE41 magnesium alloy using HVOF thermal spray for corrosion protection,” *Surf. Coatings Technol.*, vol. 287, pp. 9–19, 2016.
- [104] P. H. Suegama, C. S. Fugivara, A. V. Benedetti, J. Fernández, J. Delgado, and J. M. Guilemany, “Electrochemical behavior of thermally sprayed stainless steel coatings in 3.4% NaCl solution,” *Corros. Sci.*, vol. 47, no. 3, pp. 605–620, 2005.
- [105] C. Zhang, K. C. Chan, Y. Wu, and L. Liu, “Pitting initiation in Fe-based amorphous coatings,” *Acta Mater.*, vol. 60, no. 10, pp. 4152–4159, Jun. 2012.
- [106] J. Wu, S. D. Zhang, W. H. Sun, Y. Gao, and J. Q. Wang, “Enhanced corrosion resistance in Fe-based amorphous coatings through eliminating Cr-depleted zones,” *Corros. Sci.*, vol. 136, no. October 2016, pp. 161–173, 2018.
- [107] S. Kuroda, M. Watanabe, K. Kim, and H. Katanoda, “Current Status and Future Prospects of Warm Spray Technology,” *J. Therm. Spray Technol.*, vol. 20, no. 4, pp. 653–676, 2011.
- [108] A. Dolatabadi, J. Mostaghimi, and V. Pershin, “Effect of a cylindrical shroud on particle conditions in high velocity oxy-fuel spray process,” *Sci. Technol. Adv. Mater.*, vol. 3, pp. 245–255, 2002.
- [109] Z. Zeng, N. Sakoda, T. Tajiri, and S. Kuroda, “Structure and corrosion behavior of 316L stainless steel coatings formed by HVOF spraying with and without sealing,” *Surf. Coatings Technol.*, vol. 203, no. 3–4, pp. 284–290, Nov. 2008.
- [110] S. D. Zhang, J. Wu, W. B. Qi, and J. Q. Wang, “Effect of porosity defects on the long-term corrosion behaviour of Fe-based amorphous alloy coated mild steel,” *Corros. Sci.*, vol. 110, pp. 57–70, 2016.
- [111] M. M. Verdian, K. Raeissi, and M. Salehi, “Corrosion performance of HVOF and APS thermally sprayed NiTi intermetallic coatings in 3.5% NaCl solution,” *Corros. Sci.*, vol. 52, no. 3, pp. 1052–1059, 2010.
- [112] A. Lasia, “Impedance of Porous Electrodes,” in *Electrochemical Impedance Spectroscopy*, 2014, pp. 203–250.
- [113] L. Chen, “Ni-Al Powder Electrocatalyst for Hydrogen Evolution,” *J. Electrochem. Soc.*, vol. 140, no. 9, p. 2464, 1993.
- [114] C. Hitz and A. Lasia, “Experimental study and modeling of impedance of the her on porous Ni electrodes,” *J. Electroanal. Chem.*, vol. 500, no. 1–2, pp. 213–222, 2001.
- [115] A. Vackel, G. Dwivedi, and S. Sampath, “Structurally Integrated, Damage-Tolerant, Thermal Spray Coatings,” *Jom*, vol. 67, no. 7, pp. 1540–1553, 2015.

- [116] J. Kawakita and S. Kuroda, "Oscillational corrosion potential of HastelloyC coatings fabricated by GS-HVOF spraying," *Corros. Sci.*, vol. 47, no. 8, pp. 2053–2062, Aug. 2005.
- [117] J. M. Guilemany, J. Fernández, N. Espallargas, P. H. Suegama, and A. V. Benedetti, "Influence of spraying parameters on the electrochemical behaviour of HVOF thermally sprayed stainless steel coatings in 3.4% NaCl," *Surf. Coatings Technol.*, vol. 200, no. 9, pp. 3064–3072, 2006.
- [118] E. Sadeghimeresht, N. Markocsan, and P. Nylén, "Microstructural characteristics and corrosion behavior of HVOF- and HVOF-sprayed Fe-based coatings," *Surf. Coatings Technol.*, vol. 318, pp. 365–373, 2017.
- [119] G. Bolelli, L. Lusvarghi, and M. Barletta, "Heat treatment effects on the corrosion resistance of some HVOF-sprayed metal alloy coatings," *Surf. Coatings Technol.*, 2008.
- [120] A. Milanti, V. Matikainen, H. Koivuluoto, G. Bolelli, L. Lusvarghi, and P. Vuoristo, "Effect of spraying parameters on the microstructural and corrosion properties of HVOF-sprayed Fe–Cr–Ni–B–C coatings," *Surf. Coatings Technol.*, vol. 277, pp. 81–90, 2015.
- [121] B. Tribollet and M. E. Orazem, "Kinetic Models," in *Electrochemical Impedance Spectroscopy*, 2008, pp. 163–181.
- [122] G. Mauer, R. Vaßen, and D. Stöver, "Comparison and applications of DPV-2000 and accuraspray-g3 diagnostic systems," *J. Therm. Spray Technol.*, vol. 16, no. 3, pp. 414–424, 2007.
- [123] S. Marcelin, N. Pébère, and S. Régnier, "Electrochemical characterisation of a martensitic stainless steel in a neutral chloride solution," *Electrochim. Acta*, vol. 87, pp. 32–40, 2013.
- [124] F. Velasco, a. Bautista, and a. González-Centeno, "High-temperature oxidation and aqueous corrosion performance of ferritic, vacuum-sintered stainless steels prealloyed with Si," *Corros. Sci.*, vol. 51, no. 1, pp. 21–27, 2009.
- [125] A. Bautista, A. Gonzalez-Centeno, G. Blanco, and S. Guzman, "Application of EIS to the study of corrosion behaviour of sintered ferritic stainless steels before and after high-temperature exposure," *Mater. Charact.*, vol. 59, no. 1, pp. 32–39, 2008.
- [126] C. C. Silva, J. P. Farias, H. C. Miranda, R. F. Guimarães, J. W. A. Menezes, and M. A. M. Neto, "Microstructural characterization of the HAZ in AISI 444 ferritic stainless steel welds," *Mater. Charact.*, vol. 59, no. 5, pp. 528–533, 2008.
- [127] T. Juuti, L. Rovatti, a. Mäkelä, L. P. Karjalainen, and D. Porter, "Influence of long heat treatments on the laves phase nucleation in a type 444 ferritic stainless steel," *J. Alloys Compd.*, vol. 616, pp. 250–256, 2014.
- [128] R. K. Kent and R. Baggerly, "Intergranular Corrosion of Stainless Steels," in *Failure Analysis and Prevention, Vol 11, ASM Handbook*, 2002, pp. 761–795.
- [129] S. M. Gateman, L. I. Stephens, S. C. Perry, R. Lacasse, R. Schulz, and J. Mauzeroll, "The role of titanium in the initiation of localized corrosion of stainless steel 444," *npj Mater. Degrad.*, vol. 2, no. 1, p. 5, 2018.
- [130] N. H. Pryds and A. S. Pedersen, "Rapid solidification of martensitic stainless steel atomized droplets," *Metall. Mater. Trans. A Phys. Metall. Mater. Sci.*, vol. 33, no. 12, pp. 3755–3761, 2002.
- [131] S. Pandya, K. S. Ramakrishna, A. Raja Annamalai, and A. Upadhyaya, "Effect of sintering temperature on the mechanical and electrochemical properties of austenitic stainless steel," *Mater. Sci. Eng. A*, vol. 556, pp. 271–277, 2012.

- [132] N. Ahmed, M. S. Bakare, D. G. McCartney, and K. T. Voisey, "The effects of microstructural features on the performance gap in corrosion resistance between bulk and HVOF sprayed Inconel 625," *Surf. Coatings Technol.*, vol. 204, no. 14, pp. 2294–2301, Apr. 2010.
- [133] C. O. a Olsson and D. Landolt, "Passive films on stainless steels - Chemistry, structure and growth," *Electrochim. Acta*, vol. 48, no. 9 SPEC., pp. 1093–1104, 2003.
- [134] T. Hong, T. Ogushi, and M. Nagumo, "The effect of chromium enrichment in the film formed by surface treatments on the corrosion resistance of type 430 stainless steel," *Corros. Sci.*, vol. 38, no. 6, pp. 881–888, 1996.
- [135] J. B. Jorcin, M. E. Orazem, N. Pébère, and B. Tribollet, "CPE analysis by local electrochemical impedance spectroscopy," *Electrochim. Acta*, vol. 51, no. 8–9, pp. 1473–1479, 2006.
- [136] D. B. . Miracle and S. L. Donaldson, "Bismaleimide Resins," in *ASM Handbook, Volume 21: Composites*, 2001, pp. 97–104.
- [137] M. Keddam, O. R. Mattos, and H. Takenout, "Reaction Model for Iron Dissolution Studied by Electrode Impedance. II," *J. Electrochem. Soc.*, vol. 128, no. 2, pp. 266–274, 1981.
- [138] I. Epelboin, M. Keddam, O. R. Mattos, and H. Takenouti, "The dissolution and passivation of Fe and Fe-Cr alloys in acidified sulphate medium: Influences of pH and Cr content," *Corros. Sci.*, vol. 19, no. 7, pp. 1105–1112, 1979.
- [139] M. Keddam, O. R. Mattor, and H. Takenouti, "Mechanism of Anodic Dissolution of Iron-Chromium Alloys Investigated by Electrode Impedances. II. Elaboration of the Reaction Model," *Electrochim. Acta.*, vol. 31, no. 9, pp. 1159–1165, 1986.
- [140] L. I. Stephens, S. C. Perry, S. M. Gateman, R. ober. Lacasse, R. ober. Schulz, and J. Mauzeroll, "Development of a Model for Experimental Data Treatment of Diffusion and Activation Limited Polarization Curves for Magnesium and Steel Alloys," *J. Electrochem. Soc.*, vol. 164, no. 11, pp. E3576–E3582, 2017.

## Appendix A – Processing of Polyimide Composites

### Introduction

In this work, polyimide discs were produced from the VTEC™ PI 1031 powder purchased from Richard Blaine Inc. (Reading, PA 19602 USA). The only information available on the composition of VTEC's PI 1031 powder is that it is a thermosetting bismaleimide (BMI) resin. Synthesis of BMIs involves the chemical dehydration of N,N'-arylene bismaleamic acid (Figure 48). The BMI monomers usually make up to 50 to 75 wt.% of the resin. The remaining fraction corresponds to aromatic co-monomers (CO-M), reactive diluents, processing additives, elastomers and catalysts. Each formulation is combined differently to enable their use as highly concentrated solutions, powders or hot melts. BMIs are known to retain outstanding high-temperature mechanical properties, which allowed their use in formula 1 vehicles as well as on super jet-fighters like the F-22 [136].

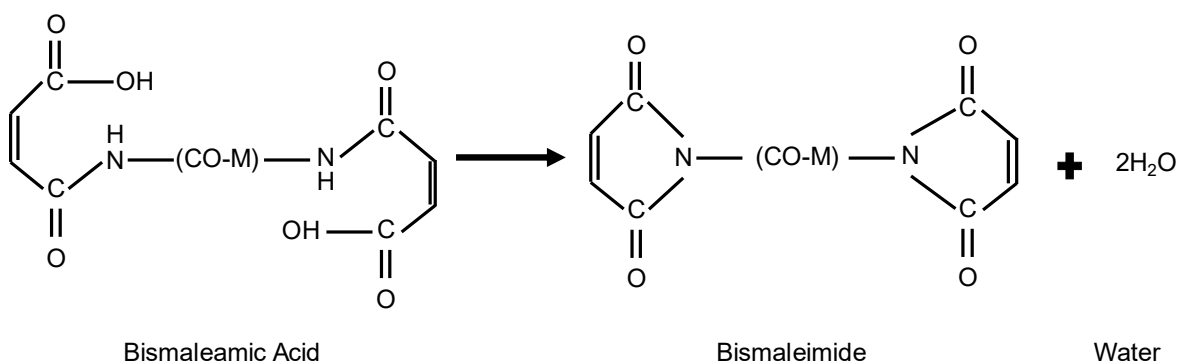


Figure 48 - Synthesis of BMI by chemical dehydration of bismaleamic acid. The symbol (CO-M) represents an aromatic co-monomer [136].

As presented in the second manuscript (section 2.3), a BMI + 25 wt.% graphite composite was infiltrated in porous stainless steel coatings. The methodology for the development of this multi-layer coating is presented in this appendix A, along with preliminary assessments of BMI composite tribological performance.

### Materials and Methods

VTEC's PI 1031 powder was mixed with two solid lubricant additives: 5-8  $\mu\text{m}$  average diameter PTFE (NanoFLON 160N Shamrock Inc) particles and 5  $\mu\text{m}$  average diameter graphite (micro450 Asbury Inc). Three different formulations were prepared: pure PI, PI + 15wt.% Graphite (PI+Gr) and PI + 15wt.% Graphite + 10wt.%PTFE (PI+Gr+PTFE). The mixing was done by using a planetary ball milling. A maximum of 25 grams of PI and lubricant particles were put in a carbon steel vessel with 3 C-steel balls (10 mm diameter). Milling was carried out at 100 RPM for 1 hour.

Three different preparation methods were investigated. In the manual preparation, the powder mixture was transferred to a mold (Figure 49) on top of a hot plate at 150 °C by using a spoon. It was observed that the pure PI powder melts at approximately 130 °C and quickly starts to polymerize, which drastically increases the material's viscosity, reaching a jellified state in a few seconds. As each laid powder bed melted, more of the powder mixture was transferred to the hot plate. The procedure was repeated for approximately 1 hour, until the mold was full. The mold and PI were then transferred to a stove at 240 °C where the PI mixture cured for 1 hour.

Due to the potential use of the PI composites in self-lubricated bearings, ball-on-disk tests were carried out at dry atmospheric pressure, with two different normal loads (5 kgf and 7 kgf) and two sliding velocities (86 mm/s and 114 mm/s). Only the samples produced by the manual method were evaluated.

Hot pressing was used to produce PI composites in two different ways. In *hot pressing I*, the powder mix is laid in the mold at room temperature. The mold is then assembled (Figure 49) between two sheets of PTFE, to prevent PI from sticking to the press, and two aluminum plates which help the heat transfer between the press and the mold. The process consisted in heating the platen to 132 °C at a pressure 22 kPa (0.5 ton) for 1 hour, during which the melting and jelling of the resin takes place. The temperature is then increased to 235 °C and the pressure to 66 kPa (1.5 ton) when the curing takes place for another hour. Finally, the system can cool down to room temperature.

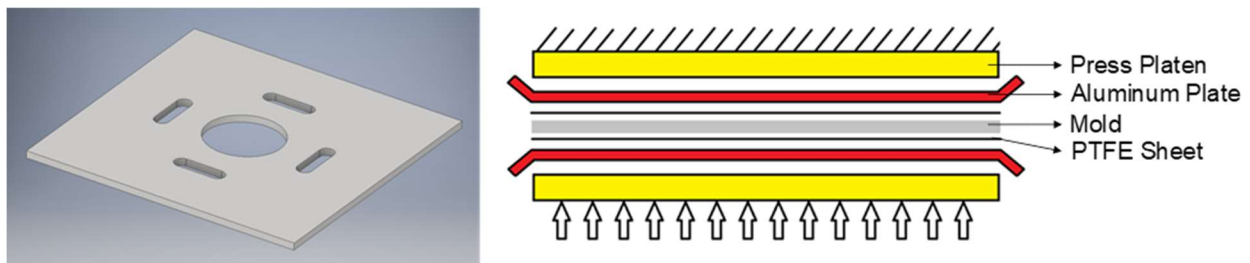


Figure 49 - 3D model of the mold used to produce PI composites in manual preparation and hot pressing I methods.

In *hot pressing II* method, a different mold (Figure 50) is used, allowing one to transfer the load to the PI powder mixture more effectively. In this method, the powder mix was compacted in the mold at room temperature at a pressure of 247 kPa (0.5 ton). The mold was then transferred without the lid into the oven at 132 °C for 1 hour, for melting and jelling. Subsequently, the oven temperature was increased to 180 °C for 60 minutes, so that the mixture achieves enough strength for the following step, which consisted in placing the mold (with lid) back in to the press,

which was then heated to 200 °C at a pressure of 247 kPa (0.5 ton). After another hour, the system was air cooled to room temperature.

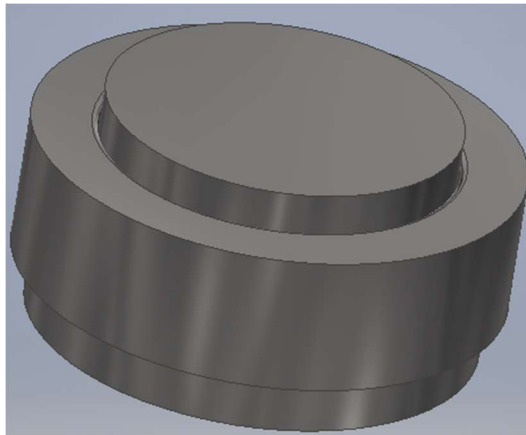


Figure 50 - 3D model of the mold used to produce PI composites in hot pressing II method.

## Results

### Manual Preparation

The main problem noticed in PI discs produced with the manual preparation method was porosity. As illustrated in Figure 51, all formulations showed a significant amount of porosity throughout the materials cross section.

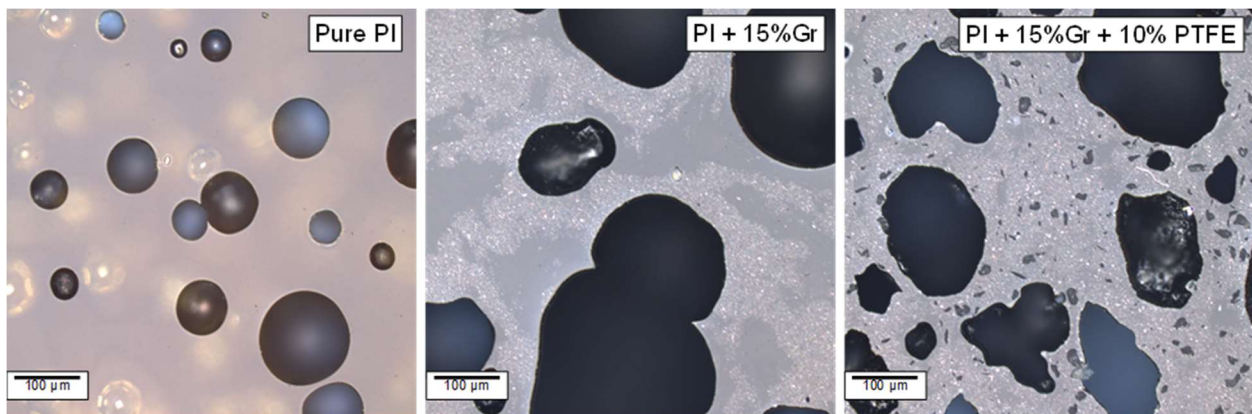


Figure 51 - Porosity present in the cross section of PI discs prepared by the manual method.

One may argue that the pores in the PI discs originate from gases formed during BMI polymerization. It was possible to confirm this assumption by melting pure PI resin in vacuum. As illustrated in Figure 52, in a time span of 30 minutes several bubbles form and coalesced but, due to the high surface tension of the BMI resin, the gases are not able to escape.

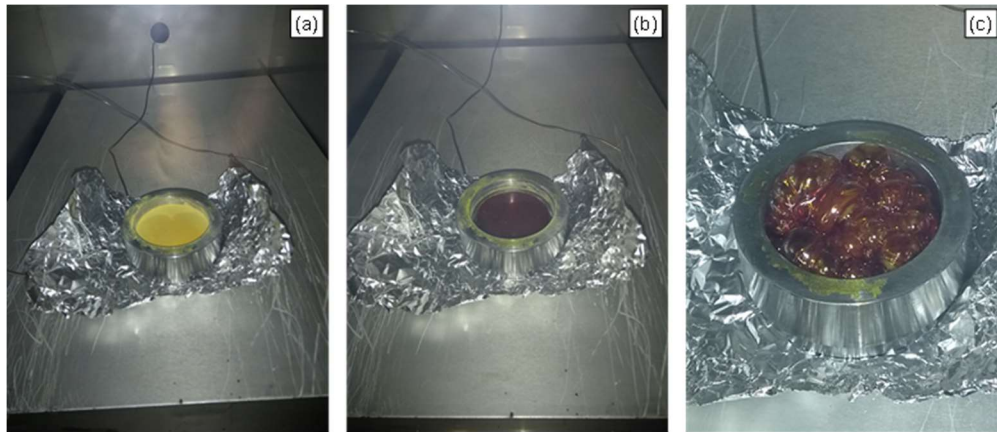


Figure 52 - Formation of gases during PI polymerization at 132 C in vacuum. (a) Pre-compacted pure PI powder. (b) As-molten PI. (c) Formation and coalescing of gas bubbles. The time span between (b) and (c) is approximately 30 minutes.

Table 14 summarizes the ball-on-disk test results. It may be argued that due to excessive porosity, the wear rate of the PI discs produced in this work was one order of magnitude higher than that of similar PI composites reported in [58]. Another important remark concerns the effect of the PI formulation: the use of 15 wt.% graphite promotes a reduction of the friction coefficient and wear rates. On the other hand, further addition of PTFE decreases the friction while increasing the wear rate in two orders of magnitude. The effect may be caused by the decreased fraction of BMI resin that provides the load bearing capacity and/or by the inherent lower wear resistance of PTFE.

Table 14 - Summary of the ball-on-disk test results performed on PI discs produced manually.

			Present Work		Reference [58]	
Material	Load	Velocity	COF	Wear Rate	COF	Wear Rate
	Kg	mm/s	-	mm <sup>3</sup> .N <sup>-1</sup> .m <sup>-1</sup>	-	mm <sup>3</sup> .N <sup>-1</sup> .m <sup>-1</sup>
Pure PI	5	86	0.58	2.25E-04	0.4	2.0E-05
	7	114	0.51	1.69E-04		
PI + Gr	5	86	0.29	2.96E-05	0.35	2.0E-06
	7	114	0.27	3.87E-05		
PI+Gr+PTFE	5	86	0.13	2.91E-03	-	-
	7	114	0.12	7.52E-03		

Another important observation in the manual preparation of samples was that the BMI can penetrate the pores in the stainless steel coatings by capillarity, as illustrated in Figure 53.

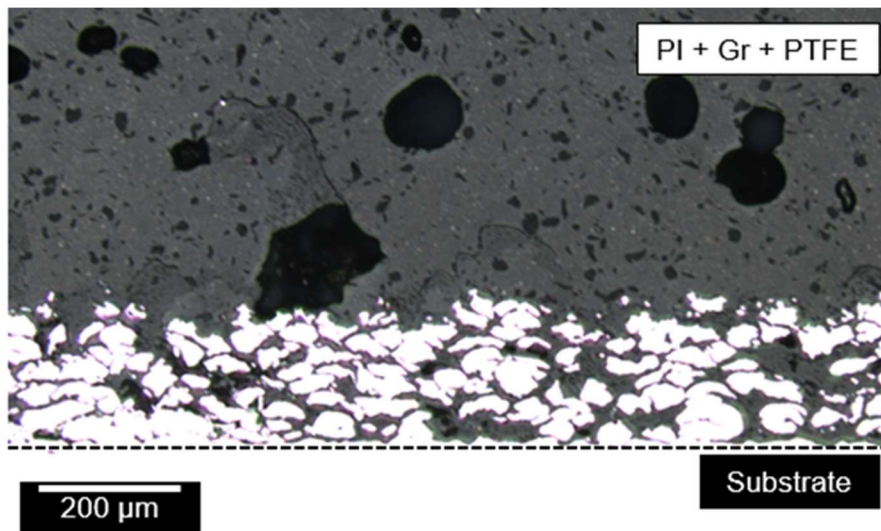


Figure 53 - The BMI resin can penetrate the narrow pores of the stainless steel coating by capillarity.

#### *Hot Pressing I*

Several issues were noticed during the hot pressing I method. Firstly, the mold was designed to the same dimensions of the press platens ( $150 \times 150 \text{ mm}^2$ ), which affects the amount of pressure that one may exert on the center disc where the powder rests.

Another problem occurs during the PI infiltration in the porous coatings, which were cut to small discs of 16 mm diameter and placed inside the mold along with the powder. The presence of the stainless steel substrates in the hot pressing I assembly changes the heat transfer dynamics, which affects the BMI polymerization rates and ultimately, the PI composite porosity. While in some instances relatively dense PI layers were produced on the porous coatings, in other cases the porosity persisted, as illustrated in Figure 54.

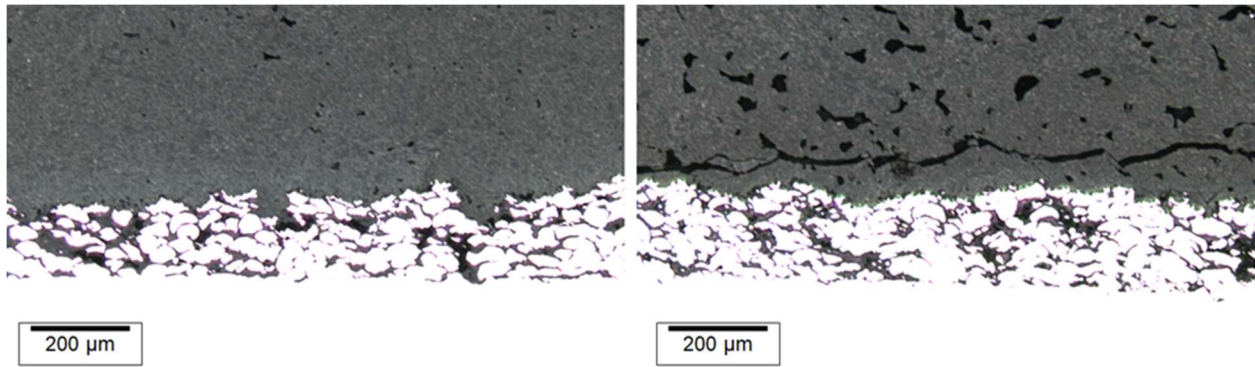


Figure 54 - Two examples of PI+Gr-infiltrated coatings produced with method hot pressing I. The different results are attributed to poor control of pressure and heat transfer from the platens to the PI composite.

To further illustrate the effect of heat transfer rates on the PI properties, one may refer to Figure 55, where two pure PI discs produced with the same amount of powder are compared. The disc on the right was produced in the mold (Figure 52) without the lid, while the one on the left had the lid on, with which the heat transfer to the powder is increased.



Figure 55 - The heat transfer rates have a drastic effect on the polymerization of the BMI. Both discs were produced with the same quantity of PI powder. The PI disc on the left was produced in contact with a stainless steel lid, which increased the heat transfer from the furnace to the powder bed.

### Hot Pressing II

The optimal approach found to produce dense PI discs requires a controlled heat transfer to the powder, allowing the BMI to polymerize slowly, so that the volatiles do not create significant porosity. Additionally, the PI composite must achieve appreciable strength and toughness during melting. If the PI jell is too “fluid”, the pressure of 247 kPa can force the material through the gaps outside of the mold. If the PI becomes too stiff, it will crack during the hot pressing.

In Figure 56, three bulk PI disc sections are illustrated. One may notice that the pure PI disc produced with the method hot pressing II is nearly free of pores while the one produced with graphite (PI+Gr(a)) still showed some pores, while much smaller than those produced with the manual method. By decreasing the curing time in the oven from 60 to 30 minutes, it was possible

to produce (after pressing) a dense PI+Gr(b) disc. However, part of the material was still very fluid and was forced outside of the mold during the pressing, resulting in a thinner sample.

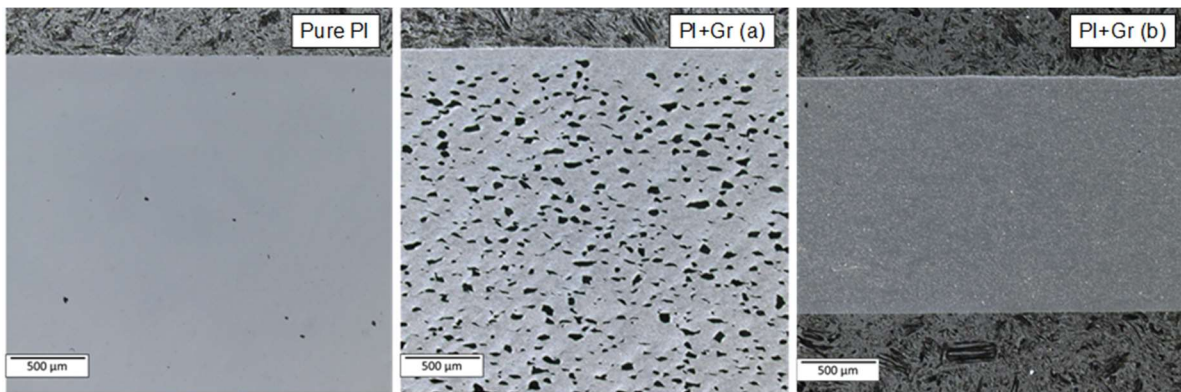


*Figure 56 - Bulk PI sections produced with method hot pressing II.*

The results suggest that the elimination of porosity requires pressure to collapse the pores and enough temperature to eliminate the interfaces by sintering. Optimal temperatures and pressures vary depending on the composition of the powder mix.

## Appendix B – Supplementary Material: Corrosion of Thermally Sprayed Stainless Steel Coatings

### Arc Melting

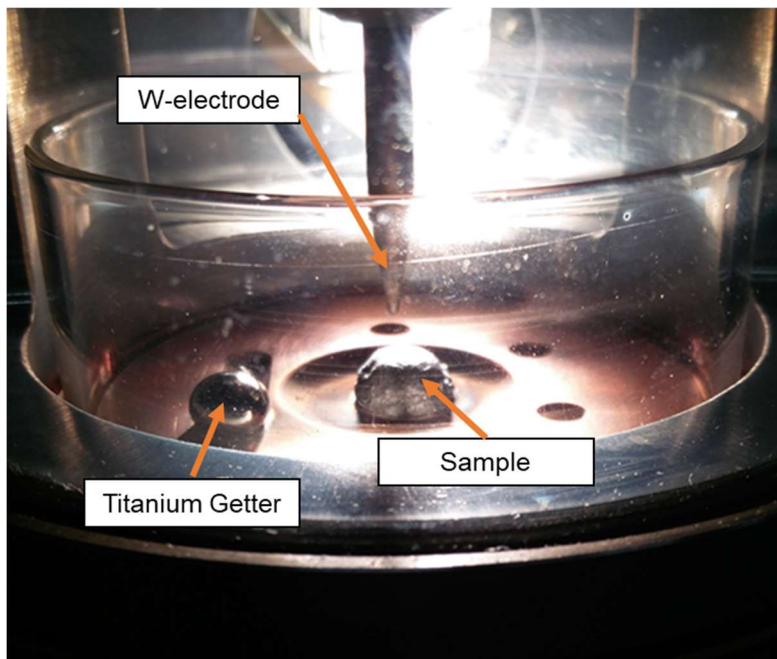


Figure 57 - Arc melt furnace chamber containing a water-cooled Cu substrate, a titanium oxygen getter and a tungsten electrode.

### Effect of Electrode Potential on EIS Spectra

The response of an electrode to potential perturbations  $\tilde{V}$  at a given range of potentials may provide insights about the nature of the reactions occurring at the interface. This type of investigation has been used to propose reaction mechanisms governing iron dissolution in neutral chloride solutions [137] as well as the passivation of several Fe-Cr alloys [138], [139]. While determining the reaction mechanism is not in the scope of the present work, the methodology developed in [121] allows one to establish relationships between the linear polarization and the electrochemical impedance of an electrode.

Let there be an aqueous electrochemical interface where the established potential and pH are well within the active domain of a metal, i.e. the surface atoms spontaneously dissolve into the solution. A single pair of anodic and cathodic reactions is operant, and both obey Tafel's kinetic rule. No corrosion products are formed on the electrode surface and mass transfer does not limit the reaction rates. Under these assumptions, the faradaic currents depend only on the electrode potential. The charge transfer resistances of each reaction are  $R_{t,a} = \tilde{V}/\tilde{i}_a$  and  $R_{t,c} = \tilde{V}/\tilde{i}_c$ ,

where  $\tilde{i}_a$  and  $\tilde{i}_c$  are respectively, the anodic and cathodic current responses to the potential perturbation  $\tilde{V}$ . In kinetic terms,  $R_{t,a} = [i_{corr} b_a \exp(b_a \eta)]^{-1}$  and  $R_{t,c} = [i_{corr} b_c \exp(-b_c \eta)]^{-1}$  where  $\beta_a = 1/b_a$  and  $\beta_c = 1/b_c$  are the anodic and cathodic slopes in volts per decade,  $i_{corr}$  is the corrosion current density and  $\eta$  is the applied overpotential (absolute voltage shift from the open circuit potential). As the anodic and cathodic reactions must occur concomitantly, the total charge transfer resistance  $R_{ct}$  can be described by the equation  $\frac{1}{R_{ct}} = \frac{1}{R_{ct,a}} + \frac{1}{R_{ct,c}}$  which has a maximum value depending on the Tafel slopes and on the overpotential. If  $\beta_a = |\beta_c|$ ,  $R_{ct}$  is maximum at the OCP. However, if  $\beta_a \neq |\beta_c|$ , the maximum  $R_{ct}$  is shifted in the direction of the higher absolute Tafel slope value as illustrated in Figure 58 for a case where  $\beta_a \ll |\beta_c|$ .

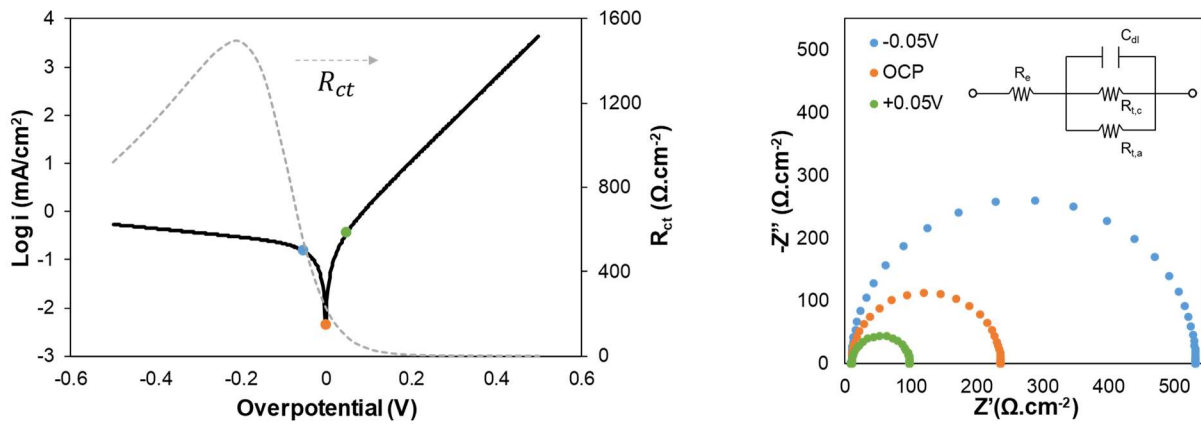


Figure 58 - Application of a simple kinetic model to describe the effect of an applied potential to the impedance spectra of a hypothetical interface with  $i_{corr} = 1 \times 10^{-4} \text{ A.cm}^{-2}$ ,  $\beta_a = 0.05 \text{ V.dec}^{-1}$ ,  $|\beta_c| = 0.5 \text{ V.dec}^{-1}$ , electrolyte resistance  $R_e = 10 \text{ } \Omega \cdot \text{cm}^{-2}$  and double-layer capacitance  $C_{dl} = 20 \text{ } \mu\text{F.cm}^{-2}$ . Notice that each loop in the complex plot corresponds to a potential value highlighted in the polarization curve.

The presence of pores in thermal sprayed coatings suggests the possibility of corrosion reactions to occur inside such voids, requiring mass transfer of reacting species in and out of the enclosed space. If a linear concentration gradient across the electrochemical interface is formed, it may be shown [121] that the charge transfer resistance of a mass-transfer limited reaction to be  $R_{mt} = [i_{corr} \cdot \bar{c} \cdot b_{mt} \cdot \exp(-b_{mt} \eta)]^{-1}$ . Notice that  $R_{mt}$  only distinguishes from  $R_{t,c}$  by the average concentration at the interface  $\bar{c}$ . The effects of activation (electrode potential) and mass transfer are coupled and the effect of the electrode potential on EIS spectra would be qualitatively like a system controlled only by activation. Even if the relative contributions of activation and mass transfer were decoupled, that would not prove that the reactions are occurring solely inside pores. Corrosion in wrought metals such as magnesium alloys are also limited by mass transfer through a partially protective film [140].

Depending on total porosity and pore geometry, the ohmic drop inside pores may be such that, for a given frequency range, the EIS spectra does not depend on the electrode potential. This phenomenon has been theoretically and experimentally addressed by Andrzej Lasia [112]. It was shown that the spectra of porous Ni electrodes [113], [114] immersed in 1M NaOH display two capacitive loops. By changing the electrode potential in a range of 180 mV, the low frequency loop diameter was significantly affected and hence associated with the faradaic (potential-dependent) hydrogen reduction reaction. In contrast, the high-frequency loop was not affected by the electrode potential and was associated with the geometric potential drop inside the pores. If such effect was observed in stainless steel coatings produced by spray, it would constitute a definitive proof that the electrode reactions are influenced by porosity.

### HVAF #1 Electrode

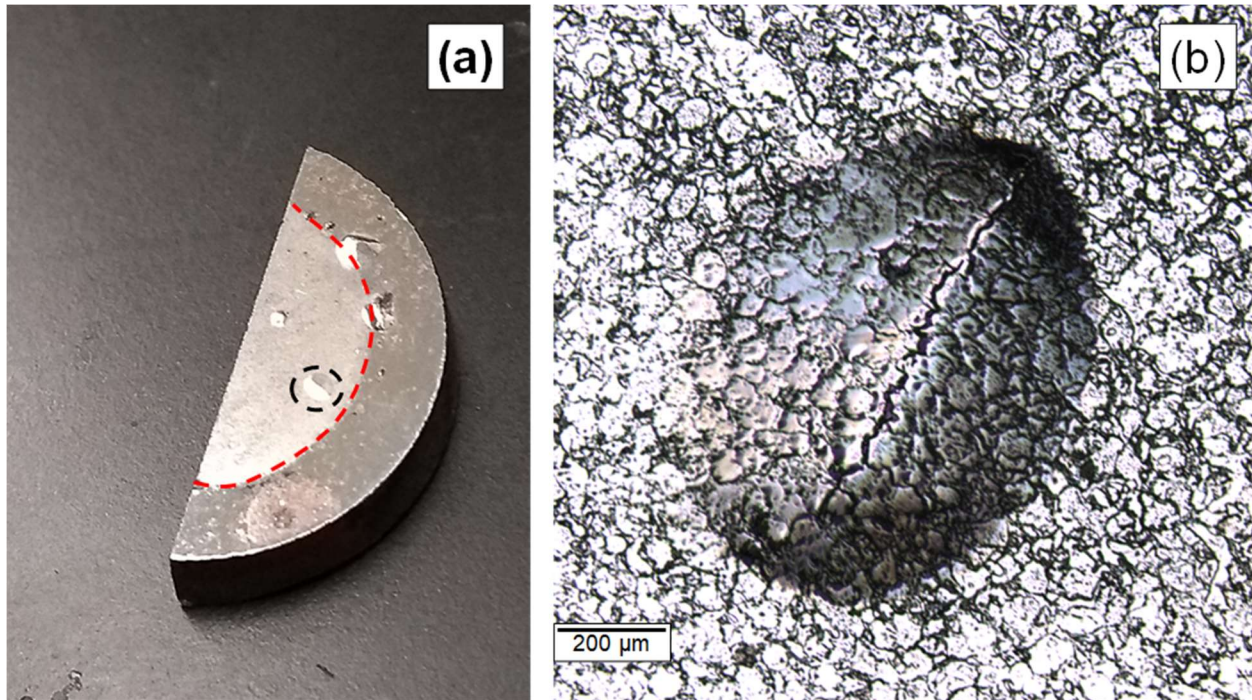
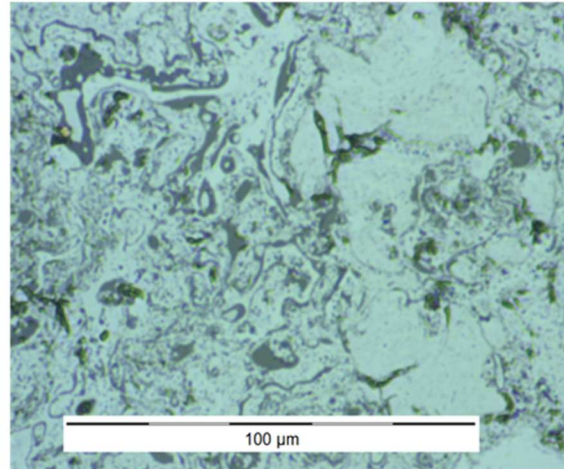
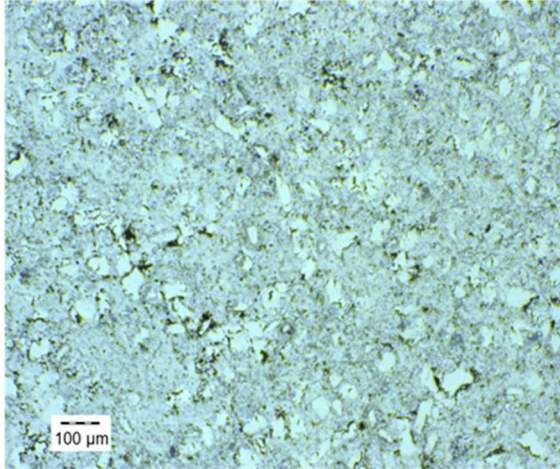


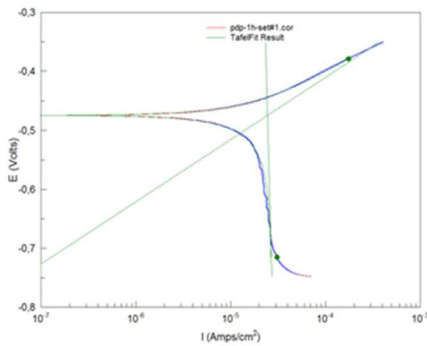
Figure 59 - (a) Sectioned coating HVAF #1 after the 3-week test period. The dashed red line separates the center exposed to the electrochemical tests, and the outer area, covered by the sample holder's O-ring. The dashed black circle highlights a blister which is magnified in (b) by means of a confocal microscope.

In the following section, the reader may find the polarization curves and impedance spectra of the stainless steel coatings produced by HVOF and HVAF. The summary includes the fitting curves used to determine important parameters such as the cathodic and anodic slopes, as well as the charge transfer resistances and constant-phase parameters  $Q$  and  $\alpha$ .

**Electrode Surface State**



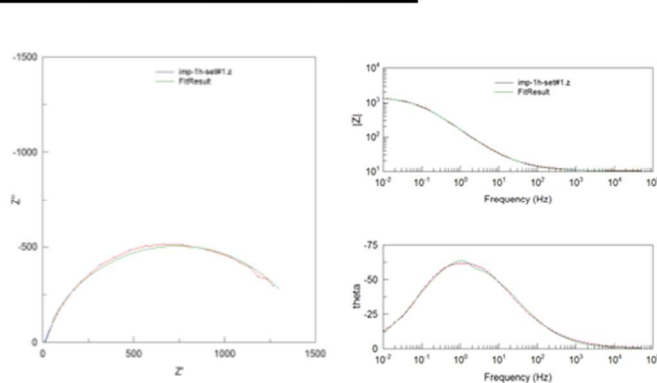
**Electrochemical Behavior**



**Polarization Curve Data**

Fit Quality ( $\chi^2$ )	8.098
$E_{corr}$ (V vs Ag/AgCl)	-0.47
$i_{corr}$ (A/cm <sup>2</sup> )	2.45E-05
Vmin (V vs Ag/AgCl)	-0.71
Vmax (V vs Ag/AgCl)	-0.37
$\beta_a$ (V)	105.59
$ba$ (V <sup>-1</sup> )	2.18E-02
$\beta_c$ (V)	6070.9
$bc$ (V <sup>-1</sup> )	3.79E-04
$R_p$ ( $\Omega \cdot \text{cm}^{-2}$ )	1675.6

**Impedance Spectroscopy**

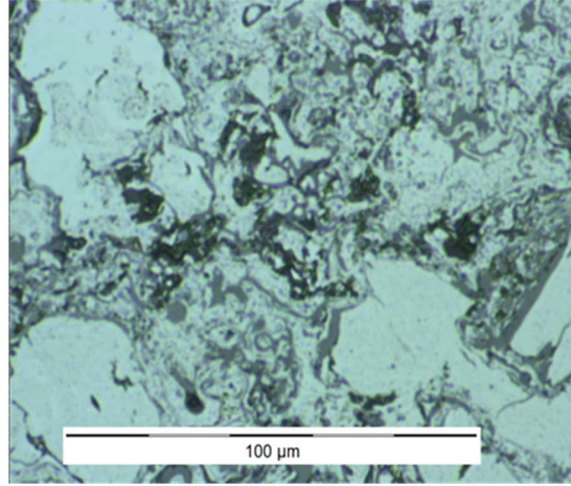
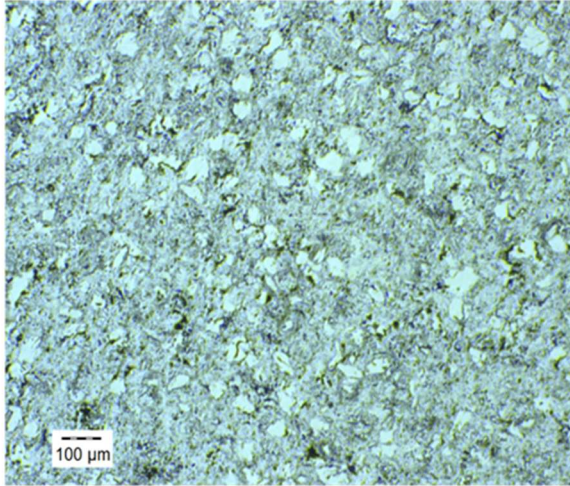


	Value	Error (%)
DC (V)	-0.492	-
$R_e$ $\Omega \cdot \text{cm}^{-2}$	10.59	0.41853
$R_{pore}$ $\Omega \cdot \text{cm}^{-2}$	24.97	44.906
W-R $\Omega \cdot \text{cm}^{-2}$	1459	1.4651
W-t (s)	0.45489	6.313
W-p -	0.68951	2.0136
CPE-C $F s^{-(1-\alpha)}$	0.0013318	0.91756
CPE- $\alpha$ -	0.74374	0.63575
Fit ( $\chi^2$ )	0.0019324	

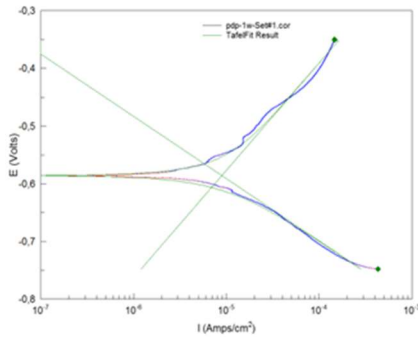
HVOF Spray Set # 1  
Immersion Time 1 Week

Date 08/Aug/2018

**Electrode Surface State**



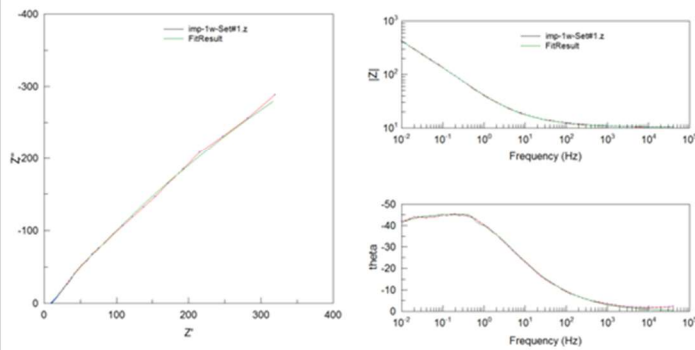
**Electrochemical Behavior**



**Polarization Curve Data**

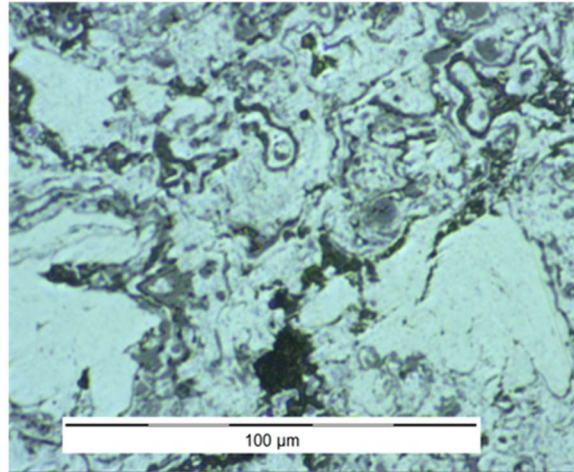
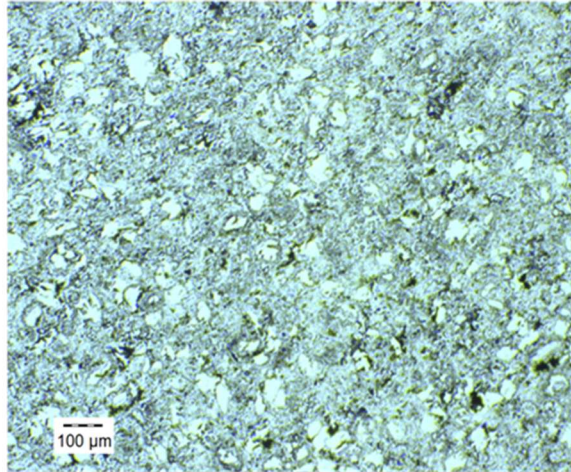
<b>Fit Quality (<math>\chi^2</math>)</b>	46.26
<b><math>E_{corr}</math> (V vs Ag/AgCl)</b>	-0.59
<b><math>i_{corr}</math> (A/cm<sup>2</sup>)</b>	8.90E-06
<b>Vmin (V vs Ag/AgCl)</b>	-0.75
<b>Vmax (V vs Ag/AgCl)</b>	-0.35
<b><math>\beta_a</math> (V)</b>	186.2
<b><math>\beta_c</math> (V)</b>	107.99
<b><math>bc</math> (V<sup>-1</sup>)</b>	2.13E-02
<b><math>R_p</math> (<math>\Omega \cdot \text{cm}^2</math>)</b>	2605

**Impedance Spectroscopy**

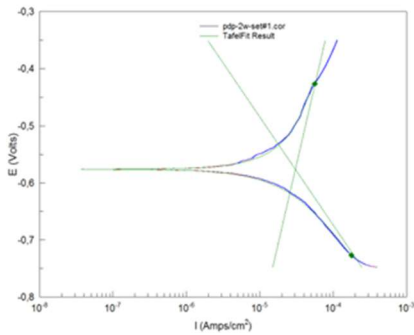


	Value	Error (%)
<b>DC (V)</b>	-0.478	-
<b><math>R_e</math> <math>\Omega \cdot \text{cm}^2</math></b>	10.4	0.1847
<b><math>R_{ct}</math> <math>\Omega \cdot \text{cm}^2</math></b>	50.01	15.998
<b>W-R <math>\Omega \cdot \text{cm}^2</math></b>	2315	4.0168
<b>W-t (s)</b>	1.167	5.069
<b>W-p -</b>	0.80396	2.1458
<b>CPE-C <math>F s^{-(1-\alpha)}</math></b>	0.0098358	0.31353
<b>CPE-<math>\alpha</math> -</b>	0.5564	0.24817
<b>Fit (<math>\chi^2</math>)</b>	0.00048966	

**Electrode Surface State**



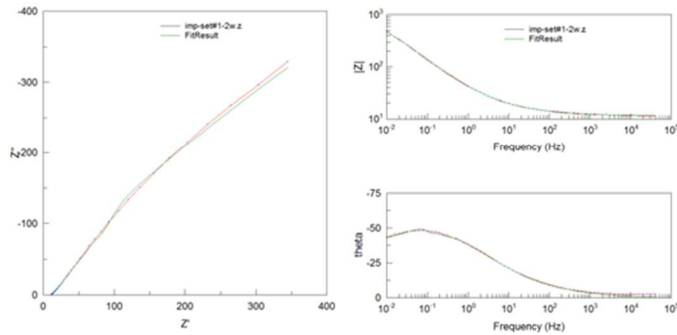
**Electrochemical Behavior**



**Polarization Curve Data**

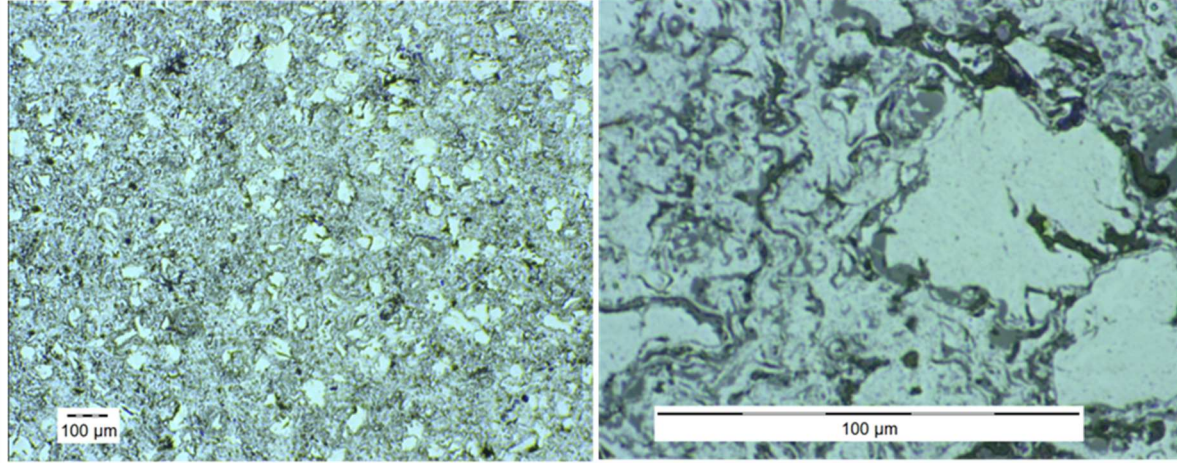
Fit Quality ( $\chi^2$ )	12.632
$E_{corr}$ (V vs Ag/AgCl)	-0.576
$i_{corr}$ (A/cm <sup>2</sup> )	3.05E-05
Vmin (V vs Ag/AgCl)	-0.73
Vmax (V vs Ag/AgCl)	-0.43
$\beta_a$ (V)	555.56
$\beta_c$ (V <sup>-1</sup> )	4.15E-03
$\beta_c$ (V)	189.2
$\beta_c$ (V <sup>-1</sup> )	1.22E-02
$R_p$ ( $\Omega \cdot \text{cm}^2$ )	1944

**Impedance Spectroscopy**

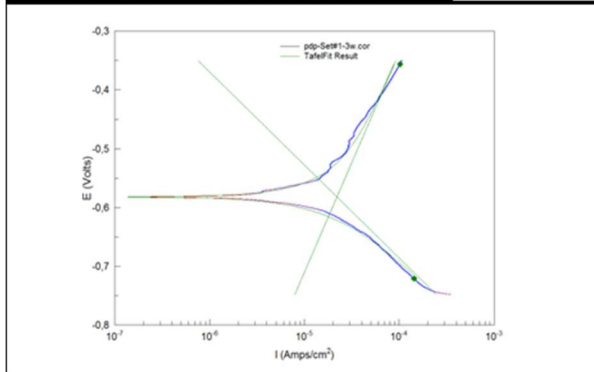


	Value	Error (%)
DC (V)	-0.4591	-
$R_e$ $\Omega \cdot \text{cm}^2$	11.58	0.30918
$R_{ct}$ $\Omega \cdot \text{cm}^2$	34.91	15.359
W-R $\Omega \cdot \text{cm}^2$	3329	9.9084
W-t (s)	8.282	5.5936
W-p -	0.74216	2.8033
CPE-C $F s^{-(1-\alpha)}$	0.0087531	1.2501
CPE- $\alpha$ -	0.54339	0.44809
Fit ( $\chi^2$ )	0.0010536	

**Electrode Surface State**



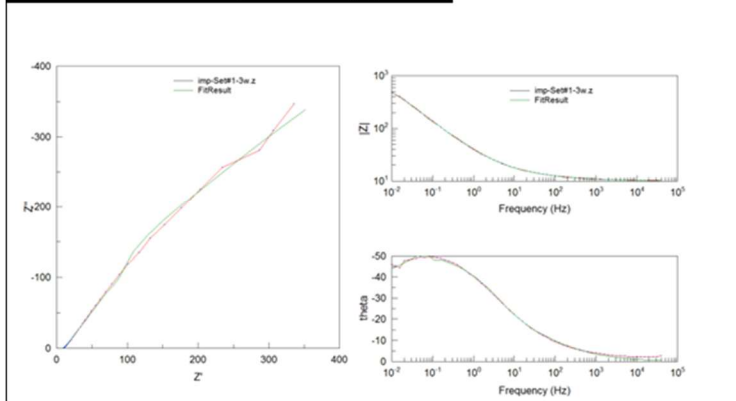
**Electrochemical Behavior**



**Polarization Curve Data**

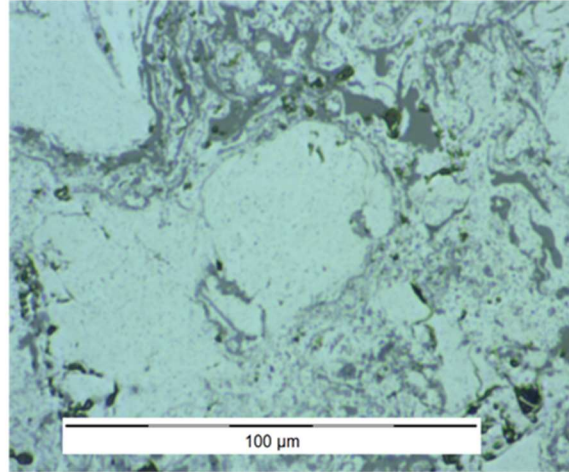
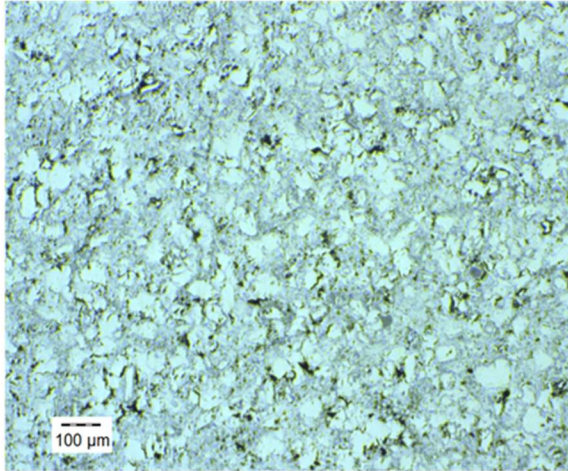
<b>Fit Quality (<math>\chi^2</math>)</b>	32.258
<b><math>E_{corr}</math> (V vs Ag/AgCl)</b>	-0.582
<b><math>i_{corr}</math> (A/cm<sup>2</sup>)</b>	2.20E-05
<b>Vmin (V vs Ag/AgCl)</b>	-0.72
<b>Vmax (V vs Ag/AgCl)</b>	-0.35
<b><math>\beta_a</math> (V)</b>	373.26
<b><math>ba</math> (V<sup>-1</sup>)</b>	6.17E-03
<b><math>\beta_c</math> (V)</b>	158.35
<b><math>bc</math> (V<sup>-1</sup>)</b>	1.45E-02
<b><math>R_p</math> (<math>\Omega \cdot cm^2</math>)</b>	1989

**Impedance Spectroscopy**

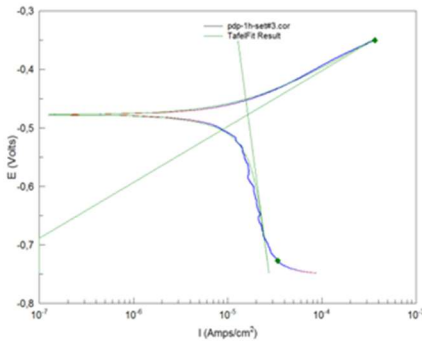


	Value	Error (%)
<b>DC (V)</b>	-0.4805	-
<b><math>R_e</math> <math>\Omega \cdot cm^2</math></b>	10.22	0.31953
<b><math>R_{ct}</math> <math>\Omega \cdot cm^2</math></b>	23.16	13.064
<b>W-R <math>\Omega \cdot cm^2</math></b>	3309	9.1478
<b>W-t (s)</b>	9.274	4.8186
<b>W-p -</b>	0.75211	2.3572
<b>CPE-C <math>F s^{-(1-\alpha)}</math></b>	0.0086392	1.3214
<b>CPE-<math>\alpha</math> -</b>	0.55392	0.44425
<b>Fit (<math>\chi^2</math>)</b>	0.0010896	

**Electrode Surface State**



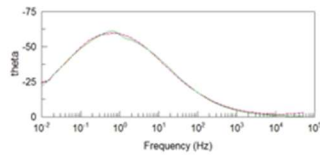
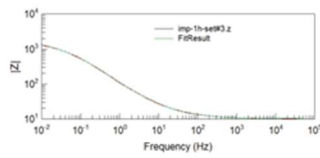
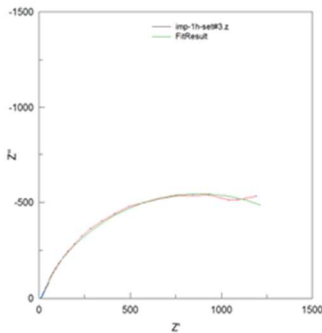
**Electrochemical Behavior**



**Polarization Curve Data**

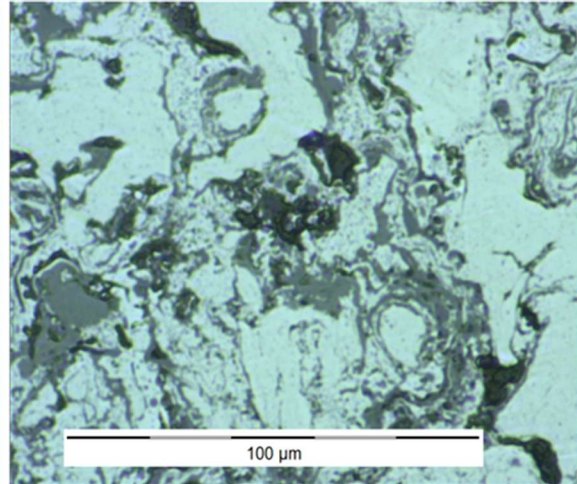
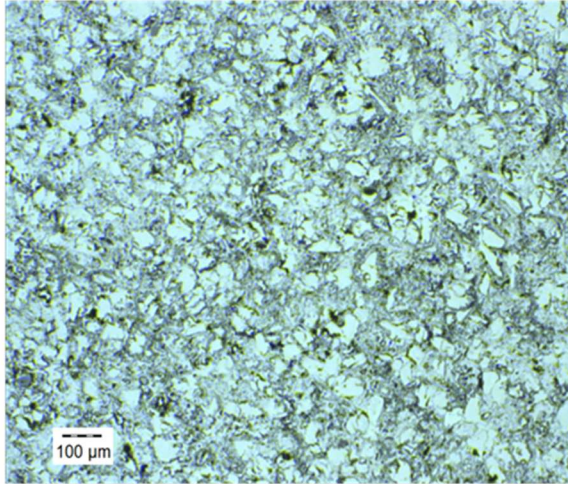
Fit Quality ( $\chi^2$ )	17.769
$E_{corr}$ (V vs Ag/AgCl)	-0.47
$i_{corr}$ (A/cm <sup>2</sup> )	1.63E-05
Vmin (V vs Ag/AgCl)	-0.73
Vmax (V vs Ag/AgCl)	-0.35
$\beta_a$ (V)	95.457
$ba$ (V <sup>-1</sup> )	2.41E-02
$\beta_c$ (V)	1205.5
$bc$ (V <sup>-1</sup> )	1.91E-03
$R_p$ ( $\Omega \cdot cm^2$ )	1983.4

**Impedance Spectroscopy**

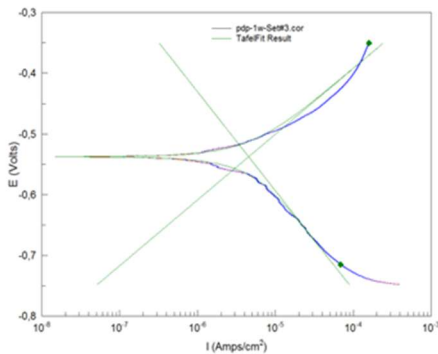


	Value	Error (%)
DC (V)	-0.4873	-
$R_e$ $\Omega \cdot cm^2$	10.35	0.36529
$R_{pore}$ $\Omega \cdot cm^2$	30.44	27.831
W-R $\Omega \cdot cm^2$	1730	1.5645
W-t (s)	0.76532	5.3945
W-p -	0.71668	1.8429
CPE-C $F s^{-(1-\alpha)}$	0.0022144	0.62522
CPE- $\alpha$ -	0.69808	0.50627
Fit ( $\chi^2$ )	0.0015224	

**Electrode Surface State**



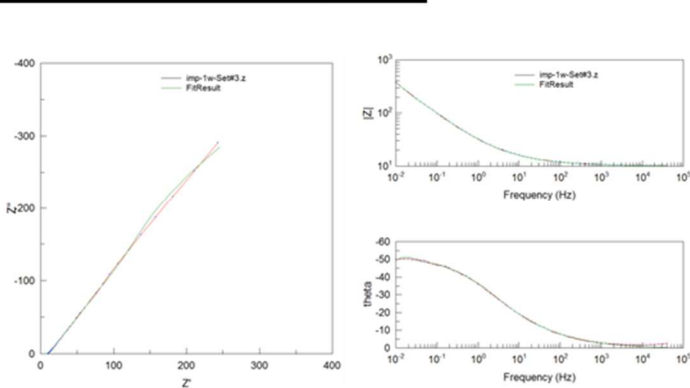
**Electrochemical Behavior**



**Polarization Curve Data**

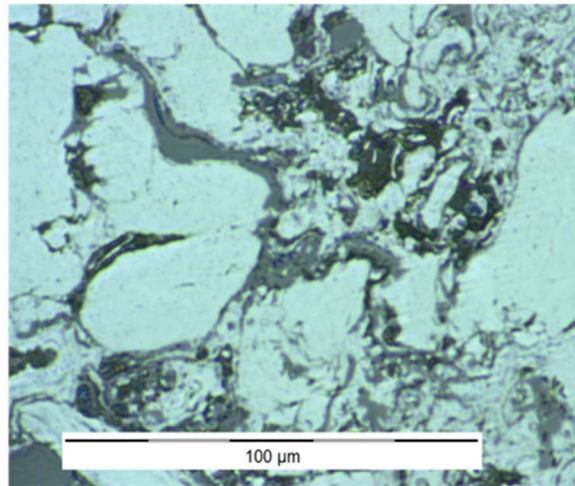
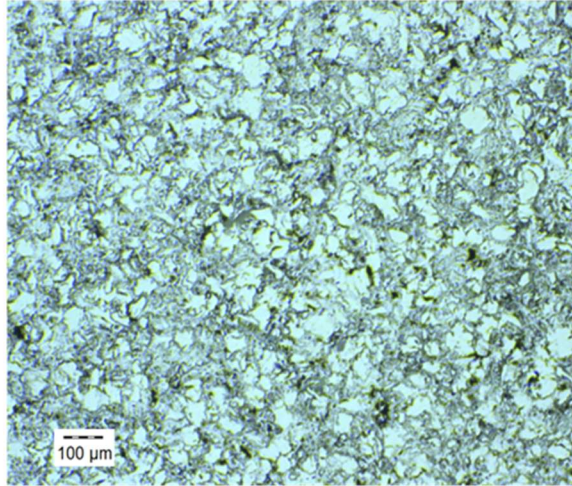
Fit Quality ( $\chi^2$ )	101.18
$E_{corr}$ (V vs Ag/AgCl)	-0.53
$i_{corr}$ (A/cm <sup>2</sup> )	4.53E-06
Vmin (V vs Ag/AgCl)	-0.72
Vmax (V vs Ag/AgCl)	-0.35
$\beta_a$ (V)	108.37
$\beta_b$ (V <sup>-1</sup> )	2.13E-02
$\beta_c$ (V)	163.08
$\beta_d$ (V <sup>-1</sup> )	1.41E-02
$R_p$ ( $\Omega \cdot \text{cm}^2$ )	7550

**Impedance Spectroscopy**

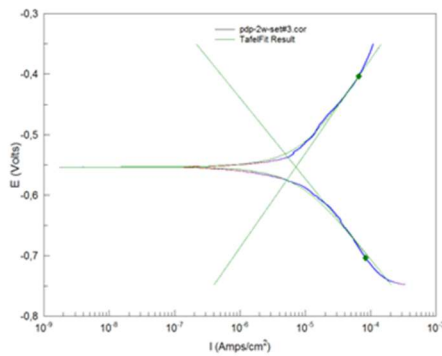


	Value	Error (%)
DC (V)	-0.4784	
$R_e$ $\Omega \cdot \text{cm}^2$	10.19	0.21752
$R_{ct}$ $\Omega \cdot \text{cm}^2$	14.39	20.566
W-R $\Omega \cdot \text{cm}^2$	2585	15.28
W-t (s)	35.41	6.4778
W-p -	0.62904	2.9833
CPE-C $F s^{(1-\alpha)}$	0.01054	4.0257
CPE- $\alpha$ -	0.56257	0.68955
Fit ( $\chi^2$ )	0.00047257	

**Electrode Surface State**



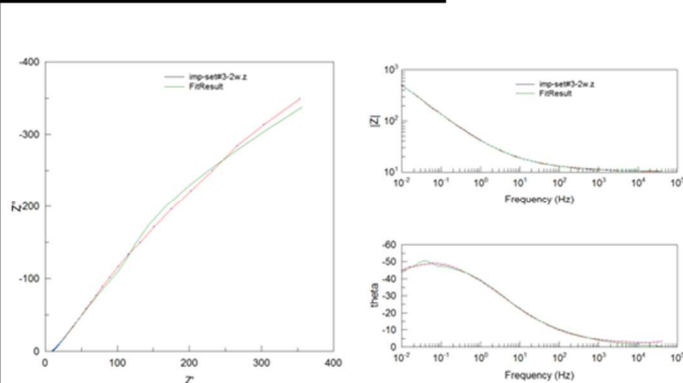
**Electrochemical Behavior**



**Polarization Curve Data**

Fit Quality ( $\chi^2$ )	62.101
$E_{corr}$ (V vs Ag/AgCl)	-0.55
$i_{corr}$ (A/cm <sup>2</sup> )	7.18E-06
Vmin (V vs Ag/AgCl)	-0.7
Vmax (V vs Ag/AgCl)	-0.4
$\beta_a$ (V)	155.81
$ba$ (V <sup>-1</sup> )	1.48E-02
$\beta_c$ (V)	133.6
$bc$ (V <sup>-1</sup> )	1.72E-02
$R_p$ ( $\Omega \cdot cm^2$ )	3793.7

**Impedance Spectroscopy**

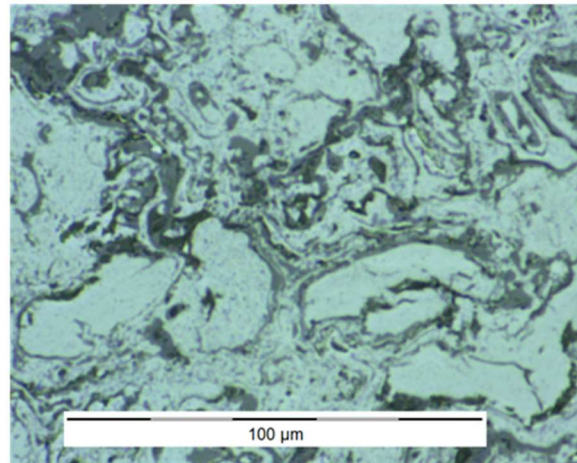
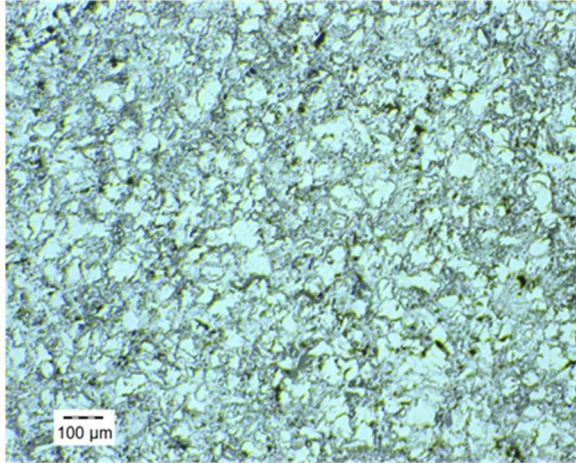


	Value	Error (%)
DC (V)	-0.4709	-
$R_e$ $\Omega \cdot cm^2$	10.29	0.3764
$R_{ct}$ $\Omega \cdot cm^2$	20.1	15.218
W-R $\Omega \cdot cm^2$	2890	11.716
W-t (s)	15.37	5.5928
W-p -	0.68878	2.792
CPE-C $F s^{-(1-\alpha)}$	0.0079545	2.4457
CPE- $\alpha$ -	0.53818	0.57709
Fit ( $\chi^2$ )	0.0010697	

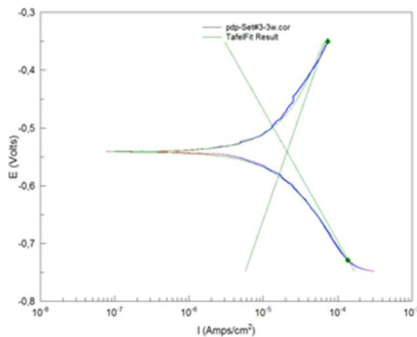
HVOF Spray Set # 3  
 Immersion Time 3 Weeks

Date 22/Aug/2018

**Electrode Surface State**



**Electrochemical Behavior**



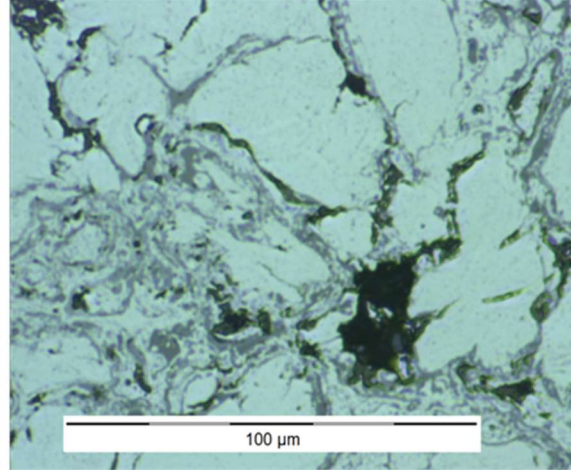
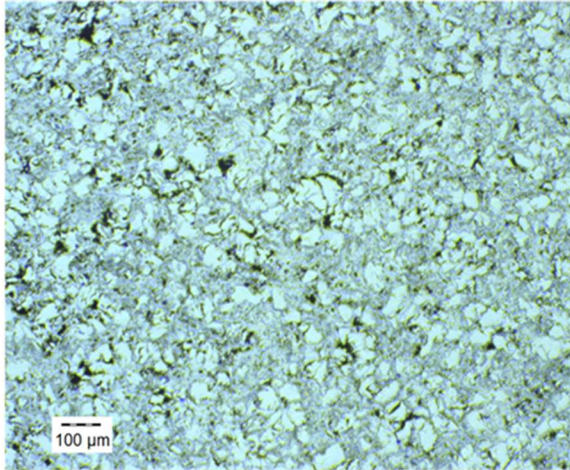
**Polarization Curve Data**

Fit Quality ( $\chi^2$ )	19.473
$E_{corr}$ (V vs Ag/AgCl)	-0.54105
$i_{corr}$ (A/cm <sup>2</sup> )	2.08E-05
Vmin (V vs Ag/AgCl)	-0.73
Vmax (V vs Ag/AgCl)	-0.35
$\beta_a$ (V)	369.83
$\beta_a$ (V <sup>-1</sup> )	6.23E-03
$\beta_c$ (V)	227.271
$\beta_c$ (V <sup>-1</sup> )	1.01E-02
$R_p$ ( $\Omega \cdot \text{cm}^2$ )	2712

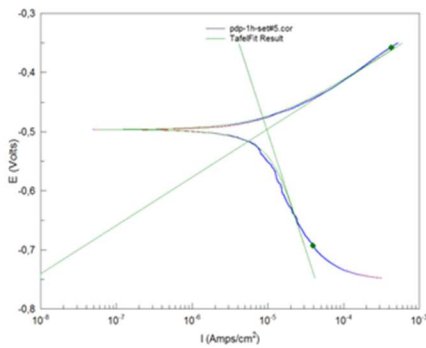
**Impedance Spectroscopy**

	Value	Error (%)
DC (V)	-0.4663	-
$R_e$ $\Omega \cdot \text{cm}^2$		
$R_{ct}$ $\Omega \cdot \text{cm}^2$		
W-R $\Omega \cdot \text{cm}^2$		
W-t (s)		
W-p -		
CPE-C $F s^{(1-\alpha)}$		
CPE- $\alpha$ -		
Fit ( $\chi^2$ )		

**Electrode Surface State**



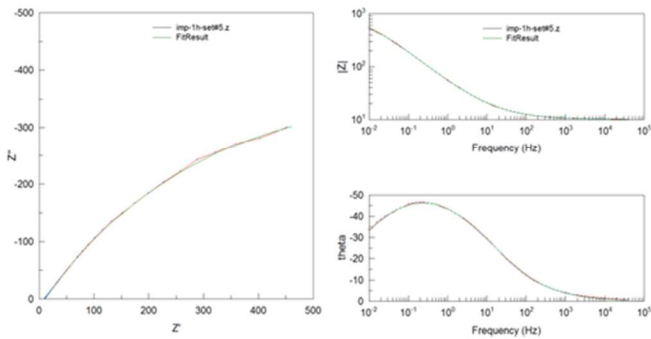
**Electrochemical Behavior**



**Polarization Curve Data**

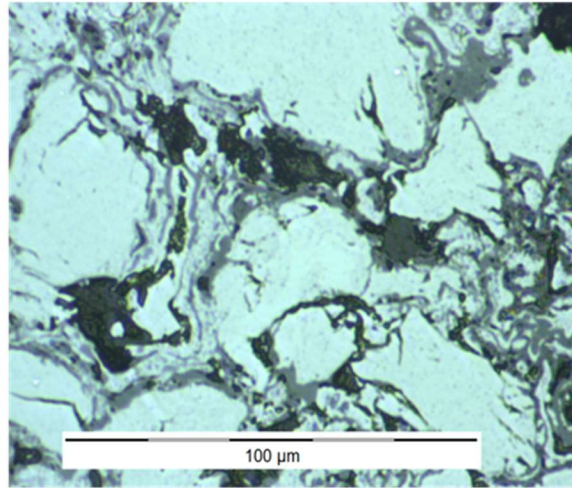
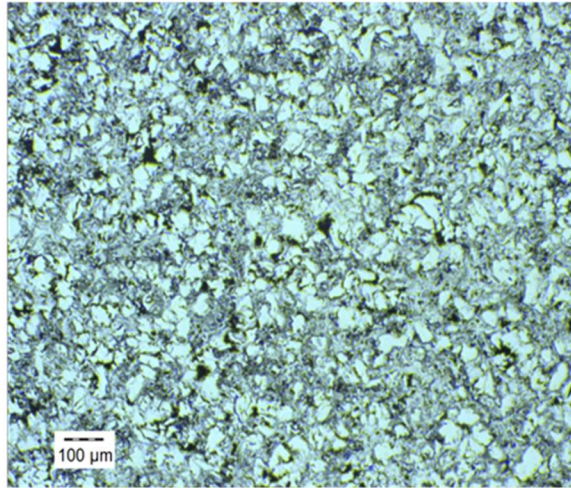
Fit Quality ( $\chi^2$ )	28.244
$E_{corr}$ (V vs Ag/AgCl)	-0.496
$i_{corr}$ (A/cm <sup>2</sup> )	9.66E-06
Vmin (V vs Ag/AgCl)	-0.693
Vmax (V vs Ag/AgCl)	-0.36
$\beta_a$ (V)	81.7
$\beta_b$ (V <sup>-1</sup> )	2.82E-02
$\beta_c$ (V)	395.2
$\beta_d$ (V <sup>-1</sup> )	5.83E-03
$R_p$ ( $\Omega \cdot \text{cm}^2$ )	2709.6

**Impedance Spectroscopy**

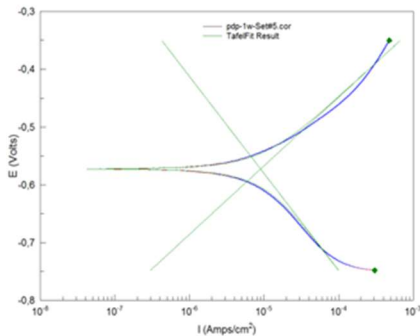


	Value	Error (%)
DC (V)	-0.467	-
$R_e$ $\Omega \cdot \text{cm}^2$	10.13	0.13921
$R_{pore}$ $\Omega \cdot \text{cm}^2$	8.229	380
W-R $\Omega \cdot \text{cm}^2$	1289	4.0509
W-t (s)	1.389	15.204
W-p -	0.45905	5.3016
CPE-C $F s^{(1-\alpha)}$	0.0063292	0.74983
CPE- $\alpha$ -	0.58632	0.74425
Fit ( $\chi^2$ )	0.00017379	

**Electrode Surface State**



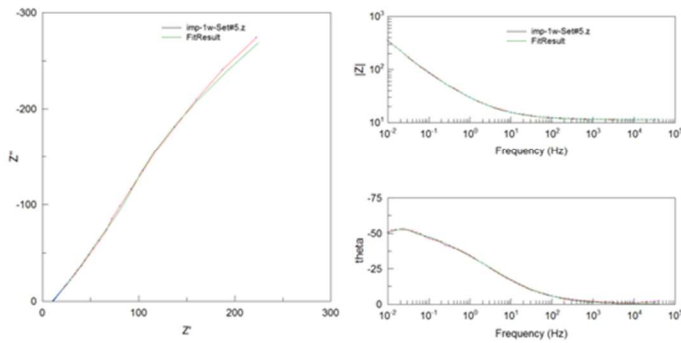
**Electrochemical Behavior**



**Polarization Curve Data**

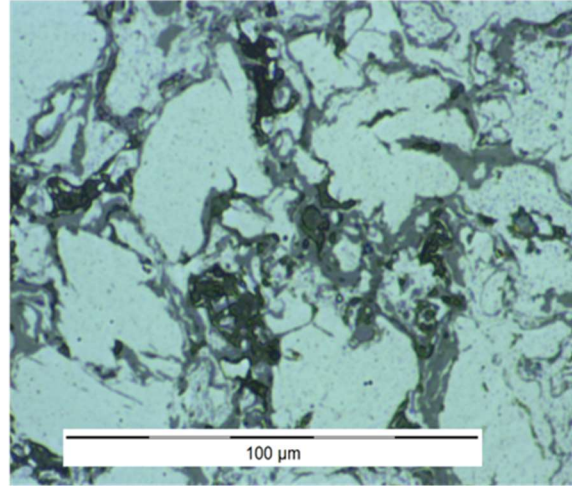
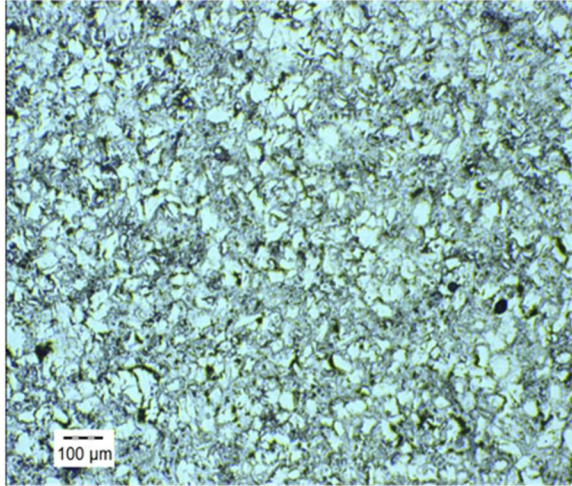
Fit Quality ( $\chi^2$ )	65.947
$E_{corr}$ (V vs Ag/AgCl)	-0.57
$i_{corr}$ (A/cm <sup>2</sup> )	8.98E-06
Vmin (V vs Ag/AgCl)	-0.75
Vmax (V vs Ag/AgCl)	-0.35
$\beta_a$ (V)	118.78
$\beta_b$ (V <sup>-1</sup> )	1.94E-02
$\beta_c$ (V)	167.77
$\beta_d$ (V <sup>-1</sup> )	1.37E-02
$R_p$ ( $\Omega \cdot \text{cm}^{-2}$ )	3672.2

**Impedance Spectroscopy**

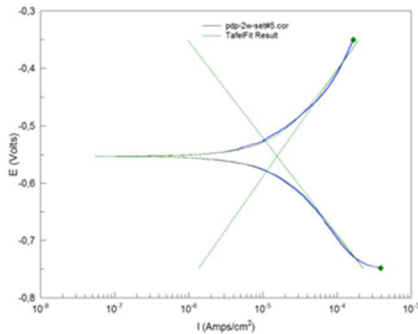


	Value	Error (%)
DC (V)	-0.5297	
$R_e$ $\Omega \cdot \text{cm}^{-2}$	11.25	0.20202
$R_{ct}$ $\Omega \cdot \text{cm}^{-2}$	94.73	28.704
W-R $\Omega \cdot \text{cm}^{-2}$	2290	21.127
W-t (s)	23.42	9.6892
W-p -	0.65619	5.362
CPE-C $F s^{-(1-\alpha)}$	0.01346	3.5379
CPE- $\alpha$ -	0.60499	0.99495
Fit ( $\chi^2$ )	0.00086624	

**Electrode Surface State**



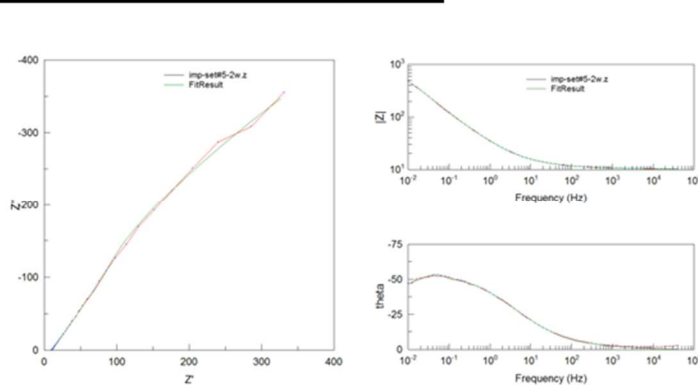
**Electrochemical Behavior**



**Polarization Curve Data**

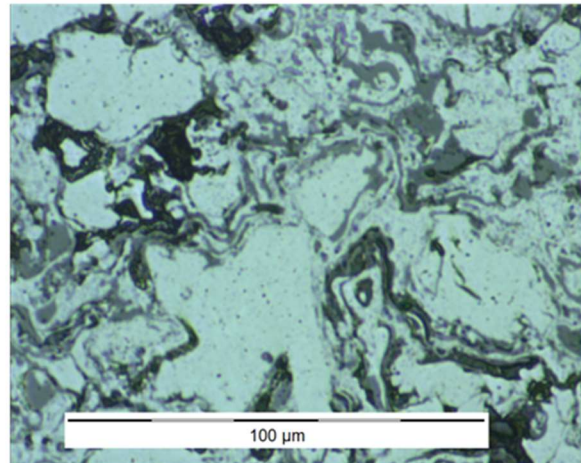
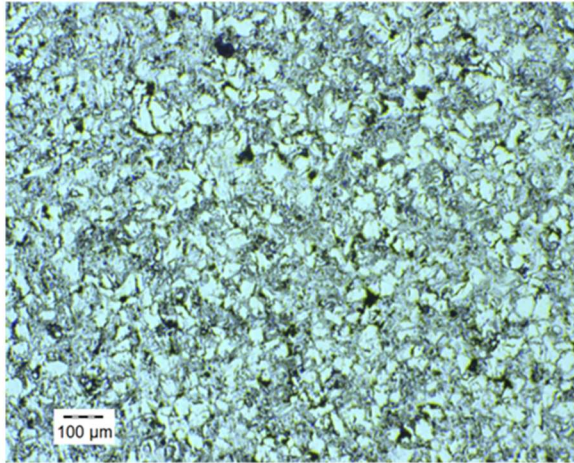
Fit Quality ( $\chi^2$ )	17.309
$E_{corr}$ (V vs Ag/AgCl)	-0.55
$i_{corr}$ (A/cm $_2$ )	1.55E-05
Vmin (V vs Ag/AgCl)	-0.75
Vmax (V vs Ag/AgCl)	-0.35
$\beta_a$ (V)	184.7
$\beta_a$ (V $^{-1}$ )	1.25E-02
$\beta_c$ (V)	168
$\beta_c$ (V $^{-1}$ )	1.37E-02
$R_p$ ( $\Omega \cdot \text{cm}^2$ )	2581

**Impedance Spectroscopy**

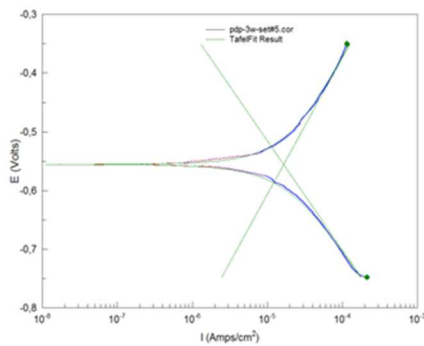


	Value	Error (%)
DC (V)	-0.4898	-
$R_e$ $\Omega \cdot \text{cm}^2$	10.32	0.23757
$R_{ct}$ $\Omega \cdot \text{cm}^2$	11.98	19.796
W-R $\Omega \cdot \text{cm}^2$	2729	8.4793
W-t (s)	11.41	5.3111
W-p -	0.68275	2.6871
CPE-C $F s^{-(1-\alpha)}$	0.0096894	1.4011
CPE- $\alpha$ -	0.59577	0.58403
Fit ( $\chi^2$ )	0.00079608	

**Electrode Surface State**



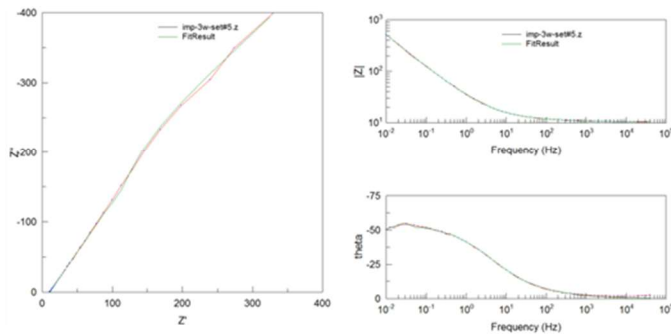
**Electrochemical Behavior**



**Polarization Curve Data**

Fit Quality ( $\chi^2$ )	40.553
$E_{corr}$ (V vs Ag/AgCl)	-0.55
$i_{corr}$ (A/cm <sup>2</sup> )	1.65E-05
Vmin (V vs Ag/AgCl)	-0.73
Vmax (V vs Ag/AgCl)	-0.35
$\beta_a$ (V)	233.38
$\beta_c$ (V)	186.5
$ba$ (V <sup>-1</sup> )	9.87E-03
$bc$ (V <sup>-1</sup> )	1.23E-02
$R_p$ ( $\Omega \cdot cm^2$ )	2571

**Impedance Spectroscopy**



	Value	Error (%)
DC (V)	-0.4795	-
$R_e$ $\Omega \cdot cm^2$	10.44	0.22184
$R_{ct}$ $\Omega \cdot cm^2$	8.737	19.942
W-R $\Omega \cdot cm^2$	4744	11.669
W-t (s)	19.13	4.6354
W-p -	0.72487	2.1907
CPE-C $F s^{(1-\alpha)}$	0.0094503	1.8293
CPE- $\alpha$ -	0.59535	0.44659
Fit ( $\chi^2$ )	0.00070125	

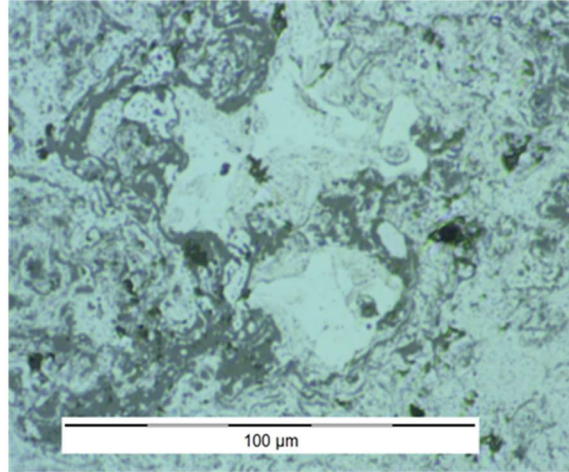
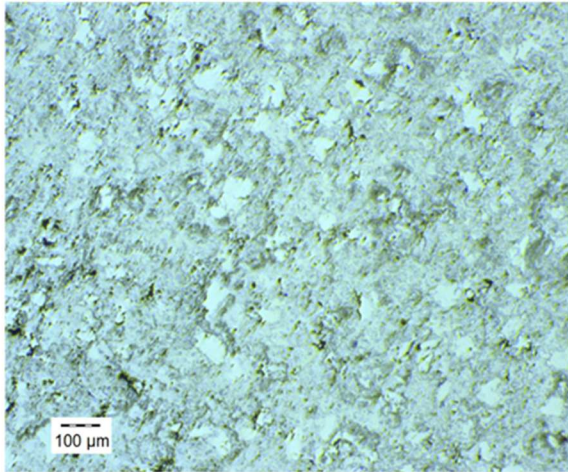
HVOF Spray Set #  
Immersion Time

8  
1 Hour

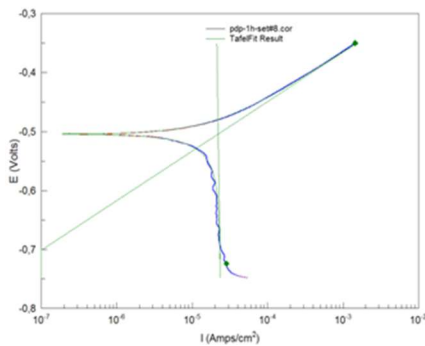
Date

02/Aug/2018

**Electrode Surface State**



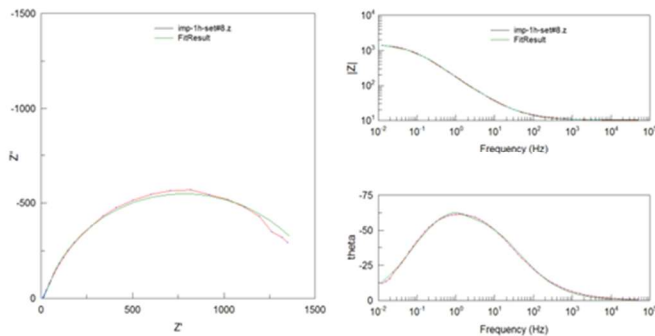
**Electrochemical Behavior**



**Polarization Curve Data**

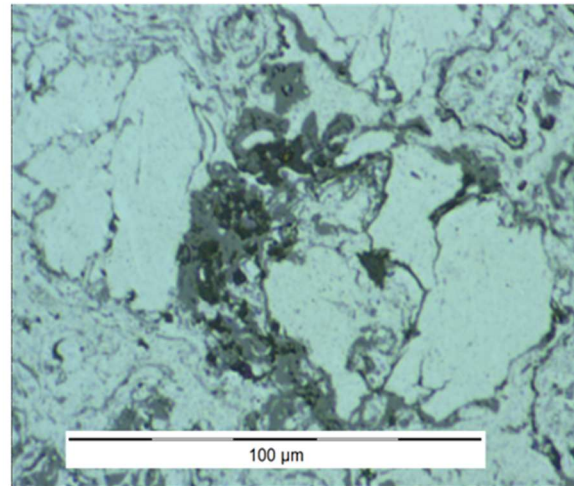
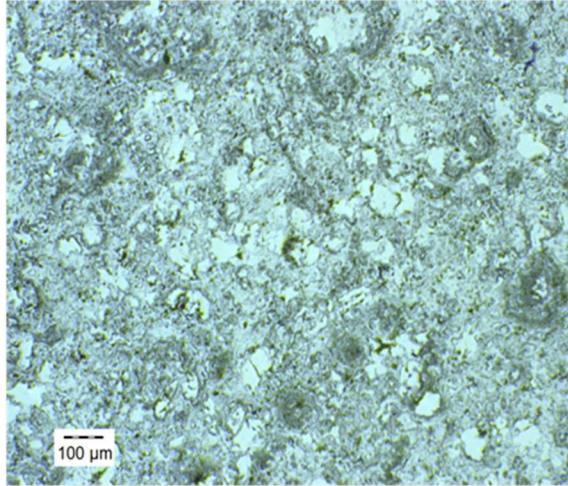
Fit Quality ( $\chi^2$ )	8.11
$E_{corr}$ (V vs Ag/AgCl)	-0.50438
$i_{corr}$ (A/cm <sup>2</sup> )	2.20E-05
Vmin (V vs Ag/AgCl)	-0.72
Vmax (V vs Ag/AgCl)	-0.35
$\beta_a$ (V)	83.933
$\beta_c$ (V)	8420.7
$ba$ (V <sup>-1</sup> )	2.74E-02
$bc$ (V <sup>-1</sup> )	2.73E-04
$R_p$ ( $\Omega \cdot \text{cm}^2$ )	1542.2

**Impedance Spectroscopy**

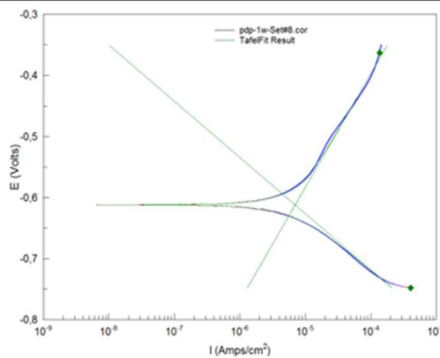


	Value	Error (%)
DC (V)	-0.5187	-
$R_e$ $\Omega \cdot \text{cm}^2$	10.32	0.38552
$R_{pore}$ $\Omega \cdot \text{cm}^2$	22.96	97.134
W-R $\Omega \cdot \text{cm}^2$	1552	2.0313
W-t (s)	0.55014	8.5104
W-p -	0.60729	2.2739
CPE-C $F s^{-(1-\alpha)}$	0.0012004	1.1678
CPE- $\alpha$ -	0.75268	0.76442
Fit ( $\chi^2$ )	0.0013399	

**Electrode Surface State**



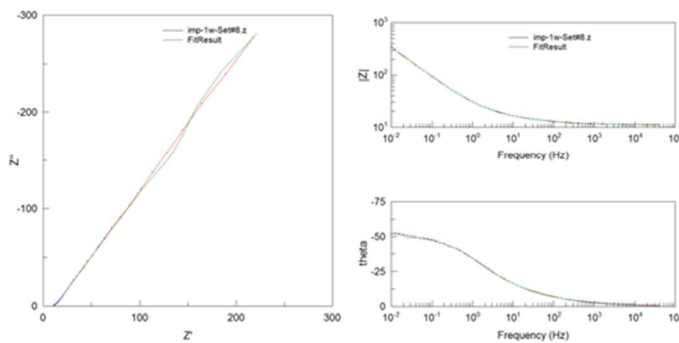
**Electrochemical Behavior**



**Polarization Curve Data**

Fit Quality ( $\chi^2$ )	12.647
$E_{corr}$ (V vs Ag/AgCl)	-0.61224
$i_{corr}$ (A/cm <sup>2</sup> )	7.00E-06
Vmin (V vs Ag/AgCl)	-0.75
Vmax (V vs Ag/AgCl)	-0.36
$\beta_a$ (V)	186.14
$ba$ (V <sup>-1</sup> )	1.24E-02
$\beta_c$ (V)	92.085
$bc$ (V <sup>-1</sup> )	2.50E-02
$R_p$ ( $\Omega \cdot cm^{-2}$ )	3570

**Impedance Spectroscopy**



	Value	Error (%)
DC (V)	-0.4874	-
$R_e$ $\Omega \cdot cm^{-2}$	11.19	0.17599
$R_{ct}$ $\Omega \cdot cm^{-2}$	17.72	4.0633
W-R $\Omega \cdot cm^{-2}$	4168	2.97
W-t (s)	42.7	3.0126
W-p -	0.72612	0.9065
CPE-C $F s^{-(1-\alpha)}$	0.011574	0.21096
CPE- $\alpha$ -	0.55348	0.34303
Fit ( $\chi^2$ )	0.00045562	

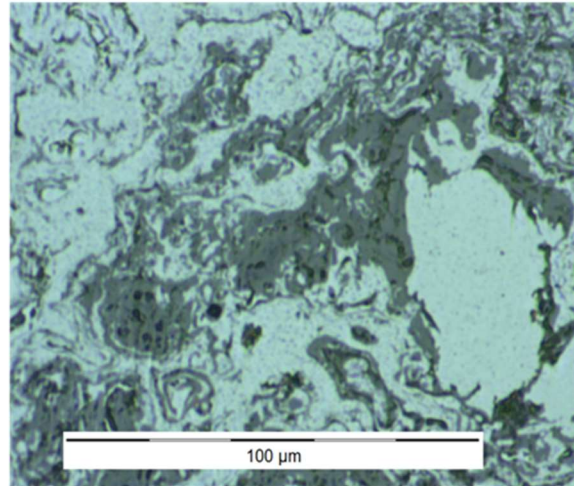
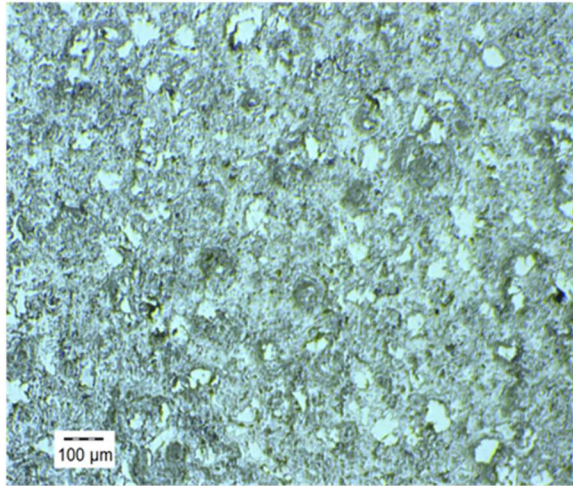
HVOF Spray Set #  
Immersion Time

8  
2 Weeks

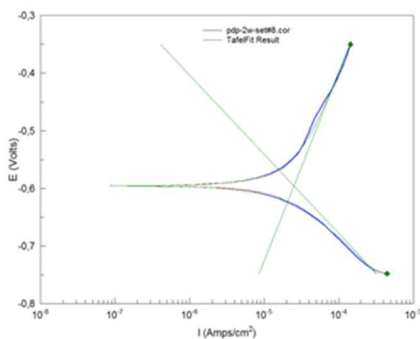
Date

17/Aug/2018

**Electrode Surface State**



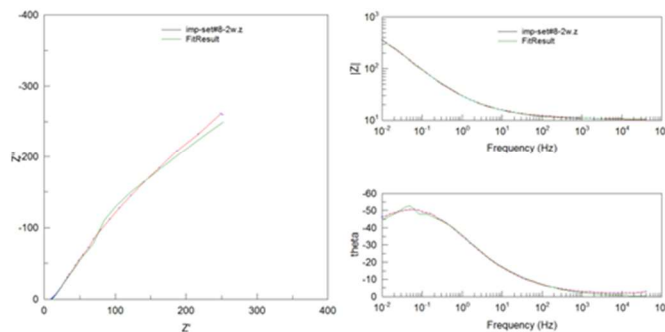
**Electrochemical Behavior**



**Polarization Curve Data**

Fit Quality ( $\chi^2$ )	11.575
$E_{corr}$ (V vs Ag/AgCl)	-0.59
$i_{corr}$ (A/cm <sup>2</sup> )	2.50E-05
Vmin (V vs Ag/AgCl)	-0.75
Vmax (V vs Ag/AgCl)	-0.35
$\beta_a$ (V)	326.52
$\beta_b$ (V <sup>-1</sup> )	7.05E-03
$\beta_c$ (V)	137.24
$\beta_d$ (V <sup>-1</sup> )	1.68E-02
$R_p$ ( $\Omega \cdot \text{cm}^{-2}$ )	1494.8

**Impedance Spectroscopy**



	Value	Error (%)
DC (V)	-0.4729	-
$R_e$ $\Omega \cdot \text{cm}^{-2}$	10.49	0.36916
$R_{ct}$ $\Omega \cdot \text{cm}^{-2}$	24.86	16.053
W-R $\Omega \cdot \text{cm}^{-2}$	2237	11.252
W-t (s)	11.18	5.0466
W-p -	0.766	2.9081
CPE-C $F s^{-(1-\alpha)}$	0.01232	1.8499
CPE- $\alpha$ -	0.56676	0.57324
Fit ( $\chi^2$ )	0.0021692	

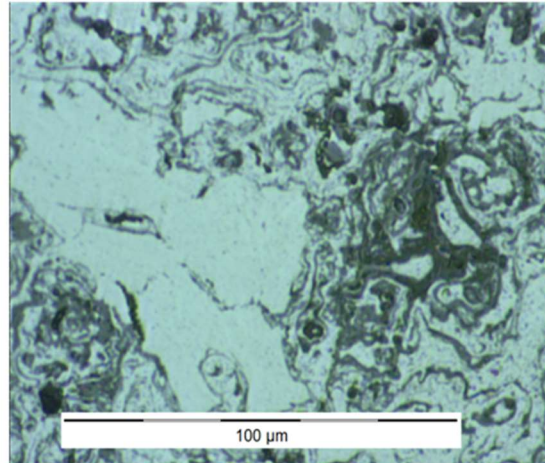
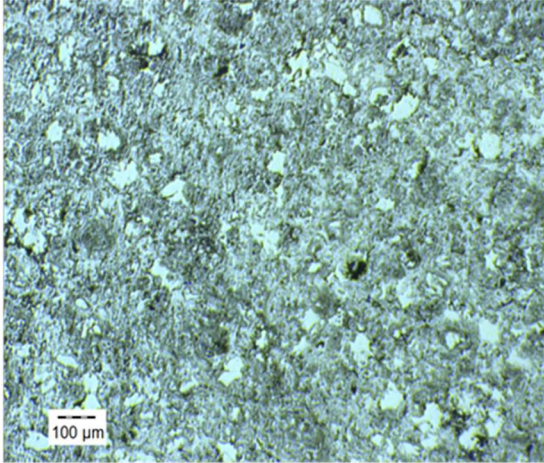
HVOF Spray Set #  
Immersion Time

8  
3 Weeks

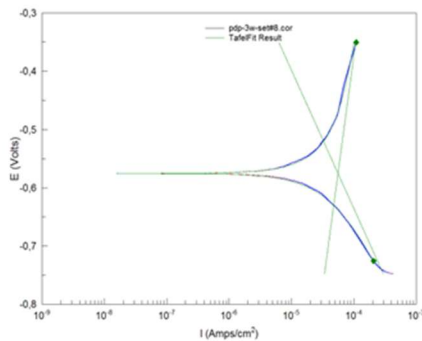
Date

23/Aug/2018

**Electrode Surface State**



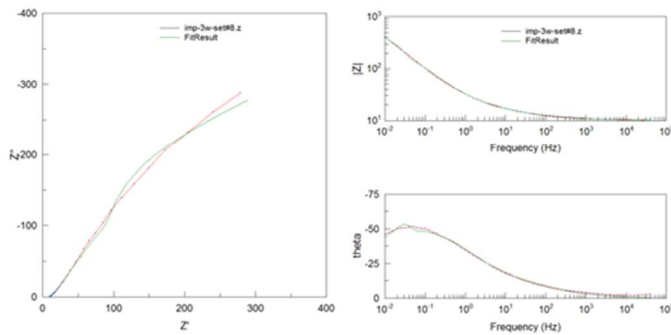
**Electrochemical Behavior**



**Polarization Curve Data**

Fit Quality ( $\chi^2$ )	6.3837
$E_{corr}$ (V vs Ag/AgCl)	-0.57
$i_{corr}$ (A/cm <sup>2</sup> )	5.57E-05
Vmin (V vs Ag/AgCl)	-0.73
Vmax (V vs Ag/AgCl)	-0.35
$\beta_a$ (V)	797.34
$\beta_c$ (V <sup>-1</sup> )	2.89E-03
$\beta_c$ (V)	237.46
$\beta_c$ (V <sup>-1</sup> )	9.70E-03
$R_p$ ( $\Omega \cdot \text{cm}^{-2}$ )	1359.7

**Impedance Spectroscopy**

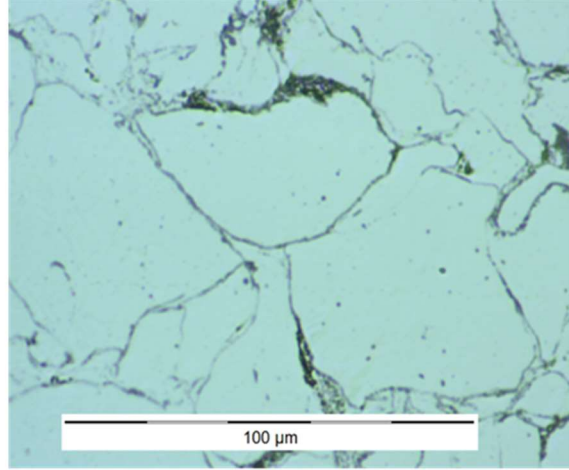
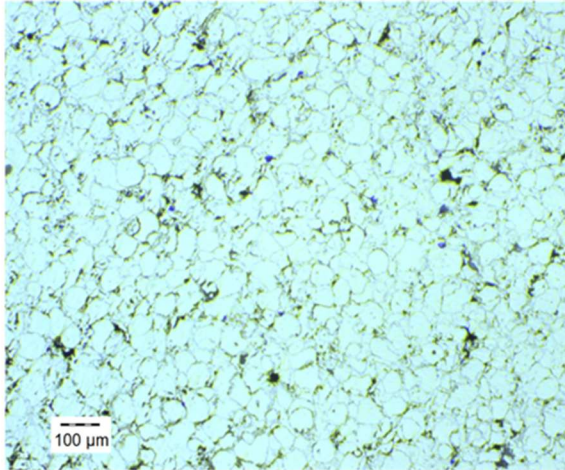


	Value	Error (%)
DC (V)	-0.4573	-
$R_e$ $\Omega \cdot \text{cm}^{-2}$	10.26	0.44592
$R_{ct}$ $\Omega \cdot \text{cm}^{-2}$	20.56	13.7
W-R $\Omega \cdot \text{cm}^{-2}$	1773	11.83
W-t (s)	17.74	4.7052
W-p -	0.71273	2.9523
CPE-C $F s^{-(1-\alpha)}$	0.0096262	3.42
CPE- $\alpha$ -	0.55013	0.76304
Fit ( $\chi^2$ )	0.0020339	

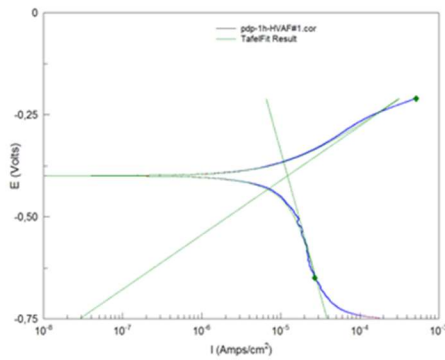
HVAF Set # 1  
 Immersion Time 1 Hour

Date 03/Aug/2018

**Electrode Surface State**



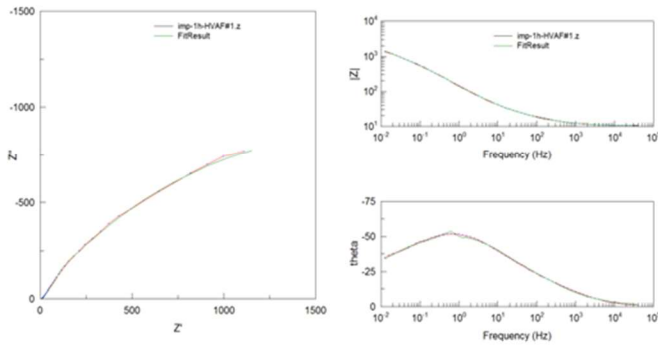
**Electrochemical Behavior**



**Polarization Curve Data**

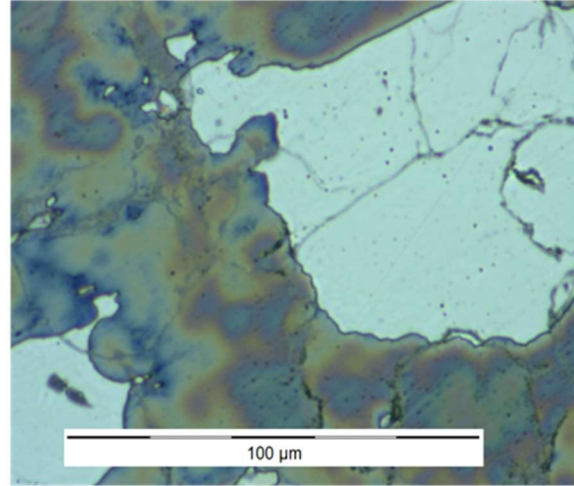
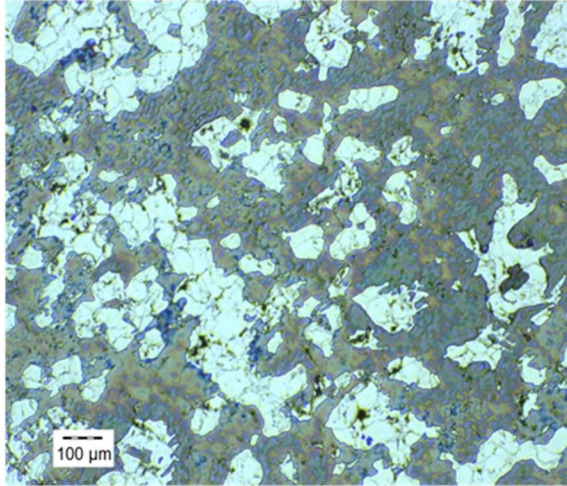
Fit Quality ( $\chi^2$ )	19.522
$E_{corr}$ (V vs Ag/AgCl)	-0.39924
$i_{corr}$ (A/cm <sup>2</sup> )	1.21E-05
Vmin (V vs Ag/AgCl)	-0.65
Vmax (V vs Ag/AgCl)	-0.21
$\beta_a$ (V)	133.23
$\beta_b$ (V <sup>-1</sup> )	1.73E-02
$\beta_c$ (V)	699.75
$\beta_d$ (V <sup>-1</sup> )	3.29E-03
$R_p$ ( $\Omega \cdot \text{cm}^2$ )	3997.2

**Impedance Spectroscopy**

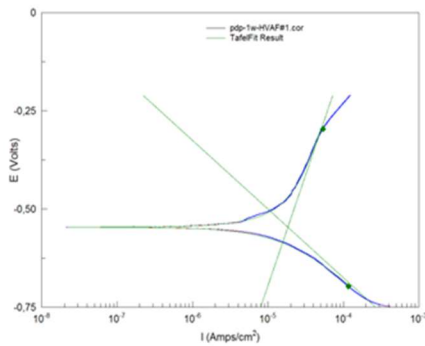


	Value	Error (%)
DC (V)	-0.3761	-
$R_e$ $\Omega \cdot \text{cm}^2$	10.32	0.30986
$R_{pore}$ $\Omega \cdot \text{cm}^2$	76.42	8.6659
W-R $\Omega \cdot \text{cm}^2$	3443	2.0217
W-t (s)	0.83833	3.5549
W-p -	0.76323	1.3062
CPE-C $F s^{-(1-\alpha)}$	0.0022232	0.42977
CPE- $\alpha$ -	0.5778	0.25978
Fit ( $\chi^2$ )	0.00043876	

**Electrode Surface State**



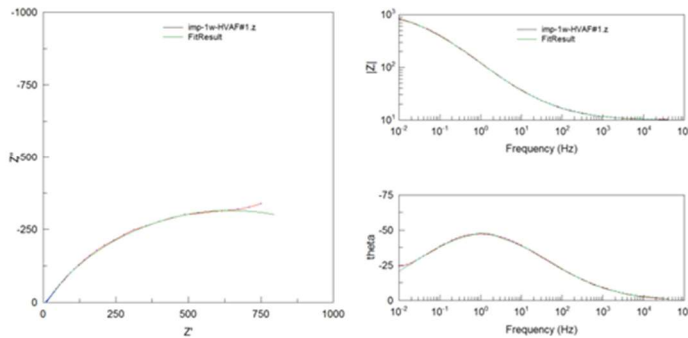
**Electrochemical Behavior**



**Polarization Curve Data**

Fit Quality ( $\chi^2$ )	9.2324
$E_{corr}$ (V vs Ag/AgCl)	-0.55
$i_{corr}$ (A/cm <sup>2</sup> )	1.80E-05
Vmin (V vs Ag/AgCl)	-0.7
Vmax (V vs Ag/AgCl)	-0.3
$\beta_a$ (V)	564.3
$\beta_b$ (V <sup>-1</sup> )	4.08E-03
$\beta_c$ (V)	174.91
$\beta_d$ (V <sup>-1</sup> )	1.32E-02
$R_p$ ( $\Omega \cdot \text{cm}^2$ )	2889.5

**Impedance Spectroscopy**



	Value	Error (%)
DC (V)	-0.4006	-
$R_e$ $\Omega \cdot \text{cm}^2$	9.955	0.34858
$R_{ct}$ $\Omega \cdot \text{cm}^2$	34.82	31.872
W-R $\Omega \cdot \text{cm}^2$	1252	1.7301
W-t (s)	0.41512	8.8912
W-p -	0.59457	2.117
CPE-C $F s^{-(1-\alpha)}$	0.0026298	0.58495
CPE- $\alpha$ -	0.57546	0.5217
Fit ( $\chi^2$ )	0.00042126	

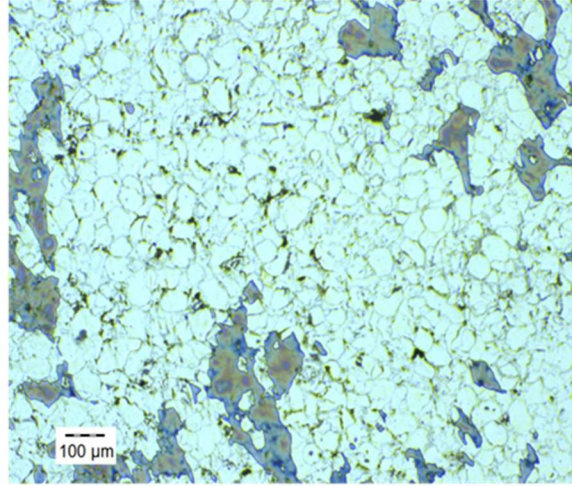
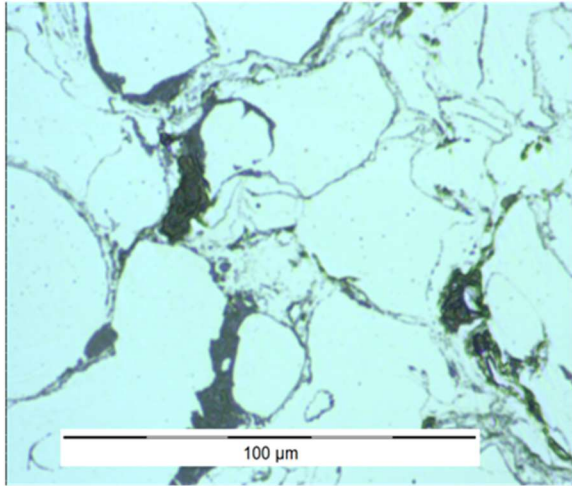
HVAF Set #  
Immersion Time

1  
2 Weeks

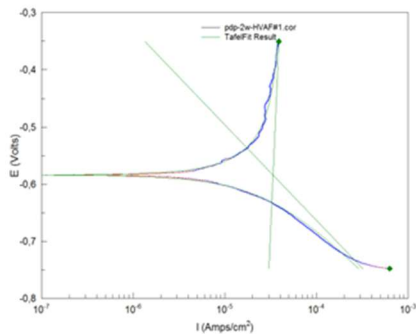
Date

17/Aug/2018

**Electrode Surface State**



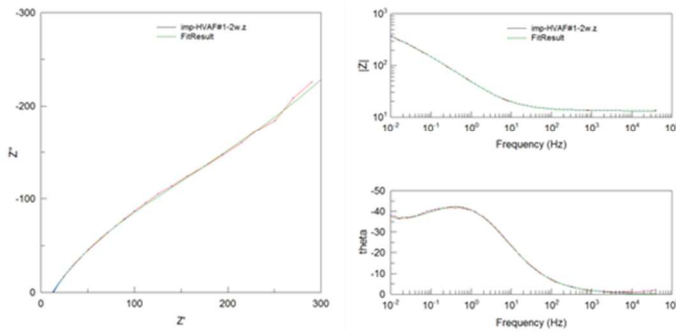
**Electrochemical Behavior**



**Polarization Curve Data**

<b>Fit Quality (<math>\chi^2</math>)</b>	24.867
<b><math>E_{corr}</math> (V vs Ag/AgCl)</b>	-0.58
<b><math>i_{corr}</math> (A/cm<sup>2</sup>)</b>	3.30E-05
<b>Vmin (V vs Ag/AgCl)</b>	-0.75
<b>Vmax (V vs Ag/AgCl)</b>	-0.35
<b><math>\beta_a</math> (V)</b>	3649
<b><math>\beta_b</math> (V<sup>-1</sup>)</b>	6.31E-04
<b><math>\beta_c</math> (V)</b>	167.36
<b><math>\beta_d</math> (V<sup>-1</sup>)</b>	1.38E-02
<b>Rp (<math>\Omega \cdot cm^{-2}</math>)</b>	1918.5

**Impedance Spectroscopy**



	Value	Error (%)
<b>DC (V)</b>	-0.3361	-
<b><math>R_e</math> <math>\Omega \cdot cm^{-2}</math></b>	13.24	0.15529
<b><math>R_{ct}</math> <math>\Omega \cdot cm^{-2}</math></b>	299.6	5.4272
<b>W-R <math>\Omega \cdot cm^{-2}</math></b>	2466	1870.6
<b>W-t (s)</b>	728	3607.8
<b>W-p -</b>	0.5157	4.178
<b>CPE-C <math>F s^{-(1-\alpha)}</math></b>	0.0070056	1.0027
<b>CPE-<math>\alpha</math> -</b>	0.65538	0.41382
<b>Fit (<math>\chi^2</math>)</b>	0.00046559	

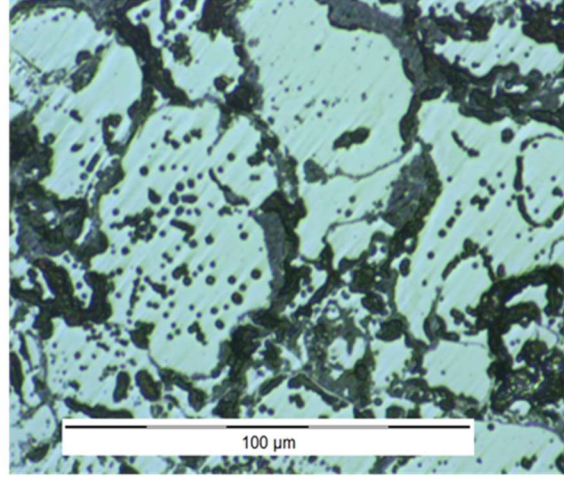
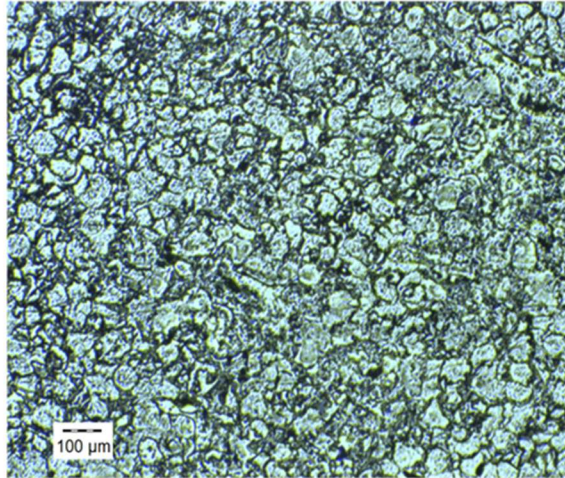
HVAF Set #  
Immersion Time

1  
3 Weeks

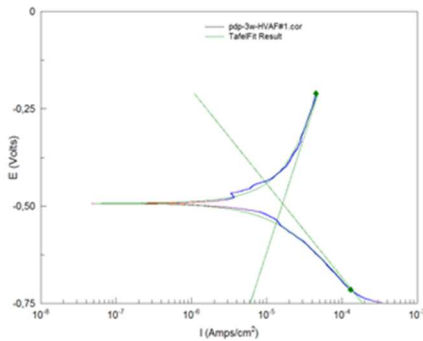
Date

24/Aug/2018

**Electrode Surface State**



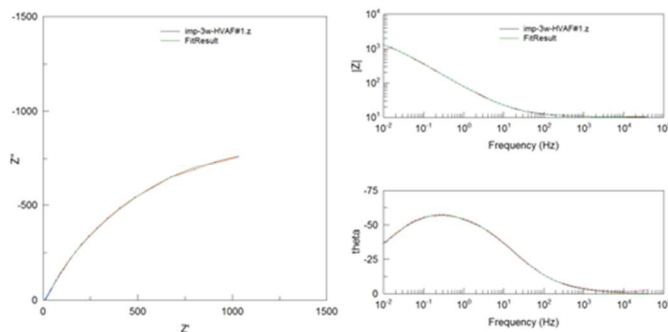
**Electrochemical Behavior**



**Polarization Curve Data**

Fit Quality ( $\chi^2$ )	49.558
$E_{corr}$ (V vs Ag/AgCl)	-0.49
$i_{corr}$ (A/cm <sup>2</sup> )	1.60E-05
Vmin (V vs Ag/AgCl)	-0.71
Vmax (V vs Ag/AgCl)	-0.21
$\beta_a$ (V)	597.22
$\beta_a$ (V <sup>-1</sup> )	3.86E-03
$\beta_c$ (V)	241.118
$\beta_c$ (V <sup>-1</sup> )	9.55E-03
$R_p$ ( $\Omega \cdot \text{cm}^2$ )	3539

**Impedance Spectroscopy**



	Value	Error (%)
DC (V)	-0.3236	-
$R_e$ $\Omega \cdot \text{cm}^2$	10.32	0.20641
$R_{ct}$ $\Omega \cdot \text{cm}^2$	34.76	100.78
W-R $\Omega \cdot \text{cm}^2$	2594	2.6347
W-t (s)	1.639	9.8548
W-p -	0.58139	2.9669
CPE-C $F s^{(1-\alpha)}$	0.0034741	0.67396
CPE- $\alpha$ -	0.6835	0.50666
Fit ( $\chi^2$ )	0.00043812	

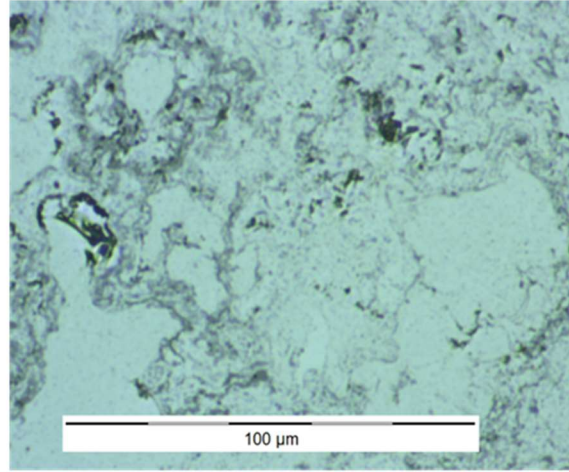
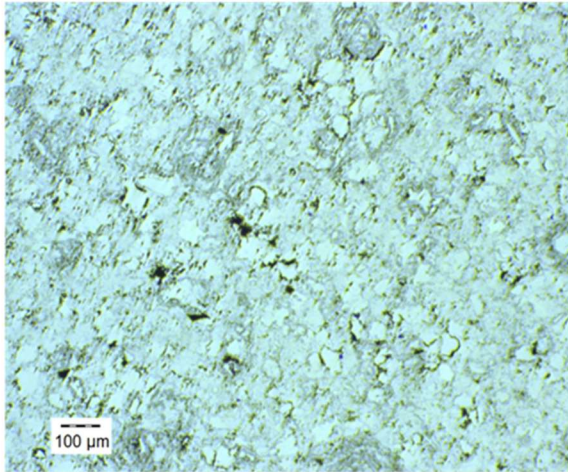
HVAF Set #  
Immersion Time

4  
1 Hour

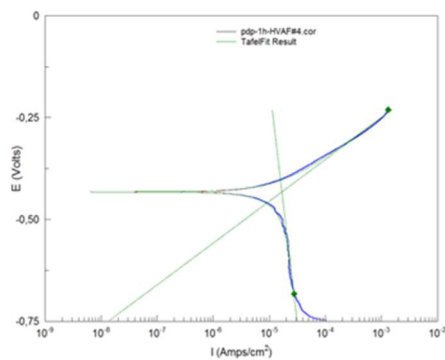
Date

03/Aug/2018

**Electrode Surface State**



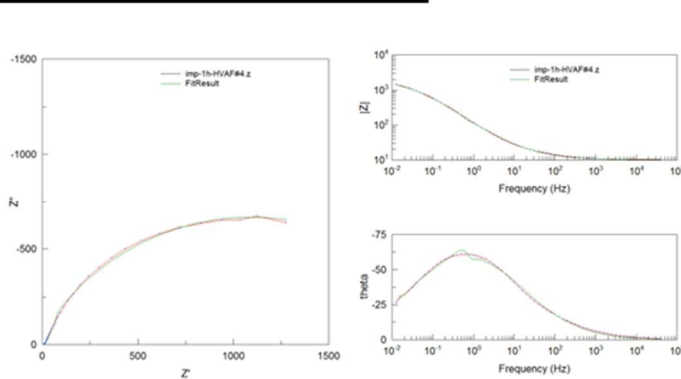
**Electrochemical Behavior**



**Polarization Curve Data**

Fit Quality ( $\chi^2$ )	15.058
$E_{corr}$ (V vs Ag/AgCl)	-0.43
$i_{corr}$ (A/cm <sup>2</sup> )	1.67E-05
Vmin (V vs Ag/AgCl)	-0.68
Vmax (V vs Ag/AgCl)	-0.23
$\beta_a$ (V)	102.64
$\beta_c$ (V <sup>-1</sup> )	2.24E-02
$\beta_c$ (V)	1174.8
$\beta_c$ (V <sup>-1</sup> )	1.96E-03
$R_p$ ( $\Omega \cdot \text{cm}^2$ )	2423.7

**Impedance Spectroscopy**



	Value	Error (%)
DC (V)	-0.4444	-
$R_e$ $\Omega \cdot \text{cm}^2$	10.31	0.49748
$R_{pore}$ $\Omega \cdot \text{cm}^2$	30.81	18.856
W-R $\Omega \cdot \text{cm}^2$	2156	2.164
W-t (s)	0.94002	4.1909
W-p -	0.78014	1.6598
CPE-C $F s^{(1-\alpha)}$	0.0020664	0.85656
CPE- $\alpha$ -	0.69023	0.54485
Fit ( $\chi^2$ )	0.002517	

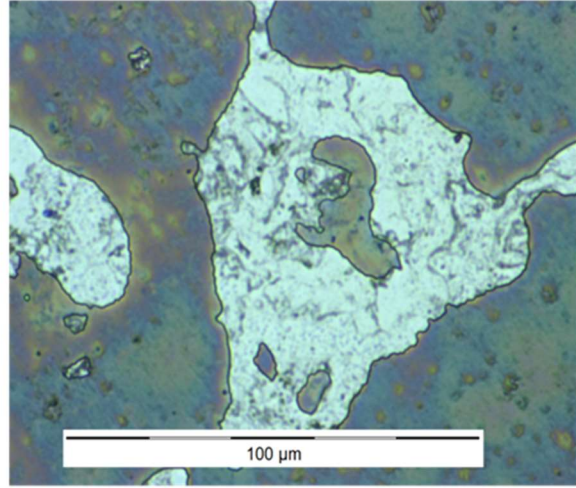
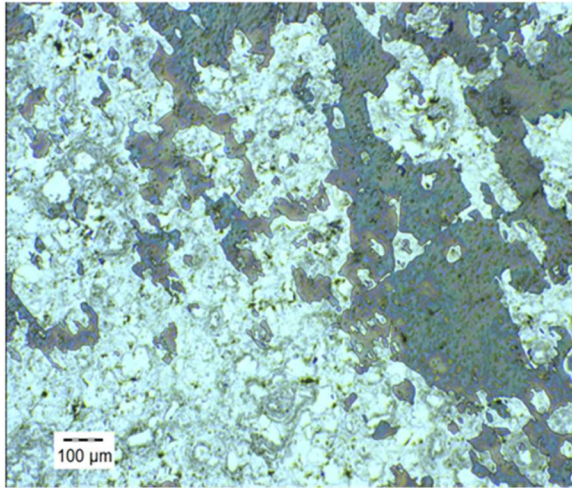
HVAF Set #  
Immersion Time

4  
1 week

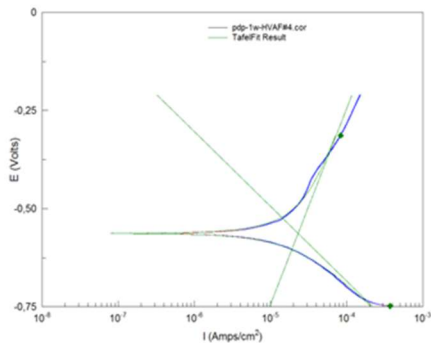
Date

10/Aug/2018

**Electrode Surface State**



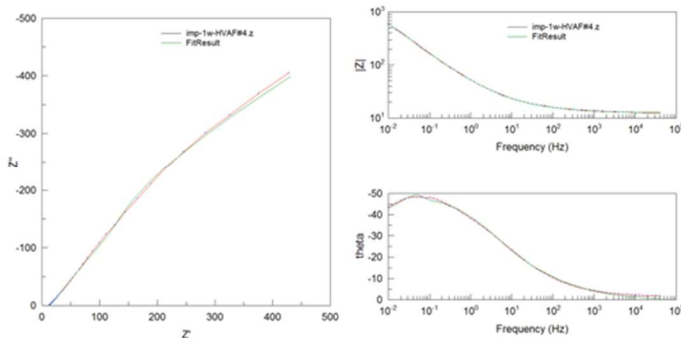
**Electrochemical Behavior**



**Polarization Curve Data**

Fit Quality ( $\chi^2$ )	18.473
$E_{corr}$ (V vs Ag/AgCl)	-0.56
$i_{corr}$ (A/cm <sup>2</sup> )	2.30E-05
Vmin (V vs Ag/AgCl)	-0.75
Vmax (V vs Ag/AgCl)	-0.31
$\beta_a$ (V)	498.65
$\beta_b$ (V <sup>-1</sup> )	4.62E-03
$\beta_c$ (V)	190.38
$\beta_d$ (V <sup>-1</sup> )	1.21E-02
$R_p$ ( $\Omega \cdot \text{cm}^{-2}$ )	2342.2

**Impedance Spectroscopy**



	Value	Error (%)
DC (V)	-0.4423	-
$R_e$ $\Omega \cdot \text{cm}^{-2}$	12.57	0.26729
$R_{ct}$ $\Omega \cdot \text{cm}^{-2}$	31.37	13.824
W-R $\Omega \cdot \text{cm}^{-2}$	3381	9.1505
W-t (s)	12.55	5.3928
W-p -	0.66133	2.4876
CPE-C $F s^{-(1-\alpha)}$	0.0066899	1.6879
CPE- $\alpha$ -	0.54124	0.46966
Fit ( $\chi^2$ )	0.00056157	

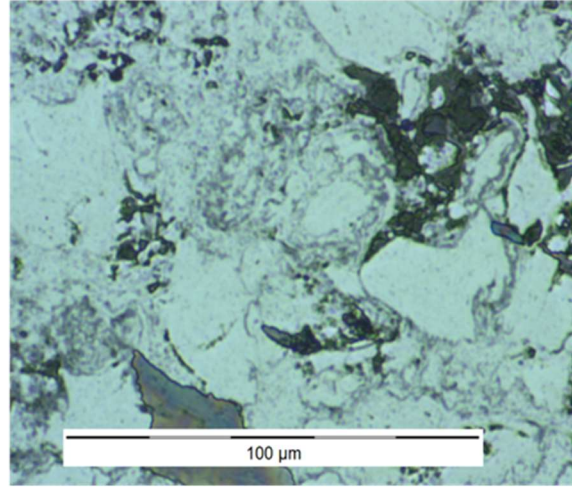
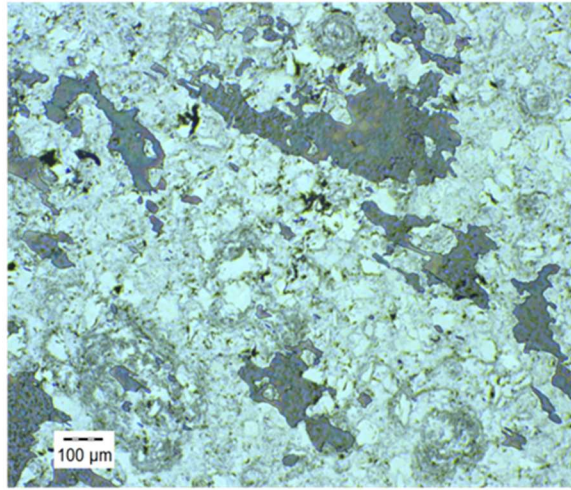
HVAF Set #  
Immersion Time

4  
2 Weeks

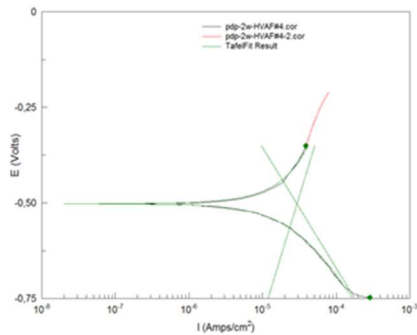
Date

17/Aug/2018

**Electrode Surface State**



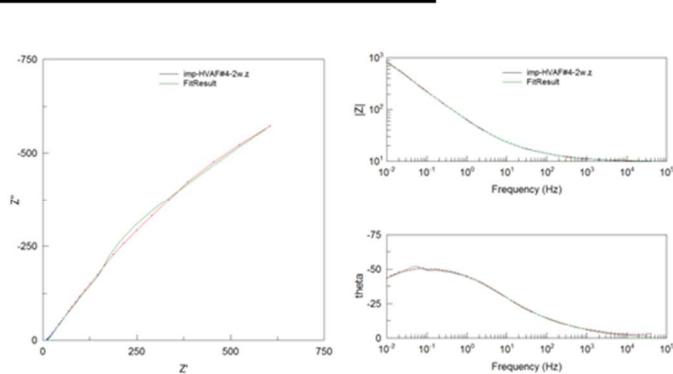
**Electrochemical Behavior**



**Polarization Curve Data**

Fit Quality ( $\chi^2$ )	16.256
$E_{corr}$ (V vs Ag/AgCl)	-0.5
$i_{corr}$ (A/cm <sup>2</sup> )	2.90E-05
Vmin (V vs Ag/AgCl)	-0.75
Vmax (V vs Ag/AgCl)	-0.35
$\beta_a$ (V)	628.89
$\beta_b$ (V <sup>-1</sup> )	3.66E-03
$\beta_c$ (V)	315.39
$\beta_d$ (V <sup>-1</sup> )	7.30E-03
$R_p$ ( $\Omega \cdot \text{cm}^2$ )	3017

**Impedance Spectroscopy**



	Value	Error (%)
DC (V)	-0.3932	-
$R_e$ $\Omega \cdot \text{cm}^2$	9.936	0.31598
$R_{ct}$ $\Omega \cdot \text{cm}^2$	25.59	9.2935
W-R $\Omega \cdot \text{cm}^2$	5017	7.2601
W-t (s)	10.9	3.88
W-p -	0.72312	1.7073
CPE-C $F s^{-(1-\alpha)}$	0.0049321	1.2652
CPE- $\alpha$ -	0.54669	0.34696
Fit ( $\chi^2$ )	0.00056827	

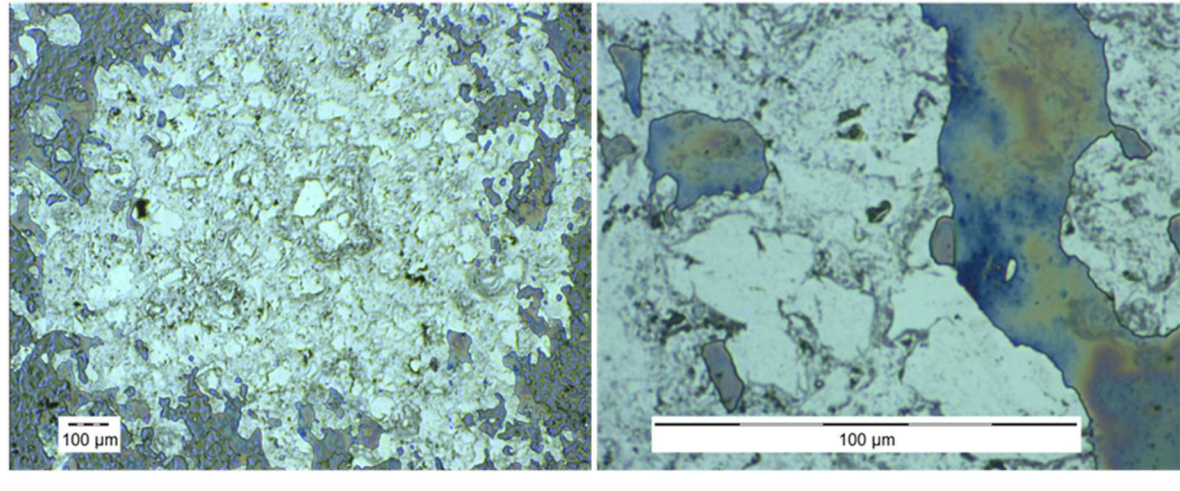
HVAF Set #  
Immersion Time

4  
3 Weeks

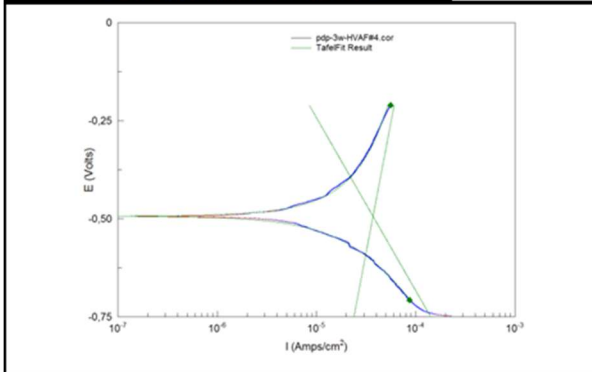
Date

24/Aug/2018

**Electrode Surface State**



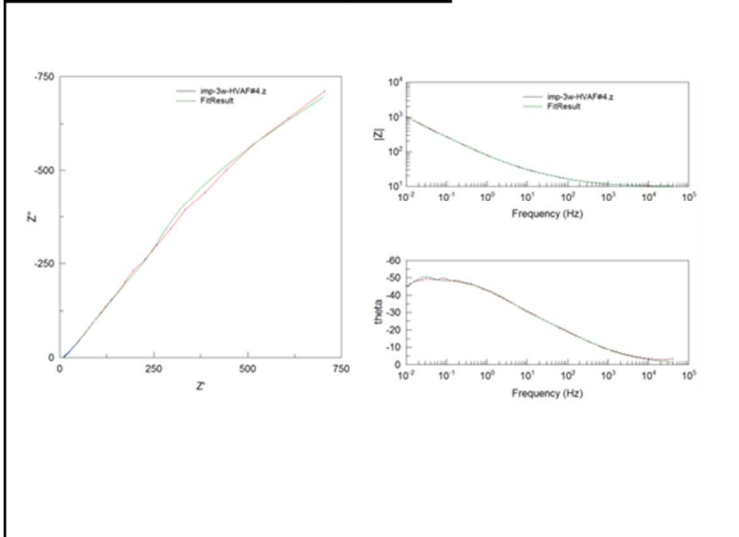
**Electrochemical Behavior**



**Polarization Curve Data**

Fit Quality ( $\chi^2$ )	18.072
$E_{corr}$ (V vs Ag/AgCl)	-0.49365
$i_{corr}$ (A/cm <sup>2</sup> )	3.72E-05
Vmin (V vs Ag/AgCl)	-0.71
Vmax (V vs Ag/AgCl)	-0.21
$\beta_a$ (V)	1329.42
$\beta_b$ (V <sup>-1</sup> )	1.73E-03
$\beta_c$ (V)	441.07
$\beta_d$ (V <sup>-1</sup> )	5.22E-03
$R_p$ ( $\Omega \cdot \text{cm}^{-2}$ )	3184

**Impedance Spectroscopy**



	Value	Error (%)
DC (V)	-0.4001	-
$R_e$ $\Omega \cdot \text{cm}^{-2}$	9.83	0.26354
$R_{ct}$ $\Omega \cdot \text{cm}^{-2}$	63.29	8.1315
W-R $\Omega \cdot \text{cm}^{-2}$	6463	8.451
W-t (s)	19.64	3.6432
W-p -	0.67848	1.9918
CPE-C $F s^{-(1-\alpha)}$	0.0038269	1.6022
CPE- $\alpha$ -	0.53152	0.31557
Fit ( $\chi^2$ )	0.00030471	